UNIVERSITÀ DEGLI STUDI DI PALERMO
Dottorato in Ingegneria dell'innovazione tecnologica
Dipartimento dell'Innovazione Industriale e Digitale (DIID)
Ingegneria Chimica, Gestionale, Informatica, Meccanica
Settore Scientifico Disciplinare ING-IND/26

CLOSING THE LOOP: STUDY OF INTEGRATED CYCLES WITH NATURAL AND ARTIFICIAL SOLUTIONS FOR THE PRODUCTION OF ENERGY, MINERALS AND FRESH WATER

IL DOTTORE
MAURIZIO BEVACQUA

COORDINATORE
Prof. Ing. ANTONIO CHELLA

IL TUTOR
Prof. Ing. GIORGIO MICALE

I CO TUTORS
Dr. Ing. ANDREA CIPOLLINA
Ing. WILLEM VAN BAAK

CICLO XXX
ANNO CONSEGUIMENTO TITOLO 2017

CONTENTS

INTRODUCTION

Nowadays the circular economy is considered as a practical solution to the planet's emerging resource crunch. Rare earth metals and minerals, reserves of key resources, are diminishing while exploration and material extraction costs are rising everyday more. Currently, the 'take-make-dispose' linear economy approach results in huge waste. Richard Girling describes in his book “Rubbish!” [1] the dramatic situation of the current approach. Almost 90% of the raw materials used in manufacturing becomes waste before the product leaves the factory, whereas 80% of products made is not used anymore within the first six months from their manufacture date. All these aspects coupled with growing tensions around geopolitics and supply risk, are pushing the commodity prices to high level. A circular economy could contribute to solve some of these issues exploiting waste material as a source of new goods.

In accordance with the circular economy concept, the main objective of this PhD thesis is to explore new methods to produce energy and minerals from waste sources, with focus on integrated cycles to “close the production loops”, thus minimizing waste production.

A huge amount of thermal energy is lost every day in the industrial sector, typically in a range of low temperatures (40-100 °C) which does not allow to exploit it in an efficient way [2–4]. A new method has been proposed in the “RED heat to power (RED HtP)” project [5], in order to convert waste heat energy into electricity by means of a reverse electrodialysis (RED) stack operating in closed-loop. In particular, the artificial solutions exiting from the RED unit are regenerated by means of waste heat in a suitable device purposely developed for this aim. The restoration of the salinity gradient can be obtained according to two ways which can be summarized as follows.

1) The more concentrated solution exiting from the Salinity Gradient Power (SGP) unit is integrated with a volume of diluted solution containing the required quantity of salt in order to restore the initial salt content in the solution. The excess water content is then removed from the concentrated solution via a suitable thermal separation (e.g. Multiple Effect Distillation, Membrane Distillation). Subsequently this excess water is added to the diluted solution to eventually re-establish the original concentration of the dilute stream. This scheme has been named “solvent extraction strategy”.

2) The quantity of salt transferred in the SGP unit can be restored by separating the same amount of salt from the dilute solution to restore the concentration of the concentrated solution. This scheme has been named “salt extraction strategy”.

One of the main focuses of this PhD is the study of this new idea of a “RED closed loop”, carried out through modelling and experimental activities. The research activities has inevitably been linked with the R&D of the EU-H2020 RED HtP research project, however maintaining the possibility to propose new ideas, e.g. the use of salt mixtures instead of a single salt.

In particular, in this PhD thesis the performance of particular salts for the case of the “salt extraction strategy” were studied. Among the possible regeneration procedures the use of thermolytic salts in aqueous solutions appears as the most promising. At ambient temperatures, these salts are soluble in water, while at a given higher temperature, they become gases that can be easily separated from the concentrated solution through a stripping process. A subsequent absorption process at lower temperatures is needed to let the concentrated solution absorb the salt. Ammonium bicarbonate is considered as the most suitable salt for this purpose as it can be degraded at very low temperatures (about 60°C) into NH_3 and CO_2. This salt was tested in a RED unit to assess its performance in a salinity-gradient power-generation device. A solution regeneration test-rig, i.e. a stripping column, was assembled in the lab to confirm the possibility to use heat at low temperature to regenerate the solutions exiting from the RED unit. In parallel two simplified models were developed, for the RED and the regeneration stages respectively, fully validated with experimental results. Finally, the two models were integrated in order to perform sensitivity analysis and calculate theoretical efficiency values of the whole closed system.

Part of the activities were also dedicated to the “solvent extraction strategy”. These activities were performed during two internships in The Netherlands at the laboratories of Fujifilm Manufacturing Europe B.V., a company that produces Ion Exchange Membrane for RED applications. New salts, mixtures of salts and combinations of solvent and salts were exploited to analyse their performances in a RED system. The main membrane properties were characterized with these artificial saline solutions. A RED simplified model was also developed to predict the performance of a specific RED unit using different salts in water.

The above activities were carried out during the first two years of the PhD Course, while the last year has been fully dedicated to develop original technological approaches for the recovery of minerals from natural waste streams. Waste brines from traditional saltworks may well be identified as the ideal source for magnesium recovery [6,7]. In this case, sodium chloride and other competitive salts (e.g. calcium salts) are already precipitated obtaining a waste-stream with an amount of magnesium thirty times higher than seawater. This mineral can be recovered by reactive crystallization in which an alkaline solution is mixed with the brine to produce magnesium hydroxide that is practically not soluble in water. The performance of traditional (CSTR) and innovative reactors (Multiple Feed – Plug Flow Reactor (MF-PFR) and Crystallizer with Ion Exchange Membranes (CrIEM)) has been investigated for this final purpose.

The present thesis has been divided into two sections to describe the procedures and the main results for the energy and mineral recovery from brine.

Section I: Energy conversion and storage from waste heat to electricity

In particular, **Chapter 1** presents an overview of the "RED closed loop system", describing the state of art of technologies that convert heat into power and reporting the process schemes, goals and strategy selection criteria of the RED HtP project.

Chapter 2 reports the theory of the RED technology and procedures to evaluate the main properties of ion exchange membranes. The performance of a RED unit with thermolytic salt and other specific salts at different operative condition are presented and discussed.

Chapter 3 describes the simplified RED model exploited to perform sensitivity analysis.

Chapter 4 presents the salt extraction strategy model implemented in a process simulator and the main results obtained with the lab test-rig. The experimental results were used to validate the model and the relevant comparison is shown.

Finally in **Chapter 5** the integrated model, which results from the merging of the two previously developed models for the RED and the regeneration sections, was used to perform a sensitivity analysis with thermolytic salts. Efficiency values are presented at different operative conditions.

Section II: Magnesium recovery from waste brine

C**hapter 6** describes the idea of an integrated cycle in which the waste of a process became a valuable raw material of another process. Fresh water, table salt, magnesium hydroxide and energy can be obtained integrating more processes all together. Market information are also reported.

Chapter 7 is devoted to describe the state of art of the methods used to recover magnesium from brine, focusing the attention on the waste brine from saltworks. The results obtained with a MF-PFR reactor were shown and discussed.

C**hapter 8** presents a new crystallizer which is based on the use of ion exchange membranes (CrIEM) in order to recover magnesium from waste brines with low value alkaline reactants, e.g. calcium hydroxide.

Finally **Chapter 9** describes the methods for the modification of magnesium hydroxide crystals. Two experimental campaigns were performed in order to better understand the growth stage in $Mg(OH)_2$ reactive precipitation. The future perspectives were also reported.

SECTION I

ENERGY CONVERSION AND STORAGE: FROM WASTE HEAT TO ELECTRICITY

Section Outline

1 HEAT-TO-POWER CONVERSION VIA CLOSED-LOOP REVERSE ELECTRODIALYSIS

Abstract

The continuous increase of global energy requirements raised the interest towards the development of new technologies to recover waste heat. Thermodynamic cycles are traditionally employed to convert heat into power but they can work normally with heat sources at medium-high temperatures. The use of closed-loop salinity gradient power (SGP) technologies has been recently presented as a viable option to generate power using low grade heat, by coupling a SGP unit with a thermally-driven regeneration process in a closed loop. Artificial solutions with different salts and solvents can be adopted for the conversion of heat-into-power. Among these, the closed-loop Reverse ElectroDialysis (RED) process presents a number of advantages such as the direct production of electricity, the extreme flexibility in operating conditions and the recently-demonstrated large potentials for industrial scale-up. This results into the concept of the "RED Heat to Power (RED HtP) engine", focused on the conversion of industrial waste heat into electrical energy and core idea of the EU-funded RED-Heat-to-Power project.

In this chapter, a literature overview of technologies able to exploit waste heat at low-medium temperature is presented. Strategies, process schemes and final goals of the RED HtP project are also reported, better highlighting the aspects which have been studied within this PhD work.

1.1 RED HtP concept and potential

The need of renewable and sustainable energy is growing as an issue of crucial importance for the sustainability of life on the Earth. Electricity is traditionally produced by heat engines, through the conversion of heat at high temperature into energy. The conversion of heat into electricity can be done at moderate temperatures (around 120-500 °C) through Organic Rankine cycles [4,8] and Kalina cycles [9]. However, there is still a lack of feasible technologies able to operate at lower temperatures (<100 °C) heat, despite the huge amount of low-grade waste heat available worldwide in this temperature range (e.g. about 833 TWh between 50°C and 100 °C only in the USA [10]). A valuable solution for the conversion of low-grade heat into available power is represented by heat engines based on salinity gradient technologies [11,12]. In these systems a Salinity Gradient Power (SGP) unit converts the chemical potential difference between two solutions at different concentration into usable power [13].

Different SGP technologies have been proposed so far. Among these, Pressure Retarded Osmosis (PRO) [14,15] and Reverse Electrodialysis (RED) [16–18] are the ones which reached the highest technological readiness level. Just as an example, a prototype able to produce almost 1 kW has been recently installed and efficiently operated in a real saltworks in Sicily (Italy) for a few months without any performance decrease [19,20].

PRO and RED perform the "controlled mixing" between the two solutions necessary for the energy generation, taking advantage from selective transport through suitable membranes. In PRO, osmotic membranes are used to guarantee the passage of pure water from the diluted solution (feed) channel towards the concentrated solution (draw) channel. The concentrated solution channel is pressurized at a pressure equal to one-half of the osmotic pressure difference between the two solutions. As a result, at the outlet of the draw channel, an additional amount of water at the applied pressure (i.e. the water flux through the membrane) is available. This quantity represents a mechanical power which can be exploited as it is or converted into electric power within a hydroturbine [21–23]. In RED, the two solutions are fed in alternatively arranged channels. One series is fed by the concentrated solution whilst the other is fed by the diluted one. The channels are separated by alternatively arranged anionic and cationic exchange membranes. Ions move from each concentrated solution channel towards the two adjacent diluted solution channels. Positive ions pass through cationic exchange membranes moving in one direction, negative ions

pass through anionic exchange membranes moving in the opposite direction. Such ionic flux is converted into an electron flux at the electrodes via redox reactions thus generating electric current supplying an external load [24–27]. Independently of the SGP technology employed, once the two streams at different salinity have been partially mixed to generate power, they can send to a "Regeneration unit" which employs heat to restore the initial salinity gradient thus closing the loop. This closed loop has been named Salinity Gradient Power Heat Engine (SGPHE) [12]. A simplified scheme is reported in Figure 1.1:

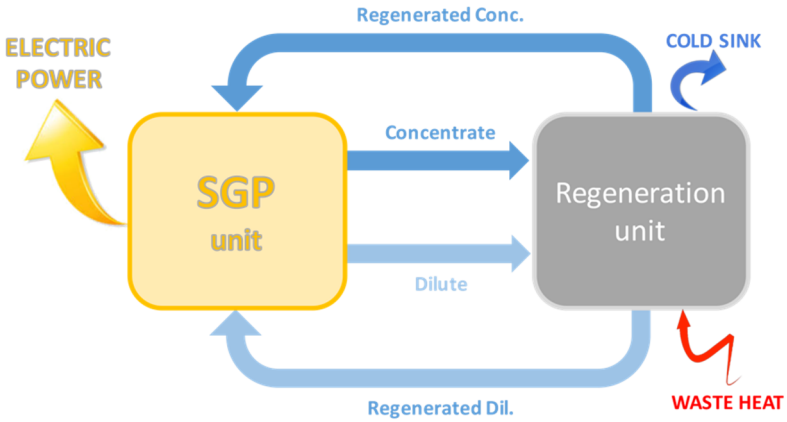

Figure 1.1: Simplified scheme of the Salinity Gradient Power Heat Engine (SGPHE).

The aim of the RED Heat-to-Power (RED HtP) project is based on the idea previously described. The project's purpose is to develop new advanced technologies and apply it for fully exploiting the potential of a Salinity Gradient Power Heat Engine to generate electricity from low grade heat in the temperature range of 40 to 100 °C (e.g. waste heat, geothermal and solar thermal). In particular, the concept is based on the generation of electricity using a Reverse Electrodialysis device as SGP unit in a closed-loop system, where limited amounts of artificial saline solutions are used as working fluids. The solutions exiting from the RED unit are then regenerated in order to restore the original salinity gradient, by means of a suitable separation process. Two different approaches can be considered for such a purpose:

1. The concentrated solution exiting from the SGP unit is mixed with appropriate volume of the diluted solution in order to restore the necessary quantity of salt

transferred in the RED unit to the dilute stream. The excess water content is then removed from the concentrated solution via a suitable thermal separation (e.g. Multiple Effect Distillation, Membrane Distillation). Subsequently this excess water is added to the diluted solution to eventually re-establish the original concentration of the dilute stream. This scheme has been named "solvent extraction strategy" [12];

2. The amount of salt transferred in the SGP unit can be restored moving it back from the dilute solution to the concentrated solution, restoring the initial concentration. This scheme has been named "salt extraction strategy" [12].

More details concerning the regeneration step are given in the next paragraphs.

The overall project objective is to prove this new concept, developing the state-of-the-art technologies necessary to achieve the final goal. The main purposes are summarized below:

- select the best technologies for the regeneration process;
- combine salts and solvents in order to maximise the system performance;
- create new knowledge for developing advanced membranes for the selected solutions;
- improve the stack design for high efficiency;
- implement and validate a process simulation tool to analyse the performance under different configurations and operating conditions;
- evaluate and improve the performance of the overall system (system efficiencies reaching 15% and power densities of 25 W/m^2 of cell pair).

1.2 Waste heat availability

In 2014, according to the International Energy Agency, global CO_2 emissions reached 32.4 Gt CO_2, an increase of 0.8% over 2013 levels [28]. In the current trend of reducing the CO_2 emissions, Industrial Waste Heat (IWH) is a potential energy source. The industrial sector is one of the top-three energy consuming sectors worldwide [29]. Therefore, the amount of IWH is expected to be important. This heat can be recovered and reused in other processes on site (to preheat incoming water or combustion air, preheating furnace loads, etc.), or transformed into electricity, cold or other types of heat. If this waste

heat is captured and used, rather than being released in the atmosphere, CO_2 emissions will be drastically reduced. In fact, the Intergovernmental Panel on Climate Change (IPCC) finds IWH recovery as one of the tools for CO_2 mitigation [3]. The identification and use of IWH is not an easy task despite produced in large quantity [3]. An estimation of the yearly produced industrial waste heat is shown in Figure 1.2:

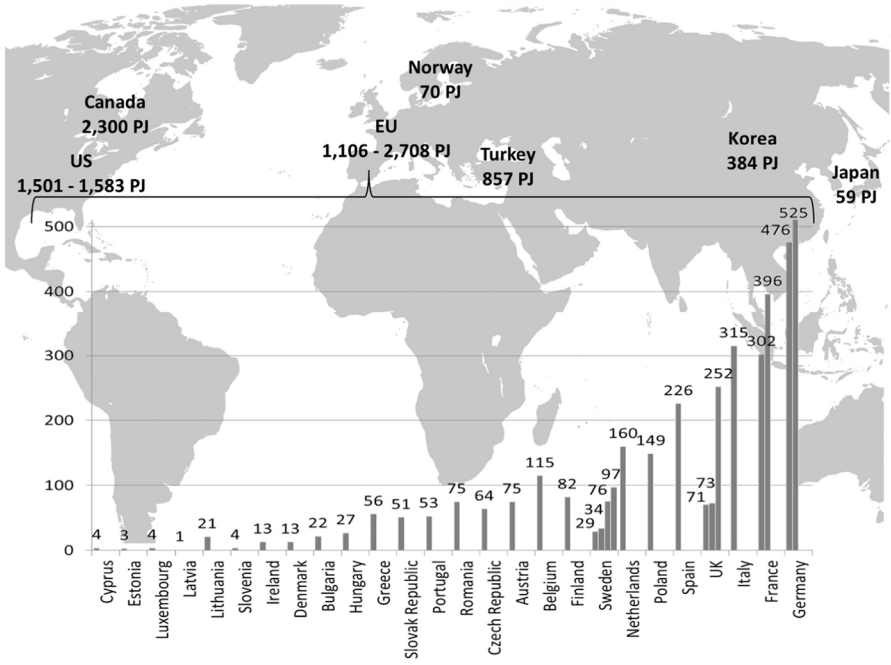

Figure 1.2: Yearly Industrial Waste Heat potential worldwide (in PJ). More than one potential is reported if more than one is found in literature [3].

The total amount of IWH reported in figure 1.2 does not include the amount produced by China. This very fast growing country is the largest energy user and CO_2 emitter in the world. Industrial waste heat in China accounts for 10–50% of total fuel consumption in various industrial sectors. As an example, in 2010 there were about 29 million tonnes of coal equivalent (Mtce), i.e. 850 PJ waste heat potential only in the Chinese ammonia industry, that is equivalent to the IWH of France and Germany [30].

Comparing the industrial waste heat potential with the energy consumed by each country (Figure 1.3), it can be seen that an important part of energy is lost as waste. If part

of this energy is recovered, in the perspective of circular economy, the industrial sector can become more energy efficient.

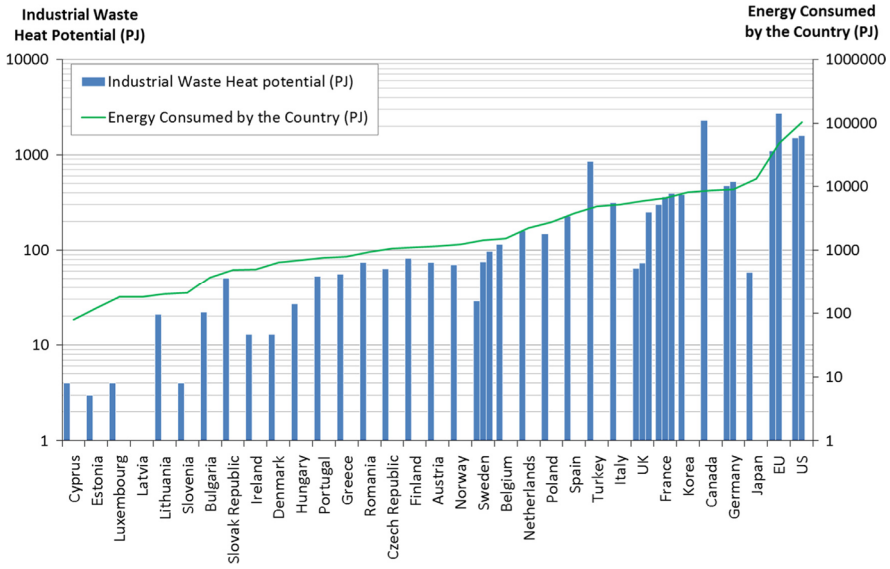

Figure 1.3: Industrial Waste Heat potential (in PJ) and Energy Consumed by the Country (in PJ). More than one potential is reported if more than one is found in literature [3].

The level of temperature is one of the most important criteria to judge if the process produces valuable waste heat to be converted into other useful forms of energy or not. There are different technologies available for high (HT > 400 °C) and medium (MT 100–400 °C) temperature with satisfying energetic efficiency, whilst only few technologies have been proposed for low temperature (LT <100 °C), yet at a very early stage of development.

A more detailed picture of possible waste heat sources is given in Table 1.1 [2]. Here exhaust gas temperatures are reported for different processes from 30 to over 1600 °C.

Table 1.1: Exhaust gas temperatures of different processes. Adapted from [2].

Temp range	Process	Exhaust gas temp (°C)
HT	Iron- and steelmaking	1450–1550
HT	Nickel refining furnace	1370–1650
HT	Steel electric arc furnace	1370–1650
HT	Glass melting furnace	1300–1540
HT	Basic oxygen furnace	1200
HT	Aluminium reverberatory furnace	1100–1200
HT	Steel heating furnace	930–1040
HT	Copper reverberatory furnace	900–1090
HT	Glass oven without regenerator	900–1300
HT	Iron cupola	820–980
HT	Cooper refining furnace	760–820
HT	Reheating furnace without regenerator	700–1200
HT	Hydrogen plants	650–980
HT	Fume incinerators	650–1430
HT	Coke oven	650–1000
HT	Glass oven with regenerator	600–800
HT	Cement kiln	450–620
HT	Heat treating furnace	430–650
HT, MT	Melting oven	400–700
HT, MT	Gas turbine exhaust	370–540
HT, MT	Reciprocating engine exhaust	320–590
HT, MT	Reheating furnace with regenerator	300–600
MT	Blast furnace stoves	250–300
HT, MT	Drying and baking ovens	230–590
HT, MT	Steam boiler exhaust	230–480
HT, MT	Finishing soaking pit reheat furnace	200–600
MT	Steam boiler	200–300
MT	Coke oven	190
MT	Stack gas	160–200
MT	Container glass melting	140–160
MT	Flat glass melting	160–200
HT, MT	Ceramic kiln	150–1000
LT, MT	Drying, baking, and curing ovens	90–230
LT, MT	Cooling water from annealing furnaces	70–230
LT, MT	Cooling water from internal combustion engines	70–120
LT, MT	Exhaust gases exiting recovery devices in gas-fired boilers, ethylene furnaces, etc	70–230
LT, MT	Conventional hot water boiler Process	60–230
LT	Process steam condensate	50–90
LT	Condensing hot water boiler	40–50
LT, MT	Hot processed liquids/solids	40–230
LT	Cooling water from air conditioning and refrigeration condensers	30–40
LT	Cooling water from air compressors	30–50
LT	Cooling water from furnace doors	30–50

When the waste heat is at high temperature, it is easier to exploit it in the production process itself, applying the concept of “thermal cascading” (i.e. the use of thermal energy for different applications, according to the required temperature range, e.g. preheating streams or as an internal utility).

Up to now there are not technologies that can exploit the exergy in an efficient way when the temperature is low. In this specific contest, the PhD work would contribute to

develop new knowledge and technologies to use the IWH at low temperature, converting waste heat into electrical power by means of a Reverse Electrodialysis system.

1.3 Alternative heat engines for waste heat conversion

According to Brückner et al. [2], technologies to use waste heat from industry can be categorized as passive or active technologies. Passive technologies use the heat directly at the same or at lower temperature level. In active technologies the heat is transformed to another form of energy or to a higher temperature heat (Figure 1.4).

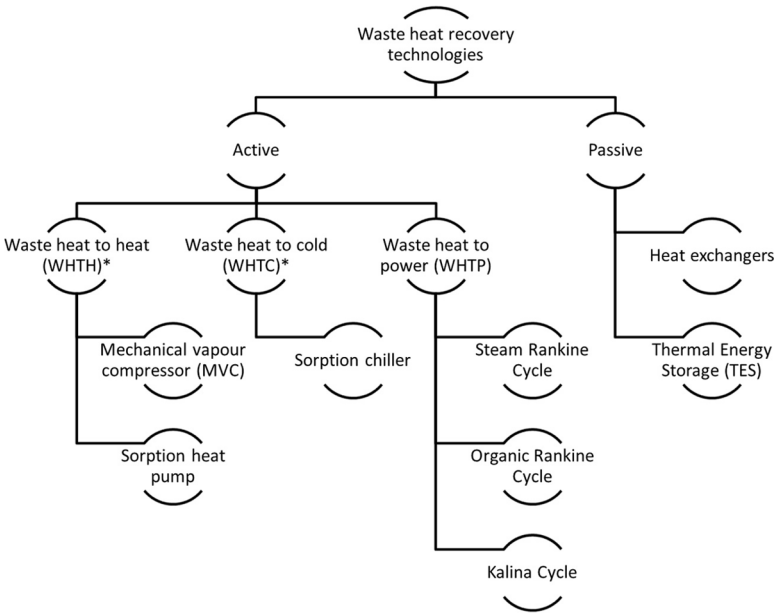

Figure 1.4: Classification of waste heat recovery technologies [2].

Heat exchangers and thermal energy storage devices are the two dominant passive technologies. These technologies can be used for recycling or reusing waste heat within an industry to heat or preheat other processes. Sorption systems, mechanically driven heat pumps and organic Rankine cycles (ORC) are active technologies. Active applications of waste heat are categorized into three types. Waste Heat to Heat (WHTH) provides heat. Waste Heat to Cold (WHTC) provides cold and Waste Heat to Power (WHTP) provides electricity. Among the active technologies, WHTH and WHTC are considered heat

transformation technologies as they modify the inlet temperature upgrading or downgrading it [2].

A key to better understand the Waste Heat to Power processes is to compare the different technologies, based on the main figures of merit which are extremely relevant to the performance analysis of processes themselves.

The energetic efficiency of each heat engine can be expressed as:

$$\eta = \frac{W}{Q_{wh}} \tag{1.1}$$

where W is the power produced by heat engine unit, while Q_{wh} is the thermal power of the waste heat. The thermodynamic limit of the cycle energetic efficiency is represented by the Carnot efficiency:

$$\eta_c = 1 - \frac{T_{cold}}{T_{hot}} \tag{1.2}$$

where T_{hot} is the heat source temperature, while T_{cold} is the temperature of the sink where residual heat is discharged [31].

Assuming a fixed ambient temperature of 292K as a cold sink for the process (T_{cold} = 292K), the Carnot efficiency becomes a function of the hot source temperature only and it is relatively low (η_c ~10-20%) using low temperature waste heat (e.g. ~ 323-373K). The actual energy efficiency of the heat engine will be inevitably lower than the Carnot efficiency. As a consequence, most technologies that are industrially adopted for recovering medium/high temperature ranges are not suitable in the low temperature range, where higher efficiency may be required to make the recovery economically feasible [32].

Another useful parameter often adopted for evaluating the cycle efficiency is the exergetic efficiency. Exergy expresses the maximum theoretical amount of work achievable when a heat flow is converted into power by an engine operating with any thermodynamic cycle. Looking at the numerical value of exergetic efficiency, for the case of a cycle for power production only, it would correspond simply to the ratio between the efficiency of the given power cycle and the efficiency of the Carnot cycle:

$$\eta_{ex} = \frac{\eta}{\eta_c} \tag{1.3}$$

For a comparison among different heat engines, the estimation of exergetic efficiency is the most appropriate.

The first technologies ever proposed to convert heat into power were thermodynamic cycles (i.e., systems that involve the use of heat to create mechanical energy to drive a turbine), but there are also more innovative technologies proposed and tested for the use of low-temperature heat [31].

1.3.1 Conventional cycles

Among thermodynamic cycles, the traditional Rankine cycle is still the most suitable process for recovery of exhaust streams with relatively high temperatures (300–550°C). In a Rankine cycle, heat is firstly converted into mechanical work, and ultimately into electricity using a turbine. The thermodynamic cycle consists of the following steps: 1) heat is used to generate steam in a boiler. 2) The steam is fed to a turbine for the generation of electricity. 3) The exhaust steam from the turbine is recovered in a vacuum condenser. 4) Finally, the condensed water is pumped to elevate its pressure and fed to the boiler [32].

Depending on the nature of the working fluid, various thermodynamic cycle can be identified, such as the steam Rankine cycle, organic Rankine cycle, supercritical Rankine cycle, Kalina cycle, Goswami cycle and trilateral flash cycle [33].

Steam Rankine Cycle (SRC). This thermodynamic cycle is the first method proposed and used to recovery waste heat. The working fluid for the conversion of heat into mechanical work is water, this makes a minimum allowable temperature for *SRC* application. Normally, the SRC systems are not adopted when the temperature of the waste heat source is below 340-370°C because, if the energy is not enough to superheat the steam, a water condensation can cause an erosion of the turbine blades. For the reason expressed above, *SRC* is largely adopted in the industry for recovering hot gases in the medium-temperature range (370-550°C). It is also applied in combined heat and power *(CHP)* systems at high temperature range (>650°C), where the Rankine cycle is directly fuelled by oil or coal. Energetic efficiencies for *SRC* are around 35% [33].

Organic Rankine cycle (ORC). This cycle applies the principle of the steam Rankine cycle, but uses organic working fluids with low boiling points. The cycle is configured with an expansion turbine, a condenser, a pump, a boiler and a superheater, provided that superheating is needed. Different pure working fluids can be used in organic Rankine cycles, such as HCFC123 ($CHCl_2CF_3$), PF5050 ($CF_3(CF_2)_3CF_3$), HFC-245fa ($CH_3CH_2CHF_2$), HFC-245ca (CF_3CHFCH_2F), isobutene ($(CH_3)_2C=CH_2$), n-pentane and aromatic hydrocarbons. Fluid mixtures were also proposed for organic Rankine cycles [33]. The organic working fluids have many different characteristics and advantages from water; e.g. the turbine built for *ORC* typically requires only a single-stage expander, resulting in a simpler, more economical system in terms of capital costs and maintenance [34].

The use of organic fluids is especially suitable for low- and medium-grade heat conversion (from 100°C to 300°C), thanks to their vapour–liquid characteristics. Typical energetic efficiencies range are between 5% and 15% [31].

Supercritical Rankine cycle. Working fluids with relatively low critical temperatures and pressures can be compressed directly to their supercritical pressures and heated to their supercritical state before expansion so as to obtain a better thermal match with the heat source. The heating process of a supercritical Rankine cycle does not pass through a distinct two-phase region like a conventional organic Rankine cycle, resulting in a better thermal match in the boiler with less irreversibility.

As a working fluid for supercritical Rankine cycle, carbon dioxide has desirable qualities such as moderate critical point, stability, little environmental impact and low cost. However, the low critical temperature of carbon dioxide, 31.1 8°C, might be a disadvantage for the condensation process. Organic fluids like isobutene, propane, propylene, difluoromethane have also been suggested for supercritical Rankine cycle [33].

Chen et al. [35] made a comparative study of carbon dioxide supercritical power cycle and compared it with an organic Rankine cycle using R123 as the working fluid in a waste heat recovery application. Their work shows that a CO_2 supercritical power cycle has a higher system efficiency than an *ORC* when taking into account the heat transfer behavior between the heat source and the working fluid. The CO_2 cycle shows no pinch limitation in the heat exchanger.

Kalina cycle (KC). In various novel thermodynamic cycles, the Kalina cycle is the most significant improvement in thermal power plant design since the advent of the Rankine cycle in the mid-1800s and it has been considered as an ambitious competitor against the Organic Rankine Cycle [36]. This variation of the Rankine cycle is based on the use of an ammonia–water mixture as working fluid. The use of a binary mixture, whose evaporation does not occur at a constant temperature but at increasing temperature, allows the efficiency to increase by 15–25% with respect to *ORC* at the same temperature level [31].

Goswami cycle. In the early 1990s, Goswami [37,38] proposed a combined power and cooling cycle now known as the Goswami cycle. The cycle as originally proposed employs ammonia water mixture as a working fluid and produces power and refrigeration, while power is the primary goal. It was later extended to other working fluid pairs also the cycle is a combination of an absorption refrigeration system and a Rankine cycle. Using ammonia-water mixtures, this cycle can be used as a bottoming cycle for waste heat from a conventional power cycle or as an independent cycle using low temperature sources such as geothermal, solar energy or waste heat. In this combined power and cooling cycle, low temperature heat (60-100 °C) is used [39].

Trilateral flash cycle (TLC). In this cycle, the liquid is heated up at constant pressure to its boiling point and then performs a flash expansion through an expander during which it delivers power. If the end point of the expansion is in the wet vapour region the process is represented in the temperature vs entropy (T-s) diagram approximately by a triangle and hence this cycle is called trilateral cycle. Due to the heat transfer without pinch point limitation, there is thermal matching between the temperature profiles of the heat source and the working fluid. TLC system is 14-85% more efficient over ORC [40].

Stirling engine (SE). This external combustion engine may well use a variety of heat sources such as solar, geothermal, or waste heat. It is however adopted when the temperature of the heat source is in the range from 120°C (i.e., low-temperature SE) up to 900°C (i.e., high temperature SE) [31].

1.3.2 Innovative devices for direct electrical conversion

New technologies have been recently developed, based on the direct conversion of thermal energy into electricity. Some of them may be promising options to recover waste heat in small-scale applications, however these technologies are currently affected by very low efficiency and high capital costs. Therefore their application for recovering industrial waste heat has not been proven yet.

Thermoelectric generation (TEG). This technology is based on the property of semiconductors able to convert a temperature difference into electric potential (Seebeck effect). These devices are very simple and compact and they are currently used to convert heat directly into electricity [41]. According to its working principle, a TEG device neither requires moving parts nor consumes liquid or gas media, implying favourable qualities such as high reliability and eco-friendliness. The research of thermoelectricity has attracted great interest from both scientific and industrial communities but the technology is still affected by rather low efficiency. The efficiency reported by Little et al. [4] for such devices is 2-3% when the temperature of waste heat source is 60-120°C respectively.

Piezoelectric power generation with waste heat-powered expansion/compression cycle (PEPG). A piezoelectric thin-film membrane is used to create electricity from mechanical vibrations from a gas expansion/compression cycle fed by waste heat (150–200°C). It is practically based on an innovative, two-stage, simple conversion mechanism. First, a constant heat source supplies a passive, auto-oscillating mechanism through an evaporator generating mechanical energy via a capillary tube. This mechanical energy is then converted into electricity using a piezoelectric membrane component during the second step of the conversion. [42]. There are still strong technological challenges, nonetheless, compared to Seebeck-effect generators, this innovative approach is not limited by material properties and significant engineering improvements can be achieved. Energetic efficiencies of about 1% are reported in the literature [31].

Carbon carrier Cycle (CC). This technology was recently patented by Karthauser et al. [43]. It is a modification of the consolidated Rankine cycle, instead of using a condenser, this technology consists of a CO_2 chemical absorption process to create

pressure reduction downstream of the turbine. The authors of the patent claim to achieve efficiencies up to the ideal Carnot efficiency, though no applications have been reported to date. Waste heat at temperature of 150°C can be theoretically exploited for such energy conversion device [32].

Organic Rankine cycle or Kalina cycle are technologies already well tested for many years and they are currently used to convent waste heat into electricity. These technologies can work with acceptable efficiency until a temperature of 100 °C, as already expressed before. Up to now, there isn't a technology able to exploit waste heat at temperature below 100°C. The aim of the RED Heat to Power project is to adapt a Reverse Electrodialysis system to generate electricity operating in a closed loop, with the regeneration the working fluids by means of waste heat.

1.4 The RED-HtP project

In the last decade, Reverse Electrodialysis technology has been widely addressed as a viable technology for the conversion of salinity gradient energy into electricity. Up to now, RED technology has been essentially focused on the use of natural streams, such as river water, seawater or brine [44–60]. This allows to exploit an extremely high potential especially in coastal regions, where large amounts of such streams are available.

On the other hand, the utilization of natural salinity gradients presents some remarkable disadvantages:

- need for energy intensive pre-treatment processes to prevent fouling/biofouling phenomena;
- geographic constraints for plant location (i.e. availability of both diluted and concentrated streams in the same area);
- large flow rates of streams required.

These disadvantages may be overcome in a RED "closed loop" (RED-CL) process, i.e. a stand-alone system where artificial solutions may be used as working fluids for the RED process. The exhausted streams can be afterwards regenerated through a proper separation process, and eventually recycle back to the RED unit.

The use of such RED-CL system presents another notable benefit: the possibility to use artificial solutions instead of natural streams results in a large number of possible

combinations for the salt and solvent to be selected in order to enhance the overall process performance. For instance, very highly soluble salts can be used, allowing to reach considerably high driving force for RED process.

The aim of the RED Heat-to-Power project, as previously explained, is to develop new knowledge and exploit the potential of this innovative concept: the generation of electricity from low grade heat in the temperature range from 40 to 100 °C (e.g. waste heat, geothermal and solar thermal) by means of a Salinity Gradient Heat Engine (SGHE). A simplified scheme of the RED Heat-to-Power process is shown in Figure 1.5 and it is defined by two main steps: i) a power generation stage (where saline solutions are used to generate electric current) and ii) a regenerative stage (where the concentration difference is restored). As the name of the project suggests, the unit to convert salinity gradient into electricity is a Reverse Electrodialysis system whilst different units can be used for the regenerative system.

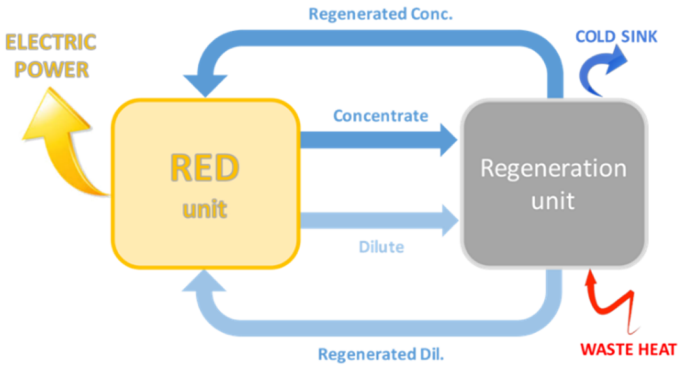

Figure 1.5: Simplified scheme of the RED heat-to-power project concept.

In a RED closed loop unit, limited amounts of artificial saline solutions are used as working fluids to generate electric current. When two salt solutions at different concentration are fed into the stack, i.e. a device containing membranes and spacers piled between two electrodes, the salinity gradient forces the ions to move through the membranes (Figure 1.6). This ionic flux is regulated by ions mobility and membrane permselectivity, i.e. the selectivity towards cation/anion transport through Ion Exchange Membranes, which generate a net ionic current through the stack. The ionic flux is then

converted into an electron current by means of redox reactions at the electrodes, positioned at the two ends of the stack.

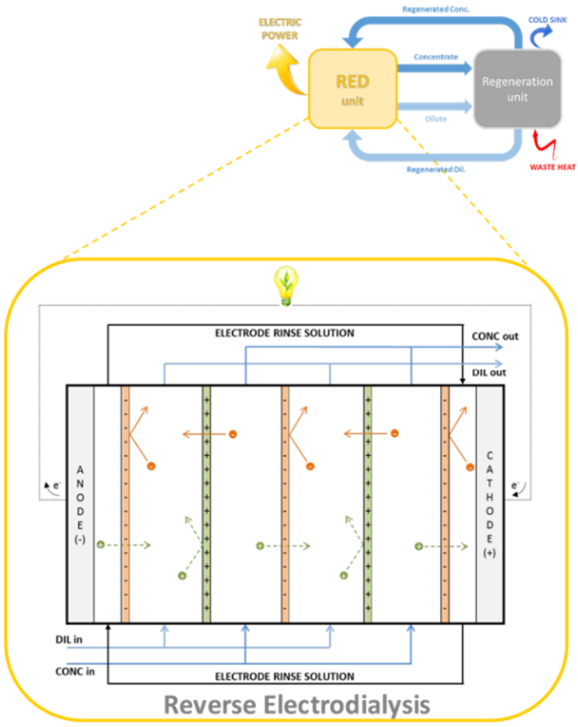

Figure 1.6: Reverse electrodialysis simplified scheme.

The solutions exiting from the RED unit are then regenerated in order to restore the original salinity gradient, by means of a separation step, which uses low-temperature heat as its energy source. The regenerated solutions can be stored at very low costs and the stack can react within seconds, providing high flexibility to the power system.

The RED Heat-to-Power concept possesses an intrinsic flexibility, opening many possible alternatives in terms of the salts, the solvents and the associated regeneration technologies that can be used. Each option has different advantages and disadvantages in terms of performance of the components and the overall system as well as in terms of cost, safety and environmental considerations.

The strategies for the regeneration, analyzed and described in more details in the next paragraphs, are divided in two categories depending on the operative temperature range: 60°C – 100 °C and 40°C – 60°C.

1.4.1 Possible system configurations: heat sources from 60°C to 100°C

The first class of processes, operating with heat sources between 60°C and 100°C is based on the solvent extraction concept outlined in Figure 1.7. The two solutions are regenerated by partial evaporation of the solvent from the concentrate stream (F2) exiting the RED unit. In order to rebalance the salt transfer within the RED unit from the concentrate solution to the dilute one, a preliminary mixing of stream F1 into F2 is performed, which restores the original amount of solute in the concentrate loop. The stream F2 is then processed in the regeneration unit, resulting into two exiting streams, i.e. a solute rich stream (the regenerated "concentrate stream", F5 or $F_{c,in}$) and a "virtually" solute free stream (F4), which is mixed with the stream F3 resulting in the regenerated "dilute stream", $F_{d,in}$.

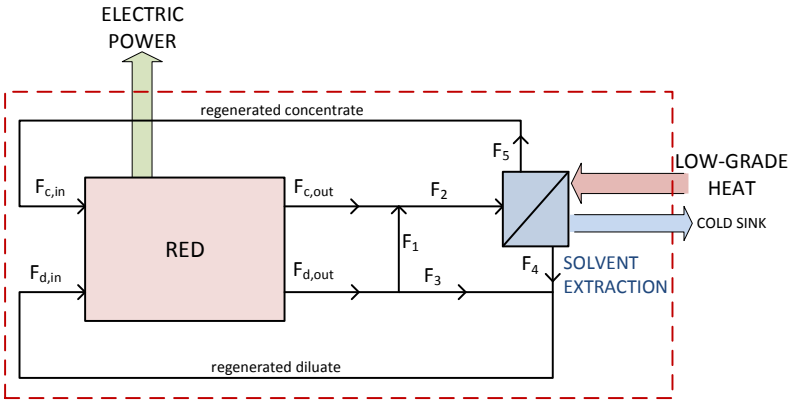

Figure 1.7: Conceptual scheme of the process with solvent extraction regeneration.

The main option considered for the regeneration unit in the solvent extraction concept (temperature range 60°C - 100°C) is the Multiple Effect Distillation (MED) technology. The main issue is the maximisation of its efficiency. The system can operate at temperatures higher than the 70°C limit adopted in seawater desalination, since it does not have to deal with scarcely-soluble salts that are present in seawater and precipitate at these

temperatures. The option to externally enhance the energetic efficiency through vapour regeneration by adsorption/desorption cycles is also considered.

The second technology for the solvent extraction concept is Membrane Distillation (MD). This is an emerging technology and there are still different approaches. In the RED Heat-to-Power project, two available alternatives, i.e. spiral-wound or vacuum multi-effect (V-MEMD) configurations, are analysed to assess which one is the most suitable. One of the main advantages of MD compared to MED is the flexibility to be easily scaled down, making MD suitable for smaller applications.

Solvent

The main solvent considered for all cases is water. One idea that has been explored for the solvent extraction is to add organic solvents to the water. This could enhance: i) the performance of the evaporative process by reducing the vaporisation enthalpy or ii) the formation of azeotropic mixtures with the aqueous solutions, resulting in a decrease of the process operating temperature.

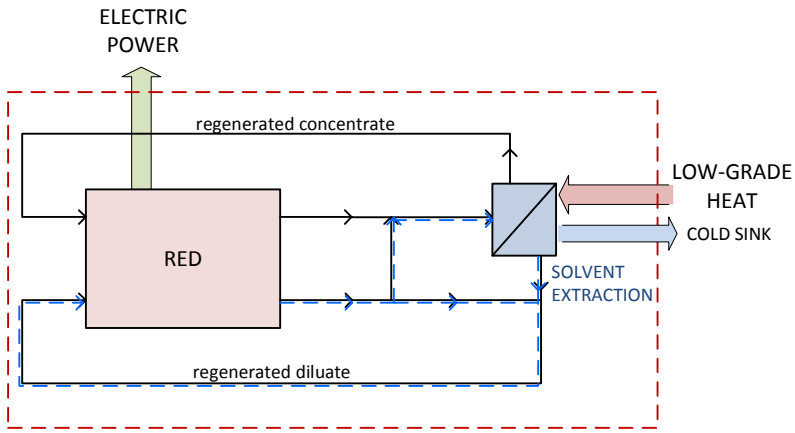

Figure 1.8: Conceptual scheme of the solvent extraction with organic solvents

A non-aqueous solvent is added to the dilute loop to reduce the heat required for the separation and the temperature at which heat must be supplied. The solvent will be initially added in the dilute loop as shown in Figure 1.8. The evaporative separation stage will separate a solvent-rich stream to be mixed with the dilute exiting from the RED unit, thus regenerating the feed dilute stream. Depending on IEMs selectivity and separation process

efficiency, some of the solvent may circulate also in the concentrate loop, but process simulation can be used to define compositions for steady-state operation. The motivation to add different solvents comes from the possible increase of the regeneration efficiency. The expected performance of the RED system with these solvents is also a matter of investigation in the EU project, to assess the viability of this approach from an overall point of view.

Salts

When the solvent extraction process is adopted, a salt has to be selected for forming the artificial solution. The starting point is NaCl, since this is the most abundant salt in seawater and both RED and the evaporation technologies have been designed to operate with that salt. However, since there is freedom to select any salt, different combination can be tested to optimize the overall performance, productivity and competitiveness.

For that purpose, tables were prepared in order to list the relevant characteristics of salts, such as solubility, activity coefficients and solutions conductivity when dissolved in the aqueous medium. A preliminary theoretical assessment provides indications on salts that could significantly increase the performance of the RED system, even if the IEMs would have to be adapted for optimal performance with these salts.

In the SGPHE, the RED performance is a crucial factor but this work takes also into account the effect that the new salts would have on the evaporative regeneration process because of the variations they cause on the (a) Boiling temperature (BPE), (b) Latent heat, (c) Equilibrium conditions (activity coefficients) and (d) Transport properties (density and viscosity). The aim is to choose the salt(s) that maximise the overall efficiency, performance and competitiveness.

1.4.2 Possible system configurations: heat sources from 40°C to 60°C

Forward Osmosis regeneration

When the heat sources are between 40°C and 60°C, regeneration can still be based on the “solvent extraction” (Figure 1.7) concept by adding a second loop connected to the RED loop by means of a Forward Osmosis (FO) unit. As illustrated in Figure 1.9, the aqueous solvent will be extracted in a Forward Osmosis unit using a temperature-sensitive drawing agent. The extracted water and drawing agent will then be separated by a

separation step powered by very-low temperature heat. This will generate two streams: the water-rich stream to be recycled in the dilute loop and the fresh draw agent to be re-used in the FO unit.

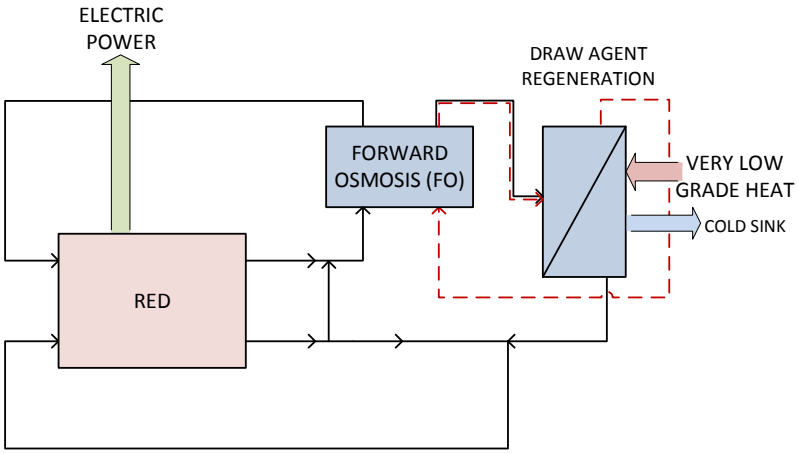

Figure 1.9: Regeneration by a second loop with Forward Osmosis solvent extraction

The use of the FO loop allows freedom for the selection of salts in the RED loop, which can be promising as described in the next section. Regarding the drawing agents to be used in the Forward Osmosis loop there are several options with a "switching behaviour" in the temperature range of 40-60°C considered, such as:

1) temperature sensitive hydrogels, capable of adsorbing/desorbing very large quantities of water following heating/cooling cycles;

2) temperature-switchable solubility solutes, i.e. salts, which can change their polarity within carbonation/de-carbonation and heating/cooling cycles (e.g. alkyl-amine salts);

3) temperature-switchable solvents, which can change their water miscibility within carbonation/de-carbonation and heating/cooling cycles (their behaviour could be assimilated to the T-switchable salts, being the only difference that the solvents are normally present in the liquid phase).

Solute extraction

An alternative to the solvent extraction strategy of Figure 1.7 is the solute extraction concept shown in Figure 1.10 where thermo-sensitivity properties are used to separate the salt from the dilute solution exiting the RED unit.

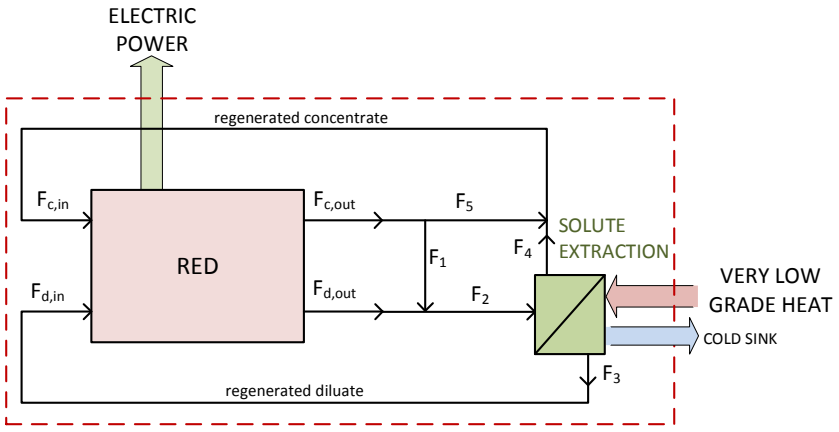

Figure 1.10: Conceptual scheme of the process with solute extraction regeneration

Excess salt in the dilute stream exiting from the RED unit (F2) is extracted by a salt extraction based on the variation of salt solubility (or salt degradation) when increasing the temperature above 40-50°C. Moreover, in order to re-balance the amount of solvent that has passed due to osmotic flux through the IEMs, a by-pass stream (F1) from the concentrate loop is mixed with the stream $F_{d,out}$ before entering the salt extraction unit. The separation stage will result in two exiting streams, a solvent rich stream (F3) and a solute stream (F4) which can be used to regenerate the original composition in the dilute and concentrate feed solutions respectively.

Within the salt extraction concept previously described, two types of salts with suitable characteristics can be considered. Switchable-solubility salts and thermolytic salts. Switchable-solubility salts can change their polarity and therefore their solubility in aqueous solutions within carbonation/de-carbonation and heating/cooling cycles. Thermolytic salts undergo a degradation process which produces gaseous species when the temperature is increased over a certain limit. NH_4HCO_3 (ammonium bicarbonate) for example is converted into CO_2 and NH_3, developing a gas phase easy to separate from the liquid solution when temperature exceeds a critical value (40°C to 60°C, depending on

unit pressure). In both cases the salts are selected because of their specific characteristics that make them suitable for regeneration with heat at very low temperatures.

In this PhD work, both strategies were taken into account, trying to select good salts and solvents to improve the power generation. However, the salt extraction salt with thermolytic salt was widely investigated, considering both power generation and regeneration stage, by means of experimental test and modelling tools.

1.4.3 Consortium structure and main goals

The primary objective of the RED HtP is to prove a new revolutionary concept and developing the necessary materials and components, but also to bring such a technology to the level of a lab prototype capable of generating electricity from low-grade heat, at higher efficiencies and lower costs than ever achieved.

Several issues have to be solved during the project period time (2015–2019) and challenging goals have to be achieved. In order to develop this new technology, the role of the project consortium is fundamental. The project consortium is constituted by seven partners from universities, research centers and industries from five countries in Europe, with extensive and complementary expertise. The partners are following listed:

1. Wirtschaft und Infrastruktur GmbH & Co Planungs-KG (WIP), coordinator - Germany;
2. Università degli Studi di Palermo (UNIPA) – Italy;
3. Fujifilm Manufacturing Europe B.V. (FUJI) – The Netherlands;
4. REDstack B.V. (REDstack) – The Netherlands;
5. Centro de Investigaciones Energéticas, Medioambientales y Tecnológicas (CIEMAT) – Spain;
6. University of Edinburgh (UEDIN) – UK;
7. Universitat Politècnica de Catalunya (UPC) – Spain.

Each partner is involved based on the particular expertise in its specific sector. Two companies are expert in the RED systems manufacturing. In particular, Fuji is a membrane producer in the main field of ion exchange membranes, whilst REDstack is a small company that assembles RED units with different geometries. CIEMAT and UEDIN are mainly involved in the regenerative stage and they are focused in the solvent extraction strategy. UPC studies the transport phenomena of ions through reverse electrodialysis

membranes, essential aspect for the performance improvement of this technology. Università degli Studi di Palermo is mainly involved in the CFD modelling, the study of regeneration systems and the performance analysis of new salts and solvents. All the partners are coordinated by WIP, an organization with established experience in the EU projects coordination.

The RED-HtP project aims to boost the development in a number of key technological research areas, given the highly interdisciplinary nature of research activities planned. Among the highly-interconnected R&D activities, some of these are here highlighted for their high-impact innovation potential:

Use of artificial ionic solutions: Starting from fundamental studies, a number of different salts solutions with potential to increase the RED power density have been analysed (e.g. LiBr, KNO_2, KCH_3COO, NH_4HCO_3). The RED process was tested for the first time with artificial feed streams and it is expected to deliver important performance enhancements with respect to the case of conventional NaCl aqueous solutions.

Use of organic solvents: Aside from water and common salts, the use of organic solvents were investigated (like Methanol, Ethanol, Acetonitrile). This was expected to deliver a significant performance enhancement during the regeneration stage, allowing the operation with lower heat source temperature and higher efficiency. Organic solvents are used for the first time in RED, giving the opportunity to generate new knowledge.

Development of new membranes for artificial solutions: Most of the Ion Exchange Membranes (IEMs) currently available on the market are purposely designed for aqueous sodium chloride solutions. The use of different salt/solvent, including the use of azeotropic water/organic mixtures, will require adaptations and new materials for the membrane compositions that maintain low electrical resistance and high permselectivity also for the conditions of RED Closed Loop applications.

Development of improved membranes: The work is focused on the development of thinner and profiled membranes. Thinner membranes will have lower resistance, resulting in increased power densities. Profiled membranes will improve the overall system fluid dynamic and energy generation performance, allowing operation without spacers and

eliminate a major cost element [61]. Also the transport properties are investigating to better understand and improve the relationship between the membrane structure and its transport properties [62,63]. These developments would allow increasing power densities and reducing costs, thus contributing to a technological breakthrough in the field of salinity gradient power and other processes using such membranes (e.g. desalination).

Development of integrated set of non-stationary electrochemical measurements with novel IEMs: To better understand and exploit the mechanisms of selective trans-membrane ion transfer one needs to separate information on the ion partitioning and diffusivities, which can be provided only by non-stationary methods. The most common non-stationary electrochemical characterization technique is Impedance Spectroscopy. Complementary techniques of current switch-off and concentration step (developed by UPC) provide useful additional information and make the interpretation more reliable. For extensive comparative studies of various membranes, a reliable standardized methodology is needed. A novel integrated set of standardized and rapid non-stationary electrical measurements and an advanced interpretation model are developed. These are used for studies of tailor-made IEMs properties in a broad range of inorganic and organic electrolyte solutions.

Improved stack design: The RED stack design used for the current applications will be revised to be adapted for the closed loop conditions. The best geometrical configuration (in terms of width/length ratio, channel thickness and geometry of profiled membranes, feed streams distribution systems and parasitic current inhibitors, etc.) are identified thanks to focused laboratory investigation and simulations predictions. Moreover new design for distribution manifolds and membrane stacking will aim at reducing ionic short cut current losses, to further enhance the process performances and scaling-up potentials.

Selection of new redox processes and electrodes for artificial solutions: New redox processes, suitable for operating with non-conventional solutions and current densities much higher than typical ones, are studied. The research aims at identifying the best redox couple, electrodes and electrolytes, but it will also investigate the possibility of adopting capacitive electrodes, which are very promising [55]. The advantage of capacitive

electrodes is that no redox couple is required and that gas evolution and other unwanted products from electrode reactions can be prevented, which represent a significant and practical advantage.

Regenerative processes:

(1) Low-temperature range (i.e. 60-100°C). the aim of solvent extraction by improved MED and MD processes is to increase energy performances thanks to the coupling with adsorption/desorption cycles for vapour regeneration, in order to halve the current energy consumptions. Moreover the use of non-aqueous solvents or selected azeotropic mixtures can contribute to further enhance the thermal efficiency of the separation.

(2) Very low-temperature range (i.e. 40-60°C). Salt extraction by the use of thermolytic salts allows to explore a new concept of regeneration strategy at such low temperature ranges. On the other side, solvent extraction through heat-powered Forward Osmosis with temperature sensitive drawing agents aims at delivering enhanced performances to the RED-HtP system. Therefore it will be of large impact also for the desalination industry, where this innovative separation technology powered by thermal energy could be successfully applied for the production of freshwater from non-conventional water resources.

Integrated system: the RED HtP technology is expected to achieve superior energy performance with respect to all other state-of-the-art competing technologies.

The main project targets are reported in the Table 1.2. As can be noted, the performance targets are challenging, expecially on the energetic and exergetic point of view. In order to achieve these targets, both stages (RED system and regeneration) have to be developed and improved with a deep collaboration of all the partners.

Table 1.2: Performance targets for the RED HtP project at month 28 and month 45

	RED technology			**Regeneration technologies**		**Integrated RED HtP system**	
	IEMs perm-selectivity[1]	IEMs areal resistance[1]	Maximum Power Density	Heat requirements for solvent extraction	Heat requirements for salt extraction	Exergetic efficiency[2]	Energetic efficiency[2]
Month 28	above 70%	Below 1.5 $\Omega \cdot cm^2$	15 W/m^2 cell pair	40 kWh/m^3	200 kJ/mol	40%	Range: 4-8%
Month 45	above 85%	Below 1 $\Omega \cdot cm^2$	25 W/m^2 cell pair	25 kWh/m^3	100 kJ/mol	75%	Range: 8-15%

1 IEMs targets refer to the novel membranes developed for non-NaCl artificial solutions. For NaCl-optimised membranes the targets are: 90% permselectivity and < 0.5 $\Omega \cdot cm^2$ areal resistance using saturated NaCl brines.

2 Exergetic efficiency targets are fixed, which result in a range of actual energetic efficiencies depending on the adopted heat source temperature (in this table considering the range 60-100°C) and, thus, maximum Carnot efficiency used as a reference.

2 THEORETICAL AND EXPERIMENTAL INVESTIGATION FOR SALTS/SOLVENT SELECTION IN RED HEAT ENGINES

Abstract

Salinity gradients are available from natural waters such as seawater and river water or they can be artificially generated by mixing solvents and solutes in order to use them within closed-loop applications. In this latter case, when the salinity gradient is adopted to operate a RED unit, the deployed gradient of the solutions exiting the RED generation stage can be regenerated in a thermally-driven unit using low-temperature heat. The regeneration of salinity gradient can be obtained through two different strategies: i) solvent extraction and (ii) salt extraction. In the first one, the concentrate solution exiting from the SGP unit is first mixed with a certain amount of exiting dilute solution, thus recovering the initial salt content. The excess water in the obtained stream can be separated via a suitable thermal separation process, and can be eventually integrated in the dilute in order to restore the water balance in the two loops. In the salt-extraction strategy, the amount of salt transferred in the SGP unit can be restored by thermally separating the same amount of salt from the dilute solution and integrate it within the concentrate one.

In this chapter, both strategies were considered, in order to analyse how the selection of solutions can influence the RED power production. Different salts and salts mixtures were studied by means of laboratory investigation carried out also at the Tilburg Research Laboratories of FUJIFILM Manufacturing Europe B.V. A wide experimental campaign was carried out using ammonium hydrogen carbonate, a thermolytic salt that degrades into gas species (i.e. ammonia and carbon dioxide) when heated at temperature above 40-50°C. This was selected as the best option for the salt extraction strategy and has been more carefully analyse in the next chapters.

---

[*] Part of this chapter has been published as:

M. Bevacqua, A. Carubia, A. Cipollina, A. Tamburini, M. Tedesco, G. Micale, Performance of a RED system with Ammonium Hydrogen Carbonate solutions, Desalination and Water Treat. 3994 (2016) 1–12.

2.1 Reverse electrodialysis process

When two salt solutions at different salinity are mixed together, an amount of energy equal to the Gibbs free energy is lost unless a suitably controlled mixing process is carried out. This can be performed in a Reverse Electrodialysis stack where two solutions are fed into different channels separated by the presence of ion exchange membranes.

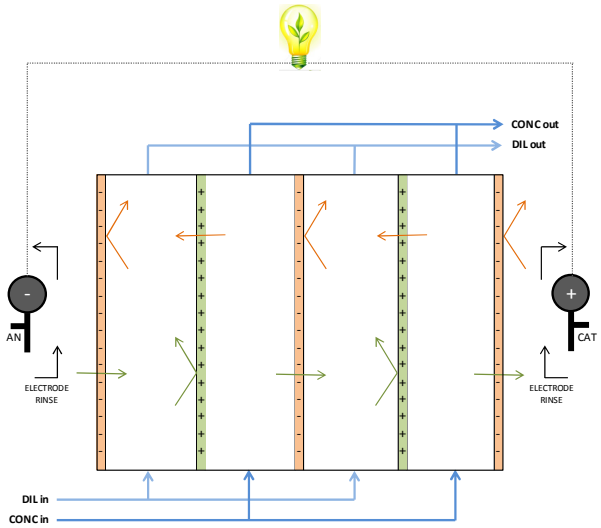

Figure 2.1: Reverse electrodialysis simplified scheme.

The concentration gradient between the two solutions forces the ions to move through the membranes. This ionic flux is regulated by ions mobility and membrane perm-selectivity, i.e. the selectivity towards cation/anion transport through Cation Exchange Membranes/Anion Exchange Membranes, respectively. This generates a net ionic current through the stack. Eventually, this ionic current is converted into electric current by means of redox reactions at the electrodes, positioned at the two ends of the stack, and can be conveyed to an external load. An important part of a RED stack are the membranes, described in more details in the next paragraph.

2.2 Ion exchange membranes

Today, membrane separation processes have become essential materials not only in industries, but also in day-to-day life. A membrane is a selective barrier that allows the

passage of specific constituents and retains others present in a dispersing medium, frequently a liquid. Many membranes have been developed for the use in nanofiltration, ultrafiltration, microfiltration, pervaporation separation, reverse osmosis, electrodialysis and in medical use such as artificial kidney. Among those, ion-exchange membranes are one of the advanced separation membranes [64]. Basically, the ion exchange membranes separate cations from anions and anions from cations and they are the main key elements in a RED process. They can be divided in two types: cation exchange membranes (CEM) and anion exchange membranes (AEM). As can be seen in Figure 2.2, cation exchange membranes have negatively charged groups attached to a polymeric matrix while anion exchange membranes have positively charged groups [65].

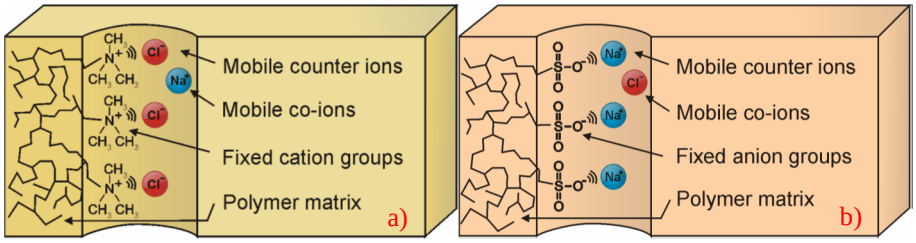

Figure 2.2: Anion exchange membrane (a) and cation exchange membrane (b) [65].

Ions are called co-ions if they have the same charge of fixed groups in the membrane whereas they are denoted as counter-ions if they have opposite charge.

In principle, the co-ions are excluded by the membranes and only counter-ions are able to permeate through it. If all co-ions are rejected, this means that the permselectivity membrane is 100%, while lower values indicate that counter-ions pass through the membranes. This concept will be widely explained in the next paragraph.

In a RED unit, a cation exchange membrane is in contact with a diluted electrolyte solution and due to the presence of the fixed charge, the cations concentration will be higher in the membranes than in the solution. On the other hand, the anions (co-ions) in the membrane will be lower than in the solution. Due to this behaviour, a concentration difference is created and the ions start to migrate from one side to the opposite in order to maintain electro-neutrality in the membrane and the bulk solution. This creates an electric field in the opposite direction to the diffusional flow. The Donnan equilibrium (an

electrochemical equilibrium) and steady state will be reached when the electric field balances the diffusional driving force of all ionic species [65].

In order to compare the performance of different aqueous solutions with pure salts, mixture of salts with ion exchange membranes, several properties were analysed in this work, in particular: permselectivity, membrane resistance, swelling, open circuit voltage (OCV) and power density.

2.2.1 Permselectivity

Charges that move though a membrane constitute an electrical current. The fraction of this current that is transported by a certain ionic species can be expressed with the transport number, defined as following:

$$T_i = \frac{z_i \cdot J_i}{\sum z_i \cdot J_i} \tag{2.1}$$

where z_i and J_i represent the valence and the molar flux of the component *i*. The sum of the transport numbers of all the ions must be equal to 1. The definition of the permselectivity for a cation and an anion exchange membrane is given by the following equations:

$$\alpha_{CEM} = \frac{T_c^{CEM} - T_c}{T_a} \tag{2.2}$$

$$\alpha_{AEM} = \frac{T_a^{AEM} - T_a}{T_c} \tag{2.3}$$

where AEM and CEM are referring respectively to the anion exchange membrane and cation exchange membrane. The subscript *c* and the subscript *a* instead indicate respectively the cations and the anions. The two terms in the numerator are the transport number in the membrane and in the bulk.

In an ideal CEM only cations diffuse, so their transport number inside the membrane and the permselectivity are equal to 1: $T_c^{CEM} = 1$ and $\alpha_{CEM} = 1$. Instead, if $\alpha_{CEM} = 0$, this means that the transport number of the cation in the membrane is equal to its transport number inside the solution $T_c^{CEM} = T_c$. Therefore, the permselectivity of a membrane

describes the charge selectivity of the ion exchange membrane. It reflects the ability of the membrane to discriminate between ions of opposite charge.

The permselectivity is determined using a static membrane potential measurement. The device exploited in all the test is shown in Figure 2.3 and consists of two cells: one is fed by dilute solution and the other one is fed by the concentrate one, separated by the membrane under investigation.

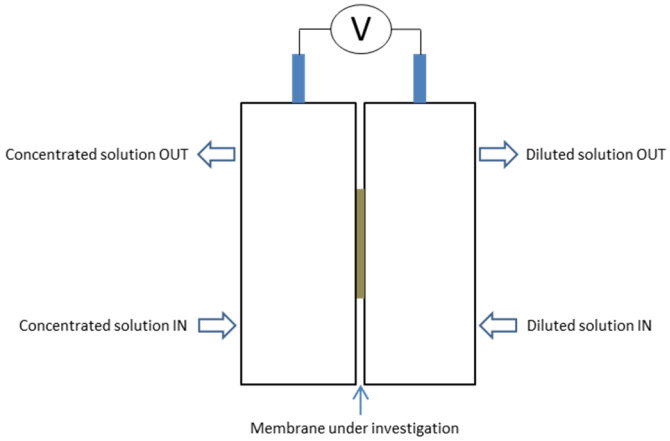

Figure 2.3: Experimental set-up for the permselectivity measurement.

The other devices necessary for the tests are listed below:

- peristaltic pumps for the concentrate and dilute solution;
- two calomel reference electrode to measure the electrical potential due to the passage of ions through the membrane;
- a thermal bath to control the solutions temperature;
- a conductivity meter to measure the solutions conductivity;
- a multimeter connected at the electrodes to measure the potential close to the membrane under investigation.

The permselectivity [%] is calculated as the ratio between the measured potential (ΔV_{meas}) and the theoretical one (ΔV_{theor}):

$$\alpha = \frac{\Delta V_{meas}}{\Delta V_{theor}} \cdot 100 = \frac{V_{meas} - V_{blank}}{\Delta V_{theor}} \cdot 100 \quad (2.4)$$

ΔV_{meas} is calculated as the difference between the measured potential (V_{meas}) and the blank potential (V_{blank}). The first value is measured by means of a multimeter connected between two electrodes inserted respectively in the dilute and concentrate channel instead the value of the blank potential is measured immersing the electrodes in 3M solution of potassium chloride, namely the difference electrodes potential itself. The theoretical potential value ΔV_{theor} [V] (for ion exchange membrane with aqueous monovalent electrolytes solution) can be calculated using the Nernst equation:

$$\Delta V_{theor} = \frac{RT}{z_i F} \ln\left(\frac{a_c}{a_D}\right) \quad (2.5)$$

in which R is the gas constant (8.314 J/mol K), T is the absolute temperature (K), z_i is the electrochemical valence, F is the Faraday constant (96485 C/mol), a_c is the activity of the concentrate solution (mol/l) and a_D is the activity of the dilute solution (mol/l).

As regards the activity coefficient, ions have not an ideal behavior in a solution due to the attraction forces among them. These forces prevent that all the ions can be independent one of each other and, therefore, not all the ions (resulting from the dissociation of the solute) can participate to a given phenomenon. For this reason, the active mass (activity) of the solute is less than the initial analytical concentration. The activity (mol/l) is defined as the "actual" concentration of a solute in solution, it is linked to the number of particles that can take active part in a given phenomenon and it is expressed by the product of the activity coefficient (γ) and the concentration C (mol/l):

$$a = \gamma \cdot C \quad (2.6)$$

The activity coefficient can be deduced on the basis of the characteristics of the solution and its value is generally between zero and one. The highest value of the activity coefficient (equal to one) is obtained for diluted solutions when interaction between the charges of the ions are negligible. In general, for concentrated solution the activity coefficient is lower than 1 because a high concentration reduces the distance between the ions, so that only a fraction of the ions becomes active in the solution. Debye and Hückel

defined a law (Debye and Hückel's law) to determine the activity coefficient across a binary electrolyte (like NaCl) in a dilute solution, but in this thesis the activity coefficients are taken from the Handbook of Chemistry and Physics and the Handbook of electrolyte solution [66,67].

2.2.2 Membrane resistance

The electrical resistance of the membrane (MR) is directly related to the RED maximum power output. It depends by the ions exchange capacity and by the mobility of the ions within the membrane matrix; it changes also with temperature and in particular it decreases at increasing temperatures. The ions mobility depends by a number of the solute properties (e.g. ion size, valence, hydration number) and by solvent content into the membrane. Lower IEMs resistance is favored by small ions size, low ion valence and high external concentration [68]. Normally, membrane structure with high charge density and low degree of cross linking are preferable to reduce the IEMs resistance.

The MR is commonly expressed as "areal" resistance ($\Omega*cm^2$) and not as specific resistance ($\Omega*cm$) generally used in engineering applications.

The electrical membrane resistance is measured by means of a six-compartment cell with four electrodes. Two electrodes are used to apply a selected current, positioned at the first and the sixth compartment. Two other electrodes are employed to measure the membrane property. The simplified scheme is shown in Figure 2.4.

All the parts of the device are made in Plexiglas. The membrane under investigation is located in the center and it could be anion or cation exchange membrane with an area of 3.14 cm^2. The external ones are always CEM while the other ones can be CEM or AEM depending on the configuration adopted for the tests. As it can be seen in Figure 2.4, two Haber-Luggin capillaries are positioned closely to the membrane under investigation in order to measure the electrical potential difference with accuracy.

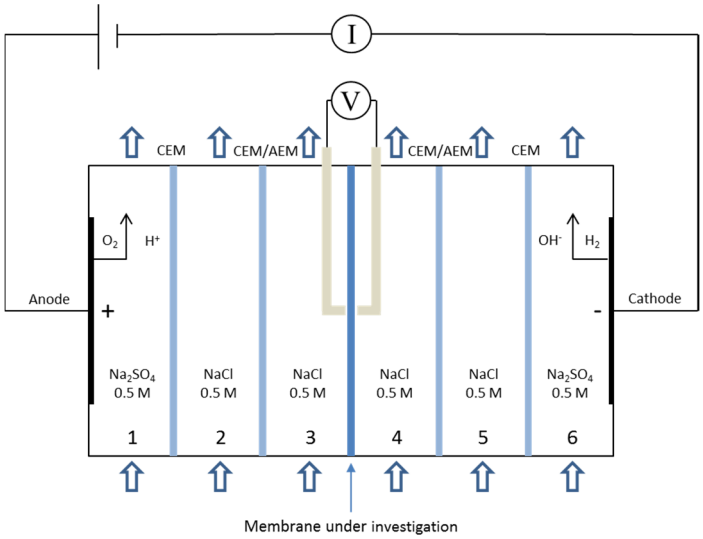

Figure 2.4: Scheme of the electrical resistance set-up with six compartments cell.

The membranes are conditioned in 0.5M of electrolyte solution for at least 24 hours before the measurements. The salt solution chosen for the test is pumped in the third and fourth compartment. The same solution is fed in the second and fifth compartment to avoid the influence of the electrode reactions that takes place in the working electrodes. Finally, the first and sixth compartments (electrode compartments) are fed by the electrode rinse solution. A different solution is used in the external compartments in order to guarantee the presence of the same cation in both central and electrode compartments. For example, sodium sulphate is used in the case of sodium chloride.

The electrode reactions are shown below:

$$\text{ANODE: } 2H_20 \rightarrow O_2(\text{g}) + 4H^+ + 4e^- \quad [2.1]$$

$$\text{CATHODE: } 2H_20 + 2e^- \rightarrow H_2(\text{g}) + 2OH^- \quad [2.2]$$

The solutions were pumped at the same flow rate (298.4 ml/min) and at constant temperature (25±0.1 °C). Before each test, all the solutions conductivities were measured by means of a conductivity meter.

All the other devices needed for the tests are listed below:

- two peristaltic pumps used at the selected flow rate to feed electrode rinse solution and salt solutions to the cells;
- two Haber-Luggin capillaries and two Ag/AgCl reference electrodes to measure the potential difference value due to the passage of ions through the membrane;
- a thermostatic bath to store the tanks containing the electrode rinse solution and the salt solutions in order to keep them at constant temperature;
- a Potentiostat/Galvanostat (e.g. Autolab PGSTAT100 – Metrohm) to apply fixed currents and record the experimental results.

Static measurements with various membranes and solutions were carried out exploiting the potentiostat/galvanostat apparatus, which applied a fixed current density and simultaneously measured the voltage drop over the membrane under investigation. The slope of the current-voltage curve (I-V curve) before the limiting current conditions, i.e. the maximum current value applicable without water splitting, gives the resistance of the IEM plus the non-compensated ohmic resistance between capillaries. Such last contribution is determined in another measurement without the membrane sample (blank). Subtract the blank value to the measurement is obtained the IEM resistance.

2.2.3 Chronopotentiometry

Another method for the membrane resistance measurement is the chronopotentiometry. This method is dynamic and it is closer to reality although RED is a stationary process.

With the chronopotentiometric method, not only the membrane resistance can be calculated but also other membrane properties, e.g. the transport number and qualitatively the permselectivity.

The set-up is the same shown in Figure 2.4. A current is set with the potentiostat. Figure 2.5 shows a typical chronopotentiometric measurement for a commercial ion exchange membrane (CMX). The membrane under investigation is the one between chamber 3 and 4. Over this membrane the voltage drop is measured with the aid of two Haber-Luggin capillaries connected with two electrodes (Ag/AgCl reference electrodes) that are filled with 3M KCl solution. The current density starts at zero (A/m^2); after a short time the current is set higher. The voltage drop is measured over the investigated membrane when a current is applied. The voltage drop is given as a function of the time

as shown in Figure 2.5. The transition time can be estimated as the period between the time when the current is applied and the time obtained by the interception of the two tangents of region 2 and region 3.

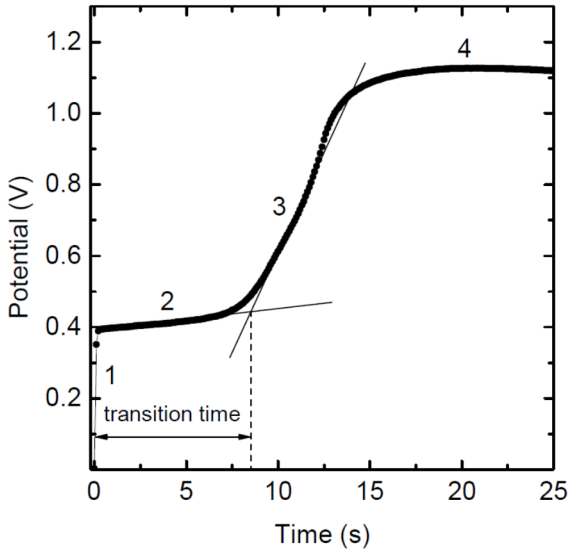

Figure 2.5: Example of a chronopotentiometric curve measurement for commercial ion exchange membrane (CMX) at 0.1 M of NaCl [65].

Three different areas are visible in Figure 2.5. The first one (area 1) is where the current is set higher than zero and the voltage drop is due to the membrane resistance. In area 2 the boundary layer is build up, this is the ohmic area. Qualitatively, short τ gives better permselectivity. When the boundary layer is completely formed, the curve goes up steep (area 3). Here where over the limiting current. A completely formed boundary layer means that, near the membrane, the diffusion is to slow to bring fresh solution. In the small boundary round the membrane only the current is the driving force. The last part of the graph, the tail (area 4), is where the water splitting occurs [65,69,70].

2.2.4 Swelling degree

Another important property of the membrane is the solvent (e.g. water) content, which is measured after dipping the membrane under investigation in pure solvent or various salt

solutions at room temperature for at least 24 hours. After this time, the solvent from the surface of the membrane is removed with blotting paper and then the weight and the wet size of the membrane can be determined. In order to measure the membrane dry size, the membrane is kept in an oven at 50°C for a least 48 hours evaluating also the dry weight [65].

The ratio between the amount of absorbed solvent and the dry weight of the membrane is equal to a swelling degree:

$$SD = \frac{m_{wet} - m_{dry}}{m_{dry}} \cdot 100 \quad (2.7)$$

When the solvent is not water but a highly flammable organic solvent, the oven isn't utilized and the membranes are slowly dried for a long time in a chemical hood for safety reason.

2.2.5 Fixed charge density

The fixed charge density of a membrane is related to the fixed charge groups attached to the polymer backbone. In particular, it is defined as the ratio between the concentration of ion exchange groups attached to polymer matrix (i.e. the number of fixed charges per unit weight of dry polymer, IEC) and the swelling degree SD (2.7):

$$C_{fix} = \frac{IEC}{SD} = \frac{meq}{l} \quad (2.8)$$

The type and the concentration of the fixed ionic charges determine the permselectivity and the electrical resistance of the membrane (e.g. in the swollen state the distance between the ion exchange groups increases and thus the fixed charge density decreases) [65].

2.3 RED performance parameters

In reverse electrodialysis a typical performance parameters is the power density, defined as the power supplied by the stack divided the number of cell pairs. A cell pair is a repetitive unit constituted by a cation exchange membrane (CEM), a dilute (LOW)

compartment, an anion exchange membrane (AEM) and a concentrate (HIGH) compartment. The tests were performed using a 10x10 cm^2 RED module but only in few tests the size was smaller (6x6 cm^2). During the operation, all the compartments are alternately fed with the two feed streams, thus generating a concentration gradient across all the membranes. The CEMs ideally allow only the transport of cations, rejecting anions; conversely, the AEMs allow the passage of anions, rejecting cations. Once the RED system is connected to a variable external electrical load, the resulting ionic currents is converted into electric current at the ends of the stack, where two electrodes are placed and a suitable solution with redox couple circulates.

Ion exchange membranes were provided by Fujifilm Manufacturing Europe BV (The Netherlands) and the woven spacers by Deukum GmbH (Germany). Furthermore, in almost all the tests, Nafion® perfluorinated membranes (DuPont, USA) were employed in the electrode compartments, because of their very high selectivity towards the active redox species.

The electrode compartments contain Ru-Ir oxide-coated Ti electrodes (Magneto Special Anodes BV, The Netherlands). The electrode rinse solution is composed by 0.1 M $K_3Fe(CN)_6$, 0.1 M $K_4Fe(CN)_6 \cdot 3H_2O$, adding the same salt solution under investigation as supporting electrolyte in an appropriate concentration, normally an average value between the high and low concentrations.

A typical apparatus exploited for the power density measurement is reported in Figure 2.6.

The test-rig consist of a RED stack with support devices and tanks that are listed below:

- inlet and outlet tanks for the two salt solutions;
- a glass tank for the electrode rinse solution covered by aluminium foil to avoid decomposition of the redox couple due to light exposure [71].
- a thermostatic bath (e.g. JULABO F33) to keep the solutions at constant temperature;
- peristaltic pumps to feed the concentrate and the dilute solutions into the RED unit;
- peristaltic pump to feed the electrode rinse solution into the electrode channels;
- a variable resistance (usually in the range 0.7-54.8 Ω) connected to the RED unit for testing the system under different load conditions;

- two multimeters to measure the current and potential value or alternatively a data acquisition system (DAQ-National Instruments), coupled with the LabVIEW™ environment as reported in Figure 2.6;
- a conductivity meter to measure all the fed solutions, both inlet and outlet.

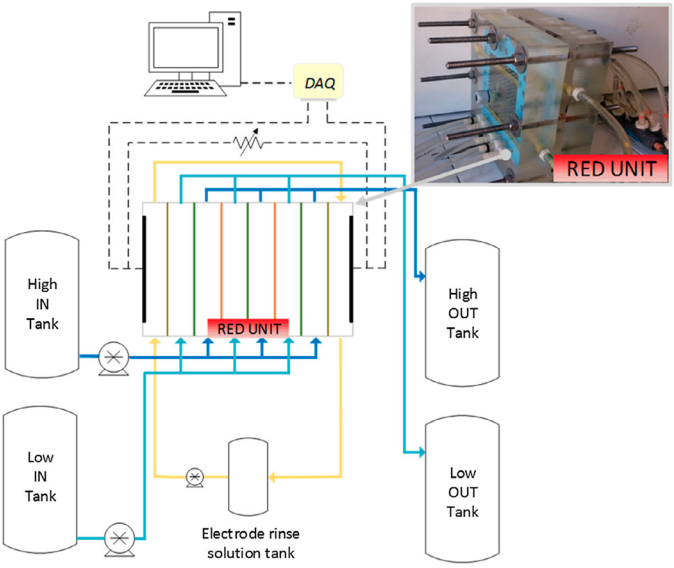

Figure 2.6: Experimental apparatus of power density measurement

All the solutions were prepared using demineralized water and salts with purity higher than 99%.

2.3.1 RED experimental test-rig and procedures

During testing, the RED unit is connected to the calibrated external resistance *(R_{ext})*, and the stack voltage *(E_{stack})* is recorded with a frequency of 1 Hz or read by a multimeter. Therefore, for each value of the external resistance *(R_{ext})*, the corresponding stack current is calculated by Ohm's law:

$$I_{stack} = \frac{E_{stack}}{R_{ext}} \tag{2.9}$$

The stack voltage*(E_{stack})*is also equal to:

$$E_{stack} = OCV - R_{stack} \cdot I_{stack} \quad (2.10)$$

where *OCV* is the open circuit voltage (i.e. the stack voltage under zero-current conditions), and R_{stack} is the internal stack resistance (which can be assessed as the slope of the straight line in a E_{stack} vs I_{stack} graph, see Figure 2.7A, a result example with NH_4HCO_3 salt). Thus, the electric power *(P)* is given by:

$$P = E_{stack} \cdot I_{stack} \quad (2.11)$$

As already said, the performance of a RED system is generally expressed in terms of power density, i.e. the amount of power generated per cell pair area:

$$P_d = \frac{P}{N \cdot A} \quad (2.12)$$

where *N* is the number of cell pairs and *A* is the active area of one cell pair (Figure 2.7B).

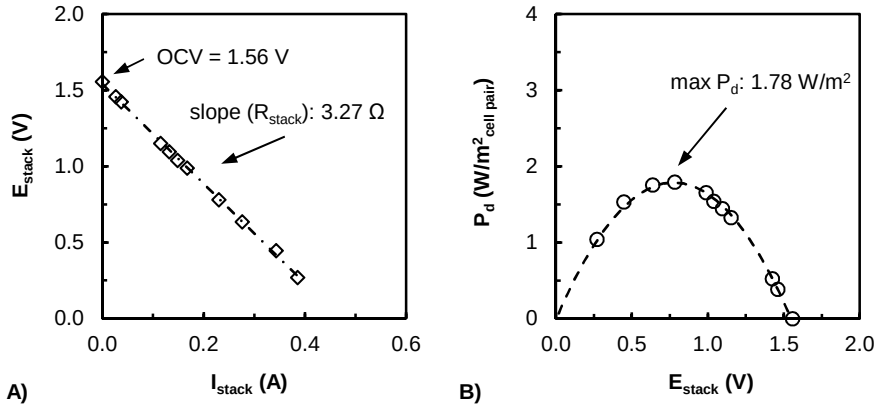

Figure 2.7: Example of data measured/inferred by the experimental procedure: A) E_{stack} vs I_{stack}; B) P_d vs E_{stack}. RED stack (10x10 cm^2, 10 cell pairs) equipped with Fujifilm membranes, 270 μm woven spacers. C_{HIGH} = 2 M NH_4HCO_3; C_{LOW} = 0.02 M NH_4HCO_3; v = 1 cm/s, T = 293 K.

The net power density is calculated as the gross power minus the pumping power required (assuming 100% pumping efficiency):

$$P_{d,net} = \frac{P - \Delta p_{HIGH} \cdot Q_{HIGH}^{tot} - \Delta p_{LOW} \cdot Q_{LOW}^{tot}}{N \cdot A} \quad (2.13)$$

where Δp are the pressure drops and Q^{tot} is the total (i.e. sum of each channel flow rate) feed flow rate; subscripts *HIGH* and *LOW* refer to concentrate and dilute, respectively. The corresponding pressure drops take into account the contribution relevant to the spacer-filled channel as well as that relevant to the inlet-outlet manifolds (e.g. distributor and collector) which in many cases may be the most prominent [13].

2.3.2 Evaluation of blank resistance and corrected power density

The power output values collected from laboratory-scale RED units are affected by the behaviour of the electrode compartments (generally identified with a so-called "blank-resistance", blank). Despite this, contribution is negligible on full-scale systems (i.e. where hundreds of cell pairs are piled in a single stack), it can be significant for a laboratory-scale unit.

The blank resistance (R_{blank}) can be estimated as the stack resistance when the number of cell pairs approaches zero [72]. For this reason, the stack resistance is experimentally measured by varying the number of cell pairs (5, 10, 15 and 20), obtained as intercept with y-axis on a R_{stack} versus N plot. Another way to measure the blank resistance is using a stack with only one membrane (CEM) and feed it with the electrode solution, measuring the potential lost for a fixed current (lower than limit current) and calculate it applying the Ohm's law.

Therefore, the internal resistance due to the cell pairs only (R_{cells}) can be calculated as:

$$R_{cells} = R_{stack} - R_{blank} \quad (2.14)$$

In this way, a corrected stack voltage can be estimated, disregarding the contribution of the blank resistance:

$$E_{stack,corr} = OCV - R_{cells} \cdot I_{corr} \quad (2.15)$$

where I_{corr} is the corrected current, calculated as:

$$I_{corr} = \frac{E_{stack,corr}}{R_{ext}} \tag{2.16}$$

Substituting eq. (2.16) into eq. (2.15) and rearranging, the corrected stack voltage is given by:

$$E_{stack,corr} = OCV - E_{stack,corr}\frac{R_{cells}}{R_{ext}} \tag{2.17}$$

Rearranging eq. (2.11), eq. (2.12), eq. (2.16) and eq. (2.17), the corrected power density ($P_{d,corr}$) can be calculated as:

$$P_{d,corr} = \frac{OCV^2}{N \cdot A \cdot R_{ext}\left(1+\frac{R_{cells}}{R_{ext}}\right)^2} \tag{2.18}$$

Eq. (2.18) provides the power density obtainable by a full-scale RED system operating under the same conditions of a laboratory-scale unit. Hence, it provides a reliable indication of the potential of the RED unit on a large scale (Figure 2.8). Figure 2.8 also shows the comparison between the relevant magnitudes of the corrected and uncorrected quantities previously described.

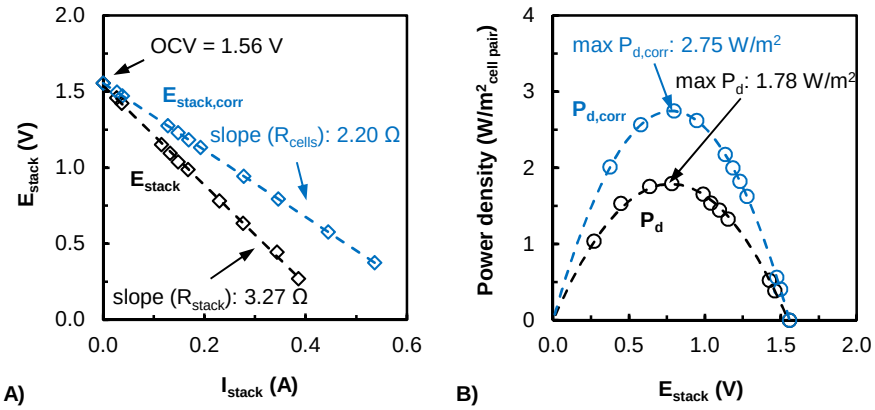

Figure 2.8: Example of data measured/inferred by the experimental procedure: A) E_{stack} vs I_{stack}; B) Power density vs E_{stack}. Black dashed line case includes the blank resistance; blue dashed line case does not include the blank resistance. RED stack (10x10 cm^2, 10 cell pairs) equipped with Fujifilm membranes, 270 μm woven spacers. C_{HIGH} = 2 M NH_4HCO_3; C_{LOW} = 0.02 M NH_4HCO_3; v = 1 cm/s, T = 293 K.

The membrane properties and the performance parameters previously explained were used as a useful tool for the selection of the best salts.

2.4 Strategy selection criteria of salts and solvents

The use of artificial salinity gradients allows new possibilities in terms of unconventional salts and solvents [73], aiming to increase the efficiency performances of the RED heat engine depending on the ratio between the energy produced and the thermal energy required.

A fundamental research was performed in order to assess the best options for both solvent and salt extraction strategies. Starting from literature review, information were collected on the main physical, chemical and transport properties (conductivity, density, viscosity, solubility, activity coefficient) of different, mainly inorganic, salts. A similar review was also conducted about the impact of different organic solvents when these are used as water alternative in the solvent extraction strategy. These results are not discussed in this manuscript. Only few tests were performed in order to assess the impact of water co-solvents on RED performance.

Promising salts were tested on Anion Exchange Membrane (AEM) and Cation Exchange Membrane (CEM) properties. The following membrane characteristics have been determined: Permselectivity (α), Open Circuit Voltage (OCV), Electrical Membrane Resistance (MR) and Power Density (Pd) in a stack.

With the obtained data set, RED modelling was applied and then validated with experimental results. Based upon all data and assumptions, a preselection of promising salts has been made.

2.5 Salts and solvents selection for the solvent extraction configuration

The aim of this section is the investigation of the most suitable salts and combination of salt and solvent for power generation by Reverse Electrodialysis (RED) in a Closed Loop system (RED-CL), with the solvent extraction strategy. Aside from literature, a number of relevant physical properties of such solutions (solubility, conductivity, density, viscosity, activity coefficients) were collected in a database.

On the basis of high solubility in water, 37 different uni-univalent salts were selected by Tedesco [32]. A simplified model was developed in order to identify the optimal

streams concentrations and estimate the achievable power output for each salt. The modelling goal was to give clear indications about salts which might be promising for RED-CL process. According to model simulations, lithium salts were promising, in particular the best prediction was obtained by lithium bromide with a theoretical power density of 35 $W/m^2_{cell\ pair}$ [32].

In the following sections, several tests are described and the results are discussed in order to identify the best salts in water, starting from the literature indications. Some tests were made with different organic solvent instead of water. The performance of ionic liquids was also tested; these are salts already in the form of a liquid phase, so they don't need solvents for their solubilisation. Moreover, new ideas were considered in order to increase the performance of RED unit, exploiting the behaviour of salts mixture instead of pure salts.

For all the test, the experimental procedures described in the section 2.3 were used and the results were normally compared with sodium chloride, considering it as the standard salt because it is the most studied in literature works.

2.5.1 Lithium Bromide

The lithium bromide-water ($LiBr/H_2O$) solution is widely used as working fluid in absorption refrigeration systems because of its characteristics. It is nonvolatile and non-toxic, can be considered environmentally friendly as it is not contributing to ozone depletion [74–78]. Employing this solution avoids the use of traditional refrigerants and its consequent environmental damage. Moreover, the LiBr/H2O solution has low crystallization temperature, high absorption capacity and low viscosity that are advantages if used as absorbent [79]. Absorption refrigeration systems are attractive and of increasing interest because they can be driven by low-temperature heat sources and provide an excellent way for converting solar energy or waste heat into useful refrigeration [80,81]

For the RED purpose, one of the most advantage is that lithium bromide is very soluble salt, with a solubility limit in water of 13.6 mol/l at 25°C [67]. Its behaviour is strongly dependent on temperature (Figure 2.9) [82].

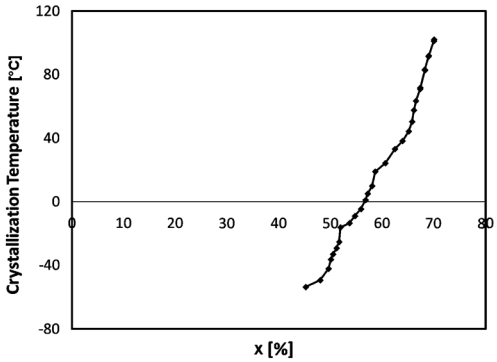

Figure 2.9: Solubility of pure LiBr in water at different temperature [82].

The effect of activity coefficients is rather remarkable, being far from unity for highly concentrated solutions as can be observed in Figure 2.10. This property may significantly affect the actual concentration at both sides of the membrane, especially at very high concentration. This may lead to a further increasing of the actual driving force available for power generation.

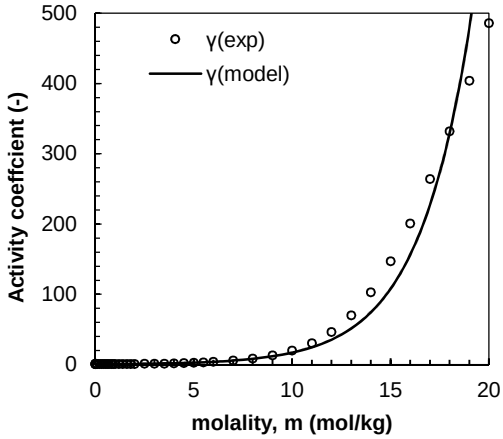

Figure 2.10: Activity coefficient of LiBr in water at 25°C [67].

In Figure 2.11 are reported the density and the electrical conductivity at different molarity (mol/lt), respectively.

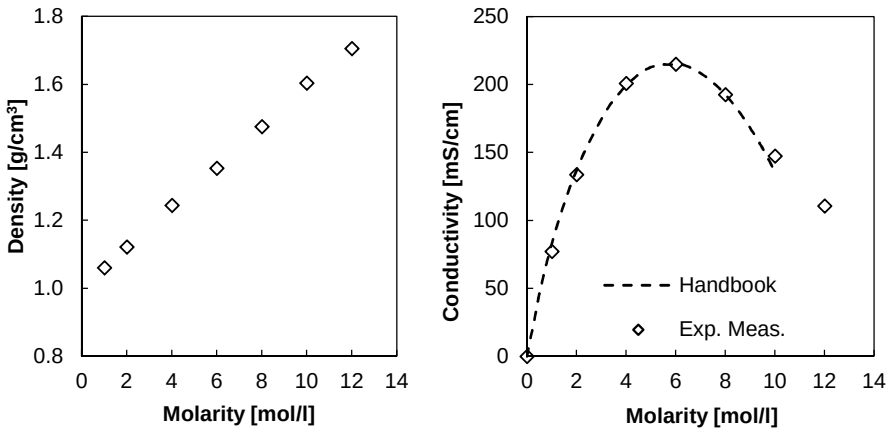

Figure 2.11: Density at 20 C° (experimental values) and electrical conductivity at 20 °C of LiBr solutions. It is also reported a comparison between experimental and handbook values [67].

Once the main physical properties were collected, LiBr solutions at different concentration were tested in a RED unit in order to confirm the forecasts made by Tedesco [32].

Power density measurements with LiBr

The experimental campaign was performed with a co-current reverse electrodialysis (RED) module with 10x10 cm^2 of membrane area and 10 cell pairs. During the operation, all the compartments are alternately fed with the two feed streams.

Ion exchange membranes (RP1) were provided by Fujifilm Manufacturing Europe B.V. and 270 μm woven spacers (Deukum GmbH, Germany) were used as stack components. The properties of the used IEMs are reported Table 2.1

Table 2.1: Properties of the two sets of IEMs adopted in the experiments*.

Membrane	**Thickness (μm)**	**Areal resistance[a] (Ω cm^2)**	**Permselectivity[b] (%)**	**Ion Exchange Capacity (meq/g)**
Fujifilm AEM RP1	120	1.84	92 %	1.28
Fujifilm CEM RP1	120	3.12	99 %	1.45

* Nominal data provided by membrane manufacturer using conventional (NaCl) solutions.

[a] electrical resistance measured in 0.5 M NaCl solution at 25°C.

[b] permselectivity measured in 0.1 – 0.5 M NaCl conditions at 25°C.

The lithium bromide was tested at different concentrations starting from 10M and using 0.15M as diluted solution because it was the best value found by Tedesco [32]. All the tests were compared with the standard NaCl salt. A preliminary test with 12M of LiBr is not reported because the result was not reproducible. The problem was the high solution viscosity at this high concentration making impossible the feed process with the peristaltic pumps available for the test.

In order to directly compare the power density results instead of the corrected power density, it was used the same electrode solution: 0.1M $K_3Fe(CN)_6$, 0.1M $K_4Fe(CN)_6$ adopted for the case of NaCl as supporting salt at concentration of 2.5M.

The results comparison is shown in Figure 2.12. The lithium bromide solution at 10M has the same OCV than sodium chloride at standard condition. However, a higher stack resistance influences negatively the RED performance with a lower power density. Decreasing the concentration of the concentrated solution, the stack resistance consequently decreases but at the same time also the OCV decreases giving a lower power density.

The power density experimentally found with LiBr is an order of magnitude lower than the value predicted by Tedesco [32]. In order to understand better why the power density of LiBr is only comparable with NaCl despite of its high solubility and high activity coefficients, the membrane properties were analyzed in terms of permselectivity, membrane resistance, water permeation and swelling degree. The results are shown in the next sections.

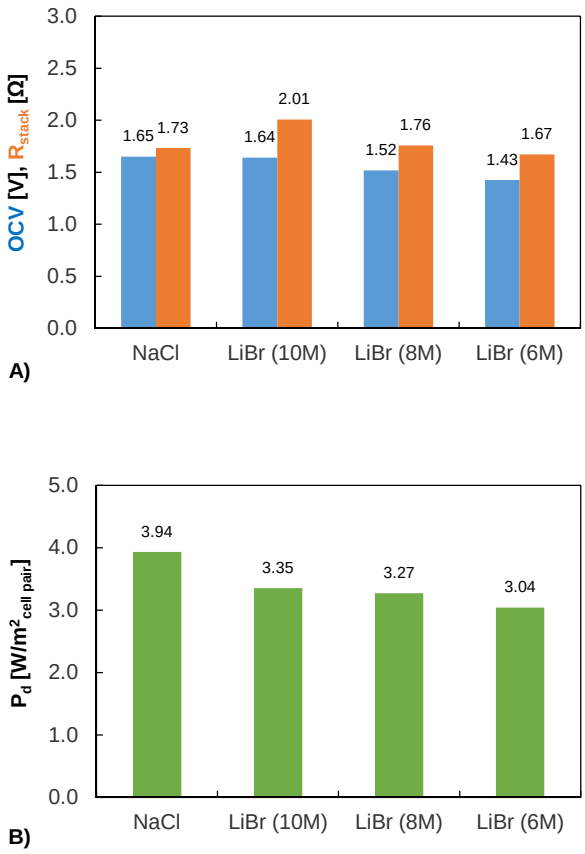

Figure 2.12: Comparison between LiBr solution at different high concentration (10M-8M-6M) and NaCl (5M). A) OCV (blue columns) and stack resistance (orange columns). B) Gross power density. RED stack (10x10 cm^2, 10 cell pairs) equipped with Fujifilm membranes RP1, 270 μm woven spacers. C_{LOW} = 0.15M LiBr and C_{LOW} = 0.05M NaCl; v = 1 cm/s, T = 293 K.

A power density measurement was also conducted at different temperature (Figure 2.13). The OCV values are identical even if the temperature allowed a good stack resistance reduction. However, the value still remain lower than the standard condition with NaCl solution.

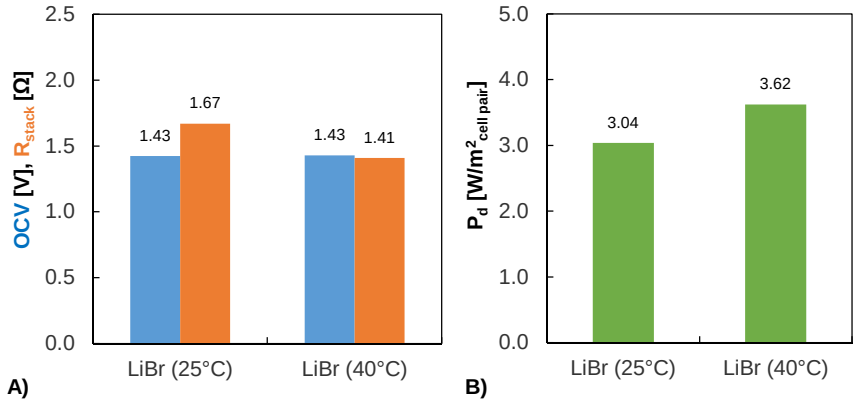

Figure 2.13: Comparison between LiBr solution at different temperature (25°C and 40°C). A) OCV (blue columns) and stack resistance (orange columns). B) Gross power density. RED stack (10x10 cm^2, 10 cell pairs) equipped with Fujifilm membranes RP1, 270 μm woven spacers. C_{HIGH} = 6M and C_{LOW} = 0.15M; v = 1 cm/s, T = 293 K.

Permselectivity measurements with LiBr

The procedure utilized for the permselectivity measurement with LiBr solutions is the same reported in the section 2.2.1. The dilute concentration was fixed at 0.05M because all the tests made in previous works [83] had this standard concentration in order to compare the results. The concentrated solution was changed from 6M to 0.5M. The results are shown in Figure 2.14.

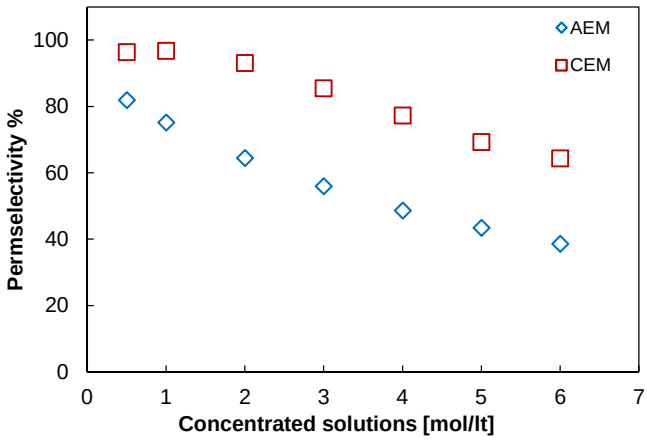

Figure 2.14: Permselectivity measurements with LiBr solutions at C_{HIGH}: 6M-5M-4M-3M-2M-1M-0.5M and C_{LOW}=0.05M; T=298K and Q_{LOW}=Q_{HIGH}=298.4 ml/min; RP1 Fujifilm membranes.

The permselectivity is strongly dependent on the concentrated solution. The value is always lower for anion exchange membrane than cation exchange membrane, behavior reported also in literature [12,32,84]. In this case, a cert amount of small lithium ions can pass through anion exchange membrane with the anions, this can have a strong effect on the selectivity membrane performance.

The results with LiBr and the standard NaCl are compared with the state of art [83]. The test were made at the same concentration (0.5M-0.05M) and the results are show in Figure 2.15. The comparison results show that the AEM permselectivity with LiBr is lower compared with other salts (only ammonium bicarbonate has the same value) whereas the CEM permselectivity is in line with the others. This poor performance contribute negatively on the power density and the values decrease rapidly at higher concentrations.

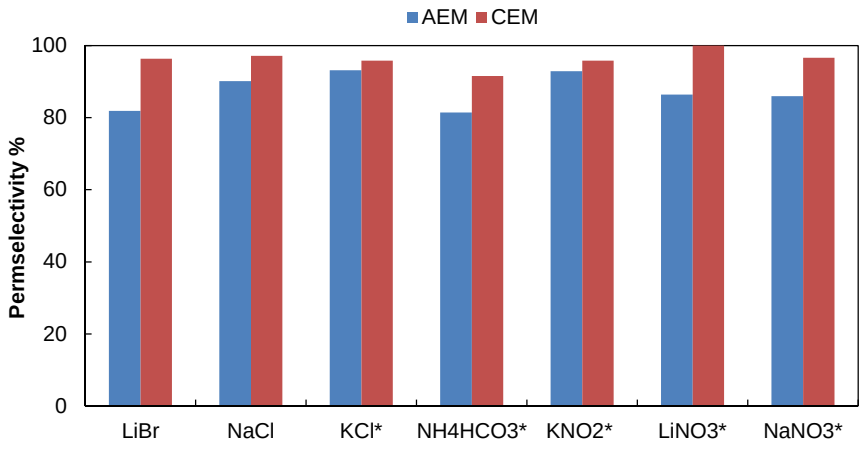

Figure 2.15: Permselectivity measurements comparison between LiBr, NaCl and literature values [83]*. RP1 Fujifilm membranes at 25°C. C_{HIGH}: 0.5M and C_{LOW}: 0.05M.

Water permeation measurements with LiBr

An ion exchange membrane is a semi-permeable polymeric support. It is interposed between two solutions at different concentration and it is able to select the species that can pass through. These are used in a RED process due to its selected property, but different concentration means also a different osmotic pressures; the ions move from concentrated channel to the diluted one whereas the solvent in the opposite direction trying to balance the concentration in the two channels. A certain amount of solvent molecules can pass with the ions but normally this is negligible.

The amount of solvent that pass from one channel to the other one depends by the membranes and by the solution concertation. This property can reduce the driving force between the concentrated and the diluted channels.

The test-rig exploited for the measurement is shown in Figure 2.16. Two solutions at different concentration are stored in two separate tanks. These solutions feed a stack composed by two channels separated by the membrane under investigation (exposed area of 224 cm^2). The solution density and the volume are measured before and after the test in order to calculate the amount of water passed through the membrane. The value is divided by the osmotic pressure difference between the average of inlet and outlet concentration and by membrane area.

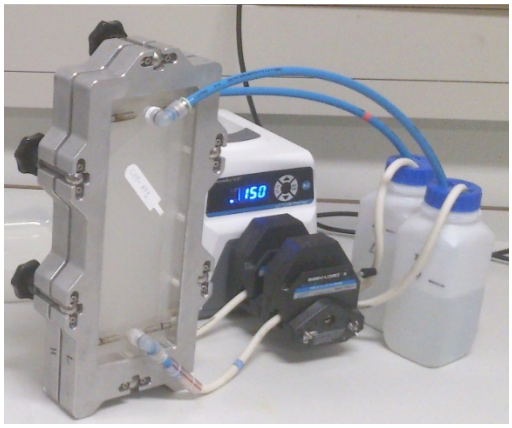

Figure 2.16: Test-rig for the water permeation measurements.

The test was made with LiBr at 5M as concentrate and 0.05M as dilute and it was compared with the standard NaCl solution. The solution were recirculated in the stack for 24h with a flow rate of 298.4 ml/min.

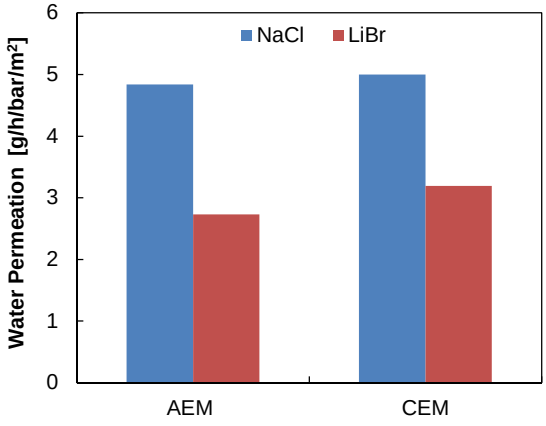

Figure 2.17: Water permeation comparison between LiBr and NaCl at the same concentration (5M–0.05M). RP1 Fujifilm membranes. Test performed for 24h.

The water permeation with LiBr is lower than NaCl, so this doesn't contribute to the poor performance of this salt in the RED unit.

Membrane swelling with LiBr solutions

A dry membrane takes up water to a certain degree when it is immersed in water. The increase in mass (in %) is called swelling degree. Swelling is restricted by the cross-links in the polymer. Because a high swelling degree lowers the charge density, a low swelling degree is desired. However, the polymers containing charged groups (active polymers) often exhibit a high swelling degree. Hence, the ratio between reinforcing polymers and active polymers is usually tuned to obtain a high charge density [12].

Measurement of the swelling degree is performed based on membrane weight. Two samples of RP1 Fujifilm membranes were immersed in a solution 0.5M of NaCl and 0.5M of LiBr for 24h. Then, the membranes were weighted and put in the oven at 65°C for 24h. The difference between the wet and dry membrane weight gives the swelling degree value. The results are shown in Figure 2.18.

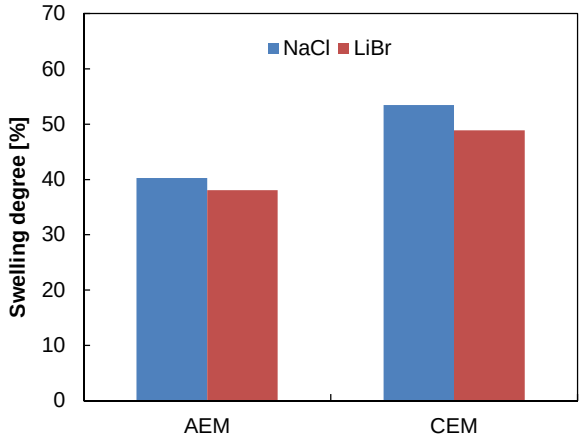

Figure 2.18: Swelling degree measurement with LiBr and NaCl solutions at 0.5M. RP1 Fujifilm membranes.

The values are comparable and in line with the those reported in the literature [83].

Membrane resistance with LiBr solutions

A chronopotentiometry measurement was performed in order to calculate the membrane resistance with LiBr and NaCl solution. As already explained in the section

2.2.3, the solution has a concentration of 0.5M in order to avoid the effect of boundary layer on the measurement.

The membrane resistance comparison for LiBr and NaCl is reported in Figure 2.19

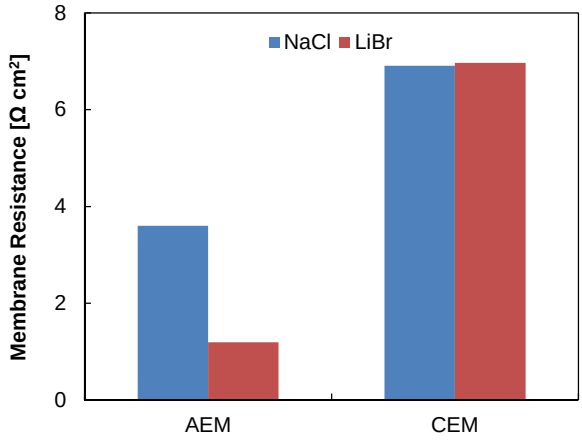

Figure 2.19: Membrane resistance comparison with LiBr and NaCl solutions. RP1 Fujifilm membranes. Concentration equal to 0.5M.

The CEM membranes have the same resistance with the two solution whereas the AEM with LiBr is one third the value measured with NaCl. Nevertheless the power density was lower than the standard salt.

Performance analysis and conclusion for LiBr solution

All the membrane properties measurements reported in the previous sections have highlighted the reasons of the poor performance of LiBr in a RED unit. Even if the membrane resistance values are more favourable for LiBr compared to NaCl, the lower permselectivity of AEM membranes strongly influence the power density. Higher concentrations mean lower permselectivity which in turn deletes the effect of the higher driving force due to high solubility and the high activity coefficient.

2.5.2 Ionic liquids

Ionic liquids (IL) are salts with very low melting temperature. They have received great interests recently because of their unusual properties as liquids [85–88]. The

characteristics of ionic liquid, in particular the organic one, can be summarized in Table 2.2.

Table 2.2: Characteristic of organic ionic liquid. Adapted from [89]

Low meting point	o Treated as liquid at ambient temperature o Wide usable temperature range
Non-volatility	o Thermal stability o Nonflammability
Composed by Ions	o High ion density o High ion conductivity
Organic ions	o Various kinds of salts o Designable o Unlimited combination

The most important properties of electrolyte solutions are non-volatility and high ion conductivity. These are essentially the properties of advanced (and safe) electrolyte solutions that are critical for energy devices in outdoor use. The non-volatile electrolyte solution will change the performance of electronic and ionic devices. These devices will become safer and have longer operational lives. But, more interesting, they will be consisting of organic ions, and these organic compounds will have unlimited structural variations because of the easy preparation of many components. So there are unlimited possibilities open to the new field of ionic liquids [90,91].

Among possible new applications of ionic liquid both electrodialysis and dialysis were proposed [92–94]. Thus these salts have been considered for their possible application to present case of the reverse electrodialysis. The idea is to exploit directly melted salts already at room temperature minimizing or even eliminating the use of solvent. These can strongly reduce the adverse effects of water in a RED unit.

In recent years, ionic liquids have been widely studied and many applications have been proposed. After a careful analysis of the works reported in the literature [95,96], ninety-nine ionic liquids were selected and the main properties were. In particular, melting point, density, viscosity, solubility in water and electrical conductivity are reported. Moreover, the safety data and the prices were also added because these are also important characteristics in the choice. Unfortunately, not all the information are available because also some of ionic liquids selected were only recently discovered.

Among the ionic liquids preselected, 1-ethyl-3-methylimidazolium ethyl sulphate was chosen due to its good electrical conductivity, good price and its health safety. However, before testing the above selected ionic liquid, (3-Acrylamidopropyl)trimethylammonium Chloride (DMAPAA-Q), an available organic salt was studied due to its similar characteristics. This organic salt is used in the ion exchange membrane production and it has good characteristic in terms of electrical conductivity and solubility in water.

(3-Acrylamidopropyl)trimethylammonium Chloride (DMAPAA-Q)

The (3-Acrylamidopropyl)trimethylammonium Chloride in water, concentrated at 74-76%, is known as DMAPAA-Q. It is an organic salt widely used in the production of ion exchange membranes. This salt has a high viscosity at 76% and it becomes more fluid when water is added. Conductivity measurements were conducted before to perform OCV tests and the trend is following reported (Figure 2.20):

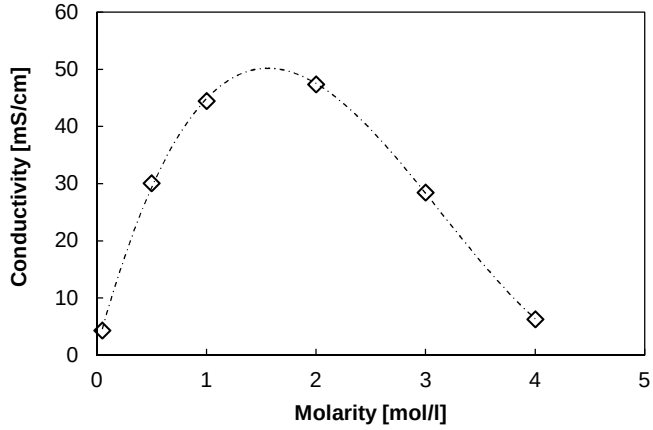

Figure 2.20: Conductivity measurement of water-DMAPAA-Q solutions at different molarity

As can be observed in Figure 2.20, the electrical conductivity has a maximum value at around 1.5M and it strongly decreases when the concentration increases. This trend can have a bad effect on power density and it is highlighted by the next results.

OCV measurement with DMAPAA-Q at different concentrations

According to the procedures of permselectivity measurement described in the section 2.2.1, the measured potential is divided by the theoretical one calculated with the Nernst equation. However, the theoretical potential cannot be calculated with this organic salt because the activity coefficients are not available in the literature. In order to overcome this problem and to have an idea of the performance of this salt with RED technology, OCV measurements were performed with the permselectivity apparatus. The sum of the absolute values of the potentials measured with the anionic and the cationic exchange membrane, respectively, is equal to the OCV value for a single cell pair. Moreover, it can give an idea on the membrane permselectivity comparing the results with the standard NaCl. The results are shown in Figure 2.21.

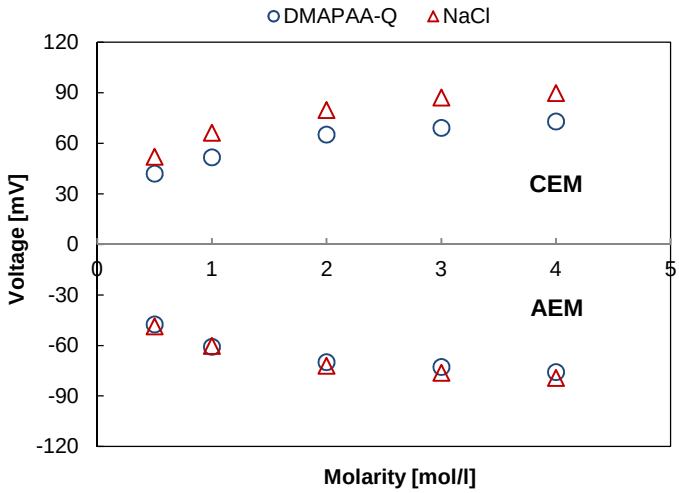

Figure 2.21: OCV measurement comparison with DMAPAA-Q and NaCl solutions at different molarity; T=298K; Fujifilm membrane RP1; C_{LOW}=0.05M.

The measured potential with AEM is comparable with all the concentrations. However, the different with CEM membrane is pronounced and the corresponding OCV per cell pair is around 12% lower for DMAPAA-Q solutions.

In order to improve the performance of this organic salt, a different membrane (Fujifilm V1) was also tested. The comparison performance is reported in Figure 2.22.

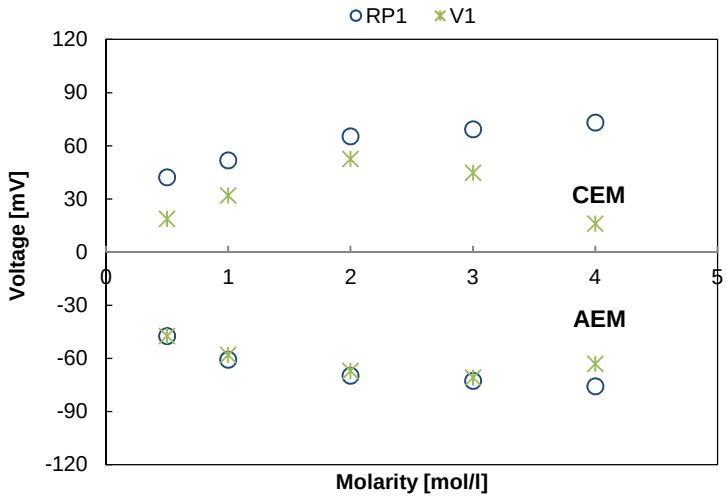

Figure 2.22: OCV measurements comparison with V1 and RP1 Fujifilm membranes using DMAPAA-Q solutions at different molarity. T=298K. C_{LOW}=0.05M.

The V1 membrane has a worst performance with DMAPAA-Q solutions compared with RP1 membrane. In this case, the best OCV per cell pair result is when the electrical conductivity has the maximum value. However have to be highlighted that the performance with AEM membranes are comparable.

The use of organic solvent instead of water can be an important alternative in the solvent extraction strategy because these organic solvents can have a low boiling point. This can improve the total process efficient because lower energy is required for the regeneration step. The OCV of DMAPAA-Q solutions in a water (80%)-methanol (20%) solvent was measured using the same test-rig. The comparison with only water solvent is shown in Figure 2.23.

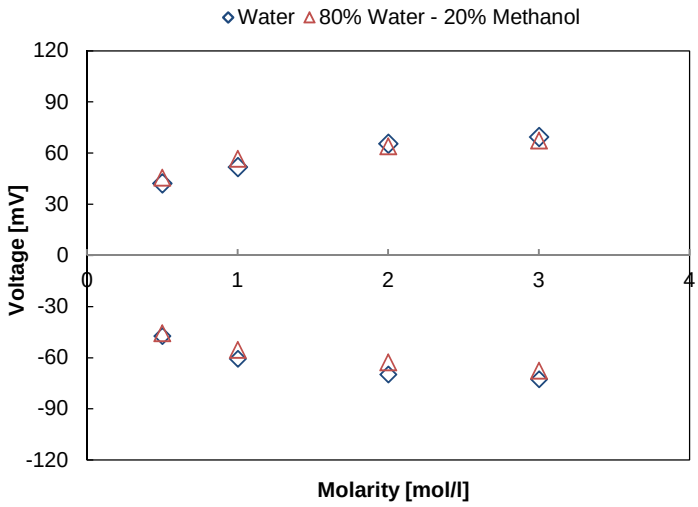

Figure 2.23: OCV measurements comparison with DMAPAA-Q in water and water (80%)-Methanol (20%) solvents at different molarity. T=298K. C_{LOW}=0.05M.

The trend shows a similar potential with both solvents allowing the possibility to use solvent with lower boiling point compared with pure water.

According to the equation (2.11) reported in section 2.3, the maximum power density can be calculated if OCV and stack resistance are known. The stack resistance depend by the membranes, by the solution and by the blank resistance. The solution resistance and the blank can be calculated or assumed considering standard electrode solution with NaCl but the membrane resistance have to be measured.

Membrane resistance measurements with DMAPAA-Q

A chronopotentiometry measurement was performed in order to measure the membrane resistance of CEM and AEM with DMAPAA-Q solution at 0.5M. The value was compared with the standard NaCl solution and the results are shown in Figure 2.24.

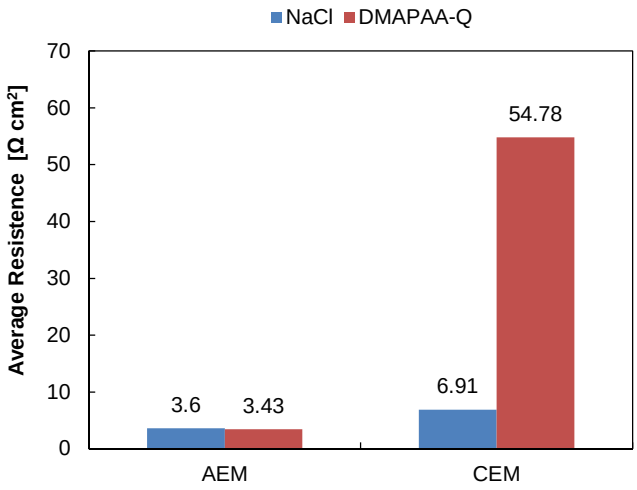

Figure 2.24: Comparison of membrane resistance with DMAPAA-Q and NaCl solution, measured with chronopotentiometry tests. C=0.5M; T=298K. Fujifilm RP1 membrane.

The membrane resistance of anion exchange membrane with DMAPAA-Q has a value slightly lower than standard NaCl but the cation exchange membrane is 8 times higher. This result makes the DMAPAA-Q unusable in a RED unit with the condition described above.

1-ethyl-3-methylimidazolium ethyl sulfate

The physical properties of the ionic liquid (IL) selected for the present study (1-ethyl-3-methylimidazolium ethyl sulfate) were not available in literature. The electrical conductivities were experimental measured and the results are reported in Figure 2.25. The maximum concentration achieved was 2M, with higher value the solution was too viscos.

This ionic liquid was studied with OCV tests. The results were compared with the standard sodium chloride and are reported in Figure 2.26.

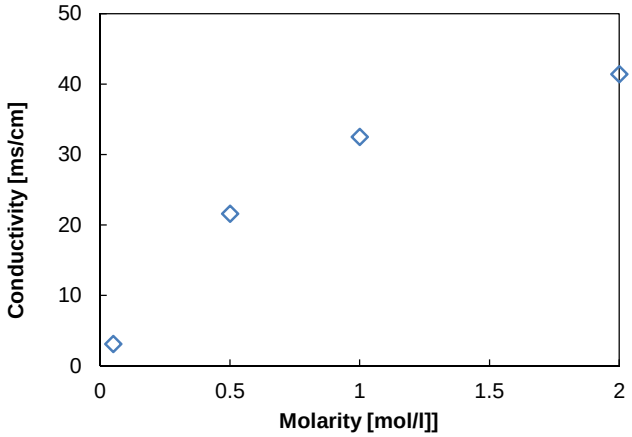

Figure 2.25: Experimental electrical conductivity of 1-ethyl-3-methylimidazolium ethyl sulfate at different concentrations.

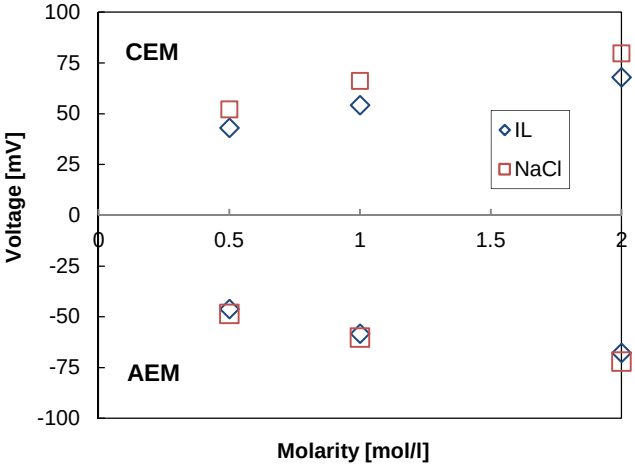

Figure 2.26: OCV measurement comparison with IL (ionic liquid) and NaCl solutions at different molarity; T=298K; Fujifilm membrane RP1; C_{LOW}=0.05M.

The OCV performance of this ionic liquid with AEM membranes was comparable to NaCl but the value with CEM membranes was lower as obtained for the case of DMAPAA-Q salt. Likely, specific membrane should be created in order to improve the performance of these particular salts.

2.6 Selection in the salt extraction strategy

An alternative strategy for the solution regenerations in a closed loop SGP process is the salt extraction. The salt is extracted from the diluted exhausted solution and re-solubilized into the concentrated one as shown in the process scheme reported in Figure 1.10. Among the possible alternatives, the thermolytic salts are selected as the most promising for the SGPHE in the range temperature of 40-60 °C. The most common thermolytic salts consist of NH_3-CO_2-based compounds, namely they are NH_4HCO_3, ammonium carbonate ($(NH_4)_2CO_3$) and ammonium carbamate (NH_4NH_2COO). Since these salts have the advantage of being degradable into NH_3 and CO_2 below 60°C, they can be used to convert very low temperature heat like industrial waste heat into electricity. Only ammonium hydrogen carbonate and ammonium carbamate were studied and their performances were investigated in a small RED unit. However, the solutions regeneration stage was studied only with ammonium hydrogen carbonate.

2.6.1 Ammonium hydrogen carbonate

According to the literature on the use of artificial salinity gradients, ammonium hydrogen carbonate (NH_4HCO_3) has been recently presented as an interesting option for both RED [97–99] and PRO [100]. The peculiar property of NH_4HCO_3 is that it can be decomposed into ammonia, carbon dioxide and water by heating above 40-45 °C [101], thus allowing in principle to operate the regeneration step of the SGP heat engine at low temperature (i.e. using very low-grade heat).

Up to now, three different applications have been proposed in the literature for the exploitation of NH_4HCO_3 in SGP heat engines: the ammonia-carbon dioxide Osmotic Heat Engine (OHE) [100], the Thermal-Driven Electrochemical Generator (TDEG) [97] and the concept of Microbial Reverse electrodialysis Cell (MRC) [99].

The ammonia-carbon dioxide OHE proposed by McGinnis et al. (2007) is a closed-loop PRO system where a NH_4HCO_3 solution is used as draw solution to create high osmotic pressures. A maximum thermal efficiency of 16% of the Carnot efficiency (likely corresponding to an actual energy conversion efficiency of 1.2%) has been predicted for an OHE that uses waste heat around 50°C [100].

The Thermal-Driven Electrochemical Generator (TDEG) presented in 2012 by Luo et al. [97] represents the first attempt to drive a RED process with NH_4HCO_3 solutions (as

working fluids). Using a laboratory RED unit with 10 cell pairs, a maximum power density of 0.33 $W/m^2_{membrane}$ was obtained feeding the system with 0.02 M (dilute) – 1.5 M (concentrate) NH_4HCO_3 solutions.

Another recent application of NH_4HCO_3 is represented by microbial RED systems in which a small RED stack is placed directly in contact with a microbial fuel cell (MFC), i.e. a biochemical reactor where exoelectrogenic bacteria are used to oxidize soluble organic matter, thus releasing electrons on an electrode surface. Using solutions with conductivity typical of domestic wastewater (~1 mS/cm), a power density over 3 W/m^2 of projected cathode area (i.e. over 0.3 W/m^2 of membrane area installed in the 5 cell-pairs set-up) has been reported in an MFC [99].

All these works suggest that employing ammonium bicarbonate solutions can be an interesting alternative to generate power by means of SGP-heat engines. Notwithstanding these promising features, insufficient data have been so far collected on the performance of a RED unit fed by NH_4HCO_3 solutions. The focus of the present work is the experimental investigation of the performance of a lab-scale RED unit operated with NH_4HCO_3 solutions. A number of different operating conditions including flow rates and salt concentrations were tested, thus providing more insight into the potential use of ammonium bicarbonate for RED closed-loop applications.

Experimental apparatus

The experimental campaign was performed with a homemade reverse electrodialysis (RED) module with 10x10 cm^2 of membrane area. The cell pair number was fixed at 10 for each test performed. During the operation, all the compartments are alternately fed with the two feed streams.

Ion exchange membranes provided by Fujifilm Manufacturing Europe BV (The Netherlands) and 270 μm woven spacers (Deukum GmbH, Germany) were used as stack components. The properties of the used IEMs are the same reported in Table 2.1.

Nafion® perfluorinated membranes (DuPont, USA) were employed in the electrode compartments and the electrode rinse solution was composed of 0.1 M $K_3Fe(CN)_6$, 0.1 M $K_4Fe(CN)_6 \cdot 3H_2O$ (Chem-lab with purity 99.5%), adding 1 M NH_4HCO_3 as supporting electrolyte. A flow rate of 225 ml/min in the electrode compartments was kept for all the tests.

The test rig is constituted by the RED unit, plus four inlet/outlet tanks (20 l capacity) for both solutions and the required monitoring device, as sketched in Figure 2.6.

Two peristaltic pumps (Cellai 530 U) were used to force the concentrate and the dilute solutions to flow within the RED unit. A similar peristaltic pump (Verderflex M025) was used for pumping the electrode rinse solution (ERS) from a glass tank covered by aluminium foil to avoid decomposition of the redox couple due to light exposure. The relevant process variables (inlet-outlet pressure drops, stack voltage) were measured and collected via a data acquisition system (DAQ-National Instruments) and monitored through LabVIEW^{TM} environment. The conductivity of the feed solutions (both at inlets and outlets) were measured by means of a conductivity meter (WTW LF196). A variable resistance (ranging between 0.7 – 54.8 Ω) was connected to the RED unit for testing the system under different load conditions. The feed solutions were prepared with demineralized water and ammonium hydrogen carbonate (Sigma-Aldrich, purity 99%).

The test-rig scheme is reported in Figure 2.6

Results and discussion

The RED unit was tested under different operating conditions, changing the feed concentration of the dilute and the flow velocity of both solutions. For the concentrated solution, an inlet concentration of 2 M NH_4HCO_3 was adopted as standard for all tests: this allows to keep a high salinity ratio (i.e. ratio between C_{HIGH}/C_{LOW}), notwithstanding the relatively low solubility of ammonium bicarbonate in water (2.7 M at 298 K [102]). A summary of the tests presented in this work is reported in Table 2.3.

Table 2.3: Summary of experimental tests presented in this work.*

Main focus of the tests	**Dilute concentration, C_{LOW} (M NH_4HCO_3)**	**Feed flow velocity, v (cm/s)**
Influence of dilute concentration (C_{LOW})	0.01 - 0.02 - 0.04 - 0.06 - 0.1	1
Influence of feed flow velocity (v)	0.02 - 0.04	0.5 - 1 - 1.5 - 2

*Overall conditions: RED stack (10x10 cm^2, 10 cell pairs) equipped with Fujifilm membranes, 270 μm woven spacers. C_{HIGH} = 2 M NH_4HCO_3; T = 293 K.

Influence of dilute concentration

The concentration of the dilute solution is a crucial factor for the performance of a RED system, since it affects both the driving force and the resistance of the stack. In

particular, a careful selection of the feed dilute concentration can significantly enhance the power output. Notably, the electric resistance of the dilute can represent even the 50% of the whole stack resistance when fresh water (0.017 M NaCl) and seawater (0.5 M NaCl) are used as feed solutions [103].

In the case of RED process with NaCl solutions, the optimal dilute concentration to maximize the power output has been identified in the range of 0.01-0.1 M NaCl, depending on the stack design (e.g. channel thickness, membrane resistance) and operating conditions [17,104,105]. However, the use of unconventional salts such as ammonium bicarbonate requires a new investigation of the optimal concentration range maximizing the performance of the RED process. Moreover, when artificial solutions are used in a closed loop, feed concentrations are not dictated by those of natural sources, and can be purposely chosen for the process.

In this regard, the RED system was tested by changing the feed concentration of the dilute in the range of 0.01-0.1 M NH_4HCO_3. Relevant results are reported in Figure 2.27: in particular, open circuit voltage (*OCV*) and stack resistance are shown in Figure 2.27A, while the corresponding maximum values of power densities are reported in Figure 2.27B.

In the investigated range, the lower the dilute concentration, the higher the *OCV* and the stack resistance are expected (Figure 2.27A). As a matter of fact, the reduction of dilute concentration corresponds to a higher salinity ratio, thus resulting in an increase of the *OCV*. Similarly, lowering the feed concentration also causes an increase of the electric resistance in the dilute compartments, which is the main contribution to the stack resistance. These phenomena have a counteracting effect on the power output, leading to a maximum in the gross power density (P_d = 1.78 W/m$^2_{\text{cell pair}}$) at C_{LOW} = 0.02 M (Figure 2.27B).

OCV values and trend very similar to those presented here were found by Luo et al. [97]. Conversely, higher R_{stack} were reported by the same authors [97] allegedly due to the higher spacer thickness and to the different membranes employed (in their case: Selemion CMV and AMV, Asashi glass, Japan). Such a difference results in a P_d three times lower on average: they found a maximum P_d at C_{LOW} = 0.02 as in the present case, but equal to 0.66 W/m$^2_{\text{cell pair}}$.

Looking at the corrected power density ($P_{d,corr}$), a different (with respect to P_d) optimal value of C_{LOW} was observed (~0.04 M NH_4HCO_3), corresponding to a maximum value for $P_{d,corr}$ of 2.85 W/m$^2_{\text{cell pair}}$ (Figure 2.27B).

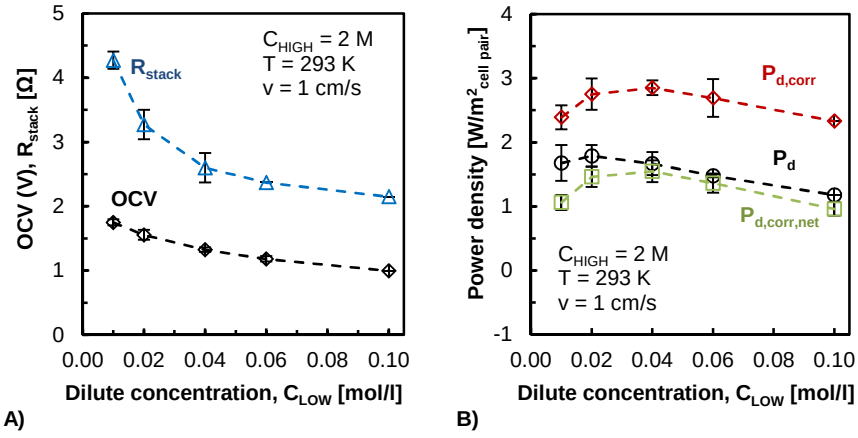

Figure 2.27: Influence of dilute concentration on process performance. A) OCV and stack resistance. B) Gross power density, corrected gross power density, corrected net power density. RED stack (10x10 cm^2, 10 cell pairs) equipped with Fujifilm membranes, 270 μm woven spacers. C_{HIGH} = 2 M NH_4HCO_3; v = 1 cm/s, T = 293 K.

Pressure losses were also measured and the relevant results are reported in Figure 2.28. This figure shows that the concentration has an effect on pressure drop as expected on the basis of the difference in solution viscosity. Clearly, when only the concentration of the dilute solution is changed (see Table 2.3) only a very slight variation in pressure drop occurs.

By taking into account these hydraulic losses, the net corrected power density was estimated and reported in the same plot of $P_{d,corr}$ (Figure 2.27B): a maximum value of 1.55 W/m$^2_{\text{cell pair}}$ was found at the same C_{LOW} of ~0.04 M as expected. For all tests, each value is provided with an error bar calculated using the maximum discrepancy among results relevant to some reproducibility tests. For the net power density, the experimental uncertainty was estimated by adopting to the uncertainty definition given by Moffat [106,107].

Since the maximum power density was found at 0.02 M, while the maximum corrected power density is at 0.04 M, the effect of dilute flow rate was investigated by fixing the dilute concentration at these two values (Table 2.3), as it will be presented in the next section.

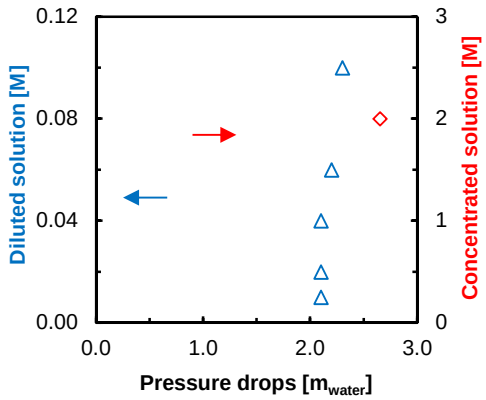

Figure 2.28: Influence of dilute concentration on pressure drops. RED stack (10x10 cm^2, 10 cell pairs) equipped with Fujifilm membranes, 270 μm woven spacers. C_{HIGH} = 2 M NH_4HCO_3; v = 1 cm/s, T = 293K.

Influence of feed flow velocity

In addition to the inlet concentration of feed solutions, another crucial parameter for the RED process is the flow velocity inside compartments, which also strongly affects the pressure drops, and hence the net power output.

The investigated RED system was tested assuming different flow velocities for both solutions, ranging from 0.5 up to 2 cm/s. Also, as mentioned above, two values of dilute concentration were tested (i.e. C_{LOW} equal to either 0.02 or 0.04 M): the results relevant to C_{LOW} = 0.02 M are reported in Figure 2.29, while those at C_{LOW} = 0.04 M are shown in Figure 2.31.

In Figure 2.29A the effect of flow rate on *OCV* and relevant R_{stack} are reported. Notably, the former would be constant if membranes were ideal. In fact, its actual variation with flow rate is due to the non-perfect permselectivity of the membranes, which allow the passage of little amounts of salt and water. Results show that an increase of flow velocity provides a slight enhancement of the *OCV* in the first range (0.5 – 1 cm/s), until

a plateau is reached (Figure 2.29A). Such effect is mainly related to the lower residence time inside the stack that allows a practically constant driving force between inlet-outlet to be maintained. Higher flow rates also cause a reduction of polarization phenomena (especially in the dilute solution), which are, however, expected to be very low according to the very low fluxes occurring under open circuit conditions. Likewise, the flow rate has a double effect on R_{stack}: a low residence time corresponds to a small variation of the dilute channel conductivity thus leading to a high R_{stack}; on the other hand, a higher flow rate reduces concentration polarization phenomena (i.e. non-ohmic resistance) thereby providing lower R_{stack}. For the present case, the first effect appears to be prominent as an increase of R_{stack} with the flow rate was recorded (Figure 2.29A). As a matter of fact, the resistance due to the dilute compartment, as shown in Figure 2.29A, represents around 30-40% of the stack resistance and its effect is determinant on the stack performance. Also Luo et al. [97] investigated the effect of feed flow rate on process performance. As already discussed for the case of Figure 2.27, they reported OCV similar to those of the present work, while the stack resistance was much higher, thus resulting in three times lower P_d [97].

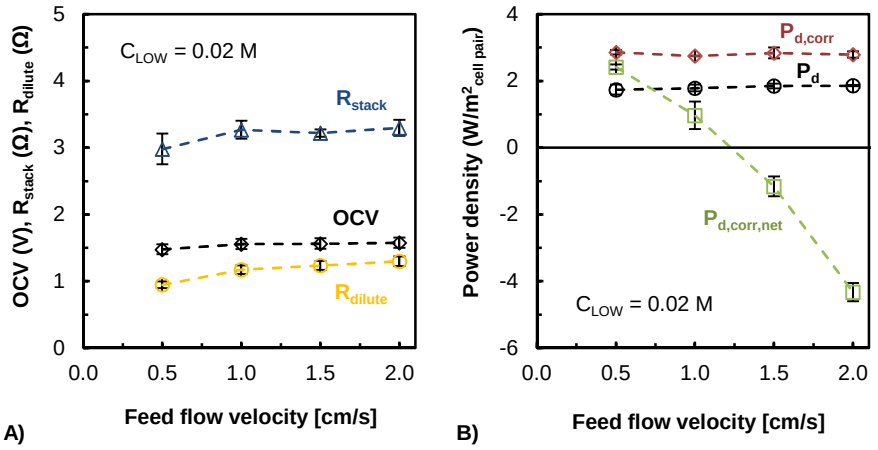

Figure 2.29: Influence of feed flow velocity on process performance. A) OCV, stack resistance, resistance of the diluted compartment. B) Gross power density, corrected gross power density, corrected net power density. RED stack (10x10 cm^2, 10 cell pairs) equipped with Fujifilm membranes, 270 μm woven spacers. C_{HIGH} = 2 M; C_{LOW} = 0.02 M; T = 293 K.

As a result of the simultaneous increase of competing variables as *OCV* and R_{stack}, the power density was found only slightly dependent on the flow rate: an average value of 1.81 and 2.81 $W/m^2_{cell\ pair}$ for P_d and $P_{d,corr}$ was found, respectively (Figure 2.29B). As already discussed, the net corrected power density (eq. 2.12 and eq. 2.13) can be calculated considering the pressure drops inside the dilute and concentrate compartments. As seen in Figure 2.30A, the experimental pressure drops increase as the feed flow velocity increases, but with a different slope depending on the solution concentration (i.e. different fluid-dynamic properties as density and viscosity). The two trends are linear, thus suggesting the existence of a stationary regime at the flow rate range investigated. The two trends were reported also in terms of non-dimensional numbers in Figure 2.30B: the void-channel Reynolds number *(Re)* and the void-channel fanning friction factor *(f)* defined as [13,108]:

$$Re = \frac{\rho \cdot v_{m,void} \cdot d_{h,void}}{\mu} = \frac{2 \cdot \rho \cdot v_{m,void} \cdot H}{\mu} \tag{2.19}$$

$$f = \frac{\Delta p}{l} \frac{d_{h,void}}{2 \cdot \rho \cdot v_{m,void}^2} \tag{2.20}$$

where v_m is the average velocity along the main flow direction in a corresponding spacer-less (void) channel, $d_{h,void}$ is twice the channel thickness H (270 μm in our case) and μ is the fluid viscosity (0.9 cP for the dilute solution and 1.88 cP for the concentrate). As it can be seen, the two trends are very similar to each other, being indeed almost. As a consequence, the $P_{d,corr,net}$ values were calculated using the linear trend instead of the experimental points.

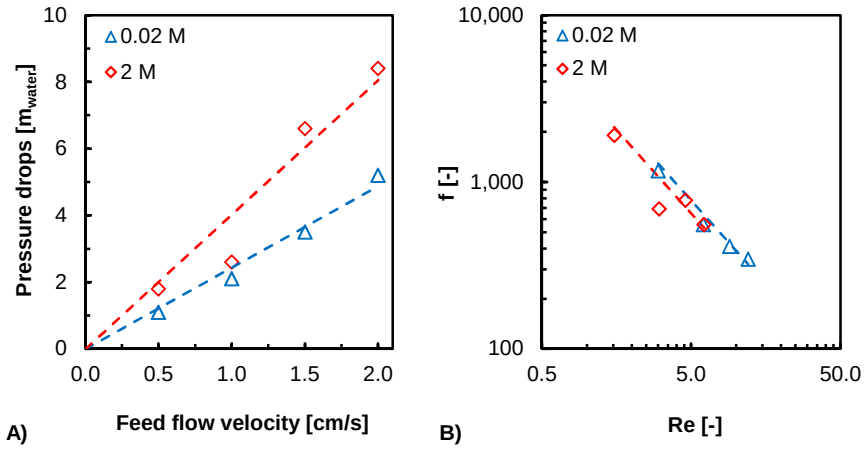

Figure 2.30: Influence of feed flow velocity on the experimental pressure drops. A) Experimental pressure drops values. B) Fanning friction factor as a function of Reynolds number. RED stack (10x10 cm^2, 10 cell pairs) equipped with Fujifilm membranes, 270 μm woven spacers. C_{HIGH} = 2 M; C_{LOW} = 0.02 M; T = 293 K.

The resulting $P_{d,corr,net}$ reported in Figure 2.29.B were found to be lower than zero for all flow velocities being higher than 1.25 cm/s (see Figure 2.29B). As it can be seen, the lowest flow velocity (~0.5 cm/s) among those tested, was found preferable to maximize the net power density under the investigated conditions (Figure 2.29B). Actually, even lower flow rates should be investigated in the future in order to recognize the maximum value of $P_{d,corr,net}$.

A similar test was performed for the case of a dilute concentration of 0.04 M NH_4HCO_3, which was the value maximizing the corrected power density (Figure 2.27B). Corresponding results are shown in Figure 2.31. Trends quite similar to those relevant to C_{LOW} = 0.02 M were found with the main difference concern the R_{stack} trend. As a difference from the case at C_{LOW} = 0.02 M, R_{stack} exhibits here a decreasing trend as the flow rate increases. This is allegedly due to the influence of polarization phenomena, which are in this case more relevant than the resident time effect (Figure 2.31A): at this higher concentration (than the previous case), the dilute channel resistance is poorly dependent on the residence time (Figure 2.31A).

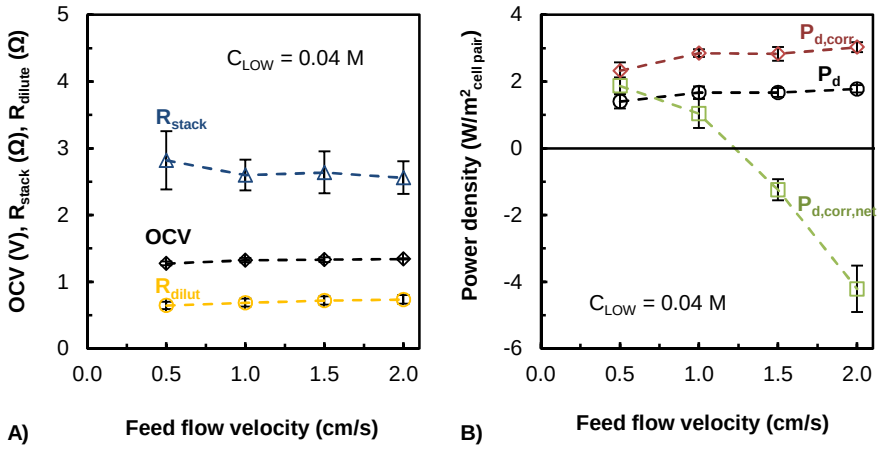

Figure 2.31: Influence of feed flow velocity on process performance. A) OCV, stack resistance, resistance of the diluted compartment. B) Gross power density, corrected gross power density, corrected net power density. RED stack (10x10 cm^2, 10 cell pairs) equipped with Fujifilm membranes, 270 μm woven spacers. C_{HIGH} = 2 M; C_{LOW} = 0.04 M; T = 293 K.

The corrected net power density was calculated using the same procedure already described for the case of C_{LOW} = 0.02 M and is not reported again here.

These results confirm that (i) the highest power density is achieved at the lowest flow rate and that (ii) flow velocities higher than 1 cm/s are unsuitable for generating electric power from the RED unit adopted in the present study.

In conclusion, this work proved that NH_4HCO_3-water solutions may be conveniently used in a RED-closed loop for converting low-grade waste heat into electric current. Results have shown that at a given flow rate (i.e. 1 cm/s) a dilute concentration of about 0.02-0.04M guarantees the largest power output. At these values of concentration, under the conditions here investigated, a maximum net power output of 2.42 $W/m^2_{cell\ pair}$ can be obtained at the lowest feed flow velocity (i.e. 0.5 cm/s). On the other hand, feed flow rates higher than 1 cm/s lead to negative power output being the power loss due to pressure drop larger than the power production.

Overall, the use of ammonium bicarbonate allowed to reach values of power density comparable with the state-of-the-art of the RED process with conventional (NaCl) solutions [104], although membranes are not optimized yet for the use of this salt. Such

finding suggests that ammonium bicarbonate could be a promising salt for the RED process. Furthermore, results highlight that the power density achieved in this work is three times higher than that reported by Luo et al. in a similar work [22] where the same salt is used. The main difference has been identified in the much lower stack resistance, likely due to an improved formulation of IEMs with a lower thickness and higher ionic conductivity, thus also emphasizing the potential for further technological improvements. The work show in the next sections are deal with the "regeneration" of the NH_4HCO_3 solutions exiting from the RED-unit in order to assess the final feasibility of the RED heat engine for waste heat-to power conversion.

2.6.2 Ammonium carbamate

Among the thermolytic salt, a valuable alternative for the salt extraction strategy is ammonium carbamate salt (NH_4COONH_2). It has similar properties than ammonium bicarbonate; at temperatures of 60 °C upwards, it decomposes completely into ammonia and carbon dioxide.

Since the first years of 1900s, this salt was well known in the agriculture industry because it is the intermediate stage in the urea (NH_2CONH_2) production, a nitrogen-rich fertiliser [109–112]. Recently, the formation of ammonium carbamate from carbon dioxide and ammonia has been extensively investigated, in aqueous and non-aqueous solutions, for the greenhouse problem. This can be a valid strategy for the CO_2 capture as such gas can be converted into feedstock and consequently in fertilizers [113,114]. It is also studied as high energy density thermal energy storage material [115] for its thermosensitive characteristic.

Thanks to its properties, ammonium carbamate can be exploited for the solution regeneration in a SGPHE with really low temperature.

According to the literature [66], the ammonium carbamate (AmCb) is more soluble than ammonium hydrogen carbonate (AmBC) in water (around 40 % wt at 20 °C). This property can be exploited in order to increase the RED performance with thermolytic salts because in this way can be increased the driving force between the concentrated and diluted solution. In order to confirm the literature value of maximum solubility in water of this salt, some basic tests were performed changing the concentration in water from 0.75 M to 8 M. Since 6M, after apparently complete salt dissolution, some salt started to

precipitate back. During the dissolution, the solution temperature decreases because the process is endothermic and this can affect the solubility.

Another important property of this salt is the conductivity because this affect the performance of RED system in terms of power production. In Figure 2.32 are reported the experimental values.

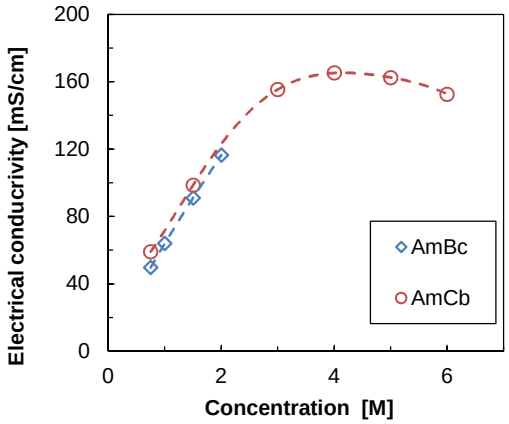

Figure 2.32: Electrical conductivity of ammonium carbamate (AmCb) and ammonium hydrogen carbonate (AmBc) at different concentrations (room temperature).

The values were measured by conductivity meter WTW TetraCon® 325. As can be observed (Figure 2.32), the conductivity increases up to a maximum value at 4M of concentration than starts to decrease again. It is much high if compared with ammonium hydrogen carbonate.

After having analysed those basic properties, an experimental campaign was made in order to investigate the performance of ammonium carbamate with a lab-scale RED unit.

Experimental apparatus

The experimental campaign was performed with a cross flow reverse electrodialysis (RED) module made by REDStack Company with 10x10 cm^2 of membrane area with 5 cell pairs. The ion exchange membranes were provided by Fujifilm Manufacturing Europe BV (The Netherlands) and 150 μm woven spacers (Deukum GmbH, Germany) were used as stack components. The properties of the used IEMs are reported in Table 2.4.

Table 2.4: Properties of the two sets of IEMs adopted in the experiments*.

Membrane	Thickness [μm]	Areal resistance[a] [Ω cm^2]	Permselectivity[b] [%]
Fujifilm AEM E1	120	1.1	89 %
Fujifilm CEM E1	120	2.9	91 %

* Nominal data provided by membrane manufacturer using conventional (NaCl) solutions.

[a] electrical resistance measured in 0.5 M NaCl solution at 25°C.

[b] permselectivity measured in 0.1 – 0.5 M NaCl conditions at 25°C.

Comparing the properties of the Fujifilm E1 membranes (Table 2.4) with the Fujifilm RP1 (Table 2.1) membranes used in the ammonium hydrogen carbonate experimental campaign, it can be seen that permselectivity and areal resistance are slightly reduced. On one hand the power energy producible can be reduced due to a lower permselectivity but in the other hand, probably the effect of lower membrane resistance can affect much more the energy production.

Fujifilm cation exchange membrane were employed in the electrode compartments and the electrode rinse solution was composed of 0.1 M $K_3Fe(CN)_6$, 0.1 M $K_4Fe(CN)_6 \cdot 3H_2O$ (Sigma Aldrich with purity 99.5%), adding 1.5 M NH_4COONH_2 as supporting electrolyte. A flow rate of 90 ml/min in the electrode compartments was kept constant for all the tests.

The test rig is constituted by the RED unit and several tanks to contain inlet and outlet solutions. A peristaltic pump with double head (MASTERFLEX L/S) was used to force the concentrate and the dilute solutions to flow within the RED unit. Another peristaltic pump (MASTERFLEX L/S) was used for pumping the electrode rinse solution (ERS) from a glass tank covered by aluminium foil to avoid decomposition of the redox couple due to light exposure.

The relevant process variables (stack voltage and current) were measured by two multimeters. The conductivity of the feed solutions (both at inlets and outlets) were measured by means of a conductivity meter (WTW TetraCon® 325). A variable resistance (ranging between 0.7 – 54.8 Ω) was connected to the RED unit for testing the system under different load conditions. The feed solutions were prepared with demineralized water and ammonium carbamate (Sigma-Aldrich, purity >99%).

Results and discussion

The RED unit was tested under different operating conditions, changing the feed concentration of the dilute and concentrate solutions. For all the tests was choice a feed flow velocity of 2 cm/sec for the high and low compartments because the pressure drops measured were very low. For this reason, net power density was not calculated.

The best concentrate concentration for the power energy production is highlighted keeping constant the dilute concentration arbitrarily at 0.05M of ammonium carbamate in water and then fixing the best concentrate concentration, the dilute concentration was changing to find the overall best condition.

It was measured the black resistance (0.584 Ω) assembled the stack with only one membranes and applying an external current. This value was used to calculate the corrected power density in all the test because the same stack and the same electrolyte concentration was used in all the experiments.

A summary of the tests presented is reported in Table 2.5.

Table 2.5: Summary of experimental tests presented in this work. *

Main focus of the tests	**Dilute concentration, C_{LOW} [M NH_4COONH_2]**	**Feed flow velocity, *v* [cm/s]**
Influence of concentrate concentration (C_{HIGH})[a]	3 – 4.2 - 5	2
Influence of dilute concentration (C_{LOW})[b]	0.005 - 0.01 - 0.02 - 0.03 - 0.05	2

*Overall conditions: RED stack (10x10 cm^2, 10 cell pairs) equipped with Fujifilm membranes E1, 150 μm woven spacers. $v_{LOW} = v_{HIGH} = 2$ cm/sec; T = 293 K.

[a] Concentration of dilute solution is fixed at 0.05M

[b] Concentration of concentrate solution is fixed at 5M

Influence of concentrate solution

The ammonium carbamate has high solubility in water, this can contribute to increase the driving force of the salinity gradient between high and low compartment. On the other hand, higher concentration means lower permselectivity and lower membrane resistance. The influence of this parameters was investigated changing the concentration from the maximum concentration achievable with ammonium carbamate in water at room temperature (5M) to a lower concentration (3M) and the concentration that according to Figure 2.32 gives the maximum conductivity value (4.2M).

All the main results are reported in Figure 2.33:

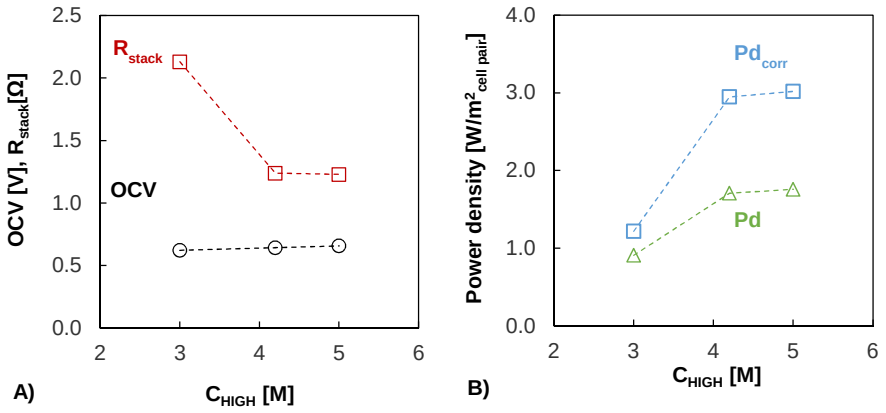

Figure 2.33: Influence of concentrate concentration (C_{HIGH}) on process performance. A) OCV, stack resistance. B) Gross power density, corrected gross power density. Cross flow RED stack (10x10 cm^2, 5 cell pairs) equipped with Fujifilm membranes E1, 150 µm woven spacers. C_{LOW} = 0.05 M; T = 293 K.

The OCV slightly increases when the high concentration (C_{HIGH}) is increased from 3M to 5M while the stack resistance markedly decreases from 3M to 4.2M maintaining the same value at 5M (Figure 2.33A). The OCV does not increase rapidly because the electrical conductivity in the range 3M-5M does not evidently change. On the other hand, the stack resistance changes because it is strongly affected by low compartment.

If the high concentration goes toward higher values, this has an indirect effect also in the other compartment. Increasing the gradient concentration increases the amount of salt that pass through the membranes growing the medium concentration in the dilute channel. This effect is also reported in literature [116].

These two opposite effects influence the stack performance, in particular at 5M the power density reaches its maximum value (1.76 $W/m^2_{cell\ pair}$) and consequently the maximum corrected power density (3.02 $W/m^2_{cell\ pair}$). The trend is shown in Figure 2.33B.

Influence of dilute solution

The dilute concentration has an important effect on the power density due to its influence on stack resistance and driving force. In particular, the stack resistance is the sum of different contributes: the resistance of high and low compartment, the resistance

of AEM and CEM and the blank resistance. The concentration of dilute solution is directly correlated to the resistance of low solution compartments (in some case more than 50% of the total stack resistance [103]) and on the membrane resistance as discussed in the previous paragraph.

The main performance parameters are measured changing the low concentration from 0.005M to a maximum value of 0.05M keeping constant the best value found for the concentrated solution (5M).

The results are shown in Figure 2.34:

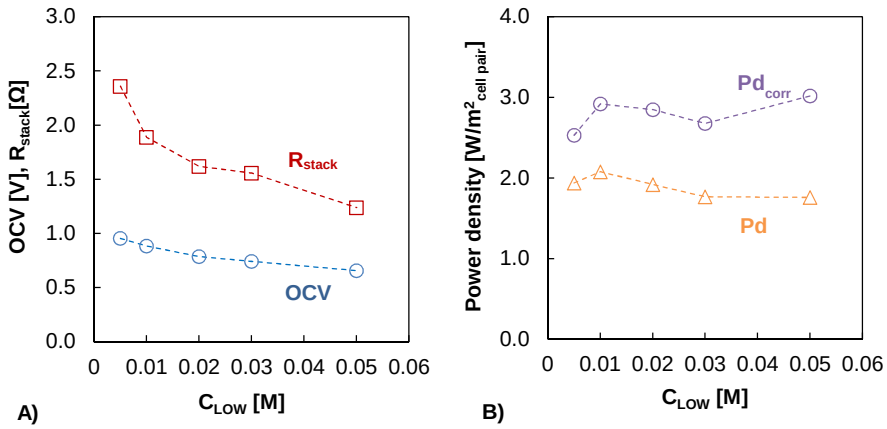

Figure 2.34: Influence of concentrate concentration (C_{HIGH}) on process performance. A) OCV, stack resistance. B) Gross power density, corrected gross power density. Cross flow RED stack (10x10 cm^2, 5 cell pairs) equipped with Fujifilm membranes E1, 150 μm woven spacers. C_{LOW} = 0.05 M; T = 293 K.

The grown of dilute concentration allows a reduction of OCV and stack resistance (Figure 2.34A). Both parameters influence the power density performance but the resistance has the strongest effect. The maximum power density (2.08 $W/m^2_{cell\ pair}$) is obtained at 0.01M of ammonium carbamate and this value decreases when the concentration increases (Figure 2.34B). Nevertheless, the maximum corrected power density (3.02 $W/m^2_{cell\ pair}$) is obtained when the concentration is equal to 0.05M, due to the marked effect of stack resistance while the OCV changes only lightly from 0.01M to 0.05M.

2.6.3 Performance comparison between ammonium hydrogen carbonate and ammonium carbamate

The performances of the two selected thermolytic salts, ammonium hydrogen carbonate and ammonium carbamate, in terms of power density and corrected power density, are comparable (paragraph 2.6.1 and paragraph 2.6.2). Nevertheless, the values were measured with different stacks and different experimental conditions. In order to compare directly the results, the test-rig used in the experimental campaign with ammonium carbamate was also exploited with ammonium hydrogen carbonate, selecting the best condition found in the previous work (i.e. 0.02M – 2M).

In order to calculate the corrected power density, the blank resistance (0.672 Ω) was also measured with the electrode solution made by 0.1 M $K_3Fe(CN)_6$, 0.1 M $K_4Fe(CN)_6 \cdot 3H_2O$ (Sigma Aldrich with purity 99.5%) and adding 1 M NH_4HCO_3. The blank resistance with ammonium hydrogen carbonate is slightly higher than ammonium carbamate due to a lower salt concentration and consequently lower electrical conductivity. The main results are shown in Figure 2.35.

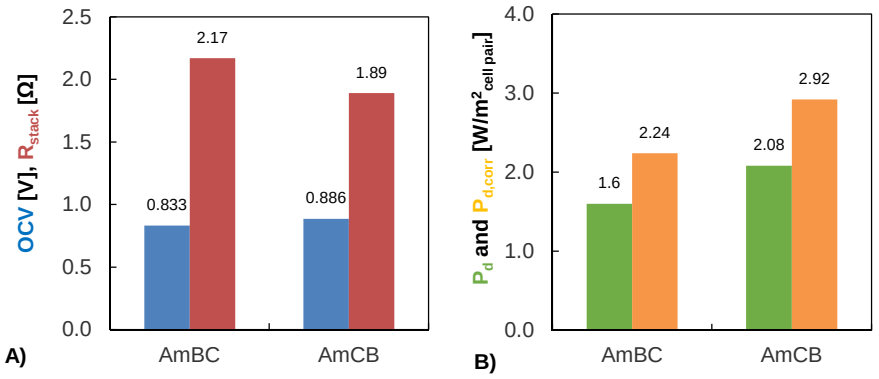

Figure 2.35: Performance comparison between ammonium hydrogen carbonate (or ammonium bicarbonate - AmBC) and ammonium carbamate (AmCB). A) OCV, stack resistance. B) Gross power density, corrected gross power density. Cross flow RED stack (10x10 cm^2, 5 cell pairs) equipped with Fujifilm membranes E1, 150 µm woven spacers. AmBC: C_{LOW} = 0.02 M and C_{HIGH} = 2M; AmCB: C_{LOW} = 0.01 M and C_{HIGH} = 5M; T = 293 K.

The performance of ammonium carbamate, in terms of power density and corrected power density, is better than ammonium bicarbonate with the same experimental set-up and conditions. This result depends by higher OCV value and lower stack resistance.

However, the corrected power densities are comparable with ammonium hydrogen carbonate reported in Figure 2.31 at 2 cm/sec and the best results with ammonium carbamate. Furthermore, it is necessary a salt concentration (5M) much higher than ammonium bicarbonate (2M) in order to obtain a power density around 3 $W/m^2_{cell\ pair}$ with ammonium carbamate. A higher gradient means also a higher amount of salt that pass through the membrane that have to be regenerated. The ammonium carbamate regeneration also need a higher temperature than ammonium hydrogen carbonate.

In view of the above, the ammonium hydrogen carbonate was selected as the best thermolytic salt for a deep study on the regeneration stage with simulation tools and experimental tests.

2.6.4 New ideas for RED high performance with thermolytic salt

Different ideas were applied and investigated in order to improve the RED performance with thermolytic salts.

One of the main problem with ammonium hydrogen carbonate is its relatively low solubility in water. To increase the amount of salt that can be solubilized, it was added a certain amount of ammonia making different tests at different concentration. Increasing the concentration increases the driving force because there is a higher salinity gradient.

As already mentioned, the stack resistance is strongly affected by the low electrical conductivity of dilute solution. In order to try to solve this issue, some tests were made adding a small quantity of another salt in such a way that the stack resistance decreases because increase the conductivity of the dilute compartment.

Ammonium hydrogen carbonate with ammonia

All NH_3-CO_2-based salts are soluble in water but ammonium hydrogen carbonate has the lowest solubility among the thermolytic salt. Moreover, their solubility depends also on the temperature, as shown exemplary for NH_4HCO_3 in Table 2.6. It should be noted that both lower solubility values [97,117,118] and higher solubility values [119] are

reported in the literature. According to [119], the solubility limits of NH_4HCO_3 at 20°C is equal to 2.78 mol/l.

Table 2.6: Solubility of NH_4HCO_3 in water depending on the temperature [66]

NH_4HCO_3-H_2O		
Temperature [°C]	Solubility [mass fraction]	Solubility [mol/l]
0	0.106	1.40
10	0.137	1.84
20	0.176	2.39
25	0.199	2.72
30	0.224	3.09
40	0.279	3.90
50	0.342	4.80
60	0.414	5.81

When NH_4HCO_3 is dissolved in water, the following chemical equilibria are established [120,121]:

$$NH_4HCO_{3(s)} \leftrightarrow NH_4^+ + HCO_3^- \quad [2.3]$$

$$2H_2O \leftrightarrow H_3O^+ + OH^- \quad [2.4]$$

$$NH_3 + H_2O \leftrightarrow NH_4^+ + OH^- \quad [2.5]$$

$$CO_2 + 2H_2O \leftrightarrow HCO_3^- + H_3O^+ \quad [2.6]$$

$$HCO_3^- + H_2O \leftrightarrow CO_3^{2-} + H_3O^+ \quad [2.7]$$

$$NH_3 + HCO_3^- \leftrightarrow NH_2COO^- + H_2O \quad [2.8]$$

where NH_4^+ is the ammonium ion, HCO_3^- is the bicarbonate ion, H_3O^+ is the hydronium ion, OH^- is the hydroxide ion, CO_3^{2-} is the carbonate ion and NH_2COO^- is the carbamate ion.

When only NH_4HCO_3 is dissolved in water and there is no outgassing, the ratio between nitrogen and carbon compounds is unity, and HCO_3^- ions are the main carbon species in the solution. Increasing the ratio between nitrogen and carbon compounds, e.g. by adding aqueous ammonia solution, the amount of NH_2COO^- ions (according to equilibrium previously presented) and, to a lesser extent, of CO_3^{2-} ions in the solution increases, while the amount of HCO_3^- ions decreases [118,122,123]. Thus, addition of aqueous ammonia to a saturated NH_4HCO_3 solution allows the adding of a further amount

of a NH_3-CO_2-based salt without the incidence of salt precipitation since the excess of free NH_3 favours the formation of NH_4NH_2COO, which is by far more soluble than NH_4HCO_3 itself [124]. Following this characteristic, batch experiments were made in order to test the possibility to use NH_4HCO_3 with ammonia at higher concentration than its maximum solubility in water.

A specific amount of pure NH_4HCO_3 (SIGMA-ALDRICH Co. LLC) was added to distilled water in a glass flask (50 ml) in order to gain an NH_4HCO_3 solution/suspension with the initial concentration of 1 mol/l to 4 mol/l (referred to 50 ml liquid). After a short time of mixing, a specific amount of aqueous ammonia (25 % by weight, SIGMA-ALDRICH Co. LLC) was added by use of a pipette in order to gain an initial concentration of 0 to 3 mol free NH_3 per litre solution/suspension. The liquid was mixed in the flask, which was closed with a lid, for 10 minutes at a constant temperature of 25°C ± 0.2°C. After the mixing, the dissolving of the salt was checked. Furthermore, the conductivity and the pH of the liquid were measured at a constant temperature of 25°C ± 0.2°C.

The measurement of the conductivity was accomplished by use of the conductivity meter WTW – LF 196. Measurements were conducted without temperature compensation since the temperature was kept constant in each measurement.

The pH values of the solutions were measured with a pH meter XS Instruments 8 Series. Also in this case, measurements were performed without temperature compensation. The pH meter was calibrated routinely with standard buffers with a pH value of 7, 4.01 and 10.01 respectively at a constant temperature of 25°C ± 0.2°C.

The measured pH and conductivity values of the aqueous NH_4HCO_3-NH_3-mixtures are shown in Table 2.7 and Table 2.8. Additionally, it is noted in the tables if the salt was fully dissolved or not.

A white background of the respective table item signifies that the salt was fully dissolved, while a grey background signifies that the salt was not dissolved. The experimental pH values match theory in a qualitative way. The higher the initial concentration of free NH_3, the higher the pH of the liquid, as expected from reaction [2.5]. The higher the initial concentration of NH_4HCO_3, and thus the initial concentration of HCO_3^-, the lower the impact of free NH_3 on the pH since a high concentration of HCO_3^- ions favours the consumption of NH_3 via reaction [2.8] which has no direct influence on the pH.

Table 2.7: Measured pH-values of aqueous NH_4HCO_3-NH_3-mixtures at 25°C; the grey cells highlighted the condition in which the salt is not completed dissolved.

pH [-]	**C_{NH_3} [mol/l]**			
$C_{NH_4HCO_3}$ [mol/l]	0	1	2	3
1	7.66	9.48	9.87	10.17
2	7.74	9.05	9.65	9.98
3	7.86	8.62	9.32	9.62
4	7.82	8.48	8.88	9.41

Furthermore, it can be seen that the adding of aqueous NH_3 to oversaturated NH_4HCO_3 suspensions can lead to a complete dissolution of the salt due to the formation of NH_2COO^- from HCO_3^- ions in accordance with reaction [2.8]. A complete dissolution of salt in a 3 molar NH_4HCO_3 suspension occurs when the initial concentration of free NH_3 is 1 mol/l, while a complete dissolution of salt in a 4 molar NH_4HCO_3 suspension takes place only when the initial concentration of free NH_3 is 3 mol/l.

As can be seen in Table 2.8, also the conductivity values match the theory qualitatively. The increase of the NH_4HCO_3 concentration leads to a strong increase of the conductivity until the solubility limit is reached.

In solutions, the increase of the NH_3 concentration results generally in a smaller increase of the conductivity since the total amount of ions in the solution is not changed but only their distribution. The increase of the NH_3 concentration in suspensions can lead to a stronger increase of the conductivity than that in solutions as the presence of NH_3 leads to an increasing amount of dissolved salt.

Table 2.8: Measured electrical conductivity of aqueous NH_4HCO_3-NH_3-mixtures at 25°C; the grey cells highlighted the condition in which the salt is not completed dissolved.

	C_{NH_3} [mol/l]			
$C_{NH_4HCO_3}$ [mol/l]	0	1	2	3
1	69.1	79.0	83.9	82.8
2	119.7	125.6	131.3	133.8
3	146.9	156.1	165.2	165.7
4	144.9	163.3	169.6	174.9

Thus, NH_3-CO_2-based salt solutions with much higher salt concentrations than that of NH_4HCO_3 solution at its solubility limit can be produced in the presence of aqueous NH_3. These solutions can be used in a RED units in order to generate a greater salinity gradient between concentrate and dilute solution, which might lead to greater power densities and efficiencies of the system.

A test with a cross flow RED stack (5 cell pairs) was made using a solution of NH_4HCO_3 and NH_3 equal to 3M and 1M, respectively. The results were compared with the "standard" solution of NH_4HCO_3 at 2M. The diluted solution concentration was for both the tests equal to 0.02M. It was used the same test-rig exploited for the experimental campaign with ammonium carbamate (paragraph 2.6.2): the same feed flow velocity and the same electrode solution were fixed.

The main results are shown Figure 2.36:

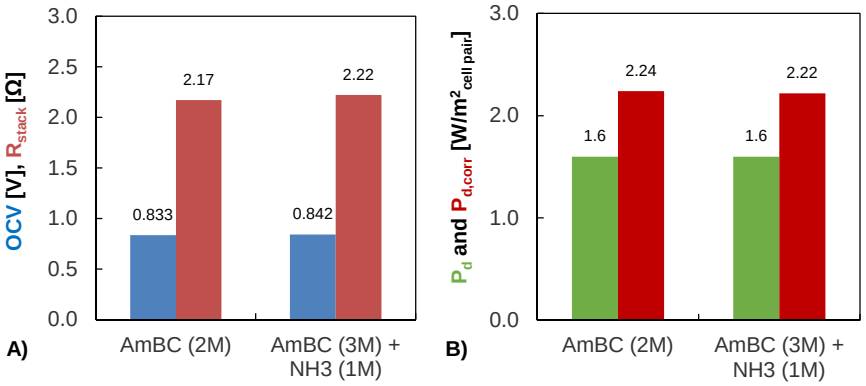

Figure 2.36: Performance comparison between pure NH4HCO3 (2M) and a mixture of NH4HCO3 (3M) and NH3 (1M). A) OCV, stack resistance. B) Gross power density, corrected gross power density. Cross flow RED stack (10x10 cm2, 5 cell pairs) equipped with Fujifilm membranes E1, 150 μm Deukum woven spacers. CLOW = 0.02 M; T = 293 K.

As can be observed in Figure 2.36, the OCV with 3M of NH_4HCO_3 (electrical conductivity equal to 158.8 mS/cm) is slightly higher than "standard" condition (electrical conductivity equal to 119.5 mS/cm), nevertheless the power density and the corrected power density have the same value because the stack resistance is slightly higher.

This idea was rejected because the results were not as expected.

Mixture of NH_4HCO_3 and NH_4COONH_2

The use of mixtures instead of pure salts can increase the performance of RED unit because it acts on important parameters. Normally, the idea works if the two salts are selected in such a way that they have good electrical conductivity and high activity coefficient. This is not fully the case, but adding ammonium carbamate at a solution with ammonium bicarbonate can be obtained a solution with higher electrical conductivity than pure ammonium bicarbonate. At the same time, the regeneration stage can be operated in the range 40-60 C° because in that range, in theory only ammonium bicarbonate, is degraded and reabsorbed in the low solution compartment.

Following this idea, different mixtures of the two thermolytic salts were tested in order to improve the performance of pure ammonium hydrogen carbonate. Moreover, in this case, both salts are NH_3-CO_2-based salt, so the salt extraction strategy is still applicable.

The experimental campaign was performed with a cross flow reverse electrodialysis (RED) module made by REDStack Company with 10x10 cm^2 of membrane area. The cell pair number was fixed at 5 for each test performed. The ion exchange membranes were provided by Fujifilm Manufacturing Europe BV (The Netherlands) and 150 μm woven spacers (Deukum GmbH, Germany) were used as stack components. The properties of the used IEMs are the same reported in Table 2.4.

The comparison of the main results is reported in Figure 2.37.

A mixture between the two thermolytic salt gives in one such specific conditions higher performance than pure ammonium bicarbonate salt. The corrected power density with a mixture 1.5M of AmBC and 1.5M of AmCB is 20% higher because the OCV is higher and the stack resistance is lower compared with pure salt.

The results are slightly lower than the pure ammonium carbamate discussed in the section 2.6.2 but with this mixture, in theory, a lower regeneration temperature is needed given probably the possibility to increase the efficiency of the overall integrated system.

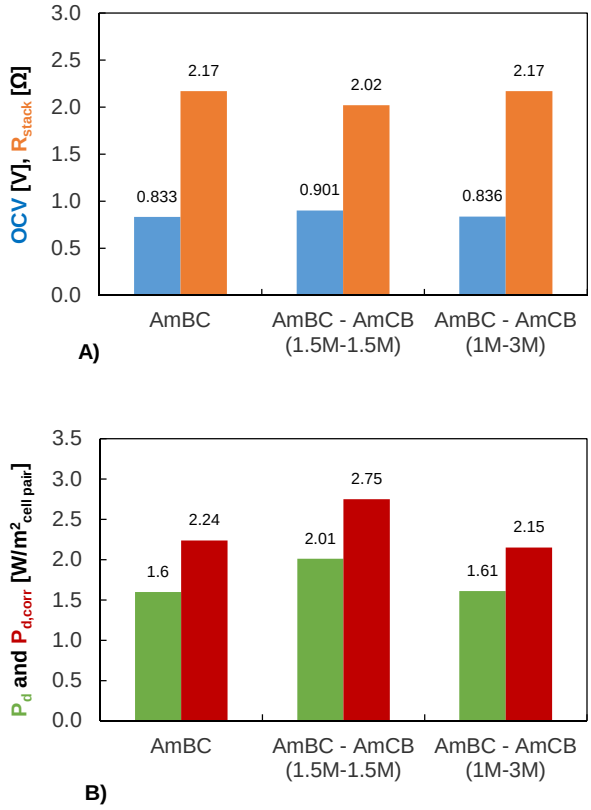

Figure 2.37: Performance comparison between pure NH_4HCO_3 (2M), a mixture of NH_4HCO_3 (1.5M) and NH_4COONH_2 (1.5M) and a mixture of NH_4HCO_3 (1M) and NH_4COONH_2 (3M). A) OCV, stack resistance. B) Gross power density, corrected gross power density. Cross flow RED stack (10x10 cm^2, 5 cell pairs) equipped with Fujifilm membranes E1, 150 μm Deukum woven spacers. C_{LOW} = 0.005 M of NH_4HCO_3 and 0.005M of NH_4COONH_2; T = 293 K.

Mixture of thermolytic salt and other selected salts

The power density and the corrected power density are influenced by some properties of the selected salt, such as electrical conductivity and activity coefficients but also by the RED unit itself, such as the channel thickness and the ion exchange membranes. All of these characteristics influences the OCV value and the stack resistance which in turn give the maximum power density and corrected power density.

Rearranging the equation (2.12) and equation (2.18) substituting at R_{ext} the stack resistance, the following equation are obtained, expressing the maximum value gained for power density and corrected power density.

$$Pd_{max} = \frac{OCV^2}{4R_{stack}NA} \quad (2.21)$$

$$Pd_{corr,max} = \frac{OCV^2}{R_{stack}(1+\frac{R_{cell}}{R_{stack}})^2 NA} \quad (2.22)$$

All the terms are previously defined; P_d and $P_{d,corr,max}$ are both expressed as ($W/m^2_{cell\ pair}$). However, the stack resistance is the sum of all the resistance in stack and can be expressed as following:

$$R_{stack} = R_{AEM} + R_{CEM} + R_{HIGH} + R_{LOW} + R_{blank} = R_{cell} + R_{blank} \quad (2.23)$$

Taking as example the tests with ammonium hydrogen carbonate (2M – 0.02M at 1 cm/sec), the resistance of cell compartments is around 70% of R_{stack}. Almost 55% of R_{cell} is the resistance of the low compartment. This last resistance can be calculated as the sum of the ratio between the channel thickness and the electrical conductivity of the solutions. Maintaining the same stack configuration and then the same channel thickness, the only way to decrease the resistance of the dilute channel is to increase the concentration and consequently the electrical conductivity but in this way the power density decreases because the salinity gradient decreases.

A new idea to solve this issue is to add a certain amount of “support” salt at the same concentration in the dilute and concentrate solution with high electrical conductivity. Likely, the second salt at the same concentration in the concentrated and diluted channel do not move, increasing the electrical conductivity in the compartments and consequently reducing the stack resistance. With the purpose to confirm experimentally the idea, several tests were made with mixtures of thermolytic salts and other selected salts (NaCl and KCl). The test-rig described in the previous section was also used in all these tests. The concentration and the electrical conductivity of the solutions are reported in Table 2.9 while the comparison results between pure ammonium bicarbonate (AmBC) and salt mixture are reported in Figure 2.38.

Table 2.9: Experimental electrical conductivity values for pure and mixed salts with AmBC.

Sample	HIGH composition	LOW composition	HIGH [mS/cm]	LOW [mS/cm]
Pure AmBC	AmBC (2M)	AmBC (0.02M)	114.8	2.09
Mix 1	AmBC (2M) + NaCl (0.5M)	AmBC (0.02M) + NaCl (0.5M)	105.4	44.8
Mix 2	AmBC (2M) + KCl (0.5M)	AmBC (0.02M) + KCl (0.5M)	156.4	60.6
Mix 3	AmBC (2M) + KCl (0.02M)	AmBC (0.02M) + KCl (0.02M)	114.2	4.72

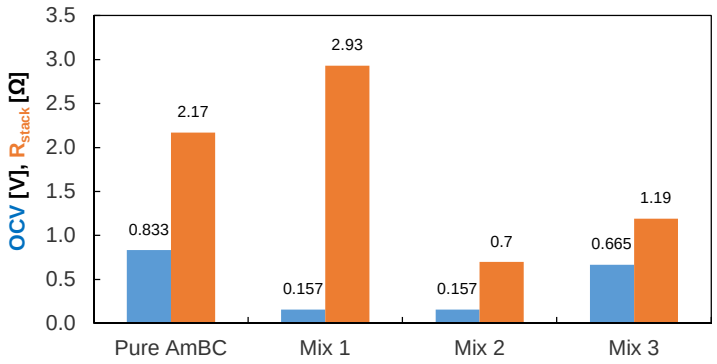

A)

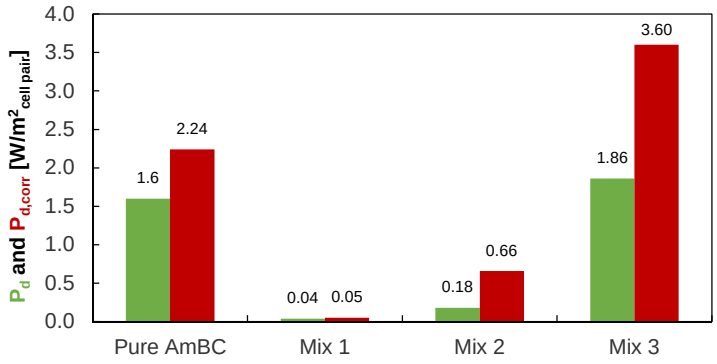

B)

Figure 2.38: Performance comparison between pure NH_4HCO_3 (2M), a mixture of NH_4HCO_3 (2M) and NaCl (0.5M), KCl (0.5M) and KCl (0.02M), respectively. A) OCV, stack resistance. B) Gross power density, corrected gross power density. Cross flow RED stack (10x10 cm^2, 5 cell pairs) equipped with Fujifilm membranes E1, 150 μm Deukum woven spacers. C_{LOW} = 0.02 M of NH_4HCO_3 with 0.5M of NaCl, 0.5M of KCl and 0.02M of KCl, respectively; T = 293 K.

In the first mixture (Mix 1), ammonium bicarbonate at standard condition (2M – 0.02M) is mixed with sodium chloride at 0.5M in both dilute and concentrate channels. The electrical conductivity in the dilute channel was increased but unlikely the opposite behaviour was obtained in the concentrate channels (Table 2.9). This gave a really low OCV and high stack resistance producing insignificant energy (Figure 2.38). A different salt was searched in order to improve the effect of the support salt. In particular, imagining that the conductivity of the mixture was a value in the middle of the pure salts, potassium chloride was chosen due to its high conductivity if compared with NaCl at low concentration.

The second tested mixture (Mix 2) is composed by ammonium bicarbonate at standard condition (2M-0.02M) and potassium chloride (0.5M). The electrical conductivity values is better than NaCl (Table 2.9), giving a three times lower stack resistance than pure salt but unfortunately a pure OCV due to a small driving force gives a low power density even if higher than NaCl (Figure 2.38).

The third mixture (Mix 3) is composed by ammonium bicarbonate at standard condition (2M-0.02M) and potassium chloride with really low concentration (0.02M). The small amount of support salt reduces only slightly the electrical conductivity of concentrate solution but the value for the dilute solution becomes twice than pure salt (Table 2.9). Even if the OCV value is reduced, the stack resistance is almost half of pure AmBC producing almost 17% higher power density and 60% higher corrected power density (Figure 2.38).

The result obtained with Mix 3 is the best results ever obtained with ammonium bicarbonate using a RED stack, higher than results described in the section 2.6.1 and results reported in the literature [97]. Similar tests were made with ammonium carbamate. The salt mixture composition and the electrical conductivity are reported in Table 2.10.

Table 2.10: Experimental electrical conductivity values for pure and mixed salts with AmCB.

Sample	**HIGH composition**	**LOW composition**	**HIGH [mS/cm]**	**LOW [mS/cm]**
Pure AmCB	AmCB (5M)	AmCB (0.01M)	162.7	1.23
Mix 1	AmCB (5M) + KCl (0.01M)	AmCB (0.01M) + KCl (0.01M)	163.4	2.61
Mix 2	AmCB (5M) + KCl (0.02M)	AmCB (0.02M) + KCl (0.02M)	163.6	3.78

The comparison between results with pure ammonium carbamate and mixtures of this salt with potassium chloride are shown in Figure 2.39.

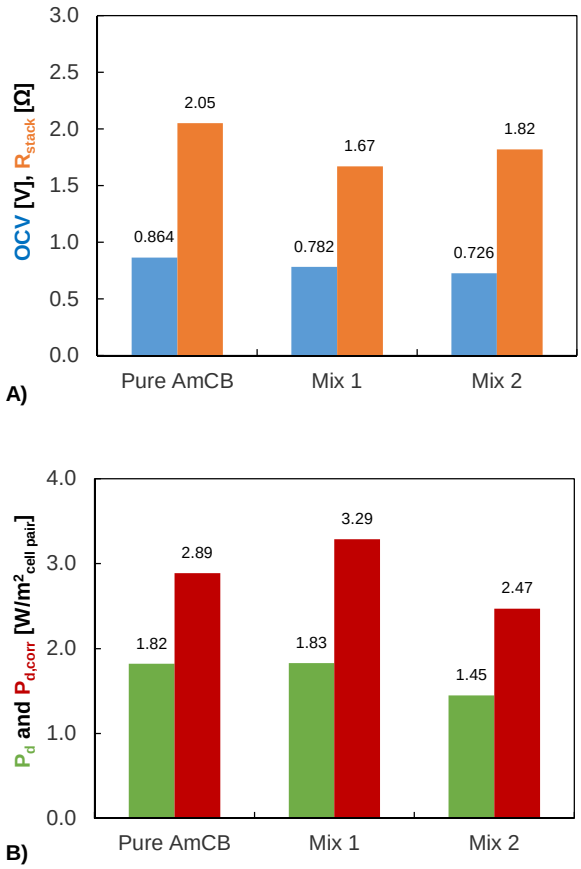

Figure 2.39: Performance comparison between pure NH_4COONH_2 (5M), a mixture of NH_4COONH_2 (5M) and KCl (0.01M) and KCl (0.02M), respectively. A) OCV, stack resistance. B) Gross power density, corrected gross power density. Cross flow RED stack (10x10 cm^2, 5 cell pairs) equipped with Fujifilm membranes E1, 150 μm Deukum woven spacers. C_{LOW} = 0.02 M of NH_4COONH_2 with 0.01M of KCl and 0.02M of KCl, respectively; T = 293 K.

The results with pure ammonium carbamate are slightly different than other tests (2.6.2), this due to a different electrode solution (0.1M $K_3Fe(CN)_6$, 0.1M $K_4Fe(CN)_6 \cdot 3H_2O$ and 0.5M NH_4COONH_2, blank resistance equal to 0.851Ω). The power

density is lower even if the corrected power density is approximately the same. The Mix 2 gives the best results compared to pure salt and Mix 3. The OCV is lower than pure AmCB but the lowest stack resistance allows to produce higher power density and corrected power density.

However, unfortunately it was demonstrated that the support salt moves from one channel to the other in the stack. The amount of potassium ions before and after a test with a Mix 1 was measured by means of ICP-AES device. The amount of potassium changed from 350 mg/l $\pm$ 5 in the inlet solution to 203 mg/l $\pm$ 5 in the outlet solution.

This behaviour can lead this solution inapplicable with SGPHE. More investigations are needed in order to better understand if this option is applicable or not but this is out of the PhD work reported in this manuscript.

3 SIMPLIFIED MODEL FOR REVERSE ELECTRODIALYSIS UNIT

Abstract

A number of process models have been proposed in recent years for the RED process, but all of them dealt with NaCl-water solutions. This chapter presents a lumped-parameters RED model able to predict the performance of the unit with 41 different salts-water solutions. The model describes all the main phenomena involved in the RED process considering actual solution and membrane properties for each salt. The model was validated comparing experimental results of five representative salts (i.e. NaCl, NH_4Cl, $ZnCl_2$, CsCl and NH_4HCO_3) with model predictions.

Specific sensitivity analysis were performed for the five selected salts in order to analyse the effect of different operative parameters such as feed flow velocity in the channel, concentrations of the high and low solutions and membrane properties on system performance.

[*] Part of this chapter has been published as:

- M. Bevacqua, A. Carubia, A. Cipollina, A. Tamburini, M. Tedesco, G. Micale, Performance of a RED system with Ammonium Hydrogen Carbonate solutions, Desalination and Water Treat. 3994 (2016) 1–12.
- M. Bevacqua, A. Tamburini, M. Papapetrou, A. Cipollina, G. Micale, A. Piacentino, Reverse electrodialysis with NH_4HCO_3-water systems for heat-to-power conversion, Energy 137 (2017) 1293-1307

3.1 RED model introduction

A number of process models have been proposed in recent years for a RED unit [72,125,126], but all of them dealt with NaCl-water solutions. In this chapter, a model will be presented to manage 41 salts including for the first time NH_4HCO_3-water solutions.

The development of good model, even if simplified, can help the research in the reverse electrodialysis field using artificial solution instead of a natural one. Given the preliminary nature of this work and the broad sensitivity analysis carried out, a number of simplifying assumptions have been made during the model formulation. In particular, some non-ideal phenomena were neglected:

- water transport through membranes due to osmotic and electro-osmotic flux;
- concentration polarization phenomena;
- parasitic currents in the manifolds.

Other simplifications:

- all solutions and cell pairs variables were evaluated at the average conditions between inlet-outlet of the feed channels;
- solutions flow rate variations between inlet and outlet were neglected.

Some of the salts were selected and experimental tests were made in order to validate the model.

3.2 Model equations

The evaluation of the physical properties represents the first modelling step. All the salt physical properties were collected from literature works and from handbooks [66,67] but they are represented and reported in different way. In order to overcome this problem, each property is described by one equation depending only by different parameters function of the salt under investigation. In this way, the same model can be used for each salt, only this parameters were automatically changed.

The equivalent conductivity was estimated using Jones and Dole' equation [127]:

$$\Lambda = \Lambda_0 - \frac{A_\Lambda C^{\frac{1}{2}}}{1+B_\Lambda C^{\frac{1}{2}}} - C_\Lambda C \qquad (3.1)$$

where Λ_0 is the equivalent conductivity of salt at infinite dilution, A_Λ, B_Λ, C_Λ are model parameters used for fitting, and C is the molar concentration.

The solutions density was estimated as a linear function of the molal concentration m for both the dilute and concentrated solutions:

$$\rho = \rho_w + \left(\frac{\Delta\rho}{\Delta m}\right) m \tag{3.2}$$

where ρ_w is water density (0.997 kg/l) at 25°C, and the slope of the line were evaluated by fitting experimental data from literature [67].

The activity coefficients were estimated by Staples equation [128]:

$$ln\gamma = \frac{-|Z_+ Z_-| A_\gamma m^{0.5}}{1 + B_\gamma m^{0.5}} + C_\gamma m + D_\gamma m^2 + E_\gamma m^3 \tag{3.3}$$

where $A\gamma = 1.17625\ kg^{1/2}\ mol^{-1/2}$, m is the molality of the solution (equal to the ionic strength, for 1:1-valent electrolyte [5]), z_+ and z_- are the cation and anion valence numbers, respectively. The coefficients B_γ, C_γ, D_γ, E_γ are evaluated for each investigated salt by fitting experimental data collected from the literature [67].

Some of the equations that are following reported are already described in the previous chapter but for a simplicity of reading some of these are again presented below.

As shown in the chapter 2, the membrane properties depend by the salt. Both membrane resistance (R_{IEM}) and permselectivity (α) are affected also by the concentration, in particular dilute solution for membrane resistance and concentrate solution for the permselectivity. A relation, as a function of concentrate solution, was introduced to better predict the permselectivity (α) value when the concentration is changed. The parameters were calculate by means of experimental tests but not all the salts were tested and for the last ones were considered the standard values (α_{CEM}=90%; α_{AEM}: 65%) calculated for NaCl (5M-0.05M). For the membrane resistances instead was considered fixed experimental value measured at 0.5M with the six cells stack (2.2.2). The values of NaCl (R_{CEM}=2.96*10^{-4} Ω m^2; R_{AEM}: 1.55*10^{-4} Ω m^2) were used in those cases where no experimental values were available. However, in some cases, relations were introduced as

function of solution concentration derived from stack measurements for a better tuning of the model.

The permselectivity for the anion and cation exchange membranes are estimated with the following equations:

$$\alpha_{AEM} = a_{AEM} C_{HIGH}^2 + b_{AEM} C_{HIGH} + c_{AEM} \tag{3.4}$$

$$\alpha_{CEM} = a_{CEM} C_{HIGH}^2 + b_{CEM} C_{HIGH} + c_{CEM} \tag{3.5}$$

where C_{HIGH} (mol/lt) is the concertation of concentrate solution while a_{AEM}, b_{AEM}, c_{AEM} and a_{CEM}, b_{CEM}, c_{CEM} are the parameters for the anion and cation exchange membranes, respectively. The permselectivity is reported as percentage [%].

The electric voltage generated by each cell pair was calculated by Nernst's equation [129]:

$$E_{cell} = (\alpha_{CEM} + \alpha_{AEM}) \frac{R\,T}{F} ln \left(\frac{\gamma_{HIGH}\ c_{HIGH}}{\gamma_{LOW}\ c_{LOW}} \right) \tag{3.6}$$

where *R* is ideal gas constant, *T* is temperature and *F* is Faraday's constant.

The corresponding Open Circuit Voltage was estimated as:

$$OCV = N\ E_{cell} \tag{3.7}$$

where *N* is the number of cell pairs composing the entire stack.

The channel ohmic resistances were calculated as follows:

$$R_{LOW} = f_h \frac{\delta_{LOW}}{\Lambda_{LOW}\ c_{LOW}} \qquad R_{HIGH} = f_h \frac{\delta_{HIGH}}{\Lambda_{HIGH}\ c_{HIGH}} \tag{3.8}$$

where δ_{LOW}, δ_{HIGH} are dilute (i.e. *LOW*) and concentrate (i.e. *HIGH*) compartment thicknesses, *f* is the spacer shadow factor perpendicular to the membrane evaluated equal to 1.212. It takes into account the presence of a non-conductive spacer between two subsequent membranes. Note that the spacer is needed (i) to provide dimensional stability

to the channel (by keeping adjacent membranes separated) and (ii) to enhance mixing within the channel thus minimizing the polarization phenomena (not accounted for by the model) [108,130,131]. The same woven spacer 270μm thick was considered in the two channels.

Clearly, the electrical resistance of the cell pair can be easily estimated as:

$$R_{cell} = R_{LOW} + R_{HIGH} + R_{AEM} + R_{CEM} \tag{3.9}$$

The overall electrical resistance of the whole stack is:

$$R_{stack} = N\, R_{cell} + R_{blank} \tag{3.10}$$

where R_{blank} is the electrical resistance of the electrodic compartments which was experimentally estimated and changed for each salt, the standard with NaCl (5M-0.05M) was used only when the value was not available for that specific salt.

Once *OCV* and R_{stack} have been defined, the voltage arising when the circuit is closed on an external load can be defined as:

$$E_{stack} = OCV - R_{stack}\, j \tag{3.11}$$

where *j* is the electrical current density circulating throughout the stack given by:

$$j = \frac{E_{stack}}{R_{ext}} \tag{3.12}$$

where R_{ext} is the electrical resistance of the external load. It can be mathematical demonstrated that the achievable power density can be maximized when this external resistance is equal to the internal one (i.e. R_{stack}) [103]:

$$R_{stack} = R_{ext} \tag{3.13}$$

As a consequence, this condition (3.13) was added to the model.

Thanks to the existing driving force between two adjacent channels, a salt flux occurs. It results from the sum of two different contributions: the one relevant to the counter-ion transport, which is a coulombic term and the other, due to the non-ideality of membranes, relevant to the co-ion transport which is accounted for via a phenomenological expression. In formula,

$$J_{salt} = \frac{j}{F} + 2\,\frac{D_{salt}\left(C_{HIGH,in} - C_{LOW,in}\right)}{\delta_m} \tag{3.14}$$

where δ_m is the IEM thickness chosen equal to 1.25E-4m according to the experiments which will be used for model validation. D_{salt} is the co-ions diffusion coefficient, formally analogous to a salt diffusion coefficient, which could be directly derived from membrane permselectivity. A constant value of 10^{-12} m^2/s was assumed for this term [17]. This assumption has been already considered as more than reliable since the co-ion contribution to overall flux was found much lower than the coulombic one. Note that the factor 2 accounts for the presence of both membranes of a cell pair. Once the salt flux is known, the mass balances in the RED unit can be closed; for the case of the diluted channel:

$$C_{LOW,out} - C_{LOW,in} = \frac{J_{salt}\,A}{Q_{LOW}} \tag{3.15}$$

where A is the membrane area and Q_{LOW} is the flow rate circulating in the dilute compartment. Clearly, a corresponding equation can be written for the case of the concentrated channel where the term on the right hand side will be negative. Flow rate can be derived from the solution velocity v_{LOW} once the membrane area and width b and the channel porosity ε (due to the spacer presence) are known:

$$F_{LOW} = N\,v_{LOW}\,\delta_{LOW}\,b\,\varepsilon \tag{3.16}$$

On the basis of measurements performed on the spacer employed in the experiments, channel porosity was found equal to 82.5%.

Finally, as process output, the power density produced by the RED unit can be calculated as follows:

$$P_d = \frac{j^2 R_{ext}}{N} \quad (3.17)$$

At lab-scale where N is quite low, R_{blank} is not negligible compared to R_{stack}. Conversely, at larger scale, electrodic compartment resistance is known to be irrelevant. Thus, a corrected power density $P_{d,corr}$ can be calculated on the basis of a "*corrected*" stack voltage, which does not take into account the R_{blank} contribution [72,132].

All the model equations were implemented in Excel spreadsheets along with purposely developed macros.

3.3 RED model with NH_4HCO_3 solutions

The simplified RED model previously described was applied for the first time at ammonium hydrogen carbonate. The parameters for the physical properties are collected from literature whereas the membrane properties derived from the tests described in the section 2.6.1. In particular, the parameters for the equivalent conductivity were calculated by fitting with equation 3.1 the experimental results reported in the Handbook of Chemistry and Physics [66].

$$\Lambda_0 = 90;\ A_\Lambda = 41.55;\ B_\Lambda = 0.6023;\ C_\Lambda = 0 \quad (3.18)$$

The quality of the fitting obtained is reported in Figure 3.1 which shows a good agreement between experimental data and equation 3.1 predictions in the whole range of concentration investigated in the present work. Only at high values of solution concentration, the small discrepancies found, exhibit in the worst case a maximum error being always way below 5% (Figure 3.1b).

Instead, the parameter for the density was evaluated by fitting experimental data from literature [67]: $\Delta\rho/\Delta m = 0.0324$ kg^2/(mol l). The quality of the fitting is high; as can be observed in Figure 3.2 there is a very good agreement at any value of molality with maximum discrepancies always lower than 0.5% (Figure 3.2b).

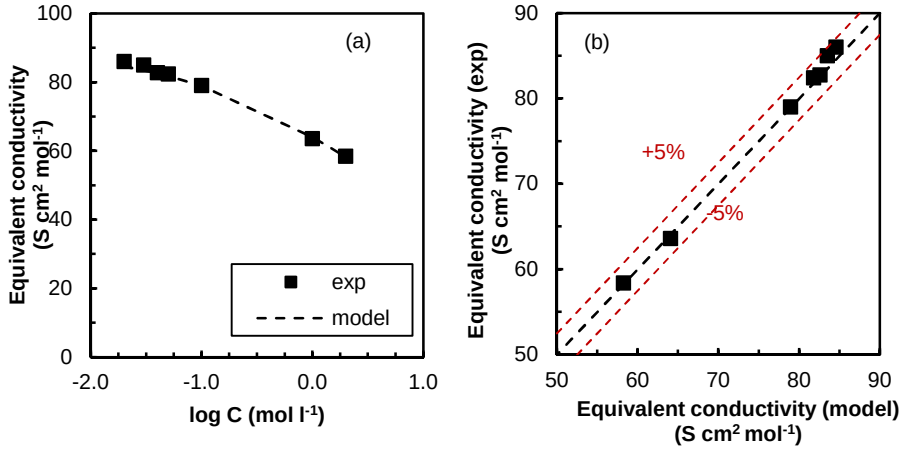

Figure 3.1: Comparison of equation 33 predictions with experimental data: (a) Λ vs log C; (b) Λ parity plot.

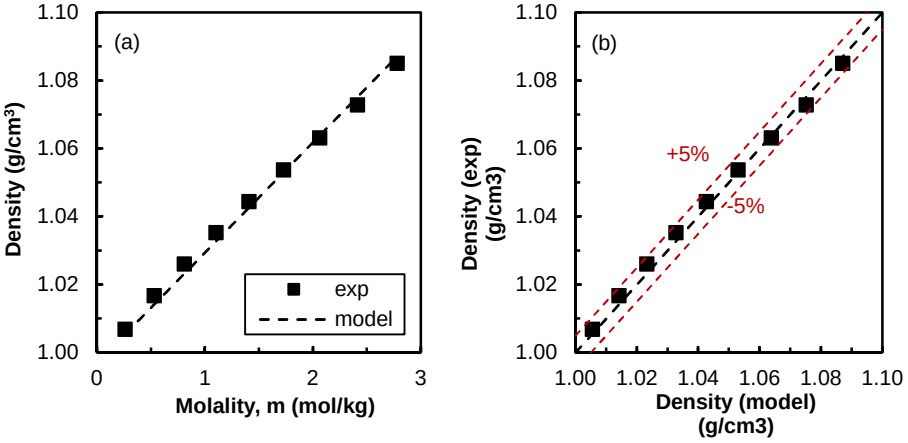

Figure 3.2: Comparison of equation 3.1 predictions with literature data [67]: (a) density vs molality; (b) density parity plot.

The activity coefficients were assessed in a different way than described in the previous section because these data are not available in literature. The values were estimated by taking advantage from the process simulator Aspen Plus® along with the ENRTL-RK electrochemical thermodynamic package. The following linear dependence of the activity coefficients on salt molar concentration was found:

$$\gamma = -0.1366\, C + 1.0007 \tag{3.19}$$

Membrane resistance was considered as dependent on solution concentration, while, for the sake of simplicity, a constant membrane permselectivity (α_{AEM} , α_{CEM}) was used and equal for both membranes to 75.4% based on experimental measurements (2.6.1).

The relation between membrane resistance (R_{AEM} and R_{CEM}) and solution concentration was extrapolated by experimental data collected described in the section 2.6.1: both R_{AEM} and R_{CEM} were found dependent on the dilute solution concentration C_{LOW}, as expected, according to the following empirical equation:

$$R_{AEM} = R_{CEM} = 0.0002 \cdot (C_{LOW})^{-0.236} \tag{3.20}$$

Note that the equation reported above is the same for anion and cation exchange membrane because only the average value between the two membranes can be calculated via power density measurements (2.6.1).

The blank resistance was experimentally estimated as 0.01068 Ω m^2 as reported in the section 2.6.1.

3.3.1 Model validation

The model described in the previous section was tested by making use of experimental data collected and reported in the section (2.6.1). Figure 3.3A shows the dependences of *OCV* and R_{stack} on the concentration of the diluted solution at given C_{HIGH} and solution velocity (set equal for *HIGH* and *LOW* channels). As it can be seen, there is a very good agreement between the model proposed and the collected experimental data: the *OCV* was found to decrease as C_{LOW} increases because of the driving force reduction. On the other hand, the increase of C_{LOW} leads to a reduction of the corresponding R_{LOW}, which is the controlling addendum in R_{stack} calculation. These two competitive effects result into an increasing-decreasing behaviour of the power trend, depicted in Figure 3.3B, which is well predicted by the model: only a slight disagreement was observed.

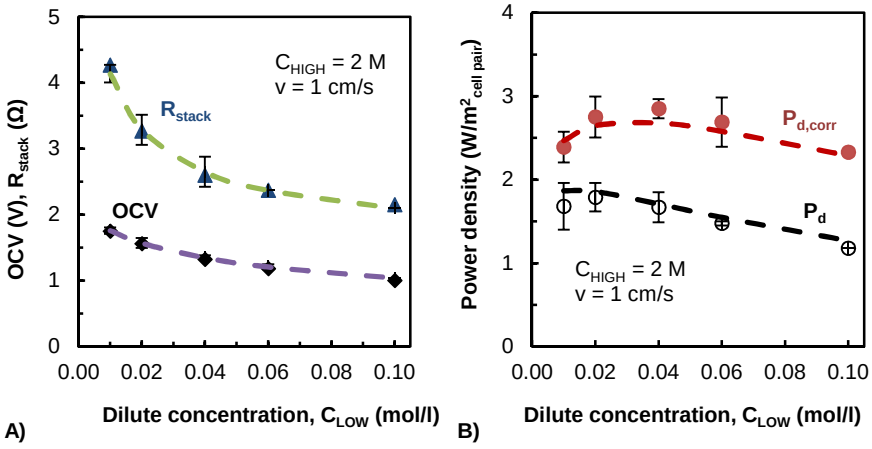

Figure 3.3: Comparison between model and experimental results. Influence of dilute concentration on process performance. A) OCV and stack resistance. B) Power density and corrected power density. RED stack (10x10 cm^2, 10 cell pairs) equipped with Fujifilm membranes, 270 μm woven spacers. C_{HIGH} = 2M; v_{HIGH}=v_{LOW}= 1 cm/s, T = 298 K.

The effect of solution velocity at fixed C_{HIGH} (set at 2M) and C_{LOW} (set at 0.02M) was also investigated and shown in Figure 3.4. Note that the chosen C_{HIGH} and C_{LOW} are the ones maximizing the power production in the previous graph.

As shown in Figure 3.4A, the model is able to predict the slight increase of *OCV* with solution velocity due to the fact the membrane are not ideal and also co-ions can pass through. The higher the velocity, the lower the residence time, the less evident the effect of velocity on *OCV* which reaches a plateau both in experiments and process simulations. Such effect is mainly related to the lower residence time inside the stack that allows a practically constant driving force between inlet–outlet to be maintained. Residence time also affects the resistance of the stack (Figure 3.4A) which is mainly due to the dilute channel conductivity: as the dilute velocity increases, its concentration is less increased by ion transfer within the system thus resulting into a higher resistance. This occurrence is well predicted by the model, notwithstanding experimental data are slightly scattered. *OCV* increase and R_{stack} decrease represent two competitive effects which yield a power production poorly dependent on solution velocity (Figure 3.4B): only a slight increase of the power vs velocity trend was found thus suggesting that, at the conditions of Figure 3.4, *OCV* effect is prominent than the R_{stack} one. The experimental and model data of P_d (Figure

3.4B) are in a good agreement, while some underestimation can be observed for the case of $P_{d,corr}$.

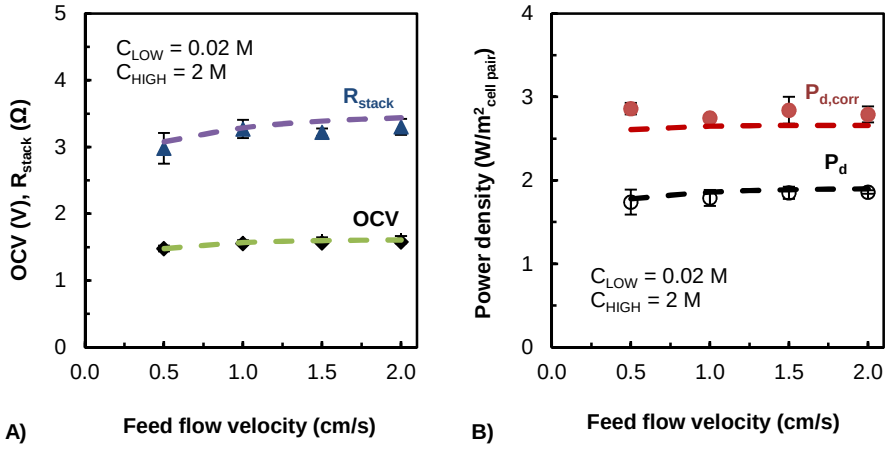

Figure 3.4: Comparison between model and experimental results. Influence of feed flow velocity on process performance. A) OCV and stack resistance. B) Power density and corrected power density. RED stack (10x10 cm^2, 10 cell pairs) equipped with Fujifilm membranes, 270 μm woven spacers. C_{HIGH} = 2 M; C_{LOW} = 0.02 M; v_{HIGH}=v_{LOW}; T = 298 K.

3.3.2 Sensitivity analysis

Once the model has been validated, it was employed to perform a sensitivity analysis aimed at finding the best operating conditions (in terms of solution concentration and flow rate) which maximize $P_{d,corr}$. The results of this sensitivity analysis are shown in Figure 3.5.

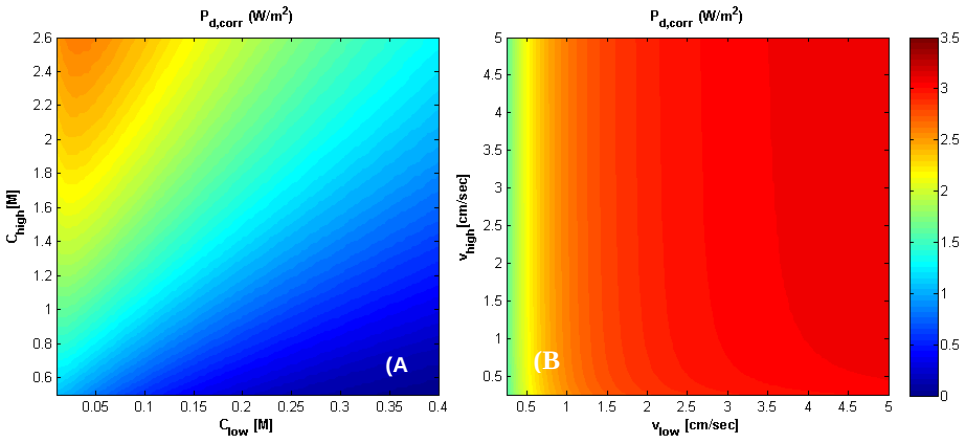

Figure 3.5: Sensitivity analysis. A) $P_{d,corr}$ as function of C_{HIGH} and C_{LOW} at v_{HIGH}=v_{LOW} = 1cm/s. B) $P_{d,corr}$ as function of v_{HIGH} and v_{LOW} at C_{HIGH}=2.6M and C_{LOW}=0.04M. RED stack (50x50 cm^2, 1000 cell pairs) equipped with Fujifilm membranes, αCEM=αAEM=75.4%, R_{CEM}=R_{AEM}=$2E^{-4}(C_{LOW})^{-0.236}$, 270 μm woven spacers. T = 298 K.

Figure 3.5A shows that C_{HIGH} must be kept as high as possible, clearly without approaching too closely the saturation value where precipitation may occur and lead to possible scaling or even clogging issues. Conversely, as expected, C_{LOW} should be around 0.02M to maximize $P_{d,corr}$ as (i) too low values yield too high R_{LOW} (the main contribution to R_{stack}) while (ii) high values are detrimental for the driving force. Sensitivity analysis on solution velocity is reported in Figure 3.5B. $P_{d,corr}$ appears to be scarcely dependent on v_{HIGH} apart from the lowest values where the residence time is so low that a deep driving force reduction occurs. On the other hand, the effect of v_{LOW} on $P_{d,corr}$ is more evident because dilute channel concentration is more sensible (than the concentrate) to residence time: clearly, the higher v_{LOW}, the higher the power output. Note that feed solution velocity lower than those reported in the figure were not included in the analysis as these would cause deep polarization effects which are not accounted for by the model. However, this unexplored range is really far from the one providing the best performance.

Under optimized conditions, a power output of about 3.5 W/m^2 can be obtained with the investigated Fujifilm membranes. Of course, membranes are not yet optimized to deal with NH_4HCO_3–water solutions: further development may enhance membrane

performance (i.e. reducing resistance and enhancing permselectivity) thereby providing higher power densities.

In this regard, the model was used to calculate the performance of a RED unit equipped with membranes with enhanced yet feasible features consisting of higher permselectivity (i.e. $\alpha_{CEM}=\alpha_{AEM}=90\%$) and lower electrical resistance (i.e. R_{CEM} and R_{AEM} are equal to 1/5 of the value resulting from equation 3.20). Model results are reported in Figure 3.6. As expected, the higher C_{HIGH} and v_{LOW}, the higher the power production. C_{LOW} value maximizing $P_{d,corr}$ was found of about 0.08M with the improved membranes, slightly higher than the one relevant to Fujifilm membranes because of the lower membrane resistances. Under these optimized conditions, a power production up to about 9 W/m^2 might be achieved.

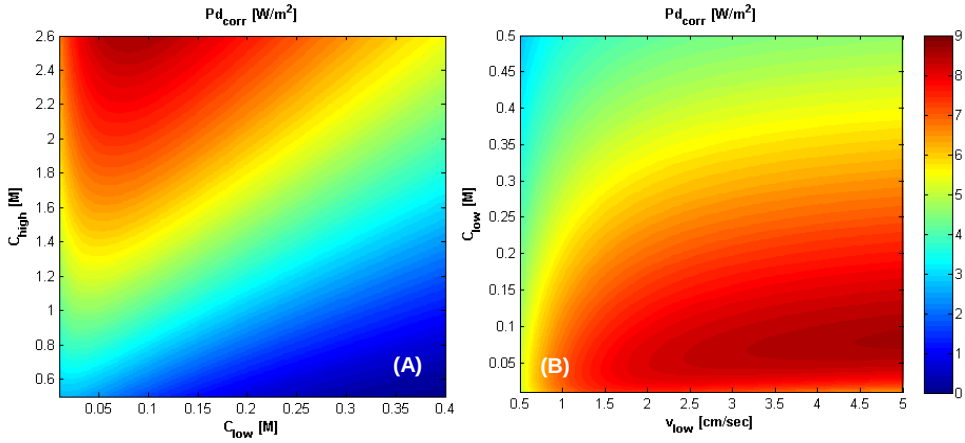

Figure 3.6: Sensitivity analysis. A) $P_{d,corr}$ as function of C_{high} and C_{low} at v_{high}=1 cm/s and v_{low}=5 cm/s; B) $P_{d,corr}$ as function of C_{low} and v_{high} = 1 cm/s and C_{high} = 2.6 M. RED stack (50x50 cm^2, 1000 cell pairs) equipped with enhanced membranes, $\alpha_{CEM}=\alpha_{AEM}=90\%$, $R_{CEM}=R_{AEM}=4E\text{-}5(C_{low})^{-0.236}$, 270 μm woven spacers. T = 298K.

3.4 RED model with NaCl, NH_4Cl, $ZnCl_2$ and CsCl

Some of the 41 salts were selected in order to confirm the validation of the RED model. In particular, both monovalent (NaCl, NH_4Cl and CsCl) and bivalent ($ZnCl_2$) chloride salts were selected. In general, the mathematical model can predict the RED stack performance and in particular the sensitivity analysis can help in understanding the way in which the

membranes properties and the solution properties influence the power density. This is an important tool for the improvement of reverse electrodialysis units.

The comparisons with the experimental data for some investigated salts are shown in Figure 3.7.

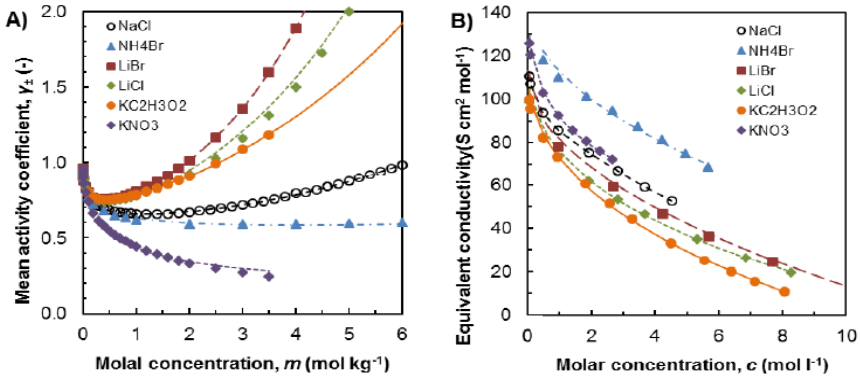

Figure 3.7: Estimated properties for some of the investigated aqueous solutions at 25°C. A) Mean activity coefficient. B) Equivalent conductivity. Symbols: experimental data [67]. Lines: model predictions [32].

Equivalent conductivity data of zinc chloride were not found in literature. For this reason, the validation of the model using this salt was performed by adding a correlation based on experimental results. Figure 3.8 shows the experimental values of conductivity for zinc chloride. Two different correlations have been used for high and low concentrations; a third grade equation for concentrate solutions (eq. 3.1) and a second grade equation for dilute solution (ep. 3.2).

$$K_{HIGH} = 1.768\, C_{HIGH}^3 - 24.358\, C_{HIGH}^2 + 91.342\, C_{HIGH} + 12.894 \qquad (3.1)$$

$$K_{LOW} = -70.90\, C_{LOW}^2 + 155.15\, C_{LOW} + 2.15 \qquad (3.2)$$

where K_{HIGH} and K_{LOW} are expressed as mS/cm while C_{HIGH} and C_{LOW} are expressed in mol/l.

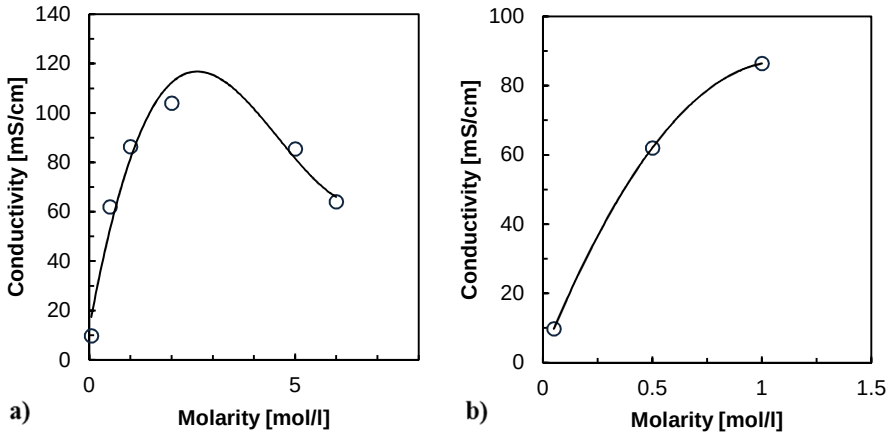

Figure 3.8: Conductivity vs molarity at higher concentrations a) and at lower concentrations b).

Moreover, the zinc chloride is a divalent ions and in order to calculate the E_{cell} by means of Nernst's equation, this have to be multiply by 3/4.

The blank resistance was fixed at 0.0052 $\Omega*m^2$, i.e. the value obtained by the standard NaCl (5M-0.05M).

Correlations based on the experimental values of permselectivity (Figure 3.9, Figure 3.10, Figure 3.11 and Figure 3.12) were added in the mathematical model both for AEMs and CEMs for all the selected salts. The parameters for the equation 3.4 and equation 3.5 are reported in the Table 3.1.

Table 3.1: Parameters for the permselectivity calculation in the RED model

Salt	a_{AEM}	b_{AEM}	c_{AEM}	a_{CEM}	b_{CEM}	c_{CEM}
NaCl	0.23	-7.00	91.20	0.57	-6.50	99.00
NH_4Cl	0.17	-7.80	97.00	0.20	-7.14	100.00
$ZnCl_2$	-0.74	-3.50	82.30	0.13	-1.01	96.00
CsCl	-0.42	-1.54	98.50	-0.39	-1.95	95.85

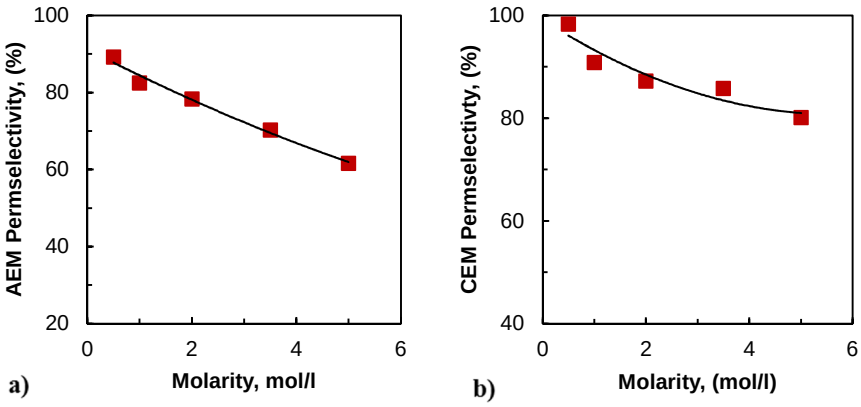

Figure 3.9: Trend line for AEMs a) and CEMs b) permselectivity using NaCl salt.

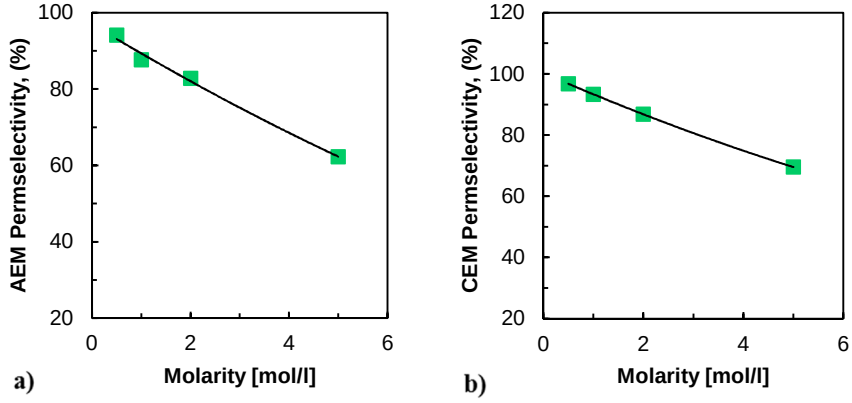

Figure 3.10: Trend line for AEMs a) and CEMs b) permselectivity using NH_4Cl salt.

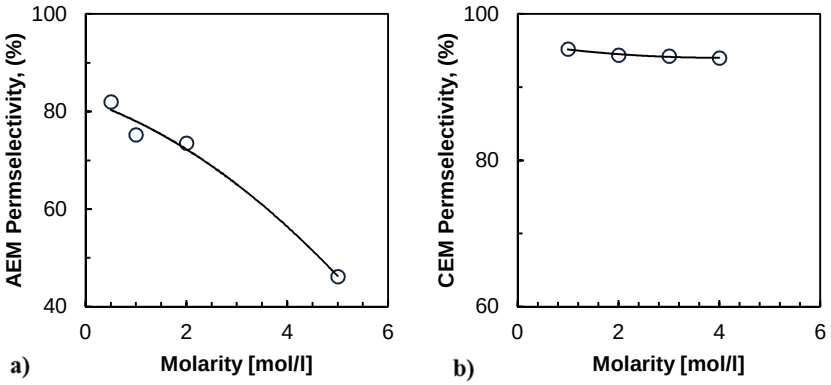

Figure 3.11: Trend line for AEMs a) and CEMs b) permselectivity using $ZnCl_2$ salt

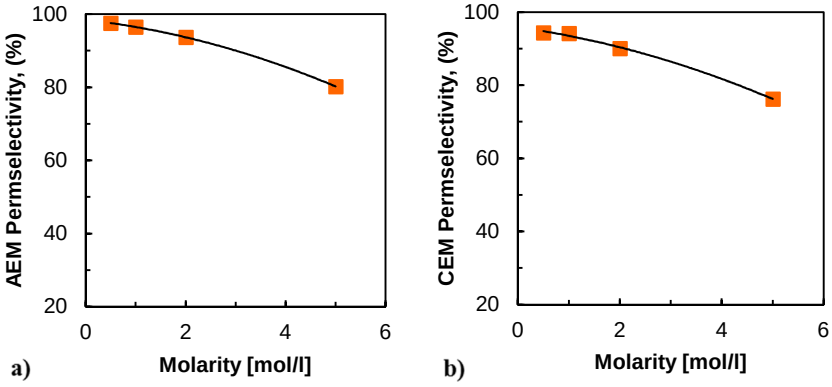

Figure 3.12: Trend line for AEMs a) and CEMs b) permselectivity using CsCl salt.

In all the cases, the permselectivity decreases when the concentration increases. The values are always higher than 60% except for the anion exchange membrane with $ZnCl_2$..

The membrane resistance were measured with the device with six compartments at standard concentration of 0.5M and are considered fixed in the model. The values are reported in the Table 3.2.

Table 3.2: Membrane resistance for different salt at 0.5M.

Membrane resistance [Ω cm^2]				
	NaCl	NH_4Cl	$ZnCl_2$	CsCl
CEM	2.84	1.86	19.69	2.07
AEM	1.82	2.00	8.85	2.14

It can be noted in the Table 3.2 that the membrane resistance are similar for all the salts except for $ZnCl_2$ with a really high values for both membranes.

3.4.1 Model validation

The following figures show the comparison between model and experimental results for the four selected salts.

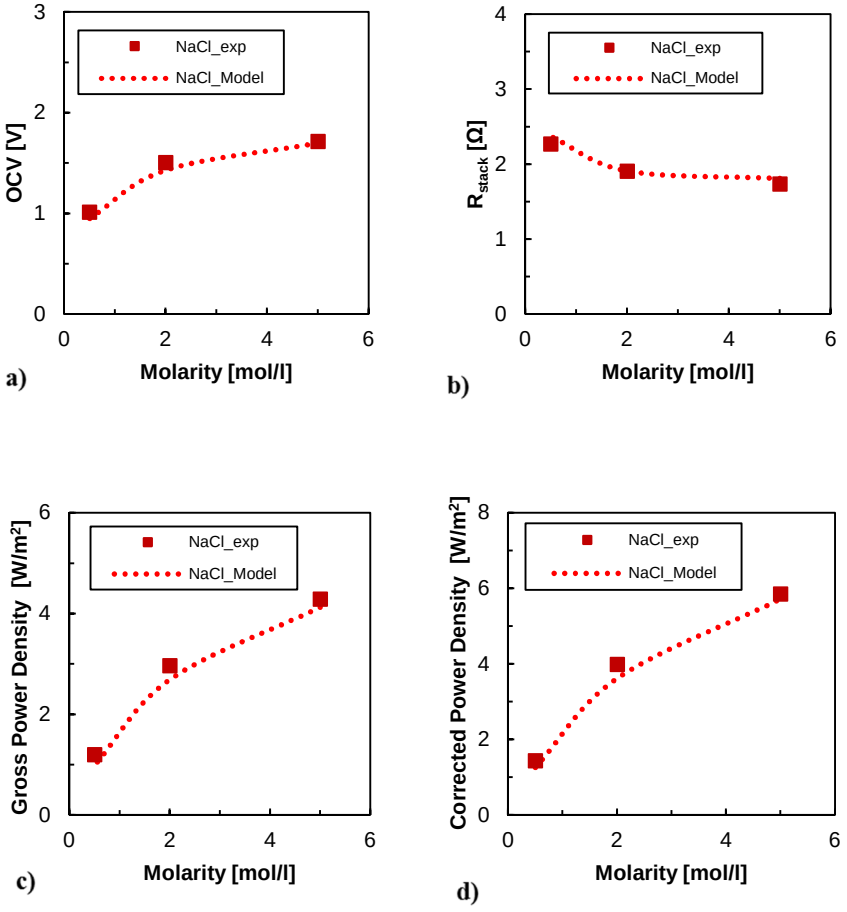

Figure 3.13: Comparison between model and experimental results for NaCl solutions. a) OCV, b) R_{stack}, c) Gross power density, d) Corrected power density. Co-current 10x10 cm^2 stack equipped with Fujifilm RP1 membranes, Deukum spacers; N=10; C_{LOW}=0.05M; T=25°C; v=1 cm/s; ERS: 0.1M $K_3(CN)_6$/0.1M $K_4Fe(CN)_6$ + xM NaCl (R_{blank}=0.52 Ω).

Figure 3.13 shows the comparison between model and experimental results for NaCl solutions. The model fit the experimental values of both OCV and stack resistance.

As regard the gross power density and the corrected power density Figure 3.13 doesn't show a perfect fitting. In both cases, the model shows lower results than experimental tests at 2M, even if the two trends are very similar.

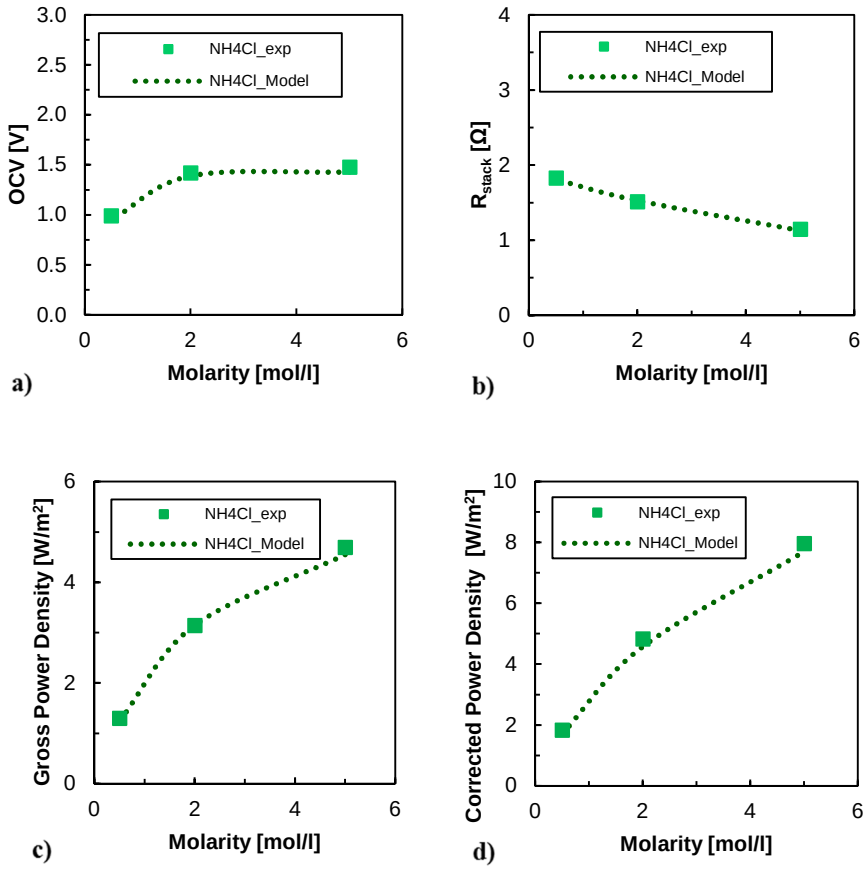

Figure 3.14: Comparison between model and experimental results for NH_4Cl solutions. a) OCV, b) Rstack, c) Gross power density, d) Corrected power density. Co-current 10x10 cm^2 stack equipped with Fujifilm RP1 membranes, Deukum spacers; N=10; C_{LOW}=0.05M; T=25°C; v=1 cm/s; ERS: 0.1M $K_3(CN)_6$/0.1M $K_4Fe(CN)_6$ + xM NH_4Cl (R_{blank}=0.52 Ω).

Figure 3.14 shows the validation of the model when ammonium chloride salt solutions have been used. Open circuit voltage and stack resistance results are fitted by the model.

As regard gross power density and corrected power density, the model fits experimental data both at lower and higher concentrations even if at higher concentrations model shows slightly lower power density values than experimental tests.

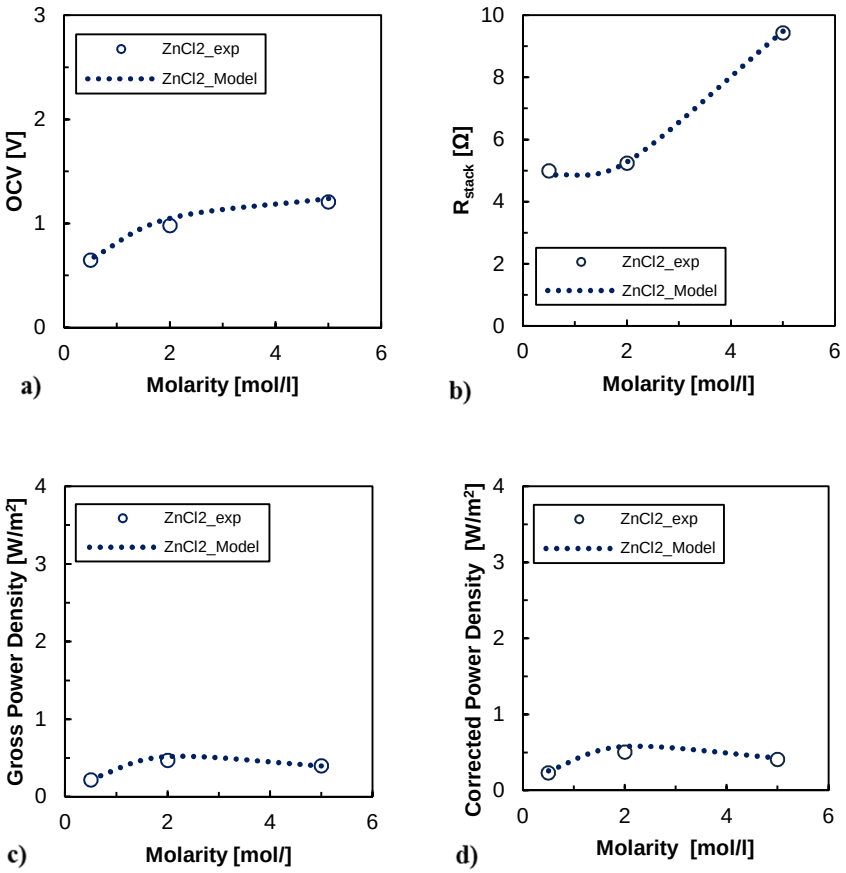

Figure 3.15: Comparison between model and experimental results for $ZnCl_2$ solutions. a) OCV, b) Rstack, c) Gross power density, d) Corrected power density. Co-current 10x10 cm^2 stack equipped with Fujifilm RP1 membranes, Deukum spacers; N=10; C_{LOW}=0.05M; T=25°C; v=1 cm/s; ERS: 0.1M $K_3(CN)_6$/0.1M $K_4Fe(CN)_6$ + xM $ZnCl_2$ (R_{blank}=0.52 Ω).

Figure 3.15 shows the validation of the model when zinc chloride salt solutions have been used. As regard the fourth analysed parameters, the model fits the experimental data. The performance of this bivalent salt is really poor, due to its bad membrane properties.

The model results for CsCl were not compared with experimental results because during the Power Density measurements, some salts precipitated in the electrode compartments invalidating the tests. More investigations are needed in order to understand the interaction between CsCl and electrode solution, likely they create an un-soluble salt that precipitate.

The model performances of NaCl, NH_4Cl and $ZnCl_2$ are following compared. CsCl will be shown separately because it was not validated with experimental tests.

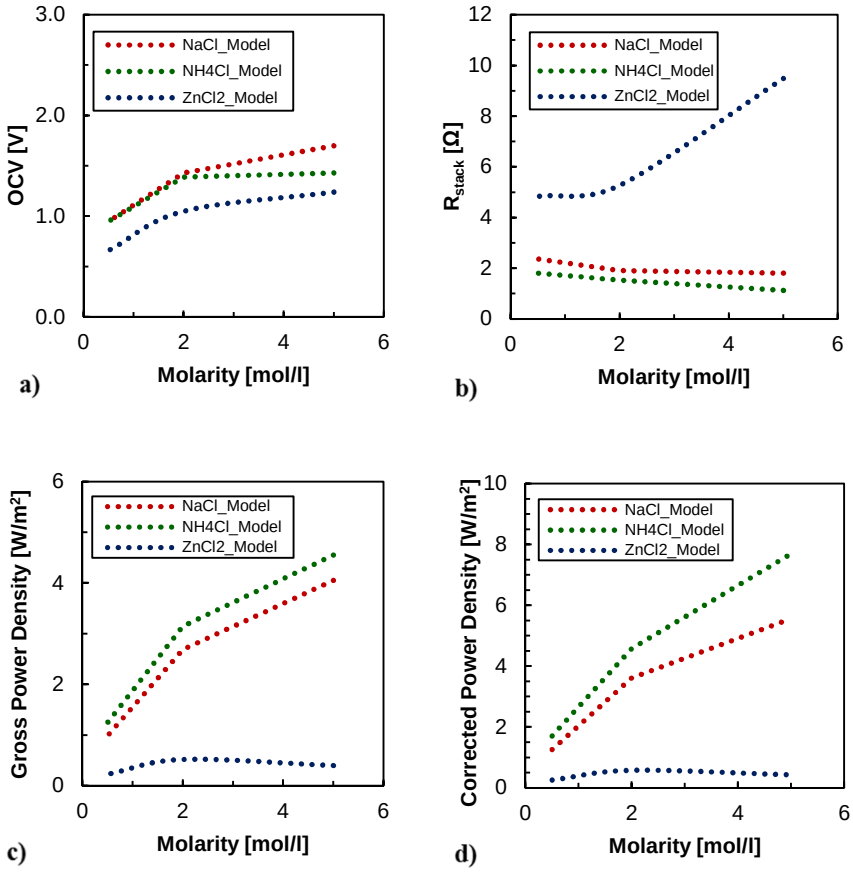

Figure 3.16: Comparison among the different model results with NaCl, NH_4Cl and $ZnCl_2$.

Figure 3.16 shows the comparison among the different model results. Ammonium chloride shows better properties than the other salts. Even if the mathematical model is based on different assumptions, the obtained results are similar to the experimental ones and this permits to use it as a prediction tools for other investigations.

As already said, for caesium chloride, only membrane resistance and permselectivity measurements were performed. The power density was only predicted by model using.

However, Figure 61 shows the comparison between model and experimental OCV results, confirming that even if not validate, good prevision can be obtained by the simplified model.

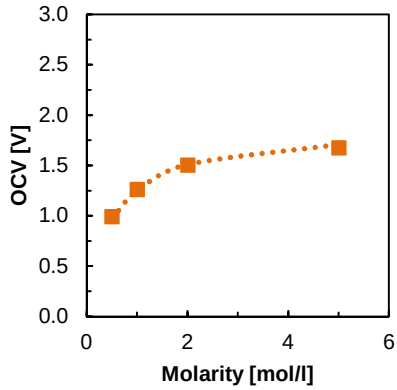

Figure 3.17: Comparison between experimental and model OCV results with CsCl solutions.

3.4.2 Sensitivity analysis

After the validation of the model, a sensitivity analysis was performed in order to have an idea about the obtainable power density results at different concentrations.

In particular, the values of corrected power density have been obtained at different concentrations of the concentrated and diluted solutions.

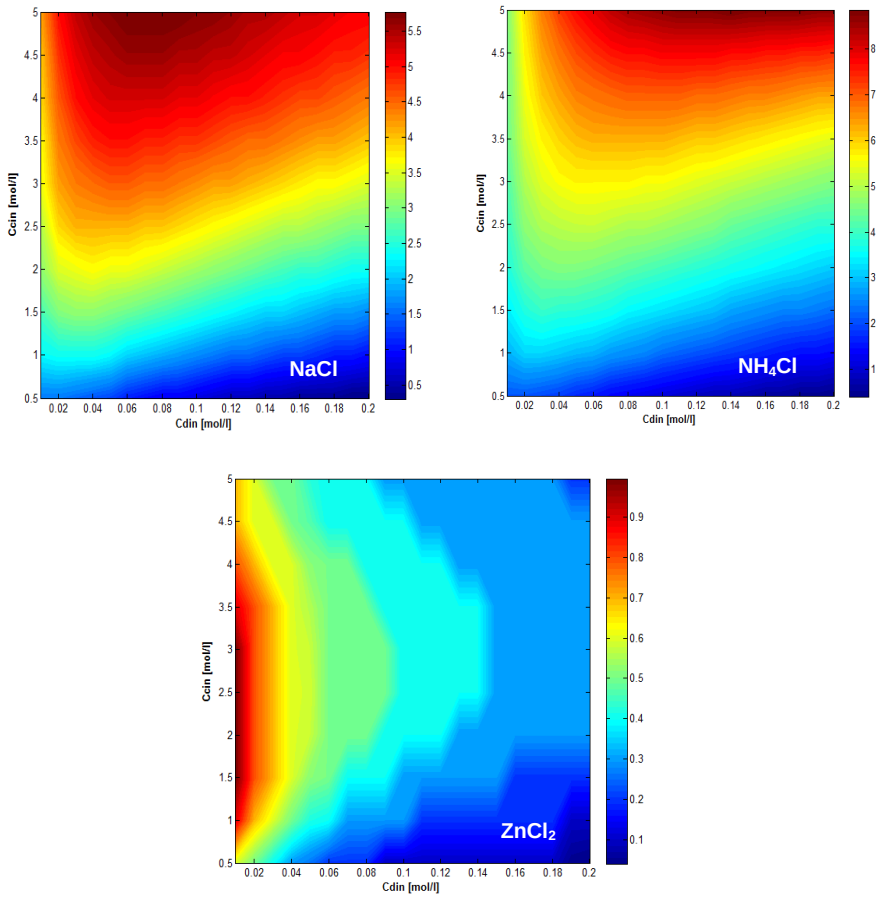

Figure 3.18: Corrected power density model prediction when concentrated solution (C_{cin}) and diluted solution concentrations changes (C_{din}). The secondary axis shows the corrected power density result expressed in W/m^2. The dark red indicates the maximum values of $P_{d,corr}$ whereas the dark blue the lowest values.

Figure 3.18 shows the corrected power density model prediction when solutions at different concentration from the tested ones are used.

Using different salts, the values of power density obtainable are very different. The maximum power density value using sodium chloride is 5.8 W/m^2 at 5-0.07M .

As regard ammonium chloride, the model result shows that by performing a measurement at 5-0.12M the value of power density obtainable is 8.85 W/m^2. For concentration of diluted solution higher than 0.12M the corrected power density decreases.

Zinc chloride shows the lowest corrected power density results.

For CsCl, a sensitivity analysis has been performed in order to have an idea about the power density obtainable with its exploitation.

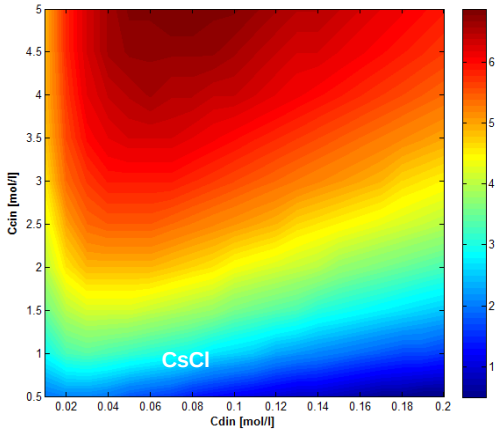

Figure 3.19: Corrected power density model prediction when concentrated solution ($C_c$in) and diluted solution concentrations changes (C_{din}). The secondary axis shows the corrected power density result expressed in W/m^2. The dark red indicates the maximum values of P_{dcorr}, the light blue the lower values.

The maximum corrected power density obtainable on the base of the model prediction is 6.9 W/m^2 at 5-0.07M.

This simplified model with ammonium hydrogen carbonate was lately integrated with a model for the regeneration stage. The integrated model is described in more details in the chapter 5.

4 SALT EXTRACTION REGENERATION STRATEGIES USING THERMOLITIC SALTS

Abstract

Thermally-driven regeneration is the second important part of a SGP-HE system. In this chapter, the use of air stripping column is presented as a viable strategy for the regeneration of ammonium hydrogen carbonate solutions outcomes from the reverse electrodialysis unit.

The process was studied by modelling and experimental activities. A process simulator (Aspen Plus®) was adopted in order to simulate the behaviour of the air stripping column. Starting from literature references and model validation with original experimental information, the ENRTL-RK thermodynamic package was chosen as the best option to model the NH_4HCO_3 aqueous solution.

A lab-scale stripping column was designed, built and tested in order to characterize its regeneration performance. Two packing materials (Raschig rings and structured packing FLEXIPAC 700Y) and different operating conditions were analysed.

Experimental results and model predictions were compared in order to develop a validated process model simulator able to predict the behaviour of the proposed regeneration unit.

[*] Part of this chapter has been published as:

M. Bevacqua, A. Tamburini, M. Papapetrou, A. Cipollina, G. Micale, A. Piacentino, Reverse electrodialysis with NH_4HCO_3-water systems for heat-to-power conversion, Energy 137 (2017) 1293-1307

4.1 State-of-the-art of regeneration strategies for thermolytic salts solutions

Since 1964 Neff [133] proposed ammonium bicarbonate solutions as thermally-regenerable drawing agent to remove water from a salt-water stream. More recently McCutcheon in 2005 [134] and McGinnis et al. in 2007 [118,124] have intensified the research on this topic, providing some more insight in the regeneration process. In particular, McCutcheon et al. [134] described a new direct osmosis process for desalination of sea water, which uses ammonium bicarbonate concentrated solution to extract water through a semipermeable osmotic membrane. The osmotic pressure gradient generates a flow of fresh water through the membrane, which dilutes the drawing solution, to be eventually regenerated. For the regeneration, low temperature heat (about 60 ° C) is needed to force the decomposition of the salt (NH_4HCO_3) into gaseous NH_3 and CO_2. The gas can be separated and recovered in a distillation/stripping column, thus obtaining desalinated water and pure NH_3 and CO_2 used to regenerate the draw solution. The scheme of the process is shown in Figure 4.1 [118].

However, the regeneration step in this work was described only qualitatively imaging a distillation column using waste heat.

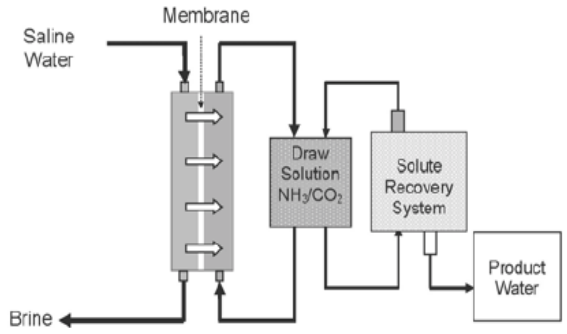

Figure 4.1: Schematic of the ammonia–carbon dioxide FO desalination process [118].

In 2007, McGinnis and Elimelech [118] described a FO process using ammonium salts as drawing agent and for the first time they provided a simplified energetic analysis indicating the requirements for the regeneration step, obtained by means of a process simulator (Aspen Hysys) using a specific thermodynamic packages for electrolyte solution with high concentration (OLI). The drawing solution is obtained by a mixture of

ammonium salts, NH_3 and CO_2 gas in water. The species eventually formed in solution are: ammonium bicarbonate, ammonium carbonate and ammonium carbamate. The last one, obtained from the reaction of carbonate ions and ammonia gas, has the highest solubility, so that overall ions concentration can be increased in the solution by increasing the ratio between the NH_3 and CO_2 gases.

The authors described two different process diagrams: one using a single distillation column and the other one using several distillation columns in series. In fact, depending on the temperature value of the heat available, more distillation columns may be used.

In particular, if heat at very low temperature is available, the use of a single distillation column operating at low pressure should give lower energy consumptions. At the contrary, if heat at a higher temperature is available, the use of multiple columns could lead to higher efficiency. In Figure 4.2, the process with a single distillation column is schematically represented:

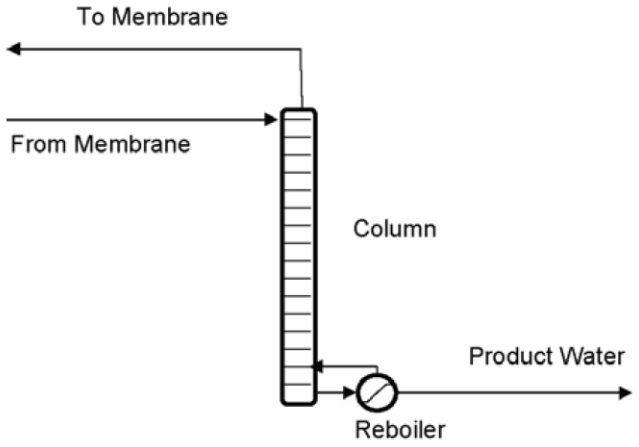

Figure 4.2: Schematic diagram of a single vacuum distillation column [118].

In the first configuration it is possible to use heat at 40° C supplied at the reboiler allowing the evaporation of water used as stripping stream within the column. The concentration of NH_3 and CO_2 in the water solution at the column bottom was fixed at less than 1 ppm. The gases contained in the stream on the top of the column, instead, are condensed (at the operating pressure in the column (<1 atm)), while incondensable (NH_3 and CO_2) are removed by means of a vapour thermo-ejector.

In Figure 4.3 and Figure 4.4 the scheme with multiple columns are shown:

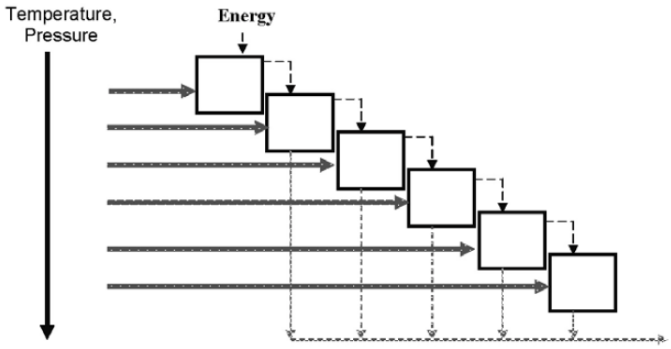

Figure 4.3: Schematic diagram of the multi stage column distillation operation [118].

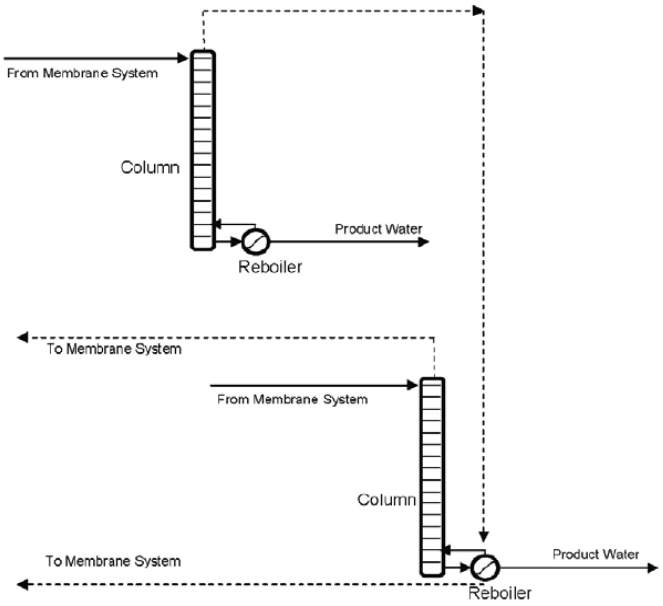

Figure 4.4: Schematic diagram illustrating the transfer of heat from one column to another in series, with material streams in parallel flow, for the FO draw solute recovery [118].

The heat introduced in the first stage allows for the vaporization of part of the liquid stream, powering the first distillation column, while the vapour/gases stream exiting the first column is condensed in the reboiler of the next stage, that operates at lower temperature and pressure, allowing the evaporation of a further amount of liquid solution, powering the second column, and so on.

A solution 5 M of ammonium salts, with a ratio NH_3/CO_2 = 1.4, was adopted for the energetic analysis. The flow rate was varied in order to obtain an outlet concentration from 0.5 to 1.5 M. The distillation columns contain *Amistico* structured packing with a height of 2.35 m, equivalent to 30 theoretical stages. The energy is expressed in kilograms of water produced per kg of condensed steam in the first reboiler (commonly known as GOR in desalination processes). The higher the value, the greater the energy efficiency.

Energy data have been summarized in Table 4.1, for both the single column and the system with more columns. Equivalent work values are reported, being defined as the theoretical power obtainable from the thermal energy consumed in the process (assuming a standard efficiency of a steam turbine operating with saturated steam at the available temperature). This value can be used to compare the efficiency of different processes. The distillation column with low pressure is the method with the lowest equivalent work due to the heat with low temperature.

Table 4.1: FO energy data for single vacuum column and multi stage column distillation [118].

Single vacuum column						
Inlet steam temp. [°C]	Draw conc. [M]	Column press [atm]	Heat duty [MJ/m^3]	GOR [-]	Equiv. work [kWh/m^3]	Number of stages
44	0.5	0.075	269.13	8.9	0.73	1
40	1	0.071	382.27	6.3	0.66	1
40	1.5	0.071	541.55	4.4	0.84	1
Multi stage column distillation						
70	1.0	0.28	185.38	12.6	1.50	2
100	1.0	0.91	140.91	16.0	2.03	3
130	1.0	2.47	113.53	19.1	2.36	4
160	0.5	5.60	78.62	26.5	2.14	5
160	1.0	5.62	103.04	20.2	2.77	5
160	1.5	5.60	140.37	14.8	3.69	5
190	1.0	11.52	97.58	20.3	3.18	6
250	1.0	37.00	94.29	18.2	3.93	8

In 2007, McGinnis et al [124] described a method for converting thermal energy into mechanical work, in a closed cycle PRO, using draw solutions of ammonium salts at high concentration, namely a mixture of NH_4HCO_3 and ammonia (i.e. hydrated ammonia). Also in this case, the properties of the electrolytic solutions are obtained using HYSYS process simulator with the OLI thermodynamic package. The scheme of the process is represented in Figure 4.5:

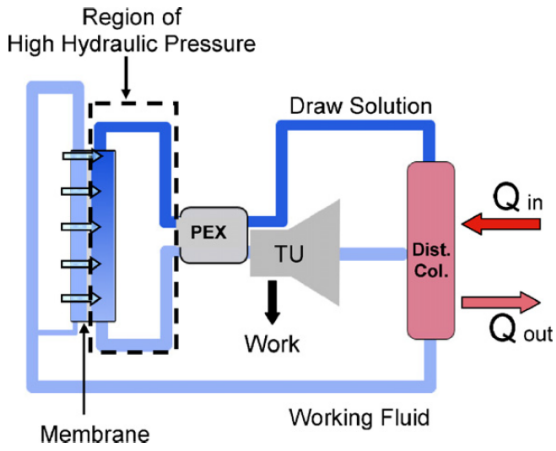

Figure 4.5: Schematic of the ammonia–carbon dioxide osmotic heat engine (OHE) for power generation. The working fluid is water containing <1ppm NH_3 and CO_2, and the draw solution is made up of concentrated ammonium salts. PEX denotes pressure exchanger, TU denotes turbine, and Qin and Qout represent the heat flows into and out of the engine. The dashed line box indicates the region of high hydraulic pressure (on the active layer side of the membrane) [124].

The thermal efficiency of the process is calculated as the ratio between the electrical power produced in the PRO device and the thermal energy required for the separation and recovery of the draw solution. The amount of heat required in the distillation column to separate NH_3 and CO_2 from the diluted draw solution is calculated using a process simulator in a single distillation column. The inlet solution concentration is 6 M (CO_2 basis), while the column is 2.35 m (7.7 ft) high, with a structured packing and heat is supplied at 50 °C. The temperature and the column bottom pressure are respectively 46.96 ° C and 0.1048 atm, while in the top the values are respectively 35.55 ° C and 0.1040 atm. The inlet stream is preheated at 32 ° C requiring about 3200 MJ/m^3. The heat duty supplied to the reboiler is 3455 MJ/m^3. Additional energy requirements are 386 MJ/m^3 to maintain all the currents at the specified temperature. Thus, the total thermal duty is 7037 MJ/m^3, while the electrical energy for the fluids handling is negligible (0.48 MJ/m^3). Table 4.2 reports the main simulation results:

Table 4.2: Several characteristics of draw solutions used in the modelling of OHE efficiency and relevant heat and electrical duties for the draw solute separation and recycling [124]

Draw solute conc. [M]	NH_3/CO_2	Heat duty [MJ/m^3]	Electrical duty [MJ/m^3]
1	1.1	358.0	0.12
2	1.2	593.4	0.13
3	1.2	865.7	0.16
4	1.3	1319.0	0.19
5	1.6	2847.7	0.26
6	1.8	7037.1	0.48

In 2013, Shim et al. [135] carried out experiments for NH_4HCO_3 removal using for the first time a Vacuum Membrane Distillation (VMD) process. The results demonstrated a gas removal efficiency around 95-99% feeding 0.8 L/min of solution at 50 °C and 60 ° C. At 40 °C, instead it reached a lower removal efficiency of 85%. They tested the system with different inlet concentrations ranging between 0.5 M and 2 M. The solutions were pre-heated at temperatures of 40 °C, 50 ° C and 60 °C and sent inside the feed side of the membrane module, while the permeate side vacuum was maintained at 70 mbar. The species permeated (NH_3, CO_2 and steam) were sent to a condenser where the vapour was condensed, while non-condensable ammonia and carbon dioxide were sent to a dilute water stream for re-sorption. The authors demonstrated that the flow rate has a little effect on the gas removal, while the removal efficiency decreases significantly if the feed solution concentration decreases, however no data on specific energy consumption are reported.

In 2015, Kim Y. et al. [136] installed a 3 ton/day pilot plant for water desalination using the forward osmosis process with a draw solution of ammonium bicarbonate. The system consists of three units: FO, water-solute separation and draw solution regeneration. In particular, the two latter processes have been integrated in a single column as illustrated in Figure 4.6:

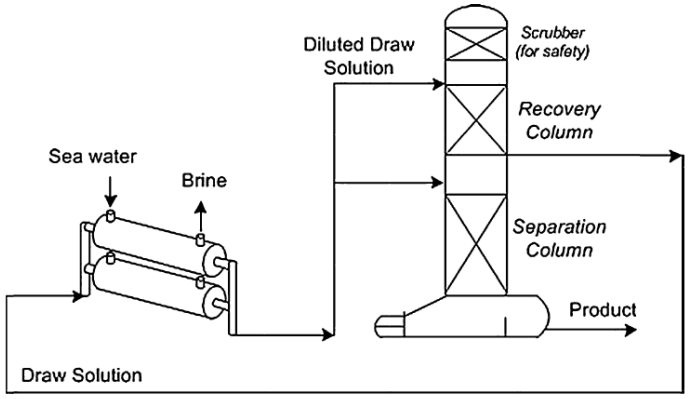

Figure 4.6: Process flow diagram of the forward osmosis desalination pilot [136].

The water-solute separation was made in a column with structured packing operating at ambient pressure and fed with a solution previously heated in the reboiler at temperatures up to 100 °C. This column has a diameter of 0.2 m and a height of 3 m. The separation efficiency was equal to 99.7 % for the NH_3 and 99.9 % for the CO_2, while the thermal energy consumption required for producing 1 m^3 of water ranged between 265 and 300 kWh.

In 2015, Zhou et al. [137] developed a model for a FO process with an integrated thermal separation process. In particular, they compared three different regeneration units:

- Distillation;
- Stripping with steam;
- Stripping with air.

The analysis was conducted by means of the process simulator ASPEN PLUS®, using the thermodynamic package NRTL-RK. They highlighted the best regeneration system from the energetic point of view. The analysis of the three regeneration systems was conducted considering three different models:

- *Rate-based model*, taking into account fluid dynamics, thermodynamics, kinetics, heat and mass balances;
- *Equilibrium-stage* model, taking into account fluid dynamics, thermodynamics and kinetics;
- *Basic chemistry* model, in which the equilibrium condition is considered instantaneous and the only thermodynamic aspects are taken into account.

The passage from rate-based to basic chemistry model causes a reduction in computation time and at the same time the result became more imprecise.

In the distillation process, the heat is supplied through the reboiler on the column bottom and due to its thermal inefficiency, this process is less efficient compared to stripping with air, but a better performance can be enhanced operating at lower temperature in a vacuum column.

In the stripping process with steam, the heat is directly transferred to the draw solution to be regenerated.

The stripping with hot air allows to reduce the partial pressure of the volatile components in the gas phase, allowing operations at atmospheric pressure, and higher temperature.

The three regeneration systems were modelled using a packed column with structured packing (Amistico) with height of 8.3 feet, in which the inlet stream, with a concentration varying from 0.5 to 1.5 M (based on CO_2), is preheated by a hot stream from the top or from the bottom of the column. The simulations were conducted both at ambient pressure and at reduced pressure (0.1 to 1 atm). The energy required is related to the production of a stream with a concentration of ammonia below 1 ppm.

The heat duty required per m^3 of water produced is reported in Figure 4.7, the three models significantly differ only for case of the stripping with air, and in particular the basic chemistry model underestimates the energy demand.

Figure 4.7.B shows the influence of operating pressure on the energy demand, also highlighting the difference when the kinetics of the reactions are not considered.

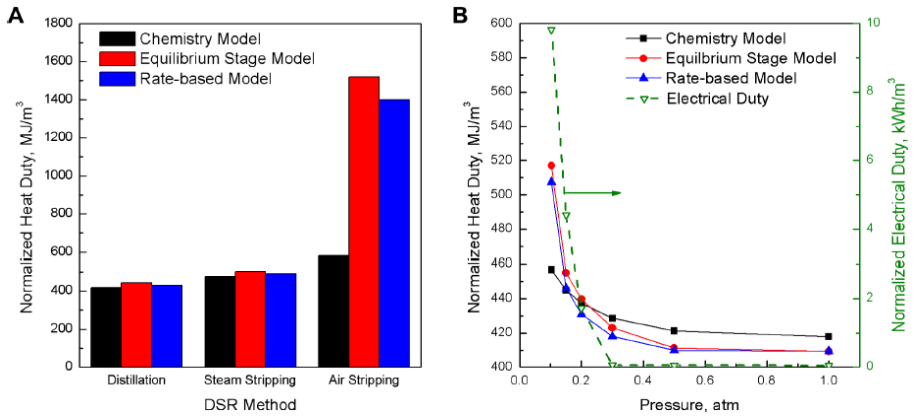

Figure 4.7: Comparison of the predicted heat duty of the draw-solute-regeneration process for three different CO_2−NH_3−H_2O separation models using ASPEN. (A) Comparison of the chemistry model, equilibrium-stage model, and rate-based model for the three DSR methods at ambient pressure. (B) Comparison of the chemistry model, equilibrium-stage model, and rate-based model under the distillation DSR configuration for different operating pressures in ASPEN. The equivalent work penalty for operating at subatmospheric pressures is plotted on the right-hand axis [137].

According to the authors' findings, the distillation system is considered the best because the stripping with air requires a higher thermal energy demand and a larger column to obtain the target purity, while stripping with steam is comparable to the distillation process in terms of thermal duty but it requires an additional compressor thus increasing the overall costs.

Table 4.3: Comparison of Distillation, Steam Stripping, and Air Stripping

	Distillation	**Steam Stripping**	**Air Stripping**
Stage number	25	25	80
Column diameter [m]	1.25	1.25	4.25
Top temperature [°C]	86.4	86.4	36.8
Sump temperature [°C]	100.6	100.6	37.7
Specific heat duty [MJ/m^3]	409.37	405.59	>680.9

For this reason, sensitivity analysis was focused on the use of distillation column in order to highlight the energy consumption dependence on some operating parameters such as:

- *Pressure*: If the pressure decreases in the column, the temperature decreases at the bottom allowing the use of heat at lower temperature, but the thermal duty increases;
- *Column height*: the use of multiple high columns can reduce the energy demand;
- *Feed solution concentration*: the lower the concentration of the solution, the lower the energy required to achieve the target separation.

In 2015, Shahid et al. [138] analysed the thermal decomposition process of aqueous NH_4HCO_3 and potassium persulphate ($K_2S_2O_8$) solutions, using a bubble column with air at 150 °C insufflated continuously maintaining optimum bubble size between 1-3 mm. The hot air does not heat too much the bulk of the solution, but it generates a hot solution layer around each bubble, which causes the local thermal decomposition of the solute. Experimental details: a semi-batch system, with a 12 cm high column with diameter of 13 cm, air flow rate of 22.5 L/min at 150 °C, batch volume equal to 250 ml of solution.

NH_4HCO_3 solutions with variable concentrations between 0.5 and 2 molar with 0.05 molar of potassium persulphate were used for the investigation.

It is interesting to note that the decomposition of a 2 molal solution of NH_4HCO_3 can be obtained at 8 °C, which is much lower than the decomposition temperature reported in literature (approximately 40 °C). This probably occurs due to the continuous removal of gases released from the hot solution layer around bubbles. However, also in this case, the greater the air temperature, the higher the % of degradation obtained.

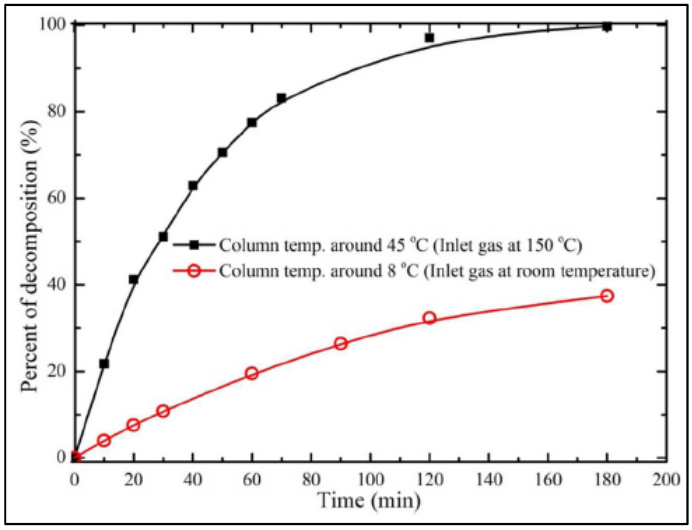

Figure 4.8: Comparison of decomposition percent for 2 m NH_4HCO_3 solution in a BCE with inlet gas (dry air) at 150 °C and at room temperature (around 22 °C) [138].

Very few works have focused on the possibility of using thermolytic salts solutions for closed-loop RED applications.

In 2012, Xi Luo et al. [97] presented an experimental campaign on a reverse electrodialysis unit (RED) fed with NH_4HCO_3 solutions. They obtained a power density of 0.33 W/m^2 of membrane area, using a solution of ammonium bicarbonate (concentrate solution 1.5 M - dilute solution 0.02 M).

Slightly later, in 2015, Kilsung Kwon et al. [117] also presented the idea to convert waste heat into electricity by means a RED process with ammonium bicarbonate and a thermal process for the solutions regeneration. The process scheme is represented in Figure 4.9. They especially focused on the experimental characterization of the RED process, characterizing this NH_4HCO_3-RED system with respect to various parameters including the concentration difference, the membrane type, the inlet flow rate, and the compartment thickness. The authors found the best power density (0.77 W/m^2 of membrane area) at the concentrated solution of 1.5 M and the diluted solution of 0.01 M. The maximum power density increased as the inlet flow rate increased or the compartment thickness decreased due to the decrease in the internal stack resistance.

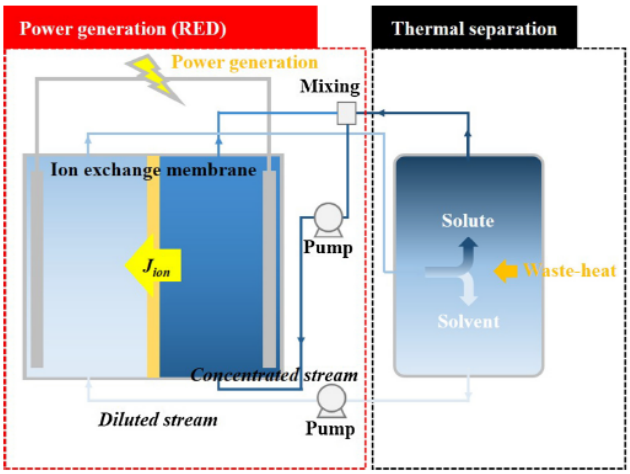

Figure 4.9: Schematic illustration of a waste heat recovery system using reverse electrodialysis [117].

In 2017, Kim et al [139] presented a RED model with ammonium bicarbonate solutions in a closed loop. They used the Plank-Handerson equations to approximate the membrane potential based on conductivity measurements. Membrane resistance were also experimentally measured and the results were used in the model. They found that the model was in good agreement with the experimental results under various operative conditions. They reported also the net power density after calculating the pumping loss. The maximum net power density (0.84 W/m^2) was obtained with an intermembrane distance of 0.1 mm, a flow rate of 3 ml/min and a concentration ratio of 200 (2M-0.01M).

4.2 Modelling of a lab-scale stripping system for ammonium bicarbonate solutions

This section illustrates the work carried out using a process simulation software (Aspen Plus®) to simulate the decomposition of ammonium bicarbonate solution by stripping with hot air. A stripping column is a device that promotes the gas release process from a liquid mixture, by contacting a dispersed liquid phase with a continuous stripping gas stream, which carries out the dissolved gases from the liquid.

The scheme of the lab-system is illustrated in Figure 4.10. The air, before entering in the stripping column, is heated and humidified in an air saturation column in order to avoid

decreasing of temperature in the stripping column and reduce the amount of water that evaporate from the NH_4HCO_3-water solution.

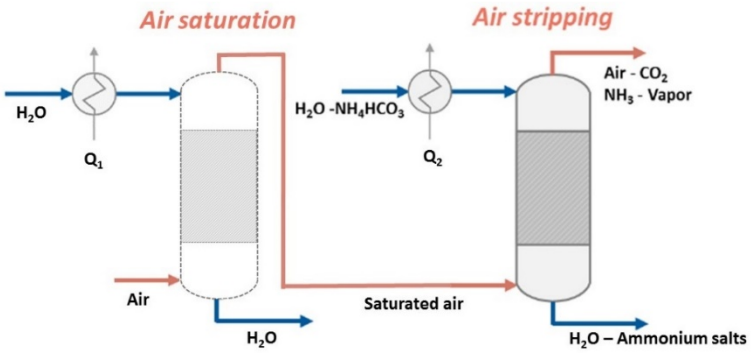

Figure 4.10: Schematic illustration of a stripping system for the controlled degradation of ammonium bicarbonate

The main reactions (equilibrium) involved when ammonium hydrogen carbonate is dissolved in water are reported in a previous section **Errore. L'origine riferimento non è stata trovata.** but for convenience are following reported again:

$$NH_4HCO_{3(s)} \leftrightarrow NH_4^+ + HCO_3^- \quad [4.1]$$

$$2H_2O \leftrightarrow H_3O^+ + OH^- \quad [4.2]$$

$$NH_3 + H_2O \leftrightarrow NH_4^+ + OH^- \quad [4.3]$$

$$CO_2 + 2H_2O \leftrightarrow HCO_3^- + H_3O^+ \quad [4.4]$$

$$HCO_3^- + H_2O \leftrightarrow CO_3^{2-} + H_3O^+ \quad [4.5]$$

$$NH_3 + HCO_3^- \leftrightarrow NH_2COO^- + H_2O \quad [4.6]$$

$$NH_4COONH_4 \leftrightarrow NH_2COO^- + NH_4^+ \quad [4.7]$$

The ions shown in the list above with a red colour are carbamate ions, which are more soluble than ammonium bicarbonate and can increase the amount of ions present in the solution, thus possibly enhancing RED potentials.

Among the input, the process simulator requires a thermodynamic package to be chosen. Since it might have a crucial impact on results, some thermodynamic models proposed by the software were tested and compared with data taken from Perry's

Handbook (Table 2-25 and 2-26 in [140]). In particular, as can be seen in Figure 4.11, the ELECNRTL and ENRTL-RK thermodynamic models were compared with each other and with experimental equilibrium curves (i.e. T-x-y) for the case of ammonia-water mixture and a very good agreement was found. The ENRTL-RK thermodynamic model was chosen for the analysis of the present work in accordance with software recommendations and with literature on NH_4HCO_3-H_2O solutions [137].

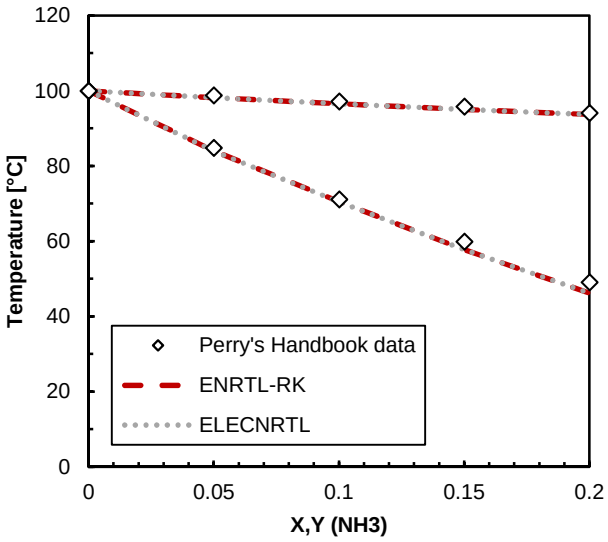

Figure 4.11: Comparison of different thermodynamic packages with literature Txy data for the case of the binary NH_3-H_20 system [140].

The construction of the model includes the following main steps:

- Specifying all components involved in the stripping process;
- Selecting the thermodynamic model;
- Drawing the graphical simulation flow sheet;
- Defining the physical properties and flow rates of the feed streams;

4.2.1 The properties environment

Within the *properties* environment of ASPEN Plus, the components involved in the stripping process are specified with the thermodynamic model. As already said, the ENRTL-RK model was chosen. However, only the heat exchanger at the bottom of the stripping column was simulated with OLI thermodynamic package because it allows to have the results directly in electrical conductivity, the only properties that can be experimentally measured.

OLI system is a specific thermodynamic package for electrolyte solutions. It has been exploited in many works on thermolytic salts (see 4.1) but it was widely demonstrated by Gatz [141] that it does not predict well the real behaviour of a NH_4HCO_3-water-air system, overestimating the results. For this reason. OLI was used only in the final heat exchanger, where the stream was only at liquid phase.

4.2.2 The simulation environment

Within the *simulation* environment of ASPEN Plus, the graphical simulation flow sheet is designed. For modelling the stripping system, the following unit operation blocks have to be placed on the flow sheet:

- Two heat exchangers
- One saturation column filled with random packing (Raschig rings)
- One stripping column filled with random (Raschig rings) or structured packing (FLEXIPAC 700 Y, provided by KOCH-GLITSCH)

The ASPEN Plus flow sheet of the stripping system, which is shown in Figure 4.12, is slightly different than the process scheme of the system illustrated Figure 4.10. The working principle of the system modelled in Aspen Plus, however, is exactly the same. As a last point of the modelling, the flow rates and properties of the feed streams are defined in the *simulation* environment.

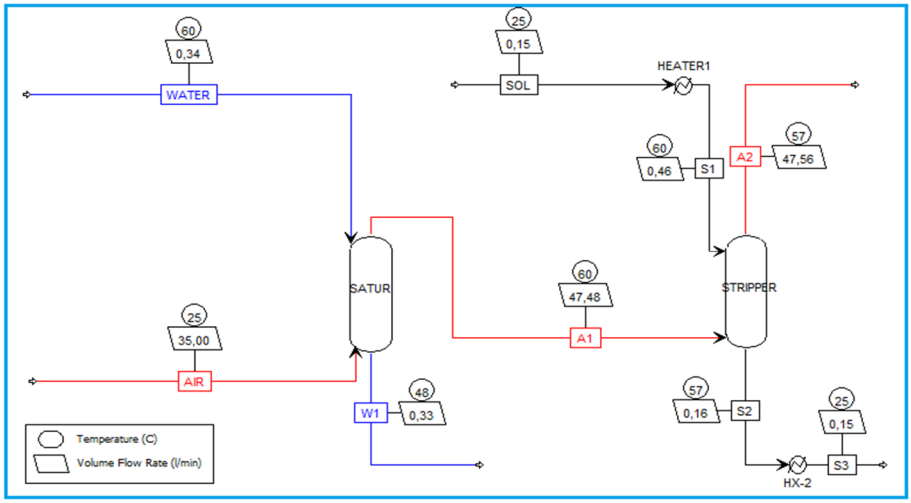

Figure 4.12: Flow sheet of the stripping system designed with ASPEN Plus

Heat Exchangers

Two heat exchangers of the type "HEATER" are selected from the library *Exchangers* of the *Model Palette* in ASPEN Plus. The unit operation blocks are placed on the flow sheet and renamed to *"HEATER1"* and *"HX-2"*.

"HEATER 1" is used to heat the NH_4HCO_3 solution from room temperature to 60°C or rather 70°C. The specifications of *"HEATER1"* are provided as follows:

- Temperature: 60°C or 70°C
- Pressure: 1 bar
- Valid phases: *Vapor-Liquid*

The liquid exiting the stripping column is cooled down to 25°C in the heat exchanger *"HX-2"* in order to generate simulation results which can be compared to experimental data. The specifications of *"HX-2"* are set to:

- Temperature: 25 °C
- Pressure: 1 bar
- Valid phases: *Vapor-Liquid*

At this point, it should be noted that a third heat exchanger for heating the water entering the saturation column is not placed on the flow sheet to simplify the system. The temperature of the water stream entering the stripping column, however, can be controlled through the specifications of the feed stream. Another heat exchanger (not represented in

Figure 4.12) is placed after HX-2 with OLI thermodynamic package in order to calculate the solutions electrical conductivities.

Saturation Column

For the modelling of the saturation column, a column of the type *RadFrac* is selected from the library *Columns* of the *Model Palette*, and placed on the flow sheet. *RadFrac* is a rigorous model for all types of multistage vapour-liquid fractional operations. The column is renamed to *"SATUR"*. The specifying of the saturation column is described in the following paragraphs.

Calculation Type

The approach for solving the saturation column is set to *rate-based* under *Blocks>SATUR>Specifications>Setup>Configuration>Calculation type*. By utilization of this calculation type, it is considered that the vapour and liquid phases in the column are not in thermodynamic equilibrium at each stage. Thus, rate-based mass and heat transfer phenomena within the stages are considered.

The rate-based calculations include:

- Mass and heat balances around vapour and liquid phases
- Mass and heat transfer rate models to calculate interphase transfer rates
- Vapour-liquid equilibrium relations applied at the interface
- Correlations to estimate mass and heat transfer coefficients and interfacial areas
- Additional equations in reacting systems in order to take the influence of chemical reactions on heat and mass transfer phenomena into account

Besides the rate-based transfer phenomena, the calculation type takes thermodynamics, hydrodynamics and chemical reactions into account.

Number of Stages

Under *Blocks>SATUR>Specifications>Setup>Configuration>Number of stages,* the number of stages of the column must be defined. Since packed columns do not have individual stages, the number of theoretical stages N_t of the saturation column filled with Raschig rings is estimated by use of the following equation:

$$N_t = \frac{Ht}{HETP} \tag{4.1}$$

where *Ht* is the total height of the packing material and *HETP* is the *height equivalent to a theoretical plate*. For randomly packed columns with an inner diameter lower than 0.67 m, the rule of thumb of Frank-Ludwig-Vital can be employed for estimating the *HETP* [140]:

$$HETP = 18\, D_p \tag{4.2}$$

where D_p is the diameter of a single element of the random packing. Here, the following must apply:

$$HETP > D_T \tag{4.3}$$

where D_T is the inner diameter of the column.

For this modelling, *Ht*, D_T and D_P are set to 1.5 m, 0.05 m and 0.01 m, respectively, which accords to the experimental set-up. Using equation (4.1) to (4.3), N_t is estimated to be equal to 9. This number is provided to ASPEN Plus.

Condenser, Reboiler, Valid Phases, Streams and Pressure

At this point of the modelling, it must be defined if the column has condensers and/or reboilers. Since there are neither condensers nor reboilers within the column, *none* is selected in the respective dropdown menu. The valid phases in the column are specified to be *Vapour-Liquid.*

Under *Blocks>SATUR>Specifications>Setup>Streams>Feed streams* it is specified that the feed stream *"AIR"* enters from the bottom of the column (*stage 9*, *on-stage*), and that the feed stream *"WATER"* enters from the top of the column (*stage 1*, *on-stage*). The pressure at the top stage is set to 1 bar. It is assumed that there is no pressure drop within the column.

Packing

The properties of the random packing of the column are specified under *Blocks>SATUR>Sizing and Rating>Packing Rating>Setup*.

The starting stage and the ending stage of the random packing is set to be 1 and 9, respectively. *RASCHIG* is chosen from the drop-down menu in order to select Raschig rings as type of the packing. The packing characteristics are specified as follows:

- Vendor: *NORTON*
- Section diameter: 0.05 m
- Material: *METAL-32*
- Dimension/external diameter: 0.01 m
- Section packed height: 1.5 m

At this point, the packing characteristics *Packing Size* and *Packing Factor* F_p are determined automatically from Aspen Plus.

The specified packing properties correspond to those of the saturation column, which was used in the experimental set-up except for the vendor and the material of the Raschig Rings. In the saturation column of the experimental set-up, handmade plastic Raschig rings were used. It is assumed that the variation of the material of the Raschig rings does not significantly affect the performance of the column as long as the dimensions of the rings stay the same.

As a last point, *Rate-based calculations* are activated under *Blocks>SATUR>Sizing and Rating>Packing Rating>Rate-based*.

Stripping Column

The stripping column is also modelled with a column of the type *RadFrac* selected from the library *Columns* of the *model palette*. The *RadFrac* column is placed on the flow sheet, and renamed to *"STRIPPER"*. The specifications of the stripping column are provided as described in the following.

Calculation Type

As for the saturation column, the *rate-based* calculation type is chosen for solving the stripping column under *Blocks>STRIPPER>Specifications>Setup>Configuration*.

Number of the Stages

The number of stages varies with the packing installed in the column. In case of using Raschig rings as packing material, *Ht*, D_T and D_P are equal to 1.5 m, 0.05 m and 0.01 m, respectively. By use of equations (4.1) to (4.3), the number of theoretical stages N_t is estimated as 9.

In case of using the structured packing FLEXIPAC 700Y, equation (4.2) cannot be applied for determining the *HETP* of the packing. However, the *HETP* of the packing is estimated by the manufacturer as 160 mm for atmospheric distillation systems with low relative volatility and good liquid/vapour distribution [142]. It is assumed that this *HETP* value also applies for the stripping column using NH_4HCO_3 solutions. Thus, N_t can be estimated by use of equation (4.1) with the total height *Ht* of the packing material being equal to 1.6 m. The result, 10 theoretical stages, is provided to ASPEN Plus.

Condenser, Reboiler, Valid Phases, Streams and Pressure

By selecting *none* in the respective drop-down menu, it is specified that there are no condensers and reboilers in the column. Furthermore, the valid phases are set to *Vapor-Liquid*. Under *Blocks>STRIPPER>Specifications>Setup>Streams* it is defined that the stream *"S1"* of hot NH_4HCO_3 solution enters the stripping column from the top (*Stage 1, On-Stage*), and that the stream *"A1"* of hot saturated air enters the column from the bottom (*Stage 9* or rather *Stage 10*, *On-Stage*). The pressure within the columns is set to be equal to 1 bar under *Blocks>STRIPPER>Specifications>Setup>Pressure*. Additionally, it is defined that there is no pressure drop in the stripping column.

Packing

The properties of the packing material are specified under *Blocks>STRIPPER>Sizing and Rating>Packing Rating>Setup>Specifications*. It is defined that the starting stage of the packing section is the first stage, and that the ending stage is the ninth stage for Raschig rings or rather the tenth stage for structured packing. In case of using Raschig rings, the packing characteristics are the same as those of the Raschig rings within the saturation column.

The packing characteristics of the structured packing FLEXIPAC 700Y are specified as follows:

- Vendor: *KOCH*
- Section diameter: 0.05 m
- Material: *METAL*
- Dimension: *700Y*
- Section packed height: 1.6 m

The packing factor F_p is specified automatically by ASPEN Plus. The packing characteristics correspond to those of the packing used in the stripping column of the test-rig except for the vendor of the Raschig rings. Handmade metal Raschig rings were used in the stripping column of the experimental set-up instead of industrially manufactured Raschig rings. It is assumed that the variation in manufacturing does not affect the performance of the stripping system as long as the material and dimensions of the Raschig rings are the same.

As a last-point, rate-based calculations are activated under *Blocks>STRIPPER>Sizing and Rating>Packing Rating>Rate-based.*

Stream Properties

In the following, it is described how the properties of the feed streams are specified.

The properties of the air stream *"AIR"*, which enters at the bottom of the saturation column, is specified under *Streams>AIR>Input>Mixed* as follows:

- Temperature: 25°C
- Pressure: 1 bar
- Total flow rate: 35 l/min
- Mole-Fraction of air: 1 [-]

The properties of the water stream *"WATER"* entering the column from the top are provided as follows:

- Temperature: 60°C or 70°C
- Pressure: 1 bar
- Total flow rate: 1 l/min
- Mole-Fraction of water: 1 [-]

The provided value of the total water flow rate is just an initial estimate. The actual flow rate, which is required for gaining saturated air at 60°C or rather 70°C at the top of the column, is calculated by use of the function *Design Specification* of ASPEN Plus.

Under *Blocks>SATUR>Specifications>Design Specifications>Specifications*, the *Stage temperature* of the first stage of the saturation column is selected as design specification. The target of the specification is specified as 60°C or rather 70°C applied to the vapour phase. Under *Blocks>SATUR>Specifications>Vary>Specifications*, it is specified that the *Feed rate* of the stream *"WATER"* is the so-called manipulated variable. The manipulated variable is kept free in order to meet the design specification provided before. The upper and lower bounds of the water feed rate are set to 0.45 kmol/hr and 2 kmol/hr, respectively. ASPEN Plus adjusts the water feed rate by creating loops, which are solved iteratively in order to achieve the vapour phase's temperature specification.

The function *design specification* can only manipulate input variables of the selected block itself or rather of the feed stream which directly enters this block. Therefore, a heat exchanger cannot be placed between source of the feed water stream and saturation column as long as the water feed rate must be adjusted.

The selected input parameters for the NH_4HCO_3 solution stream "SOL" are:

- Temperature: 25°C
- Pressure: 1 bar
- Total flow rate: 0.1 or 0.15 l/min
- Mole concentration of NH_4HCO_4 in the solvent water: in a range between 0.5 mol/l and 1.5 mol/l

All provided stream characteristics are equivalent to the properties of the feed streams of the experimental set-up (see paragraph 4.3.3).

Under *Property Sets>New*, the pH of the liquid streams, the molar concentration and the electrical conductivity of all components in the liquid streams are chosen as additional properties that are to be calculated. These properties are selected under *Setup>Report Options>Stream>Property sets* in order to show them in the results sheet.

At this point, the modelling is completed. The model can be used to simulate the performance of the stripping system of the NH_4HCO_3 solution regeneration unit within a closed-loop RED heat engine under varying operating conditions.

4.3 Experimental campaign on a lab-scale stripping system for ammonium bicarbonate solutions and model validation

An experimental campaign was carried out on a lab-scale stripping system for the regeneration of NH_4HCO_3 solutions in order to prove the model constructed in the present work. In this chapter, the set-up of the test rig is described as well as the experimental procedure of the test runs. Furthermore, the results of the experiments are depicted and confronted with the model predictions in order to identify the main discrepancies and validate the model prediction capabilities.

4.3.1 Description of the lab-scale stripping system

The test rig of the stripping system for NH_4HCO_3 solutions is schematically reported in Figure 4.13, and pictured in Figure 4.14.

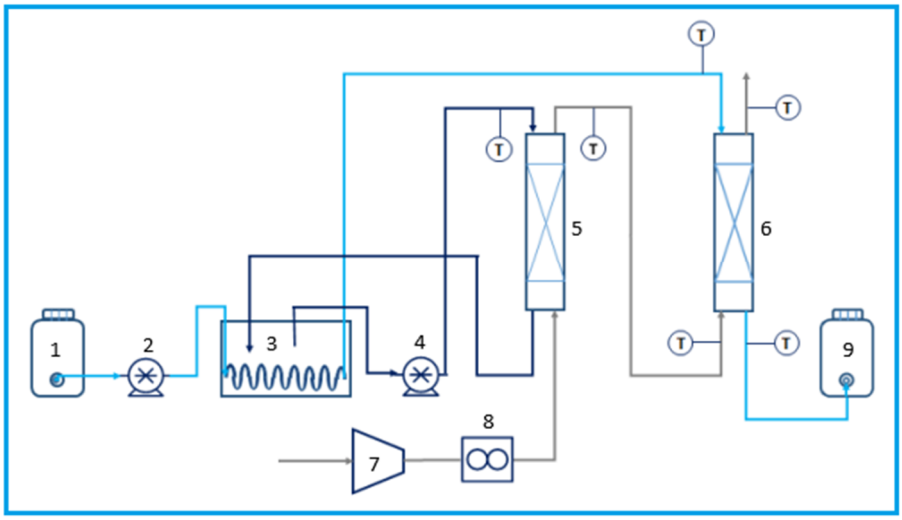

Figure 4.13: Schematic illustration of the experimental stripping system for NH_4HCO_3 solutions [143].

The aqueous NH_4HCO_3 solution stored in a plastic tank (1) is fed into a steal coil placed in a thermal bath (3) by means of a VERDERFLEX peristaltic pump (2). The flow rate of the solution is controlled by use of a voltage controller. The thermal bath is filled with hot demineralized water at a temperature in a range between 63°C and 75°C, thus heating up the NH_4HCO_3 solution to temperatures at which the degradation of the salt

begins. The heated solution is fed into the stripping column (6), where it cascades downwards in counter-current to raising hot saturated air. In the stripping column, the degradation of the salt is intensified, and the gases arising in the solution are stripped out into the air stream. The gaseous stream of NH_3, CO_2 and air leaves the stripping column at the top, and is fed into the atmosphere. The regenerated NH_4HCO_3 solution exiting the column at the bottom is stored in a further plastic tank (9).

The saturation of the air takes place in the saturation column (5). Dry air from a compressor (7) (ABAC mod. PRO B6000500T7.5), whose air flow rate is indicated and fixed by use of a rotameter (8) (KEY INSTRUMENTS), enters the saturation column from the bottom and raises upwards. Distilled water is fed from the water bath (3) to the top of the column by use of a SHURFLO membrane pump (4). From the top of the column, it cascades downwards through the random packing. The water flowrate is controlled by means of a voltage controller and a water bypass. The counter-current flow between hot water and dry air leads to the heating and saturation of the air. The hot saturated air is fed to the bottom of the stripping column, while the distilled water is fed back into the thermal bath (3). Operating, all main components, junctions and tubes of the test rig are thermally isolated.

The temperature of the liquid and gaseous streams in the stripping system are measured by use of six thermocouples, which are placed within the tubes close to the inlets and outlets of the columns. The thermocouples are connected to an USB measurement device from National Instruments, which allows the transfer of the measured values to a computer. The measured temperatures are displayed by use of the system design software LABView®.

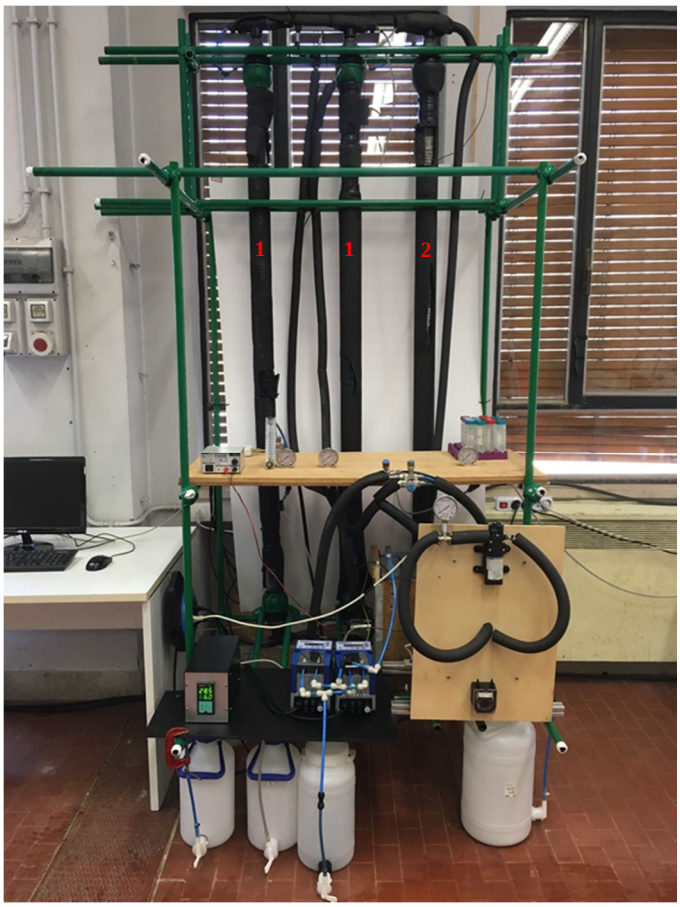

Figure 4.14: Experimental stripping system for the regeneration of aqueous NH_4HCO_3 solutions. Saturation column (1) filled with polyurethane Raschig rings; Stripping column (2) filled with metal Raschig rings.

Saturation Column

The saturation column is realized using a Plexiglas tube with a height of ca. 2 meters and an inner diameter of 0.05 meters. The column is filled for 1.5 meters with handmade polyurethane Raschig rings with a height and diameter of 0.01 meters, respectively. The gas and the liquid enter the column through a liquid and gas distributor placed at the top and the bottom of the column, respectively. In order to reduce wall effects for the liquid, O-rings are used as liquid redistributors within the column. The maximum permissible distance between two liquid redistributors can be estimated with the rule of thumb of *Schönbucher* for randomly packed columns [144]:

$$z_p \leq 6\ D_T \tag{4.4}$$

where z_p is the distance between two liquid redistributors. According to equation (4.4), at least four O-rings should be placed within the column in order to achieve the maximum permissible distance z_p between two liquid redistributors, which is equal to 0.3 meters. However, three O-rings are placed within the column, which leads to z_p equal to 0.375 meters. Notwithstanding, it is assumed that the liquid distribution within the column is sufficient due to the small inner diameter of the column.

Stripping Column

The stripping column is realized using a Plexiglas tube with the same dimensions as those of the saturation column. The stripping column is filled with one of the following kinds of packing:

- Random packing
- Structured packing

As random packing, handmade metal Raschig Rings with a height and an inner diameter of 0.01 meters are used. The height of the total packing section is equal to 1.5 meters. In order to redistribute the liquid, seven O-rings are placed within the column, which corresponds to a distance z_p between two liquid redistributors equal to 0.19 meters. According to equation (4.4) the actual distance between two liquid distributors is smaller than the maximal permissible distance.

For the second operating mode, the structured packing FLEXIPAC 700Y, which is provided by KOCH-GLITSCH, is used within the stripping column. As can be seen in Figure 4.15, the packing consists of corrugated stainless steel sheets arranged in a crisscross pattern with a nominal inclination angle of 45°.

The total packing section with a height of 1.6 meters consists of six packing units with a height of 0.27 meters. At the top, bottom and in the middle of a packing unit, a metallic liquid redistributor with a diameter of 0.05 meters is placed.

Figure 4.15: The stripping column with the structured packing FLEXIPAC 700Y

4.3.2 Experimental procedure

The test execution is described in the following. Initially, the lab-scale stripping system was run only with demineralized water in order to clean tubes and columns, heat the packing material up to operating temperature and generate a steady state. At the beginning of each experiment, the demineralized water in the thermal bath was heated up to temperatures in a range between 63°C and 75°C. Afterwards, the desired flow rate of the demineralized water (and thus of the later NH_4HCO_3 solution), which was fed from a plastic tank into the stripping column, was fixed with the voltage controller of the VERDEFLEX pump. The flow rate of the air entering the saturation column was fixed with a rotary valve until the desired flow rate of air was indicated on the rotameter.

Since the voltage of the voltage controller connected to the SHURFLO membrane pump was fixed, the flow rate of the hot demineralized water entering the saturation column was adjusted with the rotary valve of the water bypass. The water flow rate was not fixed at a certain value. It was being adjusted in operation so that the air stream exiting the saturation column was heated up to the desired temperature, however, without flooding the column.

At the same time, the NH_4HCO_3 solution with a concentration in a range between 0.5 mol/l and 1.5 mol/l was being prepared. For this purpose, pure NH_4HCO_3 (SIGMA-ALDRICH Co. LLC) was added to demineralized water.

After the stripping system operating with demineralized water had reached the steady state, the plastic tank containing demineralized water was replaced by the tank containing NH_4HCO_3 solution. It was assumed that the system had reached steady state when the stream of the hot saturated air entering the stripping column and the stream of demineralized water entering the stripping column were heated up to the required temperature (60°C), and when these temperatures stayed constant. It should be noted that the indicated temperature values fluctuated by ca. ± 3°C around the desired temperatures. At this point, the actual experiment begun.

After the water tank had been replaced by the tank containing NH_4HCO_3 solution, the steady state of the system had to be achieved again. After reaching the steady state, the stripping system was operating for about ten minutes. During operation, a temperature drop of up to 5°C between the salt solution stream entering the stripping column and the salt solution stream exiting the column was observed. Samples of the regenerated solution exiting the stripping column were taken every 2.5 minutes. The samples were cooled down to a temperature of 25°C ± 0.3°C within a cold bath. At this temperature, the pH and the conductivity of the liquids were measured by means of a pH meter (8 Series**,** designed by *XS Instruments*) and a conductivity meter (LF 196, designed by *WTW*). Furthermore, the pH and the conductivity of the inlet NH_4HCO_3 solution was measured at 25°C. The experimental data was used for the validation of the model.

4.3.3 Operating parameters of the test series

In the experimental campaign, the operating parameters of the lab-scale stripping system were chosen as follows:

- Flow rate $Q_{air,dry}$ of the dry air stream entering the saturation column: 35 l/min
- Temperature T of the salt solution and air stream entering the stripping column: 60 °C
- Type of packing: metal Raschig rings and FLEXIPAC 700Y.

In the following test series, one operating parameter was changed at a time. The operating parameters of all tests are listed in Table 4.4.

Table 4.4: Operating parameters of the test series

$Q_{air,dry}$ [l/min]	Q_{sol} [l/min]	T [°C]	Packing
35	0.15-0.2-0.25	60	Raschig rings
35	0.15-0.2-0.25	60	FLEXIPAC

In each test series, four experiments were performed operating with NH_4HCO_3 solutions with an inlet concentration C_{in} of 0.2 mol/l, 0.5 mol/l, 1.0 mol/l and 1.5 mol/l, respectively.

4.3.4 Experimental results and comparison with model predictions

Since an exact experimental composition characterisation of the liquid streams entering and exiting the stripping column is only realisable with extensive analytical efforts, only the pH and the electrical conductivity of the inlet and outlet streams were measured and compared with the model predictions in order to validate the model.

The experimental electrical conductivities and the pH of the inlet solutions are compared with the model values. The comparisons are reported in Figure 4.16 and Figure 4.17.

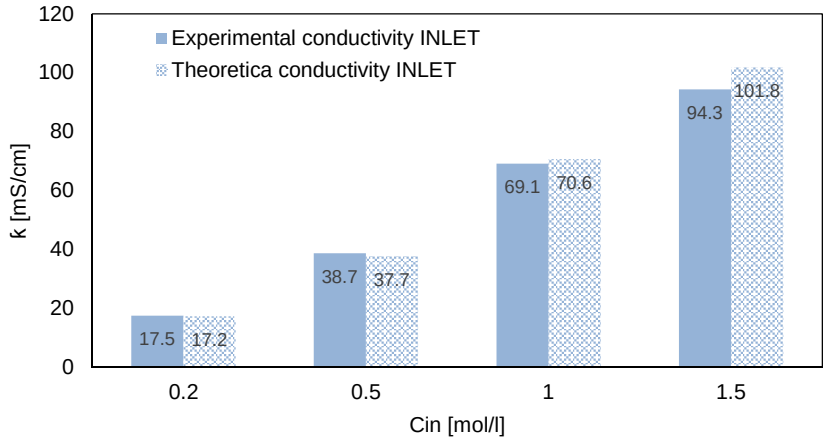

Figure 4.16: Comparison of experimental and modelled electrical conductivity of the inlet solutions

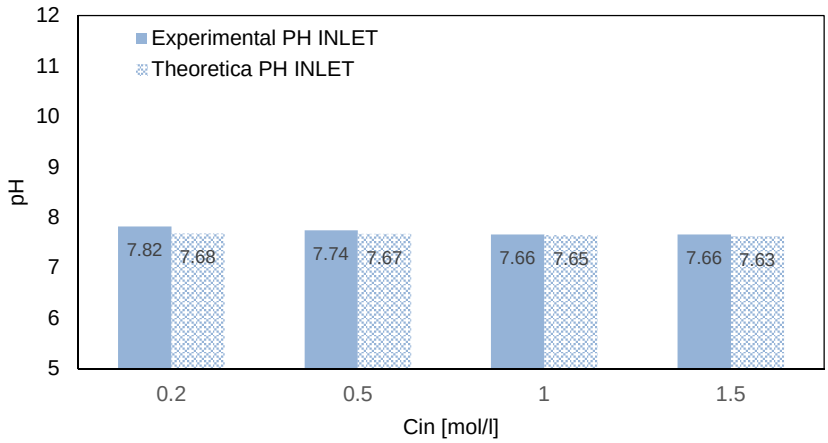

Figure 4.17: Comparison of experimental and modelled pH of the inlet solutions

The comparisons reported above shown that the experimental conductivity is lower than the value predicted by the model at high concentration while the experimental pH is higher. Likely, this discrepancy is due to the low solubility of CO_2 in water. In fact, during the solution preparation, a certain amount of CO_2 can be release into the atmosphere, reducing the conductivity at high concentration and increasing at the same time the pH

The experimental results in terms of electrical conductivity of the outlet streams of the stripping column operating under varying conditions are reported and confronted with the model predictions in Figure 4.18. While, in Figure 4.19, the experimental results in terms of pH of the inlet and outlet streams are shown and confronted with the respective model predictions.

The electrical conductivity of the output current from the stripper has, in some cases, lower conductivity values than those measured experimentally. The percentage difference between the two values decreases with increasing the concentration. In particular, when the inlet concentration (Cin) is higher than 1M, the difference is always around 5% increasing for lower concentration. However, considering the complexity of the system, the model can be considered validated despite small differences with the experimental results. Further studies are needed in order to improve the prediction also at low concentrations.

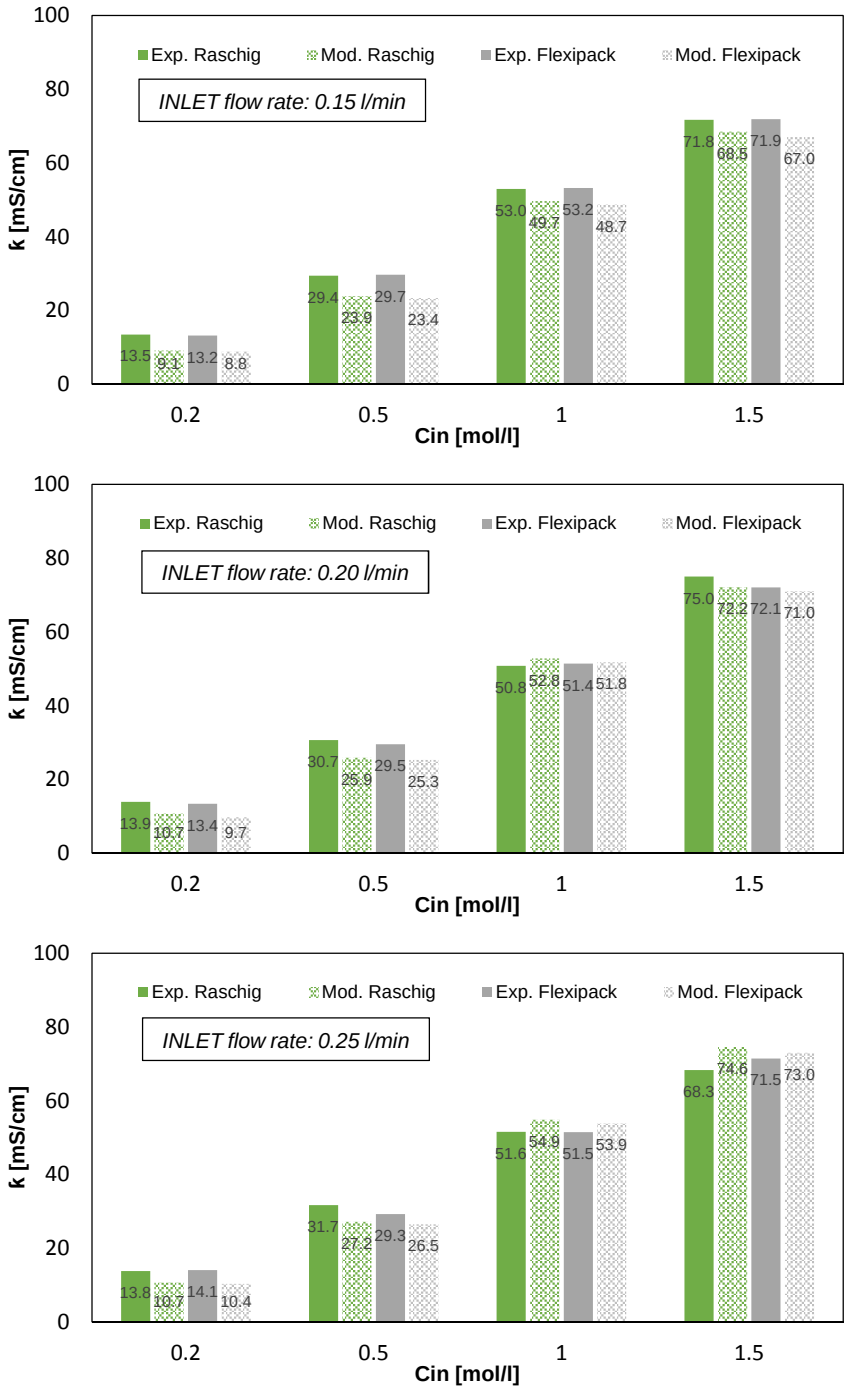

Figure 4.18: Comparison between experimental results and model predictions in terms of electrical conductivity of the outlet stream under varying operational parameters.

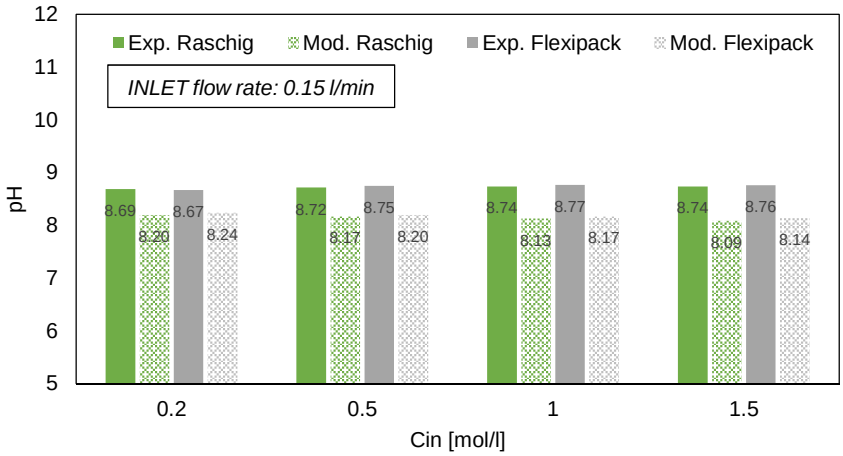

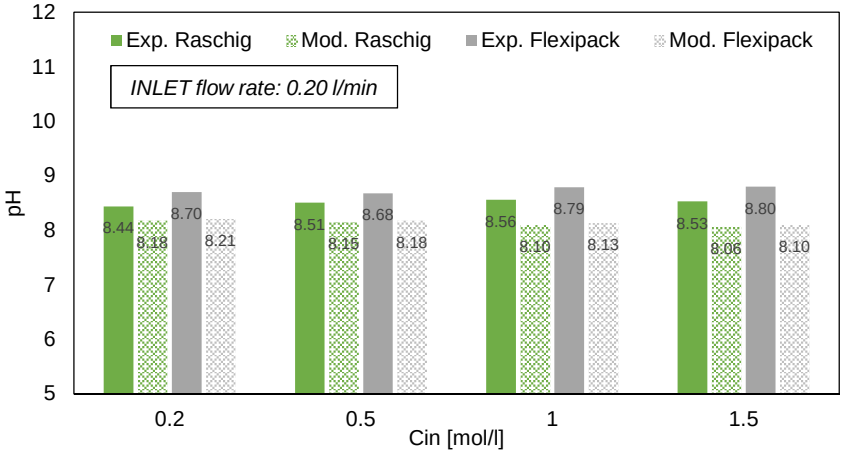

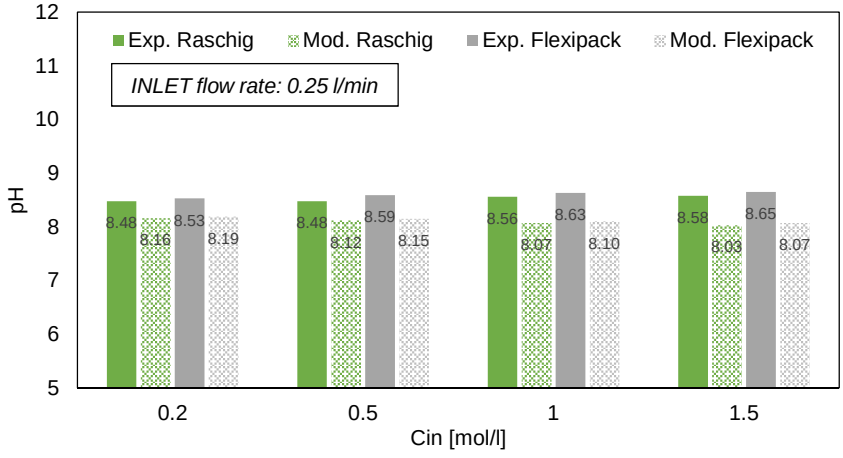

Figure 4.19: Comparison between experimental results and model predictions in terms of pH of the inlet and outlet stream under varying operational parameters

This model was integrated with the simplified RED model described in the chapter 3 in order to simulate the behaviour of the whole RED closed loop system. The results are critically analysed considering than in specific conditions the regeneration model slightly underestimated the values.

5 INTEGRATED RED-CLOSED LOOP WITH THERMOLYTIC SALTS ANALYSIS AND SIMULATION

Abstract

For the first time in the literature, an integrated model was developed in order to analyse the performance of the whole RED closed loop system fed by ammonium hydrogen carbonate solutions. For this purpose, the lumped parameter RED model (presented in chapter 3) was coupled with the air stripping Aspen Plus model (presented in Chapter 4).

The integrated model was used to perform sensitivity analysis. The effect of different operative parameters such as inlet concentrations, solution flow velocity and by-pass flow rate were investigated.

Moreover, the effect of passing from currently available membranes to future high-performance ones was investigated, highlighting the impact of membrane properties (i.e. membrane resistance and permselectivity) on the global process efficiency.

Overall exergetic efficiencies of the process ranging from 11 to 22% have been reached, which represent a good starting point for a future optimisation analysis of the integrated system.

[*] Part of this chapter has been published as:

M. Bevacqua, A. Tamburini, M. Papapetrou, A. Cipollina, G. Micale, A. Piacentino, Reverse electrodialysis with NH_4HCO_3-water systems for heat-to-power conversion, Energy 137 (2017) 1293-1307

5.1 RED closed loop with thermolytic salt

In the previous chapters, the performance of ammonium hydrogen carbonate in a SGPHE system with salt extraction strategy has been widely studied. Both main stages, the power production and the solutions regeneration, are taken into account. Two models were developed for the RED and the regeneration step, respectively, both validate by experimental tests performed with two lab test-rigs. A simplified scheme of the whole integrated system with ammonium hydrogen carbonate is depicted in Figure 5.1.

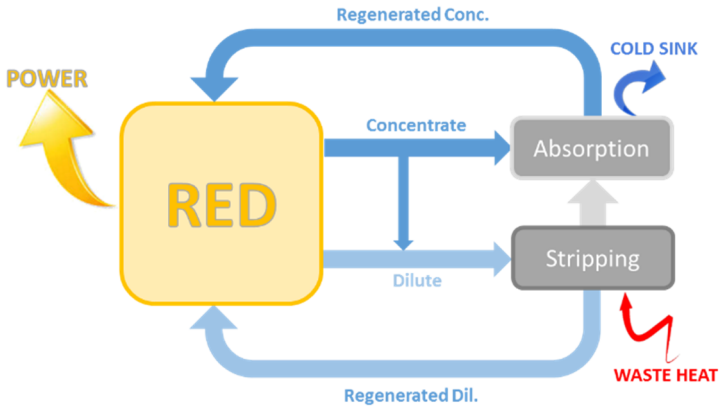

Figure 5.1: Simplified scheme of a SGPHE with salt extraction strategy and fed by thermolytic salts

The regeneration model described in the chapter 4 was used to calculate the specific duty required for the solutions regeneration at different condition. These values were elaborated and the obtained relations were added to the RED model in order to simulate the whole cycle. More details are reported in the following.

5.2 Theoretical analysis of ammonium hydrogen carbonate regeneration for the integrated simulation

Once the two solutions exit the RED system, a regeneration unit is needed to restore the initial salinity gradient. For the case of a water-ammonium bicarbonate solution, the regeneration implies (i) an air stripping column at about 60°C to separate the salt in the form of NH_3 and CO_2 from the diluted solution (ii) followed by an absorption column at environmental temperature (25°C) to let NH_3 and CO_2 to be again dissolved in the

concentrated solution. For the sake of the present work, only the air stripping column was modelled to evaluate the thermal power requirements thus allowing the efficiency of the whole cycle to be calculated. As a matter of fact, aim of the present section is that of providing a specific thermal duty to be used for the calculation of the cycle efficiency and, in this regard, the absorption column is not expected to provide any appreciable contribution.

The air stripping, along with a suitable thermal integration, to be investigated is depicted in Figure 5.2. The column is fed from the top with a NH_4HCO_3-water solution while hot saturated air is fed from the bottom. Note that air is saturated with water before entering the column to avoid sudden water evaporation at the entrance of the column, thus causing a dramatic temperature reduction and a negative impact on process performance. The high temperature and the counter-current contact between the two phases faster the salt degradation and the passage of NH_3 and CO_2 from the liquid to the gaseous phase. As a result, two outlet streams exit out from the column: i) a gaseous stream rich of NH_3 and CO_2 exiting from the top, which can be used in an absorption column to regenerate the concentrate solution from the RED unit; ii) a liquid stream exiting from the bottom, representing the "regenerated" dilute feed for the RED stage. The adopted thermal integration significantly reduces the total amount of thermal power needed to heat the two feeds column: this residual amount (i.e. $Q = Q_1 + Q_2$) represents the waste heat which is converted into electric power within the REDHE.

The system shown in Figure 5.2 was modelled by a suitable process simulation software (Aspen Plus®) which accounts for mass and energy balances, chemical and phase equilibria, as widely described in the previous chapter 4. In this section, it was exploited to carry out some specific simulations. All of these were performed at a fixed solution flow rate of 1 l/min (=0.06 m^3/h). All other inputs are reported below.

- Solution column inlet temperature: 60°C;
- Liquid minimum temperature approach for liquid-liquid heat exchanger: 2°C;
- Gas minimum temperature approach for air preheating heat exchanger: 5°C;
- Column pressure: 1 bar;
- Saturated air temperature: 60°C;
- Thermodynamic model: ENRTL-RK;
- Number of equilibrium stages: 30.

Note that the number of equilibrium stages was arbitrarily set equal to 30 as results were found to be only slightly affected by this parameter for a number higher than 20.

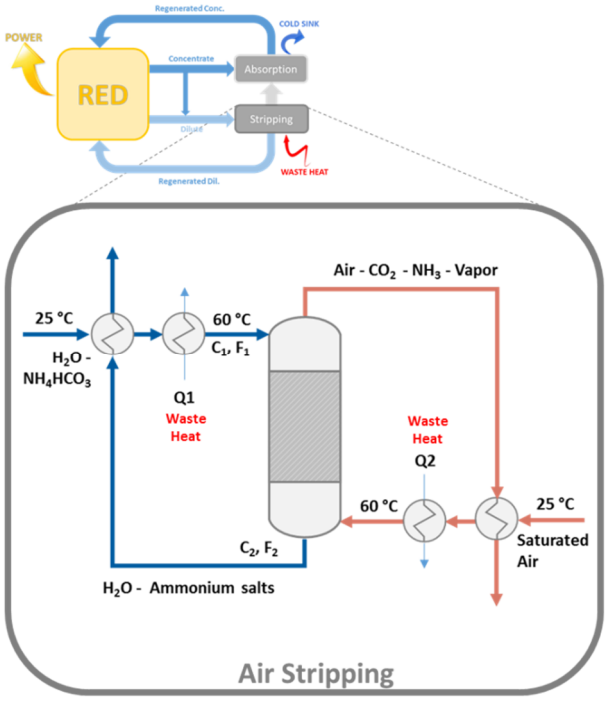

Figure 5.2: Schematic representation of a stripping column operating with hot saturated air for NH_4HCO_3 salt degradation and subsequent removal of NH_3 and CO_2 gases. A thermal integration layout is proposed for heat recovery and reduced thermal duty.

Clearly, the concentration of the feed solution C_1 and concentration of the liquid solution exiting the column C_2 should be defined to allow the software to calculate the air flow rate and the relevant process thermal duty. These two "software input" concentrations were considered as variable parameters in the parametric analysis reported in the next section.

5.2.1 Specific thermal duty assessment

For each value of C_1 and required column outlet value C_2, the process simulator calculates the saturated air flow rate (which is needed to close the mass and energy

balances) and the thermal power Q1 and Q2 required by the two heat exchangers. On the basis of this value and of the amount of salt stripped, a specific duty can be defined as regeneration performance indicator:

$$Specific\ duty\ = Q_{spec} = \frac{Q1+Q2}{F_1} \tag{5.1}$$

All the specific duties calculated, one per each couple C_1-C_2, are reported in Table 5.1. As it can be seen, the higher the difference between the inlet and the outlet concentration, the higher the specific duty.

Table 5.1: Specific thermal duty [kWh/m^3] as a function of stripping column inlet and outlet concentration [M].

Q_{spec}, Specific duty [kWh/m^3]		**C_1, Stripping column inlet concentration [mol/l]**											
		0.025	**0.05**	**0.075**	**0.1**	**0.15**	**0.2**	**0.35**	**0.56**	**0.92**	**1.28**	**1.64**	**2**
C_2, Stripping column outlet concentration [mol/l]	**0.005**	11.49	13.37	14.49	15.64	17.54	19.39	24.75	32.01	43.93	55.34	66.32	77.04
	0.024	-	9.77	12.05	13.68	16.15	18.29	23.98	31.41	43.42	54.90	65.95	76.64
	0.043	-	5.48	9.34	11.64	14.74	17.15	23.20	30.79	42.92	54.45	65.52	76.26
	0.062	-	-	6.13	9.43	13.24	15.96	22.39	30.16	42.42	54.07	65.11	75.87
	0.081	-	-	-	6.67	11.67	14.74	21.56	29.51	41.90	53.53	64.69	75.47
	0.1	-	-	-	-	9.88	13.41	20.66	28.90	41.37	53.05	64.22	75.05
	0.15	-	-	-	-	-	9.73	18.43	27.14	39.97	51.54	62.43	72.94
	0.2	-	-	-	-	-	-	16.03	25.32	38.49	50.21	61.21	71.73
	0.25	-	-	-	-	-	-	13.32	23.43	37.05	48.92	60.02	70.63
	0.3	-	-	-	-	-	-	10.68	21.44	35.40	47.91	59.47	70.56
	0.35	-	-	-	-	-	-	-	19.41	33.90	46.55	58.15	69.31
	0.4	-	-	-	-	-	-	-	17.23	32.30	45.58	56.71	67.95
	0.45	-	-	-	-	-	-	-	14.88	30.66	43.70	55.57	66.88
	0.5	-	-	-	-	-	-	-	-	29.00	42.14	54.14	65.53

The values reported in the table were converted into a suitable correlation providing the specific duty for each given couple of C_1-C_2:

$$Q_{spec} = a_1 \cdot e^{a_2 C_1} - a_3 \cdot {C_2}^{a_4} + a_5 \cdot {C_1}^{a_6} \cdot {C_2}^{a_7} \quad (5.2)$$

As shown in Table 5.2, the whole range of inlet concentration was divided into four smaller ranges, in order to guarantee the best agreement of the correlation with the data calculated by Aspen Plus®: the average error found by adopting the above step-wise correlation was about 1%.

Table 5.2: Parameters of equation (5.2) as a function of solution concentration entering into the stripping column

Concentration range	a_1	a_2	a_3	a_4	a_5	a_6	a_7
$0.025M \leq C_1 \leq 0.1M$	12.115	0.26	261.787	0.615	297.436	0.252	0.478
$0.1M < C_1 \leq 0.2M$	12.836	1.02	258.324	0.612	260	0.165	0.517
$0.2M < C_1 \leq 0.56M$	13.195	0.686	60.592	0.667	55.934	0.687	0.212
$0.56M < C_1 \leq 2M$	8.714	0.225	35.796	0.656	45.56	0.758	0.045

5.3 Sensitivity analysis of the closed loop system

In the previous sections, the RED and the regeneration unit have been separately investigated. The present section is devoted to the whole closed loop of the REDHE where the regeneration unit is represented by the stripping column only as schematically shown in Figure 5.3. The equations relevant to the RED unit and those proposed for the thermal duty of the regeneration unit were coupled to each other and with mass balances within a simplified integrated model devoted to calculating the cycle energetic efficiency defined as:

$$\eta_{corr} = \frac{Pd_{corr}}{Total\ thermal\ duty} = \frac{Pd_{corr}}{Q1+Q2} \quad (5.3)$$

A sensitivity analysis was performed to evaluate the effect of the solution concentrations entering the RED unit on the cycle performance. Moreover, the effect of a split-stream F_3 was also investigated. Note that F_3 can be written as:

$$F_3 = x \cdot \left(\frac{F_{low,in} \cdot C_{low,in}}{C_3}\right) \quad (5.4)$$

where "*x*" was fixed either at 0 or at 0.5. Clearly, the product $(F_{low,in} \cdot C_{low,in})$ must be equal or higher than $(F_3 \cdot C_3)$. Note that "x" values higher than 0.5 would provide a C_2 lower than 0.005M which is the value arbitrarily chosen as threshold in Table 5.1.

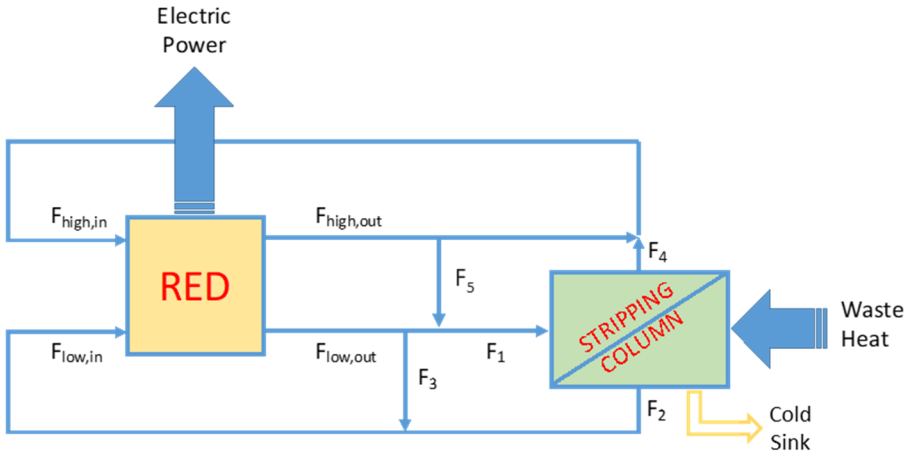

Figure 5.3: Scheme of RED closed loop system analysed for the sensitivity analysis

The influence of C_{high} and C_{low} on η_{corr} at the two "*x*" values of F_3 is reported in Figure 5.4, where the RED unit features are the same relevant to Figure 3.5.

By comparing Figure 5.4 with Figure 3.5, it can be observed that the cycle efficiency can be maximized at operative concentrations very similar to those maximizing the power density especially when F_3 is equal to zero. As F_3 increases, two competitive effects occur: on the one hand, a lower flow rate is fed to the regeneration unit; on the other hand, a higher C_1-C_2 difference is needed to regenerate the diluted solution thus leading to a larger specific thermal duty. Clearly, the power density produced by the RED unit is not affected by this "x" value. When "x" is equal to 0.5, the flow rate effect is prominent thus resulting into a lower thermal consumption (compared to $F_3 = 0$) and into a higher efficiency as it can be seen in Figure 5.4B.

Figure 5.4B also shows that with the tested Fujifilm membranes a maximum efficiency of about 1.2% can be achieved. This value should be compared with the maximum

theoretical Carnot efficiency which, under the same conditions (i.e. heat source at 60°C and cold sink at 25°C), is equal to 10.5%. Thus, the η_{corr} achieved corresponds to an exergetic efficiency (i.e. % of Carnot efficiency) of about 11.4%.

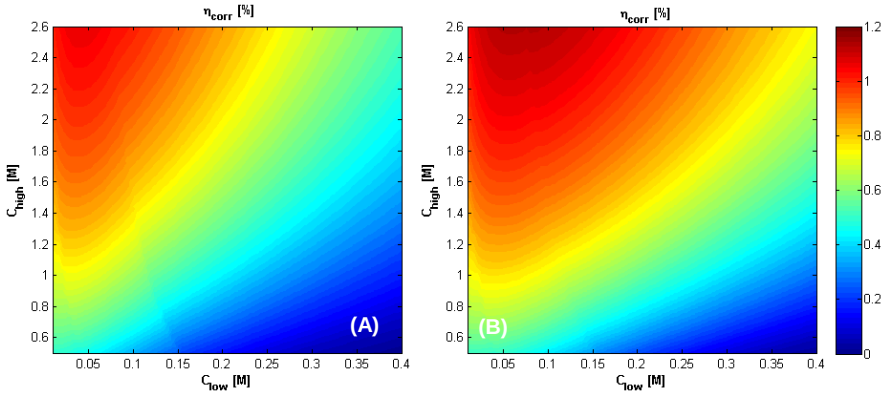

Figure 5.4: Red Closed Loop sensitivity analysis: influence of C_{high} vs C_{low} on the corrected efficiency at v_{high}=v_{low}=1cm/sec. RED stack (50x50 cm^2, 1000 cell pairs) equipped with Fujifilm membranes α_{CEM}=α_{AEM}=75.3%, R_{CEM}=R_{AEM}=2E-4(C_{low})$^{-0.236}$, 270 µm woven spacers, T = 298 K. A) F_3=0; B) $F_3 = 0.5 \cdot \left(\frac{F_{low,in} \cdot C_{low,in}}{C_3}\right)$.

The effect of solution velocity was also investigated: as expected on the basis of results of Figure 3.5B, the cycle efficiency was found very poorly dependent on v_{high}. Conversely, as a difference from Figure 3.5B, Figure 5.5 shows that smaller v_{low} are preferable when higher efficiencies are looked for. Higher residence times within the RED unit results into (i) lower flow rates and (ii) higher concentrations entering into the stripping column (i.e. higher specific thermal duty). As already mentioned while commenting Figure 5.4, the flow rate effect is prominent, thereby leading to lower thermal requirements and higher cycle efficiencies. For the same reason, as observed in Figure 5.4, the higher value of F_3 (i.e. x=0.5) provides better results, as expected.

Note that the sharp colour variations observable in Figure 5.5 derives from small discontinuities of the step-wise correlation proposed.

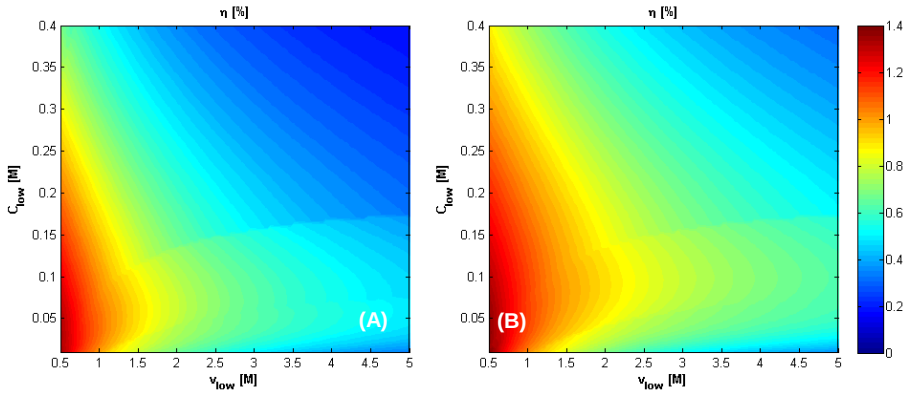

Figure 5.5: Red Closed Loop sensitivity analysis: influence of Clow vs vlow on the corrected efficiency at Chigh= 2.6M and vhigh=1cm/sec. RED stack (50x50 cm2, 1000 cell pairs) equipped with Fujifilm membranes αCEM=αAEM=75.3%, RCEM=RAEM=2E-4(Clow)-0.236, 270 μm woven spacers, T = 298 K. A) F3=0; B) $F_3 = 0.5 \cdot \left(\frac{F_{low,in} \cdot C_{low,in}}{C_3}\right)$.

The performance of a REDHE whose RED unit is equipped with tailored membranes for NH_4HCO_3-water solutions was also investigated: in particular, the same "enhanced" (α_{CEM}=α_{AEM}=90% and R_{CEM} and R_{AEM} equal to 1/5 of the value resulting from equation (3.20)) membranes adopted for the case of Figure 3.6 are here investigated. Relevant results are reported in Figure 5.6. As shown, also in this case the higher F_3, the better. Also, very low concentrations can be used in the dilute channel: in particular, the highest efficiency is achieved when C_{high} is in the range of 2.4M – 2.6M and C_{low} is lower than 0.04M (the value maximizing $P_{d,corr}$ according to [132]). Moreover, under these best operating conditions a doubled η_{corr} can be achieved corresponding to an exergetic efficiency of about 22%. Notably, when one looks at efficiency values at these very low temperature levels, it should be kept in mind that the waste heat employed is considered by industry as a burden rather than as a resource.

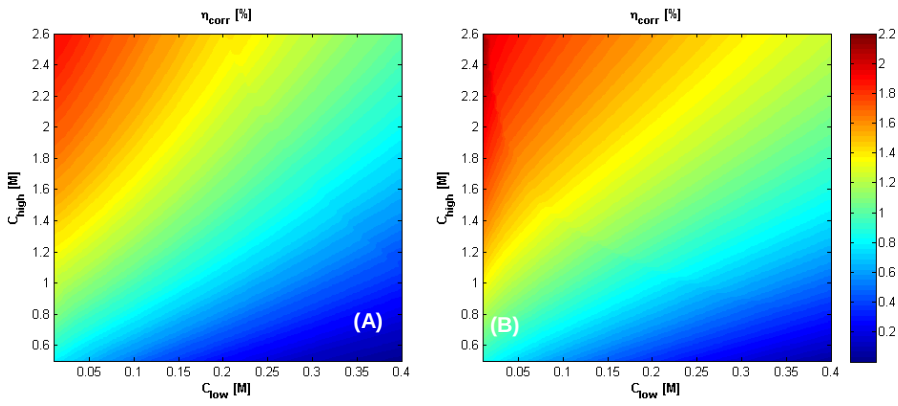

Figure 5.6: Red Closed Loop sensitivity analysis: influence of C_{high} vs C_{low} on the corrected efficiency at v_{high}=1cm/s and v_{low}=0.5 cm/sec. RED stack (50x50 cm^2, 1000 cell pairs) equipped with enhanced Fujifilm membranes $\alpha_{CEM}=\alpha_{AEM}$=90%, $R_{CEM}=R_{AEM}$=4E-5$(C_{low})^{-0.236}$, 270 μm woven spacers, T = 298 K. A) $F_3 = 0$; B) $F_3 = 0.5 \cdot \left(\frac{F_{low,in} \cdot C_{low,in}}{C_3}\right)$.

5.4 Integrated model conclusions and future remarks

The performance of a Reverse ElectroDialysis Heat Engine (REDHE) fed with ammonium bicarbonate – water solutions was investigated.

A simplified integrated model was developed encompassing two sub-models: the one for the RED unit and the other for the regeneration unit, reported in chapter 3 and chapter 4, respectively. The RED unit was modelled by a lumped parameter model which was validated against experimental data collected (see chapter 2). Once validated, the model was used for a sensitivity analysis aimed at recognizing the best operating conditions. According to this analysis, when enhanced yet feasible membranes are used, at $C_{high,in}$≈2.6M, $C_{low,in}$≈0.075M, v_{high}≈1cm/s and v_{low}≈5cm/s , a maximum power density of about 9 W/m^2 could be obtained. As far as the modelling of the regeneration unit is concerned, a process model based on the use of the process simulator Aspen Plus® was developed (see chapter 4) to model the stripping column along with suitable heat exchangers required by thermal integration. The model was used to calculate the regeneration step thermal duty which is required to heat up to 60°C the streams (i.e. saturated air stream and NH_4HCO_3-water liquid stream) entering the stripping column. Results showed that the specific thermal duty increases as the concentration difference

between the NH_4HCO_3-water solution entering the stripping column (i.e. C_1) and the one exiting (C_2) increases. A step-wise correlation was devised to account for this dependence.

Finally, the two models were coupled each other and with mass balances within a simplified integrated model which was used to find under which operating conditions the whole RED closed loop can perform better. Results show that the dilute solution concentration C_{low} maximizing the cycle efficiency slightly differ from that maximizing the electric power production, while the "optimal" dilute solution velocity v_{low} was found to be high for the power production and low for the cycle efficiency: in particular a C_{low} <0.04M and a v_{low} of about 0.5 cm/s resulted into the highest efficiency.

Under these conditions, a maximum exergetic efficiency of about 22% was found thus suggesting that Reverse ElectroDialysis Heat Engine (REDHE) with thermolytic salts could be a feasible way to convert unworthy waste heat at very low temperatures into valuable power. Note that, to the author knowledge, Salinity Gradient Power Heat Engines (SGPHE) is the only technology able to perform such conversion at these temperature levels.

On overall, the present work shows the energetic feasibility of the process, although the present analysis does not take into account some non-ideal phenomena in the RED unit, the absorption column in the regeneration unit and the overall pumping costs. As a future work, once all these aspects will be taken into account, an optimization study will be purposely performer to recognize the optimal operating conditions and the actual full potential of the heat engine.

Moreover, much effort should be still devoted to the SGPHE technology in general (including the ones with thermolytic salts) mainly aimed at identifying, among the many alternatives, the solvent-solute couple and the regeneration strategy able to maximizing the power production and the cycle efficiency.

CONCLUSION SECTION I

The present thesis is devoted to explore new methods to produce energy and minerals from waste sources, with focus on integrated cycles to "close the production loops". In particular, **Section I** was dedicated to the study of the Reverse Electrodialysis (RED) fed with artificial solutions that, after producing electrical energy, are regenerated by means of a thermal process. This is the idea of a Salinity Gradient Power Heat Engine (SGPHE), in which industrial waste heat is converted into electrical energy. A huge amount of waste heat is lost at low-medium temperature (40-100 °C), and this work has the purpose to exploit it in a RED closed loop (RED-CL) with higher efficiency than reported in literature. In order to bring up the knowledge on "RED Heat to Power" systems, the following activities were carried out:

(i) analysing theoretically and experimentally the performance of a RED unit operating with different salt solutions;

(ii) developing a simplified RED model with lumper parameters and validating it with experimental results;

(ii) developing a model for the regeneration of thermolytic salts with the process simulator Aspen Plus and validating it with experimental results;

(iv) integrating the two models for the study of the entire closed-loop process and performing sensitivity analysis focused on the enhancement of exergetic efficiency of the cycle.

(i) The Reverse Electrodialysis system was widely described showing the main properties of the Ion Exchange Membranes (IEMs). The experimental methodologies adopted for the performance analysis of different salts in a RED unit were reported. Both regeneration strategies, solvent extraction and salt extraction, were taken into account. Salts with good properties to theoretically maximize the RED output power were selected starting from literature works and two thermolytic salts able to be regenerated with waste heat at low temperature (40-60 °C).

Lithium bromide was chosen due to its high solubility and high activity coefficients for high concentrations. The power density measurements shown lower performance than sodium chloride considered as the reference salt, even if a concentration of 10 molar was adopted. Membranes properties with this salt were experimental measured showing good membrane resistance values, good membrane swelling value but poor permselectivity for

the anion exchange membrane (80% at 0.5 M LiBr). Ion liquids, salts at liquid phase already at 25 °C, were tested showing poor performance due to the high CEM membrane resistance (around 55 Ω cm^2).

Ammonium hydrogen carbonate and ammonium carbamate, two thermolytic salts, were tested with a lab-scale RED unit. The effect of different operative parameters on power output were analysed. Ammonium hydrogen carbonate resulted as the best thermolytic salt.

New ideas were presented such as the use a mixture of these two salts and the use of support salt in order to improve the power production. More than 60% higher power output can be obtained with this new ideas.

(ii) A simplified RED model with lumper parameters was developed and presented. Some simplified assumption have been made during the model formulation, neglecting some non-ideal phenomena. This model can simulate the operation with 41 salts including for the first time NH_4HCO_3-water solutions. The model was validated using experimental results of monovalent and bivalent salts. In particular, the model was tuned for the use of ammonium hydrogen carbonate. A good agreement was obtained between experimental and model values.

Finally, sensitivity analysis were carried out varying different parameters (i.e. inlet concentrations, solution flowrates and membrane properties) The best corrected power density was obtained with ammonium chloride (8 $W/m^2_{cell\ pair}$).

(iii) A regeneration model was developed using a process simulator (Aspen Plus®). In particular, the performance of hot air stripping (at 60 °C) was simulated. Starting from literature works, ENRTL-RK thermodynamic package was chosen to calculate the properties of ammonium hydroxide solutions. The main issues were the contemporary presence of liquid and gas phase and the electrolyte nature of the solutions.

An air stripping test-rig was designed, built and tested in order to investigate the performance of this device for the regeneration of NH_4HCO_3 solutions. Different operative conditions (i.e. solution concentrations, air flow rates and packing materials) were tested and the results, in terms of outlet solution conductivity and pH, were compared with the model predictions finding a good agreement.

(iv) An integrated model for ammonium hydrogen carbonate was developed merging the lumped RED model and the Air-stripping regeneration model. Specific thermal duty (kWh/m^3) were calculated as a function of air stripping inlet and outlet concentration. Different relations were extrapolated from these data and they were introduced in the simplified RED model in order to calculate the efficiency of the whole system. The model was used to perform a sensitivity analysis evaluating the impact of different operative conditions on the whole system efficiency.

An exergetic efficiency of about 11% was found using the currently available membranes but this value can increase up to 22% if future optimised membranes are used. These efficiency values suggest that Reverse ElectroDialysis Heat Engine (REDHE) with thermolytic salts could be a feasible way to convert waste heat at very low temperatures into valuable power.

SECTION II

MAGNESIUM RECOVERY FROM WASTE BRINE

Section Outline

6 THE SEAWATER INTEGRATED CYCLE

Abstract

The concept of "*circular economy*" is recently proposed as a new way of looking at the relationships between markets, customers and natural resources. In this context, a waste of a process can be used as a feed for another in order to obtain goods with added value.

In accordance with the circular economy concept, in this chapter, an integrated cycle to produce energy, minerals and fresh water from seawater is presented. Desalination plant, saltworks, magnesium hydroxide manufacturing and salinity gradient power processes are integrated each other to obtain products minimizing waste production.

Starting from seawater, fresh water and table salt are produced separately in a desalination plant and a saltworks, respectively. The two process can be integrated using the resulting brine from the desalination plant as feed in the saltworks process, thus resulting in an increase of salt production of about 30%. At the same time, saltworks produce a waste, a bittern reach of magnesium (from 30 to 45 g/l), which can be exploited to produce pure magnesium hydroxide with a reactive precipitation. The remaining exhausted brine, containing mainly monovalent salts (e.g. NaCl and KCl) can be used in a Reverse Electrodialysis unit to produce green-energy and a diluted solution to be disposed back into the sea, closing the loop.

In this chapter, the idea of the integrated cycle is widely described mainly focusing on the magnesium hydroxide production. State of art of technologies currently adopted for $Mg(OH)_2$ production from brine and market information are also reported.

6.1 Introduction on the seawater integrated cycle

In the last two centuries, after the industrial revolution, the difficulty in finding new sources of raw material has become a problem of growing importance. This PhD work, has identified new and unconventional sources of primary goods for human life (e.g. water, salt, energy, raw materials) and for a sustainable economic growth in the geographic areas where conventional resources are no longer sufficient to meet the demand. In particular, the idea is the valorization of seawater that can be considered as inexhaustible sources of goods. In this context, there are already industrial processes for the exploitation of seawater: desalination process for the production of freshwater from the sea; technologies using the sea to produce renewable energy in various forms; saltworks for the production of sea salt and industrial processes for the recovery of magnesium from seawater. However, it is possible to imagine a strong integration between all these processes by developing integrated production strategies of fundamental goods to minimize costs and reduce supply risk, which is now ranked among the criteria for assessing the level of criticality of a resource [145].

In the industrial world, there are often no interactions between the actors involved in the market sectors outlined above. But, an integrated approach might have an enormous potential, as demonstrated by recent literature studies on the re-use of brines from desalination plant to produce table salt and other minerals [6,146] and for the production of electricity with Salinity Gradient Power technologies [19,147].

In particular, focusing mainly on the possibility of "alternative mining" extraction, magnesium should be taken into account among minerals that can be extracted from seawater because of the high added value. It is present in large quantity in seawater and above all in brines generated in different industrial processes.

Recently, magnesium is counted among the twenty "critical raw materials" for Europe's economic and social development as shown in Figure 6.1 [145].

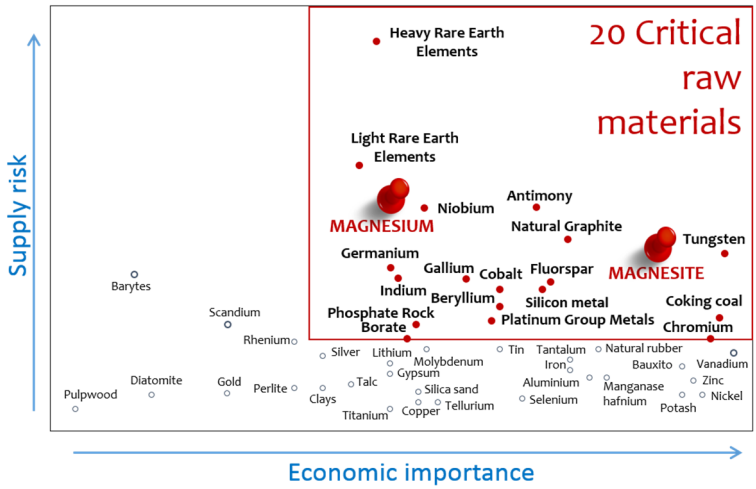

Figure 6.1: 20 critical raw material identified by European Commission according to economic importance and supply risk [145].

The worldwide magnesium production (in terms of equivalent magnesium oxide, MgO_{eq}) is about 12 Mt per year (2012), but only 14% is produced in Europe (Figure 6.2), this involves more imports to meet the increasing demand (Figure 6.3). Magnesium is today extracted mainly from mineral rocks (brucite and magnesite), although there are precipitation and/or crystallization processes of magnesium hydroxide from seawater and natural brine.

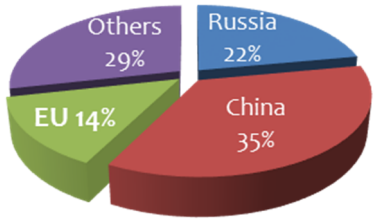

Figure 6.2: Worldwide production of equivalent magnesium oxide (2014).

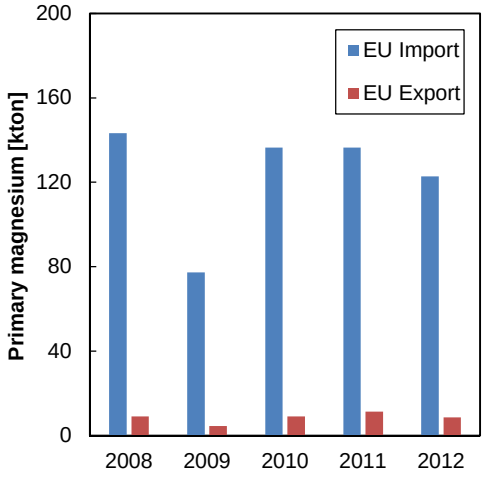

Figure 6.3: UE import and export trend [148]

However, recent studies have already demonstrated that brine from desalination plant and even better waste bitterns from saltworks, that normally are treated due to the environmental constraints imposed by the legislation, contain very large quantities of magnesium potentially recoverable with reactive precipitation processes [6,146].

The idea of integrated cycle studied in this PhD thesis is shown in Figure 6.4. It follows the concept of circular economy in which a waste process can become raw material of another process. The seawater can be used in a desalination process to produce fresh water, generating a brine as waste stream. This is considered today as an industrial waste stream that must be disposed in accordance with stringent environmental standards but in the proposed integrated cycle it can be used as saltwork inlet current, thus eliminating disposal costs for the desalination plant and increasing salt production of about 30% [6]. The salt produced can be used as table salt and/or industrial salt, or converted, through a re-crystallization step, in high purity NaCl, to be supplied to chemical companies as a high added value product. Exhausted saturated brine, from the final saltwork basins, can be used to feed a magnesium hydroxide reactive precipitation process. Finally, after the magnesium recovery, the remaining solution still saturated in NaCl, can be recirculated to the salt crystallizing basin to produce other sea salt, or further used to feed a Reverse electrodialysis unit which, also fed by sea or brackish water. The system is able to produce

electricity from the salinity difference between the two solutions, thereby helping to significantly reduce the energy required by the entire cycle.

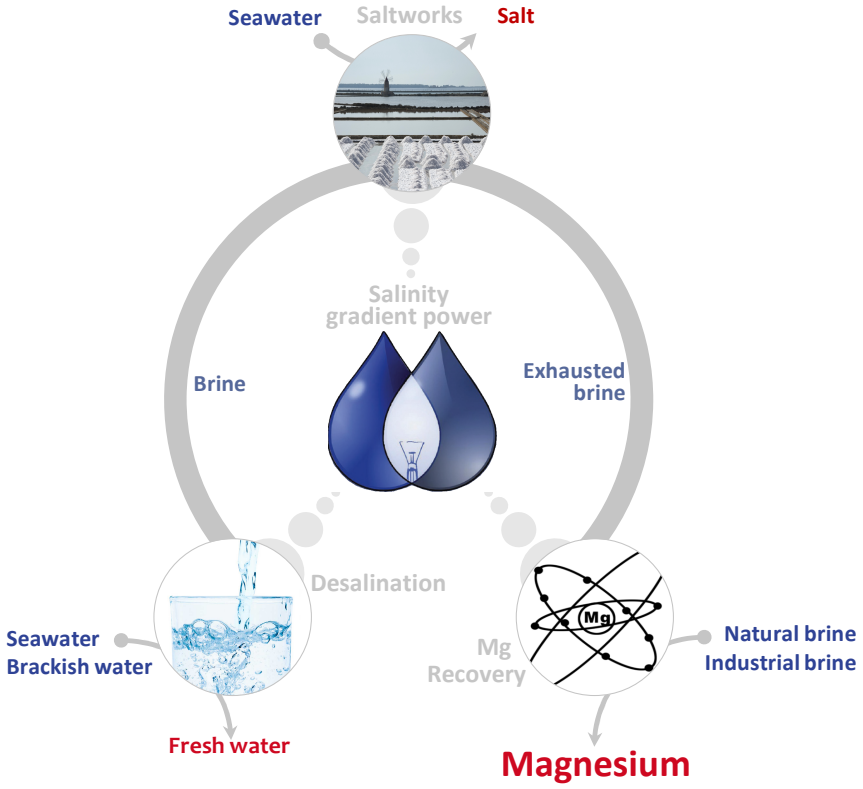

Figure 6.4: Integrated cycle scheme for the valorisation of resources from seawater.

However, the main objective of this thesis section is focused only on one step of the integrated cycle. New techniques are developing for the recovery of magnesium, in the hydroxide form, from waste brines. In particular, brines from saltworks are exploited even if all the devices and techniques presented can be applied also for industrial seawater brine that can be independent by the integrated cycle. The availability of natural and artificial brines from sea water is independent by the integrated cycle implementation and it can represent a resource with a “democratic” geographic distribution if compared with the mineral resource of magnesium.

All the tests were made using natural brines from saltworks in Trapani (Italy). In order to better understand the environment in which the brine is collected, the process adapted in a saltwork for the production of table salt, will be described in more details in the following paragraph.

6.2 The operating cycle of sea saltworks

The most ancient and basic method to obtain salt from saline water is by means of natural evaporation through the sun. Sea salt was already mentioned in a Buddhist scripture wrote in the mid-5th century BC [160] and today is still one of the main resource of salt. In a typical process, salt water is trapped in a proper ponding area, so the heat of the sun and the action of the wind evaporate the water reaching the maximum solubility of salt that arises its precipitation and harvest. The natural evaporation method has three main prerequisites:

- Geographical position close to a brine source (salted lakes, sea or other saline bodies);
- A predictable hot dry and/or windy climate;
- A flat area for the construction of saltworks.

For these reasons, normally the salt ponds are allocated in the coastal zones of countries and in a flat depression [149].

In a traditional saltwork cycle, a pre-evaporation pond is used for the organic material settling out. In this step, the salt concentration increases to around 6%, double of medium concentration in seawater. The brine is moved then to a concentration ponds where calcium and magnesium carbonate are precipitate together with gypsum. This first crystallization pond is commonly called pickle pans. When the salt content reaches 25%, the brine is moved to others large basins (often called maiden brine at this stage) where a fully evaporation is allowed. Pure salt (96 – 99 %) with thickness around 30-40 cm is harvested annually or every two years. Before the product is packaged and sold, the salt is washed with 25% sodium chloride brine. The residual brine is called bittern and may be returned to the salt water source [149].

In 2011, the world production of salt was around 290 Mt. Around 40% is produced by solar evaporation of seawater or inland brines and the remain amount is divided between rock salt (26%) and brines (34%) as reported in Figure 6.7.

More than 50% of the countries in the world have salt production facilities considering all the methods available for its production (e.g. artisanal evaporation works, advanced multi-stage evaporation in salt refines etc.). Salt has over 14,000 applications and it is the extensively used mineral after iron ore. Around 60% is consumed in the chemical industry, predominantly in the chloralkali products and synthetic soda ash. The remain part of the total production is utilized in road de-icing, human consumption and other uses including animal feedstuffs, water treatment and industrial applications [149].

As reported above, the bitterns in the sea saltworks are normally moved back to the sea but according to the idea of integrated cycle this can be further used as raw material in the magnesium hydroxide production. In order to assess this opportunity, bitterns from local saltworks are collected and exploited for all the tests performed in this PhD work. Specifically, the bittern is taken from saltworks allocated in Trapani, in the west coast of Sicily (Italy) that has all the peculiarity described above: close to sea in a flat region and with a dry/windy weather. Since the Roman times, sea salt is produced in Trapani [6] and in some of saltworks constructed there, that are natural protected area, the salt is still handmade harvested.

In order to described a typical sea saltwork cycle in Trapani, the Mariastella saltwork (in the western coast of Sicily) was chosen as example, reporting data from Cipollina et al. [6]. The concentration of salt is increasing from seawater condition (around 37 g/l) up to sodium chloride saturation concentration. The Mariastella layout is reported in Figure 6.5.

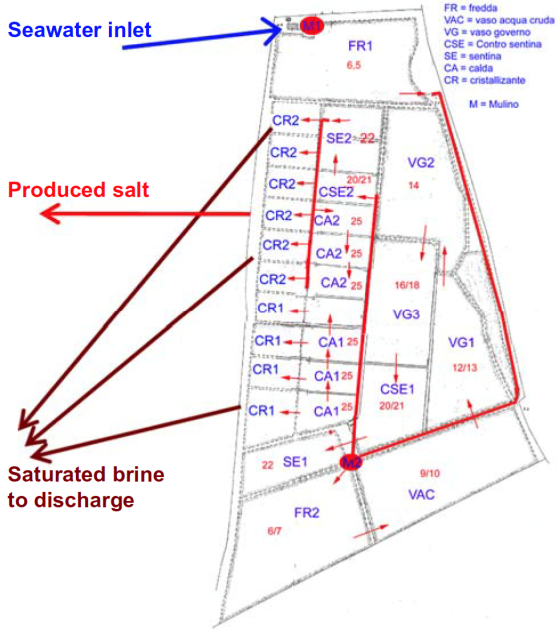

Figure 6.5: Traditional layout of Mariastella saltwork [6].

The water is moved in four orders of ponds subdivided in accordance of defined density range. All the data following reported are related to Maristella saltwork [6]:

- First order, commonly called “cold ponds” with a density range from 3.5Bè to 5-6Bè. The surface is around 20-25% of the total saltwork area with a depth of 50-100 cm. Represented in Figure 6.5 as FR1 and FR2.
- Second order, called “driving ponds” with a density range from 5–6Be` to 10–12Bè. Also in this case, the surface occupied by these ponds is around 20-25% of total area with a depth always lower than 50 cm. They are represented in Figure 6.5 as VAC, VG1, VG2 and VG3.
- Third order, so-called “hot ponds”, in which the brine from the driving ponds reaches the sodium chloride saturation condition (25.7 Bè). Many small ponds are used for this purpose and the numbers depends on the saltwork design and dimension. These ponds cover around 40-45% of the total surface with depth power than 40cm. Each sequence of hot ponds feeds one or more

the crystallization ponds, the fourth and last orders. They are represented in Figure 6.5 as CSE1, CSE2, SE1, SE2, CA1and CA2.

- Fourth order are the crystallization ponds (CR1, CR2) that commonly covered only 15% of total saltwork surface. The ponds are very shallow with a depth lower than 25 cm. During the hot season, the crust (around 10 cm) is broken and the salt is harvested once or twice per year.

All the saline solutions are moved by gravity or by means of pumps with low prevalence. The four steps described above can be considered as a “fractional crystallization”, in which step by step the salts present in the inlet seawater precipitate. “Fractional” term is used because the solubility of the salts dissolved in water are different, this can allow the precipitation of mainly calcium in the first basins and forded sodium chloride at high purity (97 -99%). The final bitter is very reach in magnesium, because it forms salts with high solubility, with a poor concentration of potassium, calcium and a saturation of sodium. The trend can be observed in Figure 6.6.

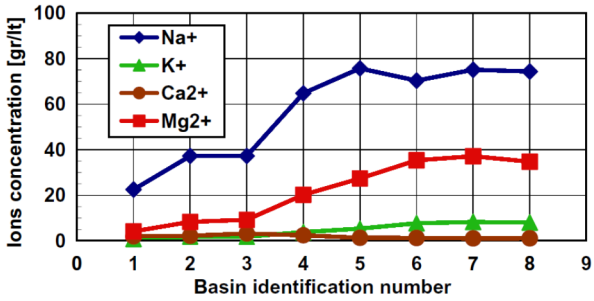

Figure 6.6: Trend of cations concentration (g/l) along Mariastella basins. [6].

In 2012, Cipollina et al. [6] demonstrated the real implementation of the first three steps of the integrated cycle proposed in this work. The waste brine from a MED-TVC plant was used to feed Mariastella saltwork, the closest traditional salt production site. In 4-year experience, they demonstrated the feasibility of the process obtaining 30% of production increasing. Moreover, some preliminary tests were performed at laboratory scale in order to prove the recovery of magnesium from waste bittern. High-purity magnesium hydroxide with high precipitation efficiency was obtained.

Starting from this preliminary results, in this PhD work was made an experimental campaign in order to study two continuous reactors for the recovery of magnesium hydroxide from waste saline brines: a multiple feed plug flow reactor (MF-PFR) and a patented ionic exchange membrane crystallizer (CrIEM).

In the following paragraphs are reported more details on magnesium hydroxide market and the main way to produce it, in order to highlight the importance of this salts in several sectors and the necessity to find alternative sources for the production, especially in Europe.

6.3 Market of integrated cycle products

The application of the integrated cycle for the enhancement of sea water involves the reference to different markets such as water, table or industrial salt and magnesium. In the following subparagraph, market details are reported for fresh water and salt while more details are described on magnesium hydroxide market and applications.

6.3.1 Fresh water and salt market

The desalination market is growing very fast: the Mediterranean region is one of the regions where this growth is happening faster. Spain, for example, is the largest user of desalination plants throughout the western world, while Malta assigns 57% of its water needs, to desalination. Moreover, desalination plants are starting to appear not only in the regions commonly called "arid": for example, the London-based company Thames Water, which supplies water to the city, built the region's first desalination plant. The capacity of desalination plants in the word is currently estimated to be around 100 million m^3/day, with a turnover of about 15 billion dollars per year. It is expected that the desalination industry will continue to grow very fast.

The only possible limiting factors are currently (i) the disposal of the brines and (ii) the energy demands, aspects that are both effectively solved by the idea of the integrated cycle and are a useful strength for a future idea implementation.

The position of the saltworks, an integral part of proposed system, is located by definition in arid, coastal and dry areas, ideal environments for the installation of desalination plants as they have easy access to sea water and often they face problems of lack freshwater.

As concerning the salt (NaCl), 40% of it in the world is produced by solar evaporation of sea water or internal salt basins. The remain used salt, is produced from mine rocks (26%) or from brines extracted from mine waters (34%) [149] as shown in Figure 6.6

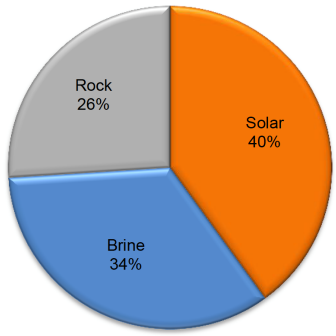

Figure 6.7: World production of salt by type in 2012 [149].

The salt used in the chemical industry covers 60% of the global market, the salt from the salt spreaders in the frozen road surface is 13-18%, while the remaining 10% is represented by the food sector (direct consumption and food processing).

Overall consumption of salt in 2013 was estimated at around 288 million tonnes, up from 277 million tonnes in 2012. It is, indeed, a trend that is expected to grow. The growth in global demand has been estimated to be about 2-3% per year as the increased salt consumption in developing countries should compensate for the reduction in per-capita consumption in the most industrialized countries for reasons related to the human health [149].

Moreover, it is expected a 70% increase in the salt requirements deriving from the chemical sector from today to 2018. Annual growth of about 4.3% is expected in the world production of chloroalkali which will increase the salt demand by about 30 million tonnes in that period, while a further increase in demand of almost 12 million tons will come from the production of caustic soda powder for which an increase of about 3.5% per year is expected. Future trends in the demand for salt for the food market are obviously linked to population growth and per-capita consumption levels.

At the same time, the production of salt also has increased by about 2.2% per year since 2000, reaching 287 million tonnes in 2013.

Regarding the production segmentation, it turns out that Asia is the leading producer of salt by covering alone 35% of world production, while 24% (about 66 million tons in 2012) is covered by the European Union countries. Among the countries of the Union stand out 7 countries (Germany, Russia, the Netherlands, the United Kingdom, Ukraine and Poland) each of which produced more than 4 million tons in 2012 and that together produce 71% of the salt of European origin.

Of all this salt production, only 7% is of marine origin, produced along the coasts of France, Greece, Italy, Portugal and Spain and the salt lakes present in Russia and Ukraine [149].

Market trend for fresh water and table salt

The balance between water demand and availability has reached a critical level in many areas of the world. This is the result of excessive resource exploitation and prolonged periods of low rainfall or drought combined with an ever-increasing demand. In 2015 the World Economic Forum in Davos classified water as the current number one threat for the society.

The water crisis has led to a rapid growth of desalination market, mainly involving the regions of the Mediterranean area but in recent years also cities not considered as arid as London.

The production capacity of desalination plants worldwide is currently estimated at around 92 million m^3 per day (Figure 6.8), which represents a 10-fold increase over the last 30 years: in fact, the capacity in 1986 was less than 10 millions of m^3 per day [150]. The annual sector turnover is estimated around 12.8 billion dollars/year and is expected to increase around 19.9 billion dollars/year in 2020 [151]. The graph below shows the installed capacity growth of desalination plants from 2000 up to now and the forecasts growth for the next 15 years. The only factors that can slow down this growth are related to the excessive energy consumption and brine disposal, problems that are solved by the application of the integrated cycle proposed in this work.

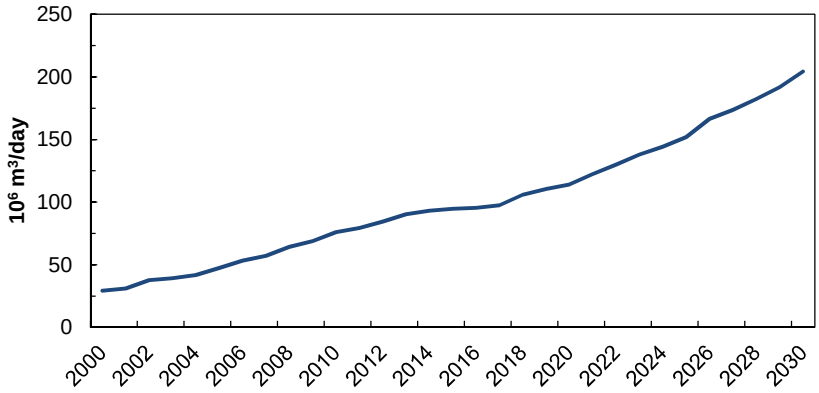

Figure 6.8: Cumulative capacity of installed desalination plants from 2000 till 2015 and forecasts for the next 15 years [151]

The cost for water desalination widely varies and depends substantially on certain parameters such as the technology, the cost of energy, the scale of the desalination plant and the composition of the feed water. The costs range is from 0.50 to over 10 $/m^3, but today the cost of fresh water produced by efficient large plants operating under normal conditions is converging to a value lower than 1 $ per m^3 of desalinated water [152].

On the other hand, the price paid for water by end users is often defined at the municipal level and it depends on many factors, including social and political aspects. As a result of this, the world variations, but also between the municipalities within the same country can be very large, as shown in the following figure (Figure 6.9).

Even if the situation should be analysed case by case, from Figure 6.8 and Figure 6.9, it can be stated that the production of desalinated water will increase in the future, opening new possibility to apply the integrated cycle concept.

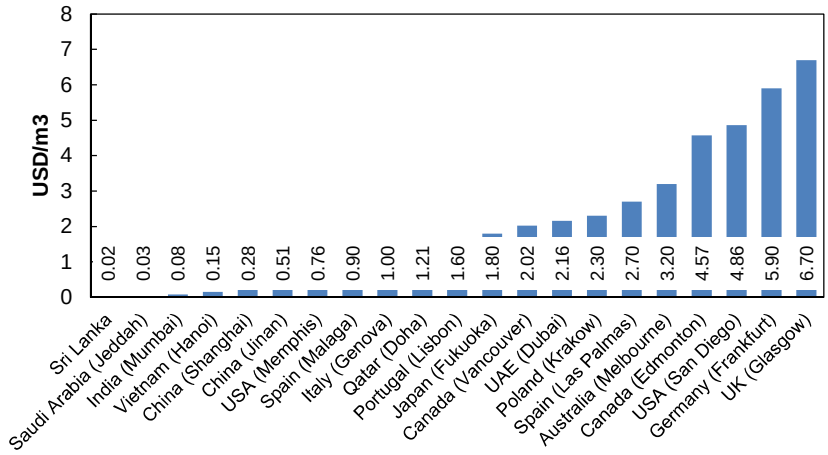

Figure 6.9: Price for municipal water (USD/m^3) that includes the fixed cost for water and wastewater, the variable cost of water and wastewater and the sales tax [153].

For the second stage of the integrated cycle, the table/industrial salt, the price varies depending by the production methodology as can easily be seen in Figure 6.10. Salt-in-brine usually holds the lowest price because mining and processing are minimal. On the contrary, the salt obtained by vacuum evaporation is usually by far the most expensive due to the high energy consumption and the high product purity.

Observing the price trends shown in Figure 6.10, it can be noted that the salt price remains essentially constant except in the case of the evaporative process due to the costs related to energy consumption.

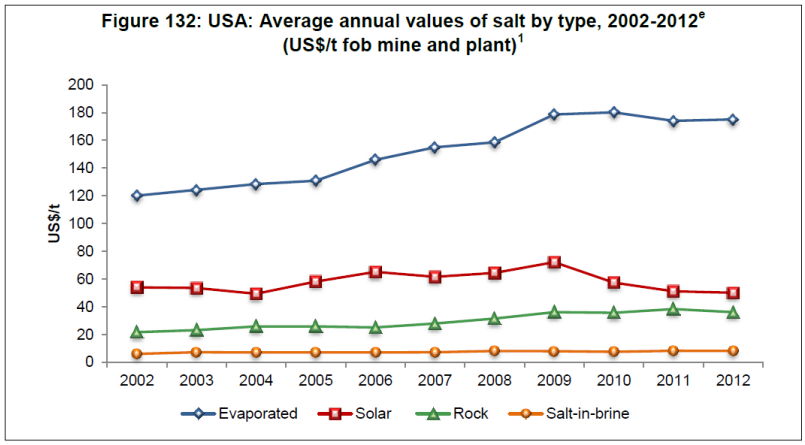

Figure 6.10: Trend annuale del prezzo medio del sale (NaCl) dal 2002 al 2012 al variare del processo di produzione (Source: Roskill, 2016)

6.3.2 Magnesium hydroxide market

Magnesium hydroxide is marketed globally for its numerous high value-added applications. The global consumption of this product has increased by around 13% from 2009 to 2013. Its main applications include its use (i) in environmental protection as agent for desulphurisation and for water treatment, (ii) in the field of flame retardants, (iii) in the pharmaceutical field and (iv) in other minor applications. The relationships between each of these applications are different from zone to zone, in particular, as shown in figure 3.1, in Europe most of the sales of magnesium hydroxide in 2015 concerned the field of environmental protection followed by that of flame retardants.

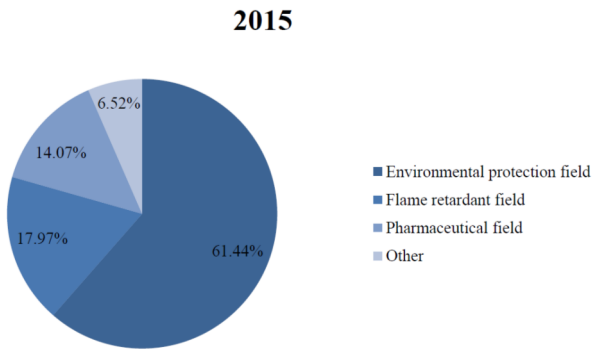

Figure 6.11: The main applications (based on sales) of magnesium hydroxide in Europe in 2015 [154]

The demand for magnesium hydroxide in Europe reached 128 thousand tons in 2015 and it is expected to grow with a CAGR (i.e. Compound Annual Growth Rate) of 2.62% from 2016 to 2021 [154] (see Figure 3.2).

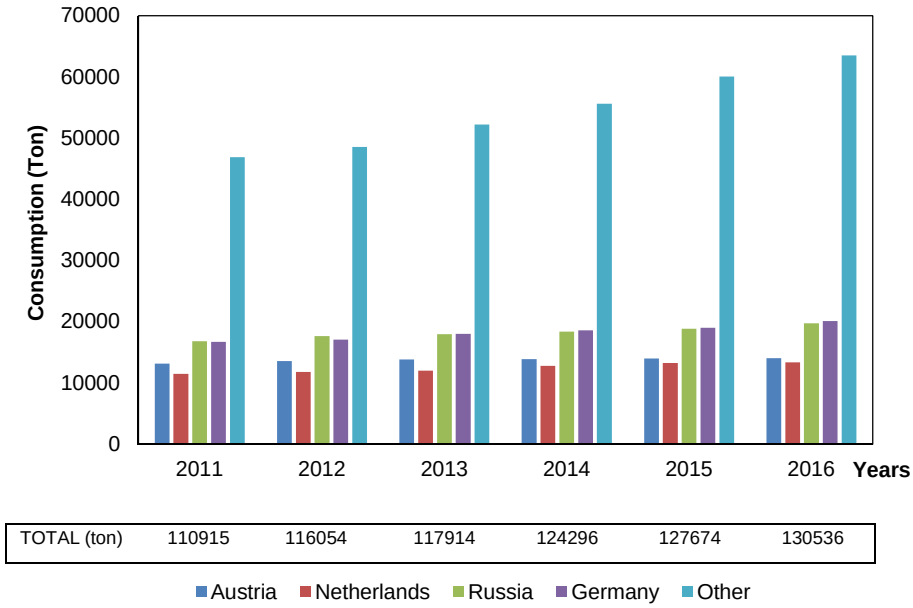

Figure 6.12: Magnesium hydroxide consumption per country in Europe in the period 2011-2016 [154]

On the other hand, on the supply side, there are seven large companies producing magnesium hydroxide that together have a production capacity of about 109 thousand tons (see Table 6.1) which covers about 85% of the European Union's needs. Obviously, this estimate is based on the assumption that all the magnesium hydroxide produced in Europe is sold within the Union. The European Union is therefore forced to import a quantity of magnesium hydroxide which is ≥15% of its needs (= 15% if the assumption was valid). There is, therefore, a part of the market that can be attacked and therefore a good margin for the insertion of a new manufacturing company already within the European market. It should also be noted that some of the companies that produce in Europe are owned by foreign stakeholders, determining a greater supply risk for the European market.

It is estimated that the European magnesium hydroxide industry has reached a revenue of about 214 million dollars in 2015, which is expected to grow with a CAGR of 1.07% from 2016 to 2021.

As far as the global magnesium hydroxide market, a growth in demand of 4.6% was expected in 2016, corresponding to a total production of about 943 thousand tons. The magnesium hydroxide market was valued at about $ 551 billion in 2015. It is also expected an increase in the consumption of magnesium hydroxide especially in the field of environmental protection, which is seen as the main promoter for the growth of the whole market. Indeed, in countries with an emerging economy, attention is also growing towards environmental problems linked to human activity. The increasing investment in the treatment of both urban and industrial wastewater in the field of oil & gas companies, in the chemical industries, and in power plants should represent a further boost to the growth of the global market.

Table 6.1: Production of magnesium hydroxide (Ton) of the main European industries in the sector in 2015 [154]

	Main European Industries in Europe	**Magnesium Hydroxide Production in Europe (Ton) in 2015**
1	Russian Mining Chemical	25000
2	RHI	24000
3	J.M. Huber	20000
4	Nabaltec	20000
5	Kisuma Chemicals	12000
6	Nedmag	6000
7	Kaustik	2000

It is worth noting that also the application field of flame retardants leaves space for enormous growth opportunities. In fact, users of halogenated flame retardants are facing the increasing criticisms that push them to move towards more reliable alternative retardants such as those based on magnesium hydroxide. This market segment involving the application of magnesium hydroxide in flame retardants showed a 4.4% growth in 2016. The North American region dominates the global magnesium hydroxide market for flame retardants followed by Europe and Asia -Pacifica. The main industries producing precipitated magnesium hydroxide are found in North America (USA and Mexico), Israel, Western Europe, China and Japan.

The market of magnesium main compounds

Magnesium hydroxide can also be sold as an intermediate for the production of other magnesium compounds such as magnesium metal and magnesium oxide. Therefore, it was considered appropriate to refer also to the magnesium metal market and to that of all magnesium compounds in their entirety.

The following graph shows the worldwide distribution of metallic magnesium consumption. It is noted that China, in addition to being the world's largest producer of magnesium, also appears to be the main consumer, following by Europe and the United States. Analysts predict that global magnesium consumption will increase by 7.7% a year until 2019.

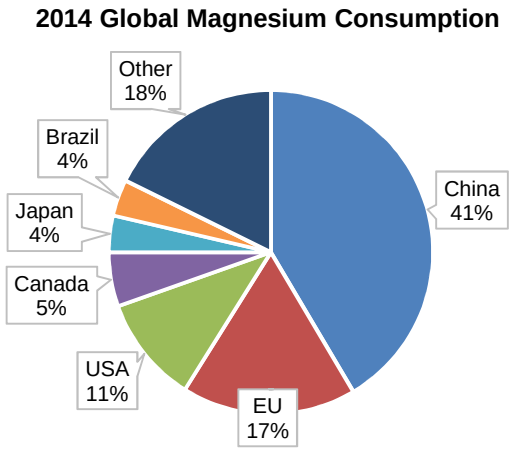

Figure 6.13: Worldwide distribution of Magnesium metal consumption in 2014

The table below shows imports and exports of magnesium over the last few years. This information is useful to understand which countries are in greatest need of magnesium and which are able to produce in such quantities that they can be exported.

Table 6.2: Magnesium import-export in the world in the period 2008-2014 [154]

	Export (kton per year)						
	2008	**2009**	**2010**	**2011**	**2012**	**2013**	**2014**
China	396.6	233.5	384	400.1	371.1	411.1	
Germany	35,2	21,2	26	26.4	27.7	32	
Israel	41	20,8	23,1	26,8	19,3	27,8	
USA	15,8	22,3	17,9	13,4	20	18,6	18
Netherlands	5,2	4,9	10	10,7	12,7	14,6	
Austria	51,9	35,8	49,7	32,3	22,7	14,3	
Canada	30,1	16	13	14,2	13,1	10,6	
	Import (kton per year)						
Germany	65,7	36,5	50,2	53,2	56,1	58,6	
Canada	52,4	26,1	47,1	47,9	52,1	50,6	
USA	86,7	47,8	52,7	48,8	52,3	46,1	55
Japan	45,9	28,4	40,5	42	38,4	33,8	
North Korea	17,7	17	18,4	21	22,8	27,2	
Austria	24,7	12	20,2	18,5	18,1	18,5	
Great Britain	13,1	10,8	18,3	16,7	15,7	15,8	
Mexico	11,2	6,7	8,4	11,7	13,6	15,8	
France	17,4	10,2	12,7	14,1	14,4	15,4	

For quantitative analysis, concerning the market of magnesium compounds (including hydroxide, magnesium oxide, magnesium metal, etc.), it is used to refer to the equivalent magnesium oxide thus to include in a single voice all the compounds. The following table [USGS] shows the world production of magnesium compounds in equivalent magnesium oxide in 2014.

Table 6.3: World production of equivalent magnesium oxide in 2014 in [154]

	Magnesite		**Seawater or brines**		
Country	**Caustic-Calcined**	**Dead-Burned**	**Caustic-Calcined**	**Dead-Burned**	**Tot**
Australia	218	110			328
Austria	76	325			401
Brazil	96	380	12		488
Canada	100				100
China	**1440**	**2740**			4180
France			30		30
Greece	90	110			200
India	20	202			222
Iran	25	40			65
Ireland				90	90
Israel			10	60	70
Italy	25				25
Japan			**50**	**70**	120
Jordan			10	50	60
North Korea	25	100			125
Republic of Korea				40	40
Mexico			15	95	110
Netherlands			**10**	**205**	215
Norway			30		30
Poland		10			10
Russia	**380**	**2500**			2880
Saudi Arabia	39	32			71
Serbia		35			35
Slovakia		465			465
South Africa	12				12
Spain	150	70			220
Turkey	**106**	**544**			650
Ukraine		170	20	80	270
United States	140		**191**	**195**	526
Total	2940	7730	378	885	12000

As can easily be deduced from the table, magnesium may have a mineral origin or be obtained from sea water and natural brines by precipitation processes. Magnesium of mineral origin generally has a lower purity than that one produced chemically which often does not correspond with higher added value applications such as flame retardants. It is worth noting that today the magnesium compounds of mineral origin are the most

produced: the production of magnesium compounds from mineral corresponds to 89% of the world production of magnesium hydroxide, while only the remaining 11% derives from processes recovery from brine/sea water.

Table 6.3 shows that China, Turkey and Russia cover about 84% of the world production of equivalent MgO: of this 84%, 67% is produced by China alone. Japan, the Netherlands and the United States together cover the 57% of the world production of MgO equivalent from brine/sea water. Note that none of the considered countries produces magnesium from saline brines, in fact the brines referred to in Table 6.3 are natural brines that determine obvious geographical-logistical limitations for the distribution of the product.

Magnesium hydroxide market segmentation on the productive process base

The main classification that generally occurs on the magnesium hydroxide product and on the relative market depends on the type of production process: certainly, each company has some peculiarities even with the same production process. However, the general process scheme, and therefore the corresponding market, can be distinguished in two macro-segments:

- Physical process;
- Chemical process.

As can be seen from the next pie chart, the physical process market segment is the largest in terms of produced and sold tonnes.

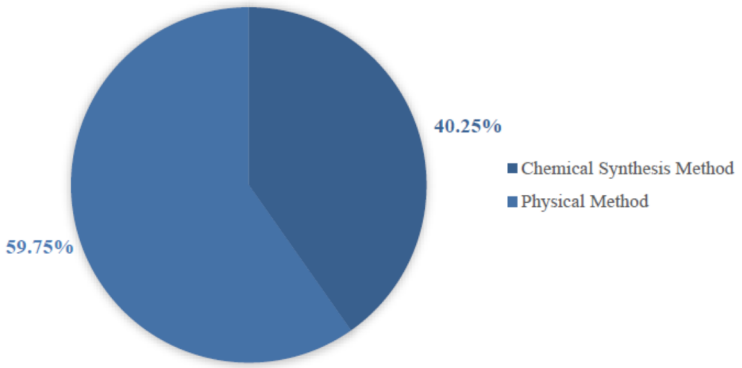

Figure 6.14: Magnesium hydroxide market segmentation on the production process base

Nevertheless, from a rapid analysis of the successive tables, it can be noticed that magnesium hydroxide obtained chemically has higher added value and consequently the segment relating to this product is more profitable.

Table 6.4: Profitability of the European market segments divided according to the production process [154]

Table Price (USD/Tonne) of Magnesium Hydroxide by Types 2011-2016						
Price(USD/Tonne)	2011	2012	2013	2014	2015	2016
Chemical Synthesis Method	2533	2454	2387	2322	2271	2201
Physical Method	1347	1305	1239	1286	1276	1204
Average	1870	1812	1762	1714	1677	1625
Table Cost (USD/Tonne) of Magnesium Hydroxide by Types 2011-2016						
Cost(USD/Tonne)	2011	2012	2013	2014	2015	2016
Chemical Synthesis Method	1628	1592	1555	1520	1497	1459
Physical Method	938	915	873	905	902	857
Average	1258	1228	1199	1171	1153	1123
Table Gross (USD/Tonne) of Magnesium Hydroxide by Types 2011-2016						
Gross(USD/Tonne)	2011	2012	2013	2014	2015	2016
Chemical Synthesis Method	905	862	832	802	774	742
Physical Method	409	390	365	381	374	347
Average	612	583	563	542	524	502
Table Gross Margin of Magnesium Hydroxide by Types 2011-2016						
Gross Margin	2011	2012	2013	2014	2015	2016
Chemical Synthesis Method	35.73%	35.14%	34.87%	34.53%	34.10%	33.70%
Physical Method	30.37%	29.88%	29.50%	29.60%	29.32%	28.82%
Average	32.73%	32.20%	31.95%	31.64%	31.25%	30.88%

The physical production process of magnesium hydroxide starts from mineral raw materials such as brucite and magnesite.

Without going too much into the technical details, the following figure shows in a block diagram the most salient aspects of the physical production process. It starts from the recovery of the mining rock by controlled explosions and mining. The collected material is transported to the plant where it is crushed in a small size. The produced matter is transported by means of a conveyor belt to the separation unit in order to separate the materials from the impurities. Once the separation has been completed, the product can be sale as mineral magnesium hydroxide or is further crushing and screening to achieve the market required specifications.

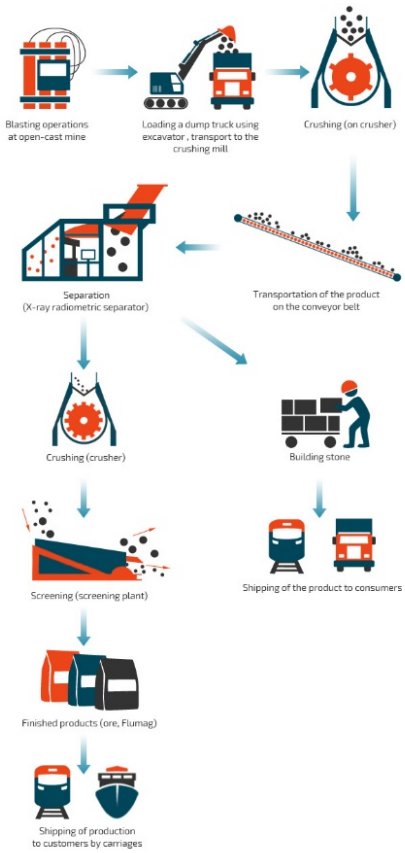

Figure 6.15: Block diagram of physical magnesium hydroxide production process

The chemical process, on the other hand, usually starts from raw material from sea water or much less frequently natural brine. Unlike the previous case, this production process involves a chemical reaction as can easily be seen from the diagram below (Figure 6.16).

Alkaline reactant is used generally in the chemical reaction forming magnesium hydroxide that is poorly soluble in water. The product precipitates (*precipitated magnesium hydroxide*) creating a slurry which is further filtered to reduce the water content. The slurry once depleted in water can be sold in this form or undergo a subsequent drying process and sold in powder form.

In the pharmaceutical field, another crystallization step is commonly expected (*crystallized magnesium hydroxide*) in order to increase its level of purity and the granulometric characteristics.

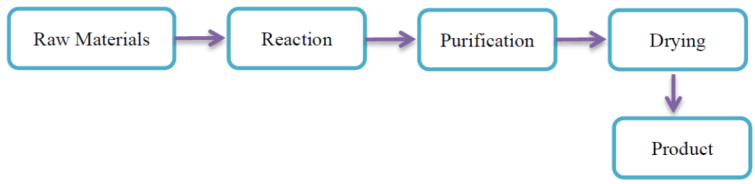

Figure 6.16: Block diagram of magnesium hydroxide production by chemical method

Magnesium hydroxide market segmentation on the application base

As already mentioned before, magnesium hydroxide is mainly used in the following field:

- environmental protection field: waste water treating and gas desulphurisation
- flame retardant
- pharmaceutical use

In the environmental protection field, the reference market is subdivided into the one related to wastewater treatment and the one related to the neutralization of acid gases. In the treatment of wastewater, the main use of magnesium hydroxide is pH control, acid neutralization and removal of heavy metals through precipitation. The customers are all those industries that have to treat industrial wastewater and even municipal wastewater treatment plants. Considering the high number of this type of plants in Italy and in the

world, this market sector is flourishing and growing. Furthermore, magnesium hydroxide is replacing more and more sodium hydroxide (sodium hydroxide) and lime (calcium hydroxide) as neutralizing agent. For this use, a magnesium hydroxide with not high purity can be sufficient considered, obviously according to the specific purpose. Therefore, it is a market slice that extensive use a mineral magnesium hydroxide, intrinsically less pure and with less controlled particle size than precipitated one.

In the flame retardants field, the main consumers of magnesium hydroxide are manufacturers of polymeric materials for construction, electrical cables and sheaths. Magnesium hydroxide is added to the polymer matrix to reduce the flammability of the final product.

Unlike what is mentioned before for waste water treatment, the field of flame retardants involves the use of a higher purity magnesium hydroxide. The presence of metal impurities could alter the final properties of the polymer and it is not recommended. Therefore, for this applications is often required a precipitated magnesium hydroxide, i.e. from sea water or natural chemical brine and not from mineral. This compound is in fact much purer and has a particle size distribution more suitable for the purpose.

In the pharmaceutical field, magnesium hydroxide is mainly used as a laxative or antacid, although recently there are niche applications related to the consumption of supplements. The pharmaceutical field requires the use of precipitated magnesium hydroxide because it guarantees high purity and fairly controlled particle size. In some cases, a very precise particle size (e.g. very narrow particle size distribution and very small particle size) is required that can be obtained by subjecting the precipitated magnesium hydroxide to a further crystallization step.

The price trend of magnesium hydroxide over the last 5 years based on the market segmentation is shown in Figure 6.17 [154]. In all cases, the trend decreases very slowly, without strong fluctuations. However, despite this decreasing trend, the analysts expect a raisin in the 2017 [154].

Furthermore, Figure 6.17 shows how the price is quite different according to the use field. In particular, the highest price is recorded in the field of flame retardants, then the pharmaceutical sector and finally the environmental protection sector. In light of this scenario, companies tend to produce magnesium hydroxide with characteristics suitable for the flame retardants production or for drugs even if the required quantities are lower in these areas.

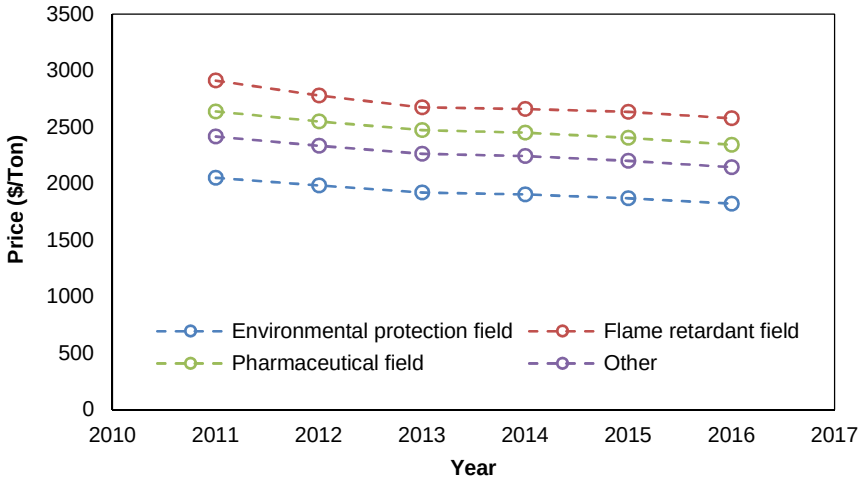

Figure 6.17: European magnesium hydroxide price trend in the period 2011-2016 for the main application fields [154].

The price trend, shown in Figure 6.17 is also confirmed by the magnesium hydroxide sale price on the production process base, shown in Figure 6.18, because the precipitated and crystalized products are used for the flame retardant and pharmaceutical fields. The values derive from an average of magnesium hydroxide prices of the same type sold by different companies. From Figure 6.18 can be observed how the value of mineral magnesium hydroxide is the lowest, indeed it is lower than thousand dollars per ton. On the contrary, the average value of the precipitated magnesium hydroxide is quite high because the chemical reaction requires the consumption of an alkaline reagent. Furthermore, as expected, the average price of the crystallized magnesium hydroxide obtained is higher than the precipitated magnesium hydroxide.

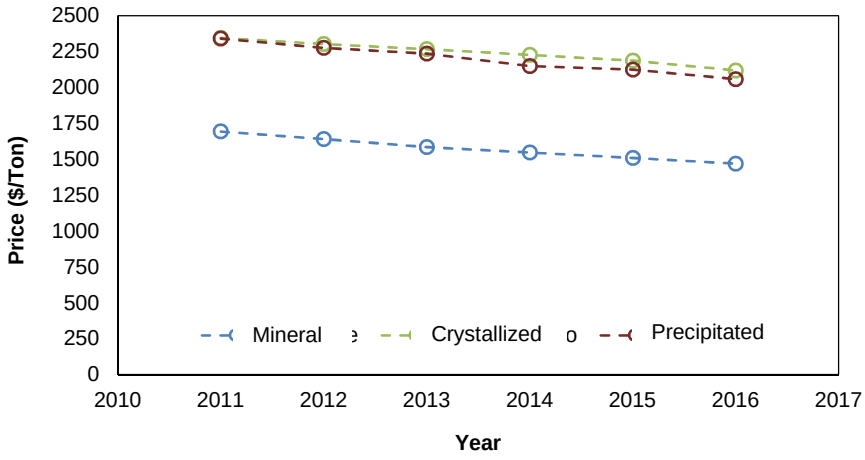

Figure 6.18: European magnesium hydroxide sale price on the production process base in the period 2011-2016 [154]

The magnesium recovery from saltwork waste brine, the objective of this PhD section, is obtained by means a chemical reaction. Due to the cost of alkaline reactant, the magnesium hydroxide produced should have high quality in terms of purity and granulometry, in order to make the process economically sustainable. For this reason, the target specifications chosen as guideline are those of flame retardant and the pharmaceutical sector. More details are in the next paragraphs.

6.4 State of art: alternative sources and production processes of magnesium and magnesium hydroxide in the world

A number of works concerning the recovery of magnesium from brines are reported in the literature. Already at the end of the 80s, Al Mutaz [155] analysed the technical feasibility of recovering minerals from the brine discharged from desalination plants in Gulf countries, starting from concentrations of total dissolved salts greater than the seawater standard. The conceptual analysis of processes for the recovery of sodium chloride, potassium salts and potassium, chlorine, bromine and magnesium, was performed underlining the importance of such application, also with regard to the large volume of brine produced in those years in Saudi Arabia (about 1,450 mgd).

Three years later, the same author [156] focused his research on the recovery of magnesium from a Saudi desalination brine as magnesium hydroxide (in 1988, the production of magnesite was around 9 million ton per year, with about 33% of this coming from seawater). The world's largest producers of magnesium were the United States, Norway and the ex USSR. The idea was inspired by the fact that although about 60% of global desalination plants were installed in Gulf Countries, no magnesium extraction was performed. Several methods were analysed for the production of magnesium, and for the first time, cost estimation was proposed for the production of 2,000 tons/year of magnesium considering the particular case of brine produced in a desalination plant in the Arabian Gulf. Adding up all cost items, a hypothetical value of 2,357 US $/ton was obtained, which was lower than the selling price of magnesium (3,370 US$/ton in the United States). In a different context, i.e. the treatment of waste brines from chlorine production industry, Turek and Gnot [157] proposed a two-stage system capable to give magnesium hydroxide (commonly used in refractories industry) as a by-product. In order to industrially precipitate magnesium hydroxide, mainly calcined dolomite, burnt lime or ammonia were employed. However, in this case, these reagents could not be used because of the risk of calcium precipitation, when employing calcined dolomite or burnt lime, or danger of explosions in the electrolytic step, when running the process with ammonia. For this reason, the use of sodium hydroxide was proposed, leading to technological complications due to the slow sedimentation of the $Mg(OH)_2$ suspension obtained (resulting in difficult filtration procedures). The experimental campaign highlighted that the formation of the first crystalline germs was virtually instantaneous. The primary crystals of magnesium hydroxide formed had the flat structure characteristic of brucite. It was found also that, if an excess of hydroxide ions was maintained during crystallisation, the sedimentation speed was low and the filterability was worse than in the case of magnesium ions excess. About 10 years later, Sung-Woo and Jun-Heok [158] proposed a multi-step reactive process for recycling magnesium chloride from brines derived from an industrial membrane process for the production of NaCl. In this case, sulphuric acid was first added in order to precipitate calcium ions, thereby leading to a higher purity product. Then, the alkaline base (NaOH) was added for precipitating magnesium hydroxide. The result was a magnesium hydroxide with a purity of 98% and a structure of hexagonal flat platelets. Furthermore, the main outcome of the work was to demonstrate how the rate of

sedimentation could be improved by adding appropriate sedimentation agents and aggregation inhibitors such as carboxy methyl cellulose and sodium stearate, respectively (added in small dosage as they can remain as impurities in the final product). Results showed that halved sedimentation times can be achieved by this addition. A final product with a magnesium purity of 99.5% and with crystal size of 0.5 microns was achieved. More recently, Henrist et al. [159] investigated how the operating conditions in a magnesium hydroxide precipitation process from artificial brines, using alkaline aqueous solutions (NaOH or NH_3), affects the size, shape and level of agglomeration of $Mg(OH)_2$ crystals. The use of NaOH leads to the formation of cauliflower-shaped globular agglomerates, while the synthesis carried out with aqueous ammonia results into platelet-shaped particles, characterised by a higher mechanical resistance. The temperature also plays an important role, mainly on the agglomeration behaviour and particles size, which show a tendency of small crystals to agglomerate more about 60°C, while lower temperatures lead to larger but fewer single particles in the shape of circular platelet. This influence was confirmed also by the study conducted by Cipollina et al. [6]. In 2011, Liu et al. [160] developed a linear regression model for a the precipitation of magnesium hydroxide from brines using NaOH, $Ca(OH)_2$ or ammonia as reactants. Interestingly, these authors propose the use of ammonia as an alkaline reactant, which can eventually be regenerated, after the $Mg(OH)_2$ precipitation, by means of a thermal treatment (NH_3 is very volatile and tend to evaporate shifting NH_4^+ /NH_3 equilibria towards NH_3). Authors found that a much more regular shape of crystals as well as a high degree of purity were guaranteed using NaOH, compared to the case in which calcium hydroxide or ammonia are used. However, the authors also found that particle agglomerate in the form of flakes, containing large quantities of water, leading to difficult filtration process as already reported in previous literature works [159]. In order to address this problem, several authors [159,161,162] investigated the use of magnesium hydroxide precipitation with hydrothermal treatment. However, this technology, characterized by high temperatures, high pressures and long residence time, does not seem to be suitable for large-scale production. The use of organic additives and catalysts was also investigated [163,164], but this leads to an inevitable increase of impurities in the final product. In 2011, Song et al. [165] analysed the batch precipitation process of high-purity $Mg(OH)_2$ through concentrated artificial solutions containing sodium chloride. Through an in-depth analysis of process performance dependences on operating conditions, the optimal ones were

identified in order to achieve $Mg(OH)_2$ crystals with spherical shape, purity higher than 99% and an average particle sizes distribution ranging from 6 to 30 μm. More recently, the same authors [166] performed experiments in a continuous Mixed Suspension Mixed Product Removal crystalliser. Also, in this case, the main identified drawback was that $Mg(OH)_2$ nanoparticles can easily aggregate forming gelatinous precipitates, which create filtration difficulties, as already underlined by some of the previous works. A fundamental study was carried out by Alamdari et al. [167] in 2008 on the kinetics of $Mg(OH)_2$ precipitation from artificial solutions and sea bittern (i.e. very concentrated brines generated from the evaporation of seawater). The authors identified three different kinetics for nucleation, growth and agglomeration, respectively. Nucleation rate was found to be the dominant phenomenon in the consumption of Mg^{2+}, while growth is comparatively slow, especially when high super-saturation is maintained. This is even more enhanced with real sea bittern, although the agglomeration rate seems to be improved in this latter case, which gives rise to larger particles more easily separated in the final separation stage. Notwithstanding the significant number of laboratory investigations on reactive crystallization of $Mg(OH)_2$ from concentrated solutions, little information is available in the literature on the investigation of precipitation phenomena from real saltworks brines. Only in 2014 a work was published by Cipollina et al. [168]. An experimental campaign was carried out for assessing the potentials and the limits of magnesium recovery from real exhausted brines, collected in saltworks for the production of sea-salt (Trapani, Italy). Experiments were conducted both in semi-batch and continuous crystallizers, confirming the possibility to use reactive crystallization to recover magnesium from waste brine. They confirmed the drawback highlighted in previous literature works, consisting in the formation of particles flakes incorporating large amounts of liquor and making it difficult their separation by simple sedimentation. Different experimental conditions were tested in order to find the best to understand the effect on the crystals size distribution. Higher concentration of Mg^{2+} allows the formation of larger particles. All the magnesium hydroxide produced had high purity (98-100% in Mg) with a total recovery of magnesium from brine.

6.5 Scope of this work

According to the idea of integrated cycle, this PhD thesis section is focused on the development of two continuous reactors for the magnesium recovery from waste saltwork brine. An alkaline solutions is added to the waste brine consequently a reactive crystallization occurs and the magnesium hydroxide produced precipitates due to its low solubility in aqueous solution (solubility product: $5.5 \cdot 10^{-12}$ [169]). The reaction is reported below:

$$Mg^{2+} + 2OH^{-} = Mg(OH)_{2\,(s)} \downarrow \qquad [6.1]$$

A typical composition of waste brine is reported in Table 6.5. The magnesium concentration is almost 40 times higher than in seawater and other competitive cations for the reactive precipitation are not very concentrated or even absent as calcium.

Table 6.5: Typical composition of waste saltwork brine (Trapani – 06.2017)

Cations [g/l]				**Anions [g/l]**				
Na^{+}	K^{+}	Ca^{2+}	Mg^{2+}	F^{-}	Cl^{-}	Br^{-}	NO_3^{-}	SO_4^{2+}
56.3	11.3	-	46.8	-	184.1	2.5	0.9	62.5

A wide experimental campaign was performed with Multiple Feed Plug Flow Reactor (MF-PFR) testing the effect of different operative parameters as feed flow velocity, alkaline solution concentration, reactor length and other parameters. The operative parameters were consequently calibrated in order to obtain the best condition in terms of purity, conversion and granulometric distribution.

In parallel, a Crystallizer with Ion Exchange Membrane (CrIEM) was also tested with real waste brine. This is a new technology recently patented by Cipollina et al [170]. Also in this case, an experimental campaign was performed in order to assess the applicability of this technology for the magnesium recovery purpose. Several set-ups were tested to solve the technological issues described in the following paragraphs.

7 DEVELOPMENT OF CONTINUOUS CRYSTALLIZATION REACTORS FOR MAGNESIUM RECOVERY FROM BRINES

Abstract

Magnesium is one of the 8 most abundant elements on the earth and the third most abundant in the sea, but practically only two countries (Russian and China) control the world market for this compound. Due to this, the European Commission has recently included magnesium and magnesite among the 20 “critical raw materials” for European economy and supply risk.

As demonstrated by previous literature works, exhausted brines or bitterns can represent a rich source of magnesium with Mg^{2+} concentration being between 20 and 30 times more than in typical seawater. Magnesium recovery from bitterns can be performed by reactive crystallization of $Mg(OH)_2$. In order to move the R&D towards, a continuous reactor for Mg recovery, namely the multiple feed plug flow reactor (MF-PFR) has been constructed and tested at laboratory scale. The lab-scale MF-PFR operations have been investigate in a wide experimental campaign focused one Mg-recovery from real saltworks bitterns generated in Trapani saltworks (Sicily, Italy).

The performance of different reactants and different operative condition was studied. Product purity (up to 99%), Mg recovery (practically 100%), crystal morphology and granulometric distribution of precipitated particles (agglomerated with particle size ranging from few to few tens of micrometers) were examined through careful laboratory analysis and are presented in this chapter.

7.1 Theory, state of art and new crystallizers for magnesium recovery from saltwork waste brines

As already mentioned before, part of this PhD thesis is focused on the development of new crystallizers for the recovery of magnesium from saltwork waste brine. The process exploited for the recovery is the crystallization. In the next paragraph, briefly the theory behind the process will be described. This method was already used for the same scope and some state of art works will be mentioned in order to understand the starting point of this work. Moreover, the two crystallizers utilized for the experimental campaign performed in this PhD thesis will be described.

7.1.1 Crystallization theory

Crystallization is the formation of solid particles within a homogeneous phase. The physical phenomenon includes the formation of particles in vapours, the solidification of melted mixtures or the species precipitation in aqueous solutions. Among the unit operations of chemical engineering, crystallization is important from a practical point of view: it provides a separation tool useful for the manufacture of high purity crystalline compounds with high industrial interest [171]. From a technical point of view, a product of a crystallizer is a suspension kwon as *magma*, constituted by a solid phase of crystals dispersed in a solution in aggregates or polycrystals form. The structure of a crystalline solid, the most ordered organization of inorganic matter, results from the space repetition of a basic cell with a well-defined geometrical shape.

The necessary condition for the formation of a crystal within a solution is that the solute is supersaturated: the species concentration must exceed its maximum solubility for the precipitation of it. The solubility is always a function of temperature. Many species increase their solubility when temperature increases, few others show a negligible variation with it, while a third category of chemical species have an inverse solubility, i.e. decreasing with temperature. A solution can be supersaturated in different ways: operating properly with the temperature, evaporating a fraction of the solvent, and adding a third component that alters the solubility of the solute. Among the different methodologies that make a particular solution supersaturated, have to be highlighted the so-called *common ion effect* because used in this PhD thesis: a third compound is added at the mother solution having a common ion with the compound of interest that has to be precipitated.

The physical processes that lead to the formation of a crystal in a saturated solution are the nucleation and the growth, phenomena responsible respectively for the formation of the nuclei, i.e. the first stable aggregates of order above the tens units, and of the growth of them through the continuous addition of solvated species in the solution. Both of these processes have the supersaturation as a driving force, defined as the difference between the current concentration (expressed in any unit of technical use) of the solution and the equilibrium concentration:

$$\Delta C = C - C_{sat} \tag{7.1}$$

The supersaturation degree, that is when the solution is more concentrated than equilibrium, is given by the ratio between the actual concentration and the saturation concentration:

$$S = \frac{C}{C_{sat}} = \frac{C_{sat}+\Delta C}{C_{sat}} = 1 + \frac{\Delta C}{C_{sat}} = 1 + s \tag{7.2}$$

In the expression (7.2) is defined the fractional supersaturation *s*, a quantity that expresses in relative terms the supersaturation with respect to a reference concentration that is the saturation [172].

Whether expressed in terms of ΔC, S or s, the physical necessity of the supersaturation in a crystallization process can be understood if it is considered that the solubility is a function of the characteristic length of the particles. The dependence is known with different denominations (Kelvin, Gibbs-Thomson, Gibbs-Kelvin, Ostwald-Freudnlich) and highlights a logarithmic relationship between the concentration and the length of the crystals:

$$\ln\left(\frac{C_{sat}(L)}{C^*_{sat}}\right) \propto \frac{1}{L} \tag{7.3}$$

A particle with a length L, and in particular a particle of micrometric dimensions, can be in equilibrium with a concentration $C_{sat}(L)$ which is higher than the maximum conventional solubility C^*_{sat}. The first logical implication of the Kelvin law is that, to precipitate a particle, it is not enough to reach and exceed the saturation C^*_{sat}, but it is

necessary to overcome it by a certain degree, useful to make the equilibrium unstable of the micrometric and sub-micrometric particles. It should be noted that with the Kelvin law, the particle returns to be in equilibrium with the saturation concentration C_{sat}^{*} if the crystal length tends to infinite (the mathematical infinite, physically corresponds to hundreds or thousands of microns) [172].

A crystal can grow only if microscopic aggregate is present in solution, called *nuclei* that can act as centres of growth. Nucleation is the phenomenon responsible for the formation of nuclei. There are different types of nucleation that can act simultaneously during the practical crystallization process. A first distinction must be made between primary or secondary nucleation. Primary here refers to the first nucleus to form, while secondary nuclei are crystal nuclei produced from a pre-existing crystal. In turn, primary nucleation can be subdivided into homogeneous or heterogeneous nucleation, depending on whether the formation of nuclei is catalysed or not by the presence of solid bodies (such as imported particles, the wall of the crystallizer, the impeller blades if are present, etc.) [173].

Homogeneous nucleation, although it is the most spontaneous form of nucleation, is rarely observable in isolation. The mechanism with which the nuclei are formed involves a continuous bimolecular collision, with the addition of a new species to the aggregates of lower orders. In this way the solvated particles in solution, and normally aggregated in a few units in structures called *clusters*, become *embryos*. The latter are unstable species, which can break up and evolve back into clusters or, for a continuous addition of units, evolve into nuclei [173].

The presence of a solid particle, however, can act as a catalyst for the process, according to the mechanisms of heterogeneous nucleation. In this case, there is a reduction for energy required by the process as a function of the wetting angle formed by the nucleus and the solid phase. It should be noted that normally atmospheric dust induces the presence of a number of particles in the order of 10^6 particles, which can act as catalysts. Even if a preventive filtration is done, this number is not less than 10^3 particles: from these numbers we can appreciate that the nuclei formation is almost never due to simple primary nucleation.

Secondary nucleation is characterized by the presence of crystalline materials in the solution. This addition can be deliberated if the crystals size distribution has to be

controlled. However, it can be happen not intentionally by means of some small crystals dispersed in the atmosphere due to collateral manufacturing activities (transportation, solid handling, etc.). Such particles are promoters for the formation of new nuclei.

A third category is normally added to these physical forms of nucleation, called *spurious nucleation*. These phenomena should be avoided in the crystallization practice. Excessive supersaturation can lead anomalous crystal growth in one direction rather than another, obtaining needle-like structures that can create new nuclei if they break [172]. Another phenomenon to take into consideration is the manufacture of crystals itself. The separation from the liquid phase takes place by filtration, which however leaves traces of liquid on the crystals or into the crystals if they are aggregates; during the subsequent drying step, this liquid can lead to the formation of solids on the surface of the crystals which, when added in solution, form new nuclei.

Whatever its origin, each nucleus acts as a growth centre during crystal formation. Theories that consider the growth on the basis of matter transport, describe the phenomenon in two steps. In the first stage the solute particle is transferred from the solution bulk to the crystal, followed by a superficial diffusion towards a growth centre where the ion is incorporated into the crystalline lattice.

Strictly speaking, the particle growth is a function of its length. This is mainly due to the different terminal velocity with which particles of different diameters are stirred in a crystallizer. Nevertheless, very often it is used an approximation assuming the crystal growth rate independent by length. This hypothesis, known as ΔL law, has a limited range of validity: a length higher than 500 μm influences the particle fluid dynamics, resulting in a variation of the transport coefficient that is no longer negligible; at the opposite condition, however, it is necessary to take into account that due to the reduced size, the supersaturation on the crystals is reduced (as explained by the Kelvin law), considering also that particles with smaller dimensions than the Kolmogorov turbulent vortexes are immersed in a laminar surrounding [172].

Given the complexity of the kinetic phenomena that contribute to crystallization, the mathematical modelling of nucleation and growth is reduced to empirical relationships that assume a power supersaturation law. The nucleation relationship is reported below:

$$B^0 = k_n \cdot s^b \tag{7.4}$$

B^0 represents the nucleation speed, i.e. number of nuclei created in the time unit and volume, while k_n and the exponent n are parameters experimentally determined. The growth rate can be expressed in different ways. The linear growth rate, intended as a variation of the crystal's length, depends on the supersaturation with a law similar to the nucleation [172]:

$$G = \frac{dL}{dt} = k_g \cdot s^g \tag{7.5}$$

The growth rate can, alternatively, be expressed as the mass added to the crystals per unit of time and exposed crystal area. In this case, it can be defined as:

$$R_G = \frac{1}{Ac}\frac{dm}{dt} \tag{7.6}$$

The two expressions are linked by the volume factors vf and form β, defined respectively as the ratio between the area and the square of a characteristic length of the crystal, and the relationship between the volume and the cube of the characteristic length. Substituting in the previous relation the following expressions it is obtain the relationship between R_G and G [172]:

$$Ac = \beta \cdot L^2 \tag{7.7}$$

$$m = \rho \cdot V = \rho \cdot Vf \cdot L^3 \tag{7.8}$$

$$R_G = \frac{3\,Vf}{\beta} \cdot G \tag{7.9}$$

The experimental values required by the kinetic equations were calculated by Alamdari et. al [167], for a batch crystallizer consisting of 100 ml of solution containing Mg^{2+} ions in which a volume of 250 ml of 1M of NaOH solution was added drop by drop. They developed a mathematical model in order to describe the system in its nucleation, growth and agglomeration aspects of the crystals through a comparison with experimental data. Kinetic parameters are presented in Table 3.1.1, both for real brines and for synthetic solutions:

Table 7.1: Estimated kinetic parameters of growth, nucleation, and agglomeration rates of magnesium hydroxide precipitation from synthetic liquor and from sea bittern [167].

Parameter	**Synthetic solution**	**Sea bittern**
Growth rate coefficient, kg ($\mu m\ s^{-1}$)		
Mean value	$3.01 \cdot 10^{-5}$	$3.01 \cdot 10^{-5}$
Standard error	$0.080 \cdot 10^{-5}$	$0.142 \cdot 10^{-5}$
Growth rate order with respect to supersaturation, g	1	1
Nucleation rate coefficient, k_n ($\#\ s^{-1}\ g_{crystal}^{-1}$)		
Mean value	0.335	0.418
Standard error	0.0595	0.0764
Nucleation rate order with respect to supersaturation, b	3	3
Agglomeration rate coefficient, k_a ($g_{solution}\ \#^{-1}\ s^{-1}\ \mu m^{-3}$)		
Mean value	$3.01 \cdot 10^{-5}$	$3.01 \cdot 10^{-5}$
Standard error	$3.01 \cdot 10^{-5}$	$3.01 \cdot 10^{-5}$
Agglomeration rate order with respect to supersaturation, a	1	1

During crystallization, nucleation and growth phenomena interact between them determining the final morphology of the crystals. However, although the process can be controlled, the final result will be a crystals population with different sizes.

The *crystal size distribution* (CSD) description is possible through a quantity known as a population density function:

$$n = \lim_{\Delta L \to 0} \frac{\Delta N}{\Delta L} = \frac{dN}{dL} \tag{7.10}$$

In the previous relation, the variable *N* is a crystals concentration (number of particles per unit of volume) while *L* is the characteristic length. The physical meaning of the newly defined population density variable is clear if it is considered the following relationship:

$$n \cdot dL = dN \tag{7.11}$$

The relation (7.10) is an arrangement of (7.11) that allows to quantify the crystals concentration with a length in the range L and L + dL. The population density is, in turn, a function of the crystals length and can be determined exactly only in simple crystallization process (for example in the MSMPR crystallizer). From the strictly theoretical point of view, if all the crystals have only one dimension, the function n = f (L) would be reduced to a line flattened on zero with a single peak corresponding to the

diameter of the crystals. In real cases, on the other hand, this curve has a more or less restricted bell shape depending on the diameters distribution. Population density, therefore, is a sufficient function to describe the CDS. Since n (L) is only a measure of the concentration of crystals at a given length, it is useful to translate this information into a cumulative curve, i.e. to plot as dependent variable not n but its integral:

$$N(L) = \int_0^L n(L)dL \tag{7.12}$$

This integral gives the number of particles with a diameter smaller than L and, by definition, is an increasing monotonic function. Note that in the transition to the limit, for $L \rightarrow \infty$, the total number of particles is obtained:

$$N_{tot} = \int_0^\infty n(L)dL \tag{7.13}$$

In the scientific technical field, it is common practice to represent the cumulative curve not in absolute terms, but by comparing the quantity N (L) to the total number of particles N_{tot}, plotting the fractional magnitude:

$$\frac{N(L)}{N_{tot}} = \frac{\int_0^L n(L)dL}{\int_0^\infty n(L)dL} \tag{7.14}$$

Once again, in the ideality of having a monodisperse particles population, this curve would be reduced to a step from 0 to 1 corresponding to the characteristic length of the crystals.

The population density function, and the magnitudes derived from it, are not only useful as they describe the CSD, but also allow to derive also other information, such as the *average characteristic length* of the distribution, or the *coefficient of variation* i.e. an amplitude measurement of the cumulative curve.

The theory described above is important to better understand the experimental results obtained in the experimental campaign devoted to the development of new crystallizers for the recovery of magnesium by crystallization process. In order to highlight the starting

point of this work, some state of art works for the recovery of magnesium from brine are following described.

7.1.2 Crystallizers state of art for the recovery of magnesium from saltwork waste brine

The ability of an alkaline solution to precipitate magnesium hydroxide has been known from long time. However, the idea of recovery magnesium from saltwork waste brine is studied since 2012 [6]. Cipollina et. al have demonstrated the concept feasibility by means of batch tests. The apparatus is reported in Figure 7.1.

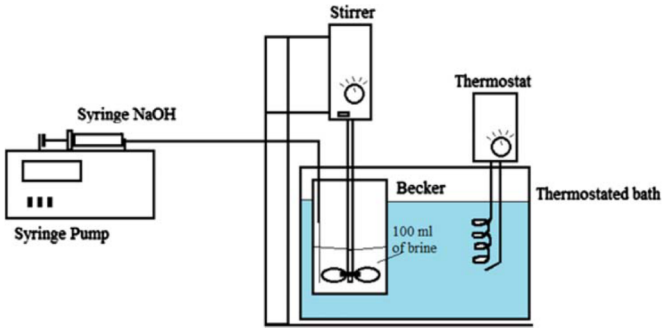

Figure 7.1: A schematic view of the experimental apparatus adopted for the reactive precipitation tests performed by Cipollina et al [6]

In this simplified configuration, the reactor was constituted by a glass becher (500 ml) stirred mechanically by a small marine impeller. An over-stoichiometric NaOH solution was added by syringe pump in order to perform a reactive crystallization between the alkaline solution and the magnesium present in the brine. All the solutions were kept at controlled temperature with a thermostatic bath. As performance parameters were chosen the purity of magnesium salts produced, the conversion and the filtration time as indicator of crystal size: big crystals give fast filtration times [6].

In their preliminary tests for the proof of concept, the concentration and flow rate of the alkaline solution and the stirring rate of the reaction medium were changed investigating their effect on the purity and nucleation/growth rates of magnesium hydroxide crystals. The experiments were performed at 25°C and 40°C in order to analyse also the effect of temperature [6].

Cipollina et. al, in their work and their experimental set-up [6], highlighted that the filtration time increases for low impeller speed, high NaOH concentration and high temperature. Probably, in all the cases reported before, the primary nucleation rate is promoted at the expense of growth. Moreover, magnesium hydroxide purity was always higher than 90% with precipitation efficiency always higher than 99%.

Two years later, the same research group [168] performed experiments with both in a semi-batch and in a continuous 5 litres crystallizer using NaOH solutions for the precipitation of magnesium from saltwork waste brine as magnesium hydroxide. The reactors schematic representation is reported in Figure 7.2.

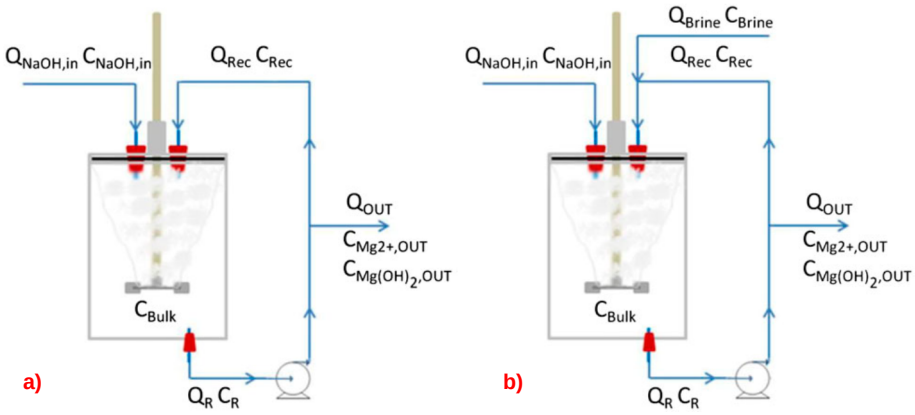

Figure 7.2: Schematic representation of the semi-batch (a) and continuous CSTR (b) [168].

The pH that was monitored shown a typical trend in which the value initially increases followed by a plateau at a pH around 9-10. When all the magnesium was converted, the pH starts to increases again [168].

The effect of several parameters were investigated: total reaction time, NaOH concentration, volumetric flow rate, magnesium concentration and the influence of different impellers [168].

Similar results than the previous work were found, in particular an over-stoichiometric concentration produces small particles influencing also the agglomeration. In almost all the case, the purity was higher than 99% with a total recovery of magnesium present in the waste brine [168].

The two works described above, highlight the characteristic of the reactive crystallization between a magnesium solution and an alkaline reactant. A local super-saturation, due to high concentration of alkaline solution and/or magnesium, promotes the primary nucleation rate at the expense of the growth rate. This is confirmed by Alamdari at al. [167] which claim that a greater estimated value for the order parameter of nucleation rate (3) than that for growth rate (1) (see section 7.1.1) indicates that nucleation is the dominant mechanism in magnesium hydroxide precipitation. This is the main difficult of this process and it has to be taken into account if particular specifications have to be obtained in order to sell the magnesium hydroxide with high price, for example in the flame retardant field.

7.1.3 New crystallizers for the recovery of magnesium from brines

As already mentioned before, part of this PhD thesis is focused on the development of new crystallizers for the recovery of magnesium from saltwork waste brine. Two reactors were designed and tested to analyze the effect of several operative parameters: a Multiple Feed - Plug Flow Reactor (MF-PFR) (Figure 7.3a) and a Crystallizer with Ion Exchange Membrane (CrIEM) (Figure 7.3b).

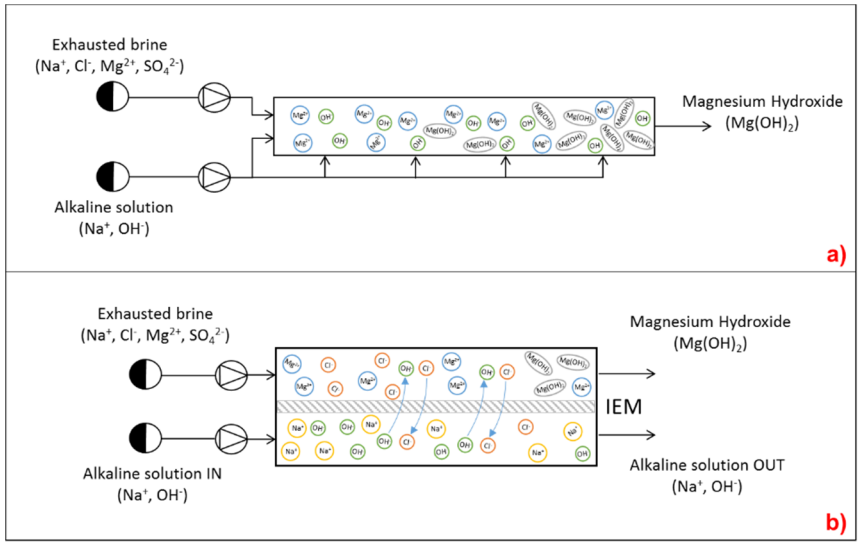

Figure 7.3: (a) MF-PFR and (b) CrIEM layout schemes.

Ideally, inside a PFR reactor the solution containing the reactants moves with a piston flow, i.e. with a speed without radial gradients; the reaction occurs along the entire length of the reactor and at the steady state, is not a function of time but only of space. Passing from ideality to reality, the piston flow hypothesis becomes only an approximation: the condition of no slip to the wall inevitably creates a velocity profile and how much this profile is flat depends on the achieved fluidodynamic regime (i.e. the size of the tube and the flow rate). Moreover, in this case, the reaction of the hydroxyl ions with the magnesium in solution is practically instantaneous, so that the properties of the system are not a function of space, but depend solely on the distribution of the reagents. A schematic representation of the MF-PFR reactor is shown in Figure 7.3a: note the input of the feed (brine) and of the alkaline solution. The results obtained with this reactor are shown in the next paragraphs.

The CrIEM, on the other hand, is a membrane reactor in which the brine is separated from the alkaline solution by means of an ionic exchange membrane (Figure 7.3b). The OH^- ions move from the alkaline solution to the brine to alloy the precipitation of magnesium hydroxide while the chlorides present in the brine move in the opposite direction to re-balance the electric charge. This reactor is patented and has already aroused interest in the many sectors of research [170]. The CrIEM will be better described in the next chapter, reporting also the results obtained with this new crystallizer.

7.2 Experimental methodologies

The experimental procedure used in all the tests with MF-PFR and CrIEM can be summarized in Figure 7.4:

Each box represents a particular operation (or set of operations); the solid lines indicate the material flow while the dashed lines virtually represent the results from different analyses.

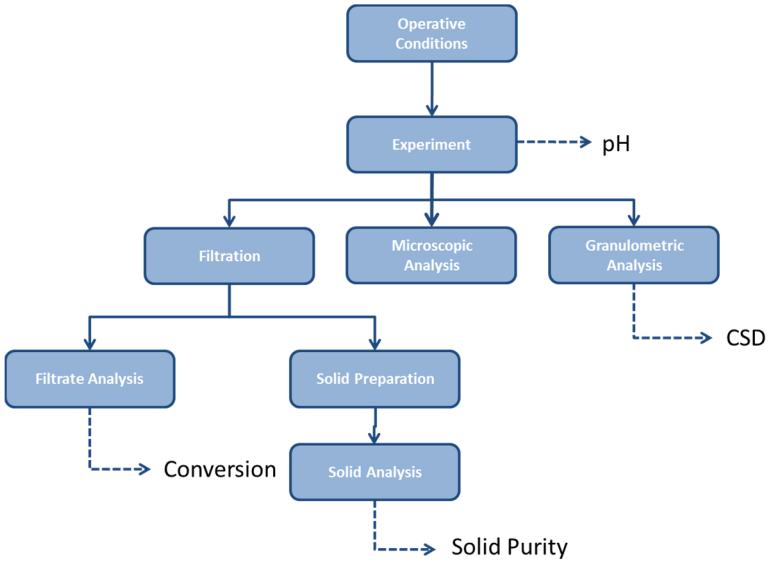

Figure 7.4: Experimental procedure for magnesium recovery from waste brine.

Operative condition. The first step is the characterization of the selected reagents, estimating the volume to be used in tests and the solutions preparation. The brine from a real saltworks operating in Trapani (Italy) was used for each test, after being slightly diluted for reducing the Mg^{2+} concentration to a value of about 1M in magnesium or slightly more, for comparison purposes with literature information [6,7]. An example of the brine properties adopted in the tests are reported in the Table 7.2 (measurements performed by an Ion Chromatograph IC 882 Compact Plus - Metrohm AG, Switzerland):

Table 7.2: Example of brine properties used in the experimental campaign

Cation	**Concentration [g/l]**
Na^+	26.0
K^+	7.3
Mg^{2+}	30.6
Ca^{2+}	0.2
Specific electrical conductivity [mS/cm]	140
pH [-]	7.9

Depending on the reactor utilized, different alkaline solutions have been used for the precipitation and the flow rate have been calculated in order to have a stoichiometric

condition (1:1) to recover the total magnesium present in the brine or in only in same case a slightly over-stoichiometric condition.

Test-run. The test is run in different way depending on the exploited reactor. In the case of MF-PFR, after circulating the brine in the main tube and injecting the alkaline reactant for a time equal to five times the residence time in the reactor, 4 samples were collected from different positions. Samples were collected from the last to the first position in order to minimize any relevant disturbance due to the previous samplings. The sample volume collected was 150ml, necessary for the entire analysis cycle. After the test, reactor tubes were washed with distillate water, with chloride acid 1 M (to remove scaling by magnesium hydroxide) and again with distillate water. The pH of the samples was measured just after sampling, by means of a digital pH-meter (Jumo 202710/20/000).

The test run for the CrIEM rector will be described in the next chapter.

Granulometric Analysis. The suspension samples were analysed by means of a Laser Granulometer (Malvern Mastersizer 2000 with Hydro 2000MU as sample dispersion system) to obtain a cumulative size distribution (CSD) of crystal agglomerates. The CSD can give also an idea on the possible ease of filtration of the product in a hypothetical continuous system

Filtration. Each sample (50 ml) was separated by filtration to obtain the solid product and liquid liquor. A Büchner filter with circular paper filter (Whatman 597, 110 mm) was used to separate over-micron crystal agglomerates from the solution. The filtrate was collected and stored for chromatographic analysis. The solid was washed with 50 ml of distillate water to remove brine traces and soluble salts co-precipitated with $Mg(OH)_2$. After washing, the solid was dried in an oven at 130 °C for 24h.

Filtrate Analysis. The filtrate liquors were analysed by ion chromatography to assess the precipitation yield by determining the magnesium ions concentration in the solution.

Solid Preparation. After drying, the solid was crumbled and washed again two times with 50 ml of water to eliminate any soluble salts possibly precipitated from traces of brine

remained trapped after the first washing. The sample was then dried in the oven at 130 °C for 24h.

Solid Analysis. The solid was prepared for ion chromatographic analysis to estimate the purity of precipitated magnesium hydroxide. A small amount of solid powder (12 mg) was stoichiometrically neutralized with 1 M chloride acid and diluted to 50 ml to obtain a concentration close to 100 ppm.

Microscopic Analysis. The suspension was also analysed by means of an optical microscope (Optika B-800), in order to assess how different reactants or other parameters can produce crystals agglomeration with different shape.

7.2.1 Performance parameters

In the experimental procedure, some parameters are immediately available while some others are obtained with the data elaboration. The performance parameters chosen allow comparing different operative conditions and are following reported:

pH. The H^+ concentration gives qualitative information on the reaction path. The hydroxide magnesium precipitation starts when the pH is around 9 and it does not overcome the pH 10 during the reaction. The pH became more than 10 when the magnesium ions present in the brine are completely reacted.

Conversion. The conversion is a measure of how much product is recovered compared to the maximum theoretically obtainable. It is defined as the local molar flow rate of magnesium ions divided by the inlet molar flow rate:

$$X = \frac{N^0_{Mg^{2+}} - N_{Mg^{2+}}}{N^0_{Mg^{2+}}} \tag{7.15}$$

Substituting volumetric flow rate and magnesium ions concentration, the equation becomes:

$$X = \frac{Q_{br}\, C_{br} - Q_L\, C}{Q_{br}\, C_{br}} \tag{7.16}$$

In the eq. (7.16), Q_{br} and C_{br} are respectively the brine volumetric flow rate and the molar concentration of magnesium ions while Q_L and C are the volumetric flow rate and the magnesium concentration in a generic reactor section. The MF-PFR used in the tests (Figure 7.3a) has a layout in which there is a volumetric flow rate variation along the device axis. The variation is associated with the alkaline reagent inlet in four (or eight) sections of the reactor. Each section has constant volumetric flow rates. A material balance between the initial and a generic reactor section allows to link Q_L to the fed flow rates under the following assumptions: (i) constant density of aqueous solutions and (ii) negligible variation of liquid flow rate with solid phase formation.

$$Q_L = Q_{br} + n\, Q_b \tag{7.17}$$

Q_b is the flow rate of one inlet alkaline solution and *n* is the number of inlets before that specific reactor section. By coupling the eq. () and eq. (), the final expression of conversion is obtained:

$$X = 1 - \frac{(Q_{br} + n\, Q_b)C}{Q_{br}\, C_{br}} \tag{7.18}$$

In the CrIEM reactor, instead, the ionic exchange membrane cannot block the flux of water from the alkaline solution to the brine, due to a different salinity. In some cases, the volume of brine at the end of the test become double or triple, so the conversion can be calculated considering the final concentration of magnesium in the brine at the start and at the end multiply it with the volume.

The magnesium concentration and all the ions concentration in different solutions were measured by means of Ion Chromatograph IC 882 Compact Plus - Metrohm AG, Switzerland.

Magma Density. The magma density measures the mass of solid in the suspension. It is calculated as the ratio of grams of dried solid and the sampled suspension volume:

$$M_T = \frac{m_s}{V_{susp}} \tag{7.19}$$

Solid Purity. The chromatographic analysis (Ion Chromatograph IC 882 Compact Plus - Metrohm AG, Switzerland) allows to estimate the solid purity, defined as the ratio between the mass of magnesium and the sum of masses of all N cations detected:

$$\vartheta = \frac{C}{\sum_{i=1}^{N} C_i} \tag{7.20}$$

CSD. The crystal size distribution is obtained by means of a granulometric analysis. The results were elaborated also to assess a cumulative crystal distribution.

Filterability. The filterability is defined as the volumetric percentage of particles with diameter larger than 10 μm or 50 μm. This parameter gives information on the ease of separation of the suspension in solid and liquid phase using common commercial filters.

Figure 7.5 shows an example of set of experimental results, consisting in the trend of pH (Figure 7.5 A), Mg^{2+} concentration in the liquor and the solid purity (Figure 7.5 B, C), crystal size distribution (Figure 7.5 D), all variables plotted versus the amount of reactant injected normalised by the total reactant adopted. The error bars, indicating the experimental error relevant to the measurements performed, are also reported.

The all parameters defined above were not always used for all the tests but from time to time are chosen the most significant ones.

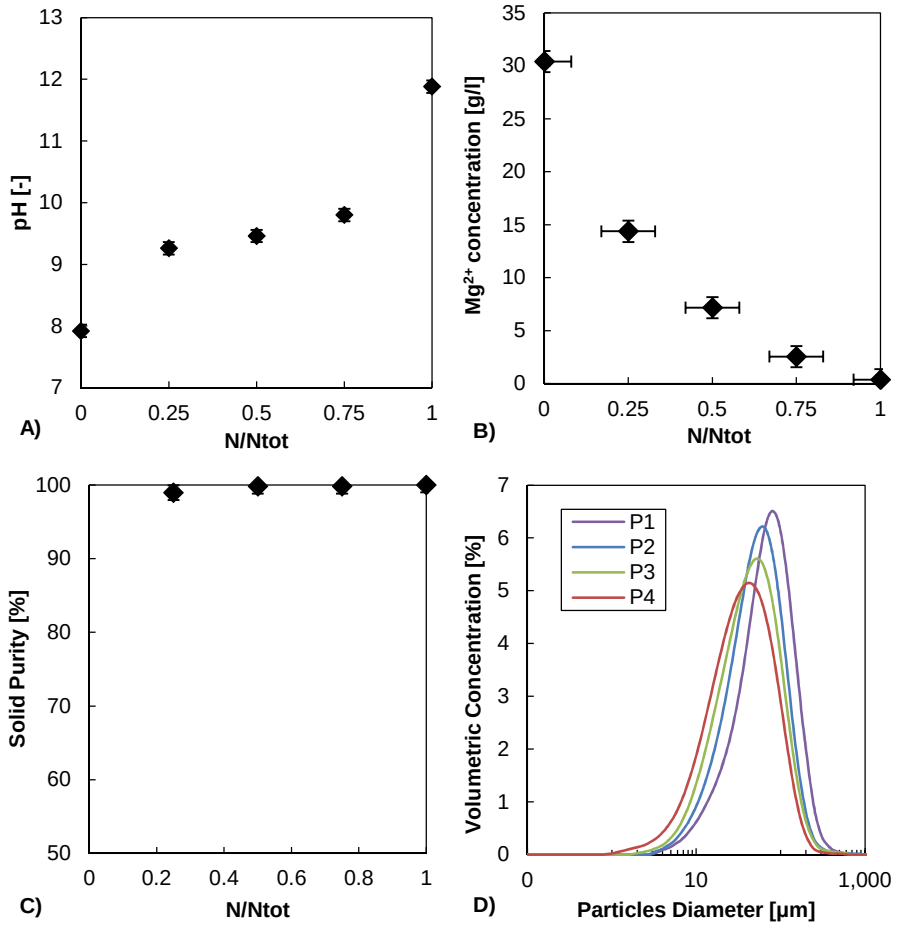

Figure 7.5: Example of experimental results. Test with saltwork waste brine and NaOH. (A) pH trend, (B) residual magnesium concentration in the brine, (C) solid purity, (D) crystals size distribution. Feed brine Mg^{2+} concentration=1.25 mol/l. Brine flowrate = 47 ml/min. N_{base}/N_{stoich} =1. NaOH concentration=4 mol/l.

7.3 Description of the laboratory pilot system: the first experimental campaign with MF-PFR

The plug flow reactor (PFR) is a cylindrical reactor, in which the "reagent" solution moves with a plug flow, with negligible radial gradient of velocity, concentration and temperature. At steady state, the reaction is only a function of space. As already said before, in real conditions, the plug flow is only an approximation because the no slip

condition near the wall tube necessarily produces a velocity profile. The MF-PFR used in the first experimental campaign (Figure 7.6) had one inlet for the feed brine and four inlets for the alkaline reactant. Since reaction is practically instantaneous, magnesium ions precipitate after each injection having enough space to react along the reactor segment.

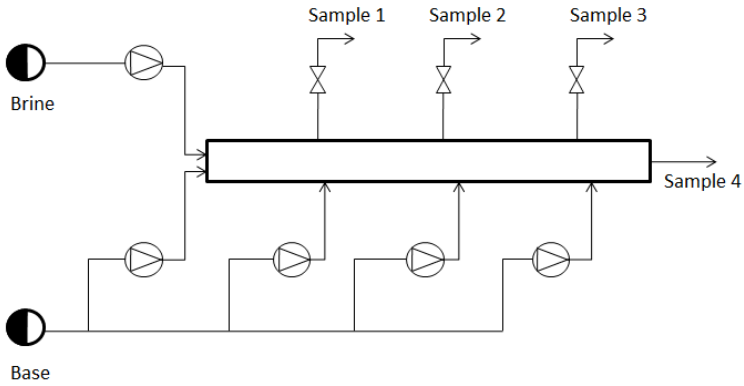

Figure 7.6: Simplified scheme of MF-PFR adopted for the first experimental campaign.

The reactor layout is very easy, essentially formed by a main tube and the distribution systems for reagents, each of them with a pump for the fluid movement. The reaction between brine and alkaline solution was performed in a silicon tube with 5.3 mm as inside diameter and 225 cm as total length. The plastic material was chosen due to the high aggressiveness of salt solutions on metallic materials. Silicon tubes were also used for the alkaline solution, from a tank to the reactor. Each inlet of alkaline solution is positioned at a distance of 45 cm from each other. The samples positions are before of each input. Verdeflex M025 pumps were used to move the brine and the alkaline solutions. The flow rate was controlled changing the revolutions per minute (rpm) and the tubes section. The delivery pipe of each pump was positioned upward to facilitate the air expulsion from the reactor.

7.3.1 Results and discussion for the first experimental campaign with MF-PFR

According to the procedure illustrated in the previous paragraph, four experiments have been carried out under the operative conditions listed in the Table 7.3. Four different

alkaline solutions were adopted, all with a stoichiometric ratio with the Mg^{2+} concentration fed in the brine ($N_{base}/N_{stoic}=1$). It is worth noting that $Ca(OH)_2$ alkaline solutions were actually a milky suspension, due to the very low solubility of $Ca(OH)_2$.

In the following paragraphs, each performance indicator was analysed in a comparison graph reporting the trend measured with four different alkaline reactants.

Table 7.3: Operative conditions adopted in the experimental campaign

Test	Reactant	Brine Conc. [mol/l]	Brine flowrate [ml/min]	Base Conc. [mol/l]	Base flowrate per inlet [ml/min]
A	NaOH	1.25	47	4	7.35
B	$Ca(OH)_2$	1.25	47	2	7.35
C	Na_2CO_3	1.25	47	2	7.35
D	NH_3	1.25	47	14.7	1.81

pH. Figure 7.7 shows pH trend as function of alkaline solution and the fraction of the total amount of base supplied in the reactor (N/N_{tot}). The shape is the same for every reactant: pH rises from the initial value of the brine up to a plateaux value, in a range between 9 and 10. In this region, OH^- injections allow the precipitation of magnesium hydroxide. When conversion is complete, pH starts to rise again due to the injection of excessive alkaline solution.

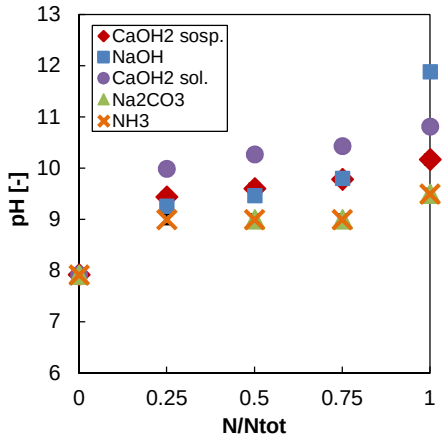

Figure 7.7: pH trend comparison for test A-B-C-D. Brine Mg^{2+} concentration = 1.25 mol/l; Brine flowrate = 47 ml/min; N_{base}/N_{stoich} =1; NaOH (4 mol/l); $Ca(OH)_2$ suspension (2 mol/l); Na_2CO_3 (2 mol/l); NH_3 (14.7 mol/l).

Conversion. Figure 7.8 presents conversion data calculated from IC analysis of filtrate. A practically linear trend is registered for all tests, with conversion increasing proportionally to the injection of reactant. On the histogram (Figure 7.8 right), the final conversion recorded at the end of the reactor. Only strong bases actually reached expected quantitative conversion. Sodium carbonate stops at 85%, while an even lower conversion is observed with ammonia. In this latter case, dilution phenomena strongly lower the initial pH of the alkaline solution following the mixing with feed brine. This physical constrains, along with the acid-basis equilibria regulating NH_3 dissociation and $Mg(OH)_2$ precipitation leads to limiting the quantitative recovery of Mg in these conditions.

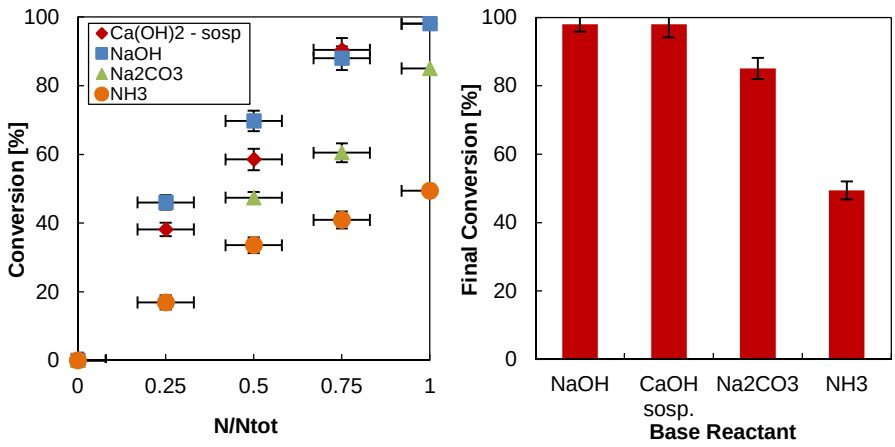

Figure 7.8: Conversion trend comparison for the Tests (left) and conversion at the end of reactor (right). Brine Mg2+ concentration = 1.25 mol/l; Brine flowrate = 47 ml/min; N_{base}/N_{stoich} =1. NaOH concentration = 4 mol/l; $Ca(OH)_2$ concentration = 2 mol/l; Na_2CO_3 concentration =2 mol/l; NH_3 concentration = 14.7 mol/l.

Purity. Purity with conversion is one of the most important parameters to be considered. As already introduced in the previous chapter, purity determines the commercial value of the product. The results of Figure 7.9 show a good purity achieved during precipitation tests, in all cases higher than 95%, but for the case of Calcium hydroxide suspension was generated a precipitate with a very poor purity, likely due to the co-precipitation of insoluble calcium salts.

It is worth noting that purity refers only to the cationic composition of the precipitate. Thus any magnesium salt, different than magnesium hydroxide, would also contribute to the high product purity. This is the case of precipitate obtained with sodium carbonate solution. In this case the solid consisted of two chemically different salts, both of them with magnesium cation, $Mg(OH)_2$ and $MgCO_3$. The co-product was identified as magnesium carbonate due to the formation of CO_2 bubbles during solid neutralization with HCl. Moreover, microscopic analyses performed on the samples (see Figure 7.11) have also showed the presence of $MgCO_3$ crystals. In fact, according to Zhang et al. [174] magnesium carbonate tri-hydrate can show different morphologies, dependently from precipitation conditions. At room temperature, with a pH below 9.5, magnesium carbonate tri-hydrate settles in a crystalline needle-like structure (in these conditions: (i) many CO_3^{2-}

ions exist in HCO_3^- form and (ii) brine viscosity prevents the collision of particles and consequently the growth phenomena prevail on nucleation) [174], as observed with a microscope in the samples (Figure 7.11).

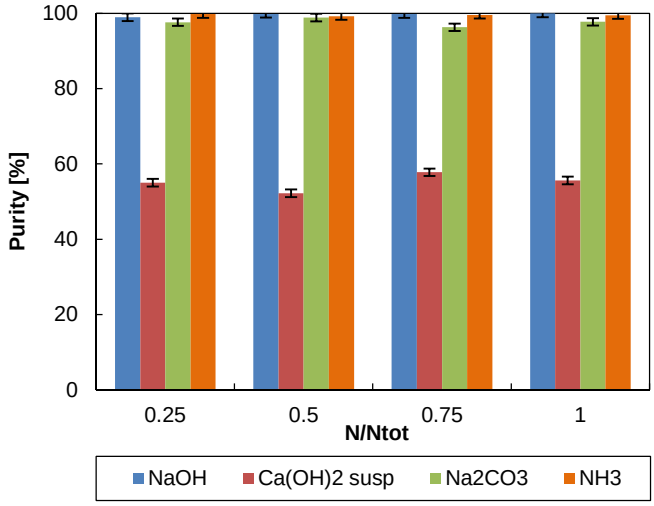

Figure 7.9: Solid purities found in the tests. Brine Mg^{2+} concentration = 1.25 mol/l; Brine flowrate=47 ml/min; N_{base}/N_{stoich} =1; NaOH concentration=4 mol/l; $Ca(OH)_2$ concentration=2 mol/l; Na_2CO_3 concentration=2 mol/l; NH_3 concentration=14.7 mol/l.

Morphology. Morphology has been investigated by laser granulometric analysis and optical microscopy, whose results are reported Figure 7.10 and Figure 7.11 respectively. A good agreement between the results of the two analytic techniques was found, indicating that particles average size decreases passing from sodium carbonate to sodium hydroxide, ammonia and calcium hydroxide. Looking in more details at the precipitate from sodium carbonate, bigger particles are observed, even if the nature of precipitate is so composite: flower-like agglomerates, identified as magnesium hydroxide [159], are mixed with needle-like structures [174]. According Figure 7.11 the purity showed (Figure 7.9) for Na_2CO_3 is mainly due to magnesium salts in a magnesium carbonate form.

Furthermore, looking at the case of calcium hydroxide, the optical microscope picture presents very fine magnesium hydroxide particle accompanied by little needle-like crystals that are representative of calcium impurities, as confirmed also by the low purities measured for this case (see Figure 7.9).

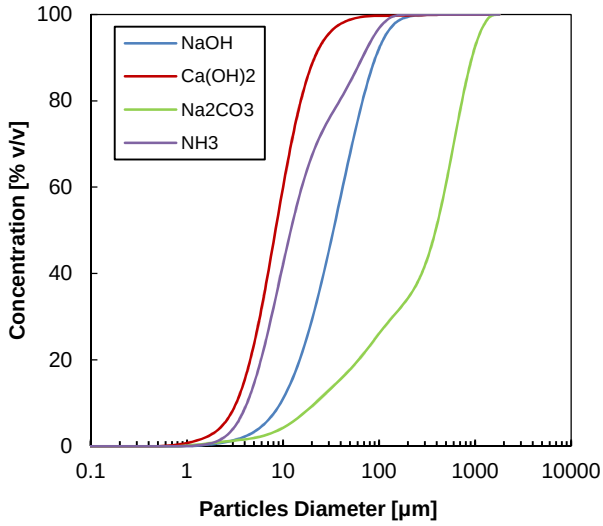

Figure 7.10: Crystals size distribution at the end of the reactor for different reactants. Brine Mg^{2+} concentration = 1.25 mol/l; Brine flowrate = 1; N_{base}/N_{stoich} =;. NaOH concentration = 4 mol/l; $Ca(OH)_2$ concentration = 2 mol/l; Na_2CO_3 concentration =2 mol/l; NH_3 concentration = 14.7 mol/l.

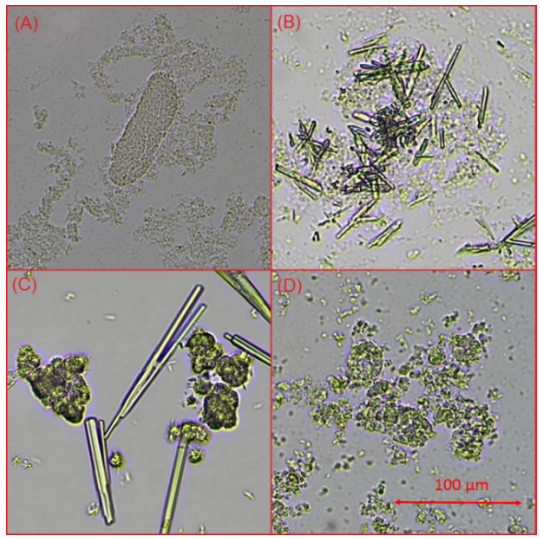

Figure 7.11: Microscopic pictures of suspensions at the end of the reactor using (A) sodium hydroxide, (B) calcium hydroxide, (C) sodium carbonate and (D) ammonia. Brine Mg^{2+} concentration = 1.25 mol/l; Brine flowrate = 1; N_{base}/N_{stoich} =1; NaOH concentration = 4 mol/l; $Ca(OH)_2$ concentration = 2 mol/l; Na_2CO_3 concentration =2 mol/l; NH_3 concentration = 14.7 mol/l; Optical miscroscope zoom: 20x.

Filterability. Filterability of solid samples was calculated from the CSD and is presented as an indicator of the particles separation complexity, as explained in the previous paragraph. Results, reported in Figure 7.12, indicate that a similar trend was found for all 4 cases, the average diameter of crystals population decreasing when increasing conversion. A possible phenomenological explanation for this result can be related to the tendency of magnesium salts crystals to form agglomerates, which are the actual particles detected by the laser granulometer. On this basis, when precipitation occurs at very high concentrations of Mg^{2+} still present in the reacting brine, large agglomerates can form due to the closeness of crystallising particles [167]. As magnesium conversion increases, crystals growth is enhanced with respect to the nucleation, however, even though large crystals may form, the lower suspension concentration reduces agglomeration phenomena, thus reducing the size of agglomerates generated. In accordance with the findings of granulometric distributions, a very high filterability has been found with sodium carbonate. Sodium hydroxide and ammonia giving rise to similar particle size and filterability. Calcium hydroxide is also a bad reactant with respect to filterability of the suspension.

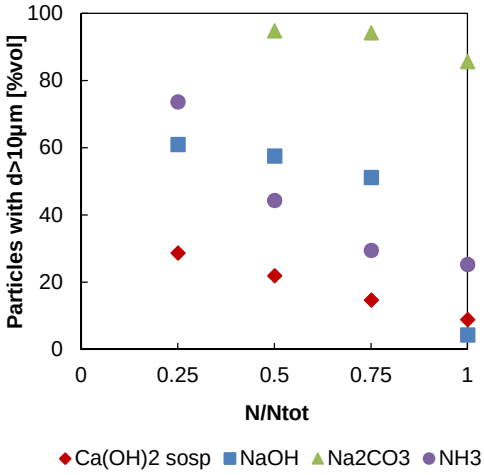

Figure 7.12: Filterability trend for different reactants. Brine Mg^{2+} concentration = 1.25 mol/l; Brine flowrate = 1; N_{base}/N_{stoich} =1; NaOH concentration = 4 mol/l; $Ca(OH)_2$ concentration = 2 mol/l; Na_2CO_3 concentration =2 mol/l; NH_3 concentration = 14.7 mol/l.

In conclusion, sodium hydroxide solutions have led to product purity higher than 95% and complete conversion for Mg^{2+} in the brine, though the gel-like nature of particles suspension makes difficult the solid filtration. Calcium hydroxide presents the higher profitability, but co-precipitation of calcium salt lowers product purity to almost 50%, thus being not suitable for this purpose. Sodium bicarbonate allows recovering magnesium in two different forms, as hydroxide and carbonating. The higher average diameter of particles improves filtration capability of the system, though no high purity in $Mg(OH)_2$ can be expected. Finally, ammonia leads to a high purity product, though the weakness of the base, along with dilution phenomena generated by the direct mixing with the brine makes impossible to reach a quantitative recovery of magnesium.

According to these preliminary tests, MF-PFR technology is a simple and effective way to conduct reactive precipitation of magnesium hydroxide from saltworks bitterns. Potentials and limitations of using different alkaline reactants have been highlighted, indicating sodium hydroxide and sodium carbonate as feasible reactants, while the use of ammonia and calcium hydroxide raised problems related to the direct mixing of the feed brine with the alkaline solution, generating a low conversion and a low product purity, respectively. The possibility of using these latter reactants (showing the highest potential in terms of process profitability) is, therefore, conditional to the development of new reacting systems overtaking the identified limits of traditional MF-PFR crystallisation reactors as the CrIEM that is described in the next chapter.

Following the indication of this feasibility experimental campaign, and due to the high performance of NaOH, this was chosen as the alkaline reactant for the further experimental tests that are following reported.

7.4 Description of the laboratory pilot system: the second experimental campaign with MF-PFR

The second experimental campaign with MF-PFR was performed with a set-up slightly different than the system described above. However, the scheme reported in Figure 7.6 can be also considered for this set-up.

It provides an input for the brine coupled with four inputs for the reacting base, one at the beginning of the rector and the other three distributed along it at the same distant between them. In this case, the reactor is made with Plexiglas pipes, with an external

diameter of 8 mm and internal equal to 5.5 mm. Polyethylene connections with the same internal diameter were exploited to assemble all the parts (avoiding metal materials due to the high pH values of the circulating solutions). After each reagent injection follows a reaction path of constant distances at the end of which are located the sample collection taps and the horizontal flow stop taps. The reactor has a total length equal to 227 cm with a section equal to 19.6 mm^2. Each alkaline solution injection is 14 cm distant to each sampling tap. The final part, after the last sampling tap, is a PP tube essentially exploited for the product collection to a tank. In order to investigate the effect of the reactor length and the number of alkaline solution inlets, for few tests the reactor length was doubled adding also other four inlets for the precipitating solution.

Plexiglas was chosen due to its good properties: it has a good chemical resistance, it is more transparent than the silicon previously used and it is a rigid material making the assembling easier. New pumps (Seko Kronos C50) were employed in order to be more accurate and avoid error in the fluid handling.

The MF-PFR was tested changing different operative parameters in order to find the best configuration in the perspective of a possible scale-up. In particular the parameters are following listed:

- *Brine velocity* in the reactor, in order to study the effect of it on the nucleation and growth process. Using literature data for the viscosity and other necessary properties [66,140], it was estimated the Reynolds number for different velocity finding a value around 10^3, confirming that the motion is laminar;
- *Stoichiometry*, making tests at stoichiometric condition or with 10% excess, then in over-stoichiometric conditions;
- *Alkaline solution concentration.* Tests were performed at different NaOH concentration;
- *Use of desalinated water* instead of ultrapure water for the preparation of NaOH solution;
- *Reactor length*, in order to assess the effect of different residence time on the performance parameters;
- *Number of alkaline solution inlets.* Effect on the performance parameters.

The experimental conditions adopted for each test are reported in the following table.

Table 7.4: Operative conditions for the second experimental campaign with MF-PFR

Test	Mg^{2+} [g/l]	v_{brine} [cm/s]	Q_{brine} [ml/min]	NaOH [mol/l]	$\frac{N_{base}^{real}}{N_{base}^{stoich}}$	Q_{base} [ml/min]	N° inlets
1	24.96	4	47.12	4	1	24.20	4
2	24.96	4	47.12	4	1.1	26.62	4
3	24.96	2	23.56	4	1.1	13.31	4
4	24.96	8	94.25	4	1.1	53.24	4
5	24.96	12	141.37	4	1.1	79.86	4
6	24.91	8	94.25	4	1	48.30	4
7	24.91	8	94.25	4	1	48.30	4
8	24.91	8	94.25	8	1	24.15	4
9*	24.91	8	94.25	4	1	48.3	8
10*	24.91	8	94.25	4	1	48.3	4

* the reactor length is double than other tests

For each collected sample was performed the same analytical procedure than the first experimental campaign with MF-PFR. The solution were pumped for at least 5 times the residence time, in order to achieve the steady state condition and the sample were collected only after a stable condition. Each sample was collected waiting an appropriate time useful to reach again a stable condition.

After each tests, the rector was washed with ultrapure water then with hydrochloric acid solution and finally washed again with ultrapure water.

7.4.1 Stoichiometric effect of alkaline solution

In the first two tests performed with MF-PFR were utilized data and part of the operating conditions used in previous experimental campaigns, to verify the effect of an excess of 10% molar flow rate compared to the stoichiometric conditions, in order to obtain more compact particle size and with a lower value of cumulative diameters d10, d50, d90 (i.e. the diameter of 10% of particles, 50% of the particles and 90% of the particles respectively). However, this solution implies an evident economic backlash thinking of the process implementation on a large scale because more sodium hydroxide is needed if this is not justified by an important performance increasing.

Test 1, was performed in a stoichiometric condition while Test 2, was performed with an over-stoichiometric condition. The peristaltic pumps were properly calibrated in order to guarantee the best accuracy that was estimated in the range ±5% of the fixed flow rate.

The samples were collected from the fourth to the first in order to be sure that this operation doesn't influence the sampling; each sample was collected only when a time equal to four times the residence time was passed.

In the following figures can be observed the pH trend along the MF-PFR.

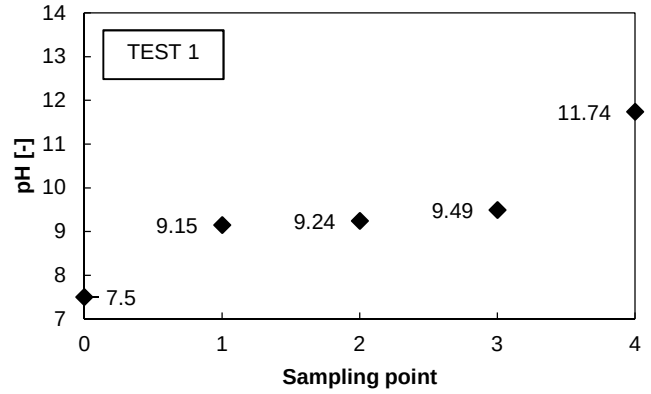

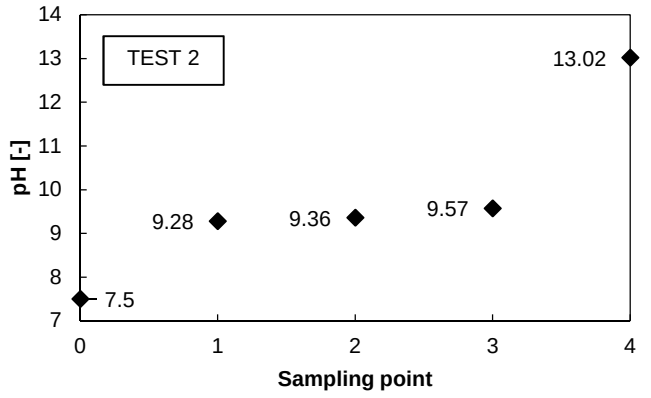

Figure 7.13: pH trend for the TEST 1 and TEST 2, stoichiometric and over-stoichiometric condition respectively.

As shown in Figure 7.13, the pH rises to a plateau value around pH 9 increasing at the fourth sample point when all the magnesium is precipitated as magnesium hydroxide. It can be observed that the pH value after the last alkaline solution injection (sampling point 4) is around 13 in the over-stoichiometric condition due to an excess of OH^- ions respect

to magnesium ions concentration in the brine. In the stoichiometric condition (TEST 1), the final pH should be slightly lower than the found value but is marginally different due to experimental error ascribed to alkaline solution preparation and flow rates.

The collected samples were also analysed with the laser granulometer Malvern Mastersizer 2000. The particles size distribution is following reported as CSD, before and after the use of an immersion sonicator (integrated at the granulometer) in order to try to de-cake the particles agglomeration. After few spot tests with different times and intensity, it was decided to use as standard value for the de-cake process a frequency equal to 20 kHz for a two minutes, finding that the CSD at this condition was the same than for higher exposition time or higher frequency. Only in this first comparison between TEST 1 and TEST 2 are shown both the CSD before and after the sonication step to show the difference but for the next results only the sonicated values will be reported.

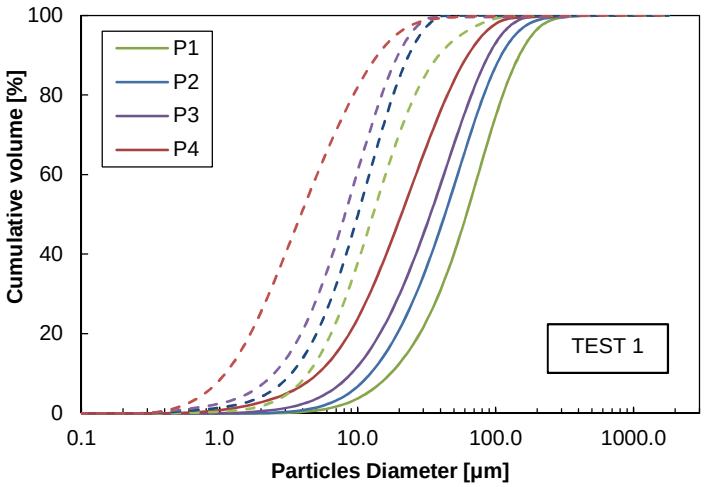

Figure 7.14: Cumulative Size Distribution for TEST 1 with sonication (dashed line) and without sonication (continuous line).

In Figure 7.14, the continuous lines represent the CSD for the unaltered samples whereas the dashed lines report the trend when the sonication, is applied. The Cumulative Size Distributions move toward lower particles diameter when a sonication is applied to the samples, demonstrating that the sonicator can broke some agglomerates.

The Cumulative Size Distribution for TEST 2 is reported in the figure below.

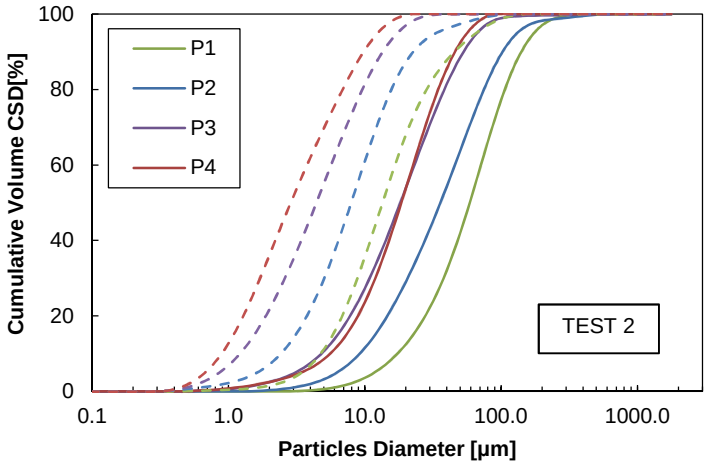

Figure 7.15: Cumulative Size Distribution for TEST 1 with sonication (dashed line) and without sonication (continuous line).

Similar trend than TEST 1 were obtained in the over-stoichiometric condition (TEST 2), showing also in this case a trend translation toward lower values when sonication is applied.

However, the most widely used method of describing particle size distributions is d values. The d10, d50 and d90 are commonly used to represent the midpoint and range of the particle sizes of a given sample. These can be calculated from the CSD as the diameter at the intercepts for 10%, 50% and 90% cumulative volume. In order to better represent the data and to better compare results from different experimental set-up, these d values will be also adopted in this work. It will be represented only the results after sonication.

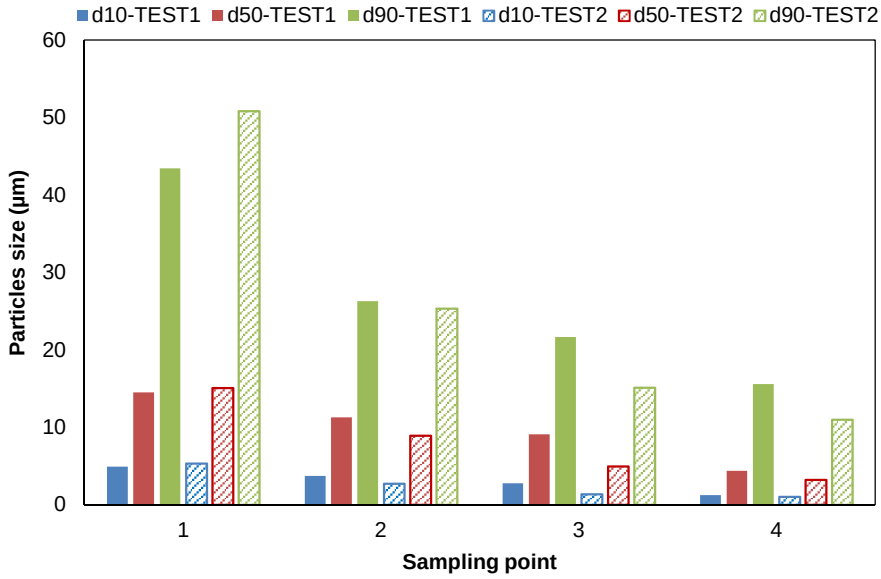

Figure 7.16: Comparison of characteristic particles size (d10, d50 and d90) for TEST 1 and TEST2, stoichiometric and over-stoichiometric condition respectively. Samples sonicated at 20 kHz for 2 minute.

According to Figure 7.16, the value in both configurations are similar for almost all the samples. Comparing the value for the last samples (4) when all the magnesium is precipitated, it can be noted that the value found in the TEST 2 with over-stoichiometric condition is only slightly lower than TEST 1.

The residual magnesium concentration in the brine solution was measured with an Ionic Chromatograph (Metrohm 882 Compact IC Plus). The Mg concentration was used to calculate the conversion, an important performance parameter (for the equation see previous paragraph). The graphs with the calculated conversion are reported below using as abscissa the ratio between the total length of the reactor (sample 4 in the rappresentative scheme Figure 7.6) and an intermediat lenght.

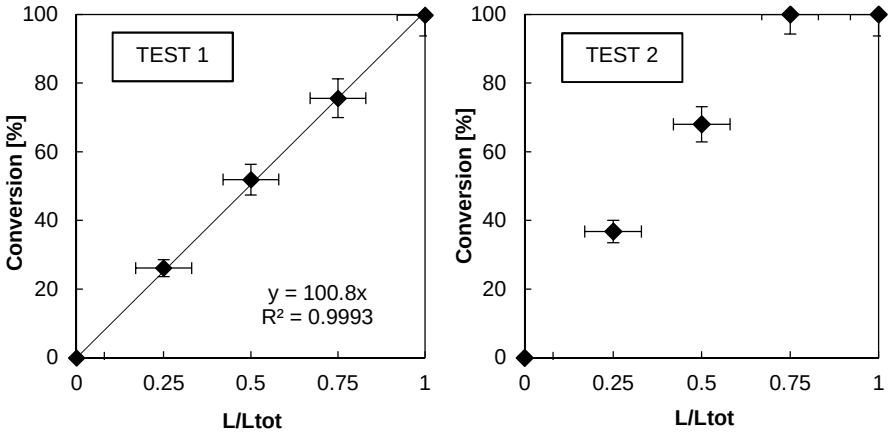

Figure 7.17: Magnesium conversion present in the brine for TEST 1 and TEST 2 as a function of L/L_{tot} (ratio between the total reactor length and an intermediat reactor length).

As can be observed in Figure 7.17, in the stoichiometric condition (TEST 1) the conversion follows perfectly a line having a total conversion in the last samples. On the other hand, in the over-stoichiometric condition the maximum conversion is already obtained before the last sample due to the excess of OH^- ions introduced in the reactor.

The purity of the magnesium hydroxide precipitated was 100% in both the tests analysed in this section.

7.4.2 Brine flow velocity effect

TEST 3, TEST 4 and TEST 5 are conducted at different brine flow velocity (2 cm/s, 8 cm/s and 12 cm/sec respectively) in order to study the influence of this parameter on the process performance indexes. On the base of this velocity, all the flow rates were adapted fixing the same other parameters equal to TEST 2 with 4 cm/s as brine flow velocity (see Table 7.4 for more details).

The pH trends give also in this cases an idea on the on the reaction progress along the reactor (see Figure 7.18)

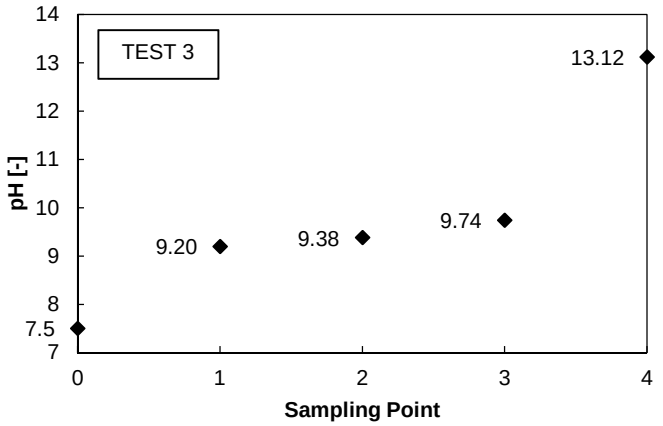

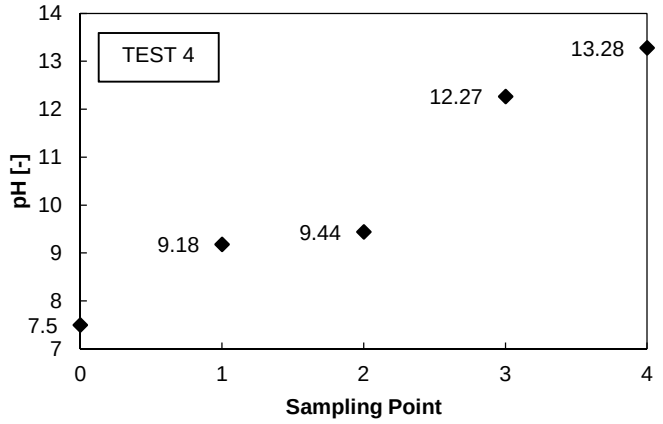

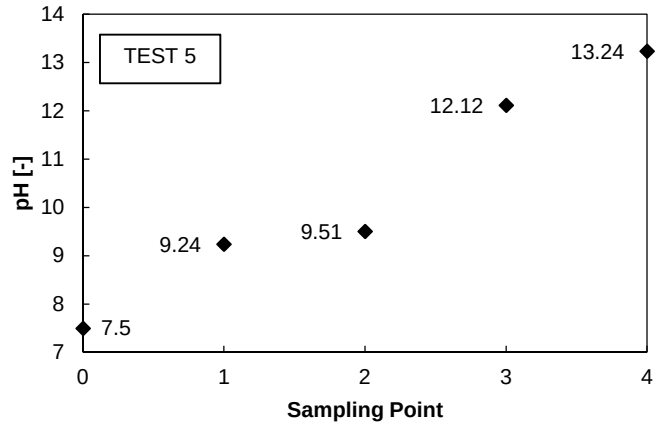

Figure 7.18: pH trend for the TEST 3, TEST 4 and TEST 5, at 2 cm/sec, 8 cm/sec and 12 cm/sec respectively.

Due to an over-stoichiometric condition in all three tests, the pH is around 13 at the final sample. Only TEST 3 shows a difference respect to the other two tests for the sample 3, likely experimental errors due to the low brine flow velocity.

These three tests were also compared on the granulometric distribution point of view. The d10, d50 and d90 values for these three tests were compared between them and with TEST 2, after the sonication treatment. The histograms are shown in the following figures:

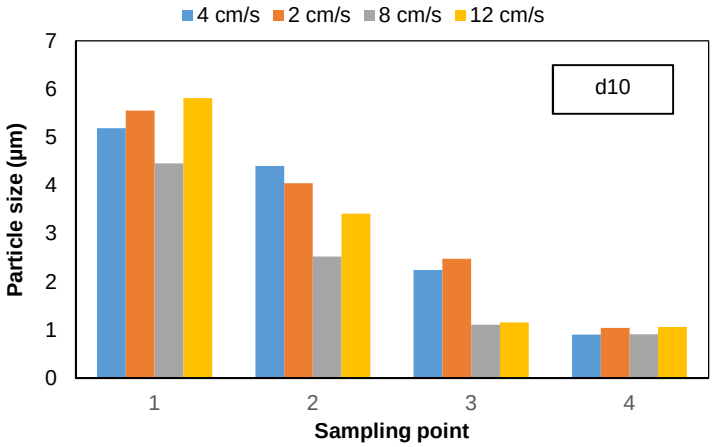

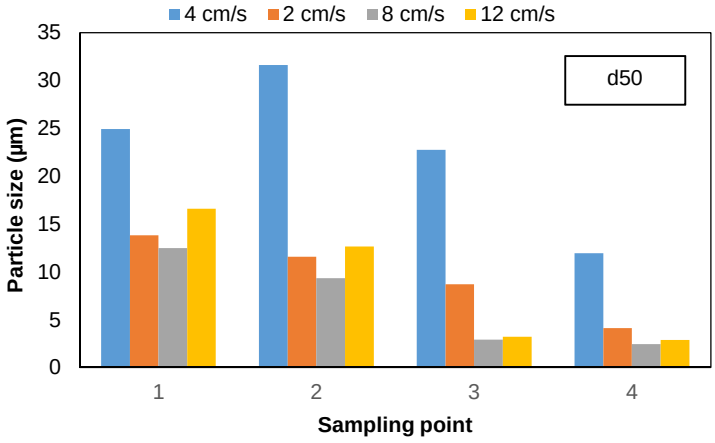

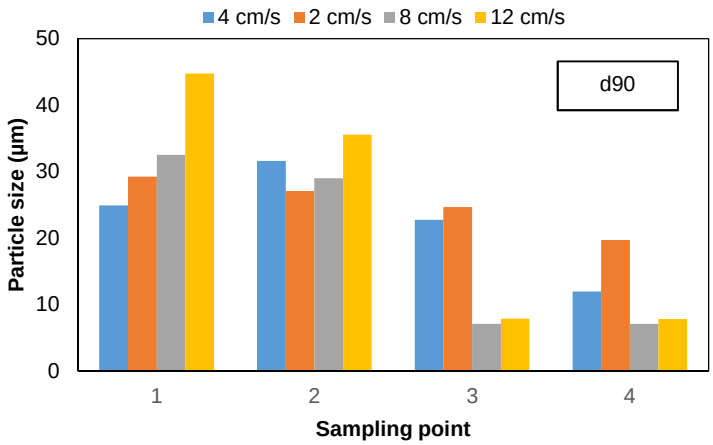

Figure 7.19: Comparison of d10, d50 and d90 between TEST2, TEST 3, TEST4 and TEST 5 (4 cm/s, 2 cm/s, 8 cm/s and 12 cm/s respectively). Samples sonicated at 20 kHz for 2 minute.

Figure 7.19 clearly shows the best performance (particles size d90 lower than 10 µm, specification of magnesium hydroxide for flame retardant) for high speed. In particular, 8 cm/sec has performance slightly better than 12 cm/sec. For this reason, further tests were performed at 8 cm/sec.

All the solid magnesium hydroxide produced, had purity around 100 %. The conversion trends are not shown because this data can be already deducted from the pH trend; after pH 10.5 all the magnesium in the brine is converted into magnesium hydroxide.

7.4.3 Confirmation of the best operative conditions with stoichiometric alkaline solution and analysis on the use of desalinated water for a possible industrial scale-up

These experimental tests (TEST 6 and TEST 7) had the objective to confirm the best condition reached with the TEST 4 (8 cm/s) in terms of granulometric distribution using a stoichiometric concentration and to evaluate the effect of artificial desalinated water (TEST 7), instead of the ultrapure water, for the preparation of the alkaline solution. In particular, 143 mg of NaCl per litre of prepared solution, were introduced in order to bring the solution to conductivity values similar to those hypothetically obtainable by means of RO process from sea water, in the perspective of an industrial scale- up.

The pH trends are reported in Figure 7.20.

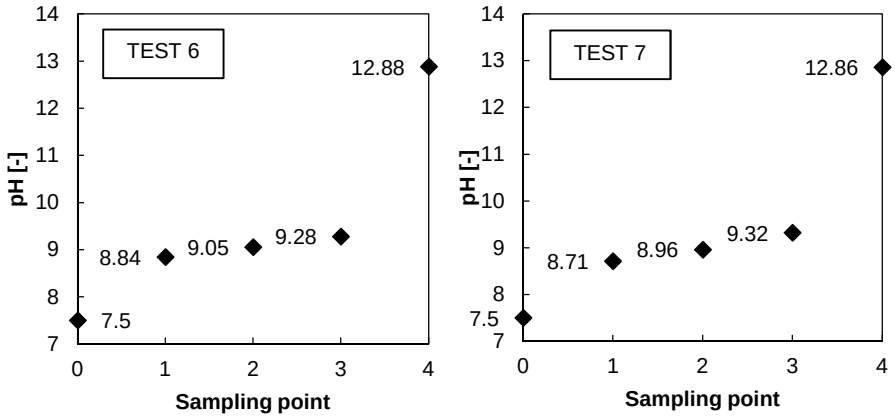

Figure 7.20: pH trend for the TEST 6, TEST 7, using ultrapure water (TEST 6) and artificial desalinated water (TEST 7) for the alkaline solution preparation.

The two trends are almost superimposable, demonstrating that the reaction path is not influenced by the solvent used for the alkaline solution preparation. The final pH value confirms the total conversion of magnesium into magnesium hydroxide.

These two tests were also compared in terms of granulometric distribution. The comparison is following reported.

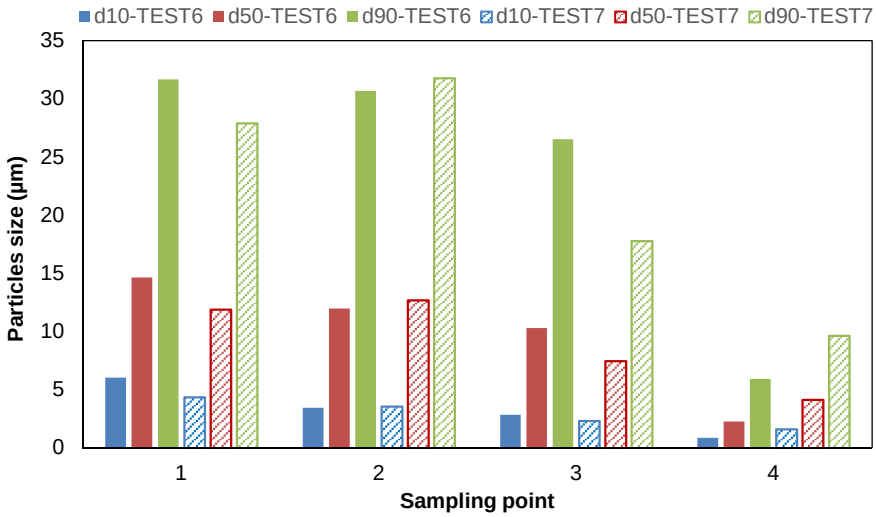

Figure 7.21: Comparison of characteristic particles size (d10, d50 and d90) for TEST 6 (alkaline solution with ultrapure water) and TEST7 (alkaline solution with artificial desalinated water). Samples were sonicated at 20 kHz for 2 minute.

The artificial desalinated water has an effect on the particles size distribution, showing higher different value compared to the value obtained using ultrapure water. However, the d90 for the final sample (4) is lower than 10 µm, confirming the possibility to use "industrial" water in a hypothetical process scale-up. Even if Test 6 is run with a stoichiometric alkaline solution, the obtained performance confirm the good results shown for the TEST4.

All the solid samples had a magnesium concentration around 100% in terms of magnesium hydroxide purity.

7.4.4 Study on the effect of the alkaline solution concentration

The set-up with short MF-PFR was exploited to evaluate the effect of a doubly concentrated alkaline solution (NaOH 8M) for the precipitation of magnesium hydroxide from saltwork brine. The use of such solution could optimize the process in terms of a lower amount of water introduced into the reactor, a lower dilution and a consequent reduction in costs associated with the movement of fluids imagining a process implementation on an industrial scale. However there are disadvantages due to more restrictive safety measures for the use of this solution, a greater risk of corrosion and

consequent damage to the pipe system and more important a possible effect of this high concentration on the nucleation, improving it at the expense of crystal growth.

The pH trend is reported in Figure 7.22

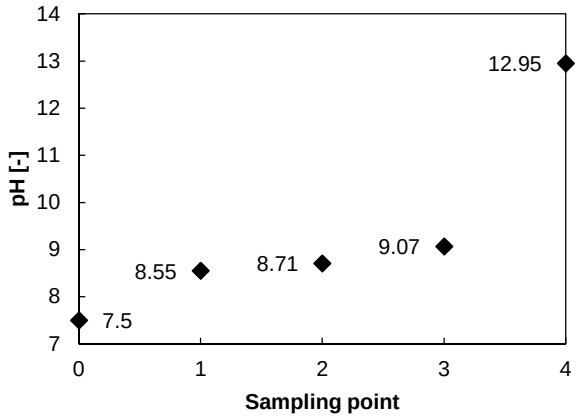

Figure 7.22: pH trend for the TEST 8, using alkaline solution at 8M.

It is evident also with high alkaline solution concentration that the pH trend has a plateau around 9 and it increases only in the last reactor section where all the magnesium is precipitated.

The granulometric distribution is compared with the TEST 6 (NaOH 4M) because it was run at the same condition but with half alkaline solution concentration, in order to highlight the effect of this parameter on the process performance.

It can be observed in Figure 7.23 that the performance in terms of particles size distribution is similar for the last samples but there are differences along the reactor.

In the magnesium recovery process, a pH control is really important in order to minimize the nucleation process and avoid waste of raw material. If the alkaline solution concentration is high, the system control became more difficult because a small deviation on the nominal flow rate has a strong effect on the pH. For all this reasons, a higher alkaline solution concentration does not give advantages respect to a typical concentration used in this experimental campaign.

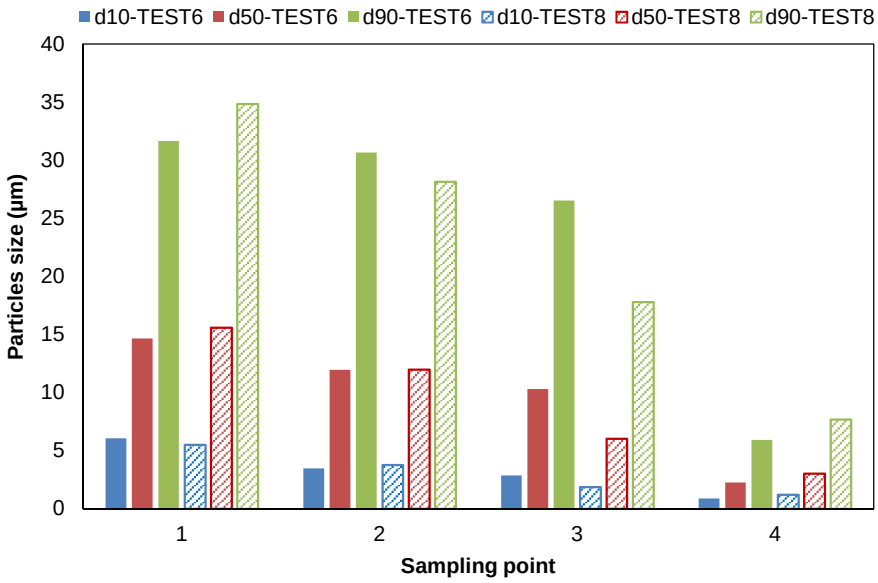

Figure 7.23: Comparison of characteristic particles size (d10, d50 and d90) for TEST 6 (4M of alkaline solution concentration) and TEST8 (8M alkaline solution concentration). Samples were sonicated at 20 kHz for 2 minute.

The purity of the solid magnesium hydroxide was also in this case more than 99.5%.

7.4.5 Effect of the length and number of injections on the reactive precipitation process

The set-up of the MF-PFR was slightly modified to double the total length and to introduce other four injection points for the alkaline solution.

In the TEST 9, the alkaline solution was divided into eight sections along the reactor. The brine flow velocity was fixed at 8 cm/s maintaining the other parameters equal to the TEST 6 with four injections. In this way, the total residence time is double and the alkaline solutions are subdivided.

The pH trend is reported in Figure 7.24.

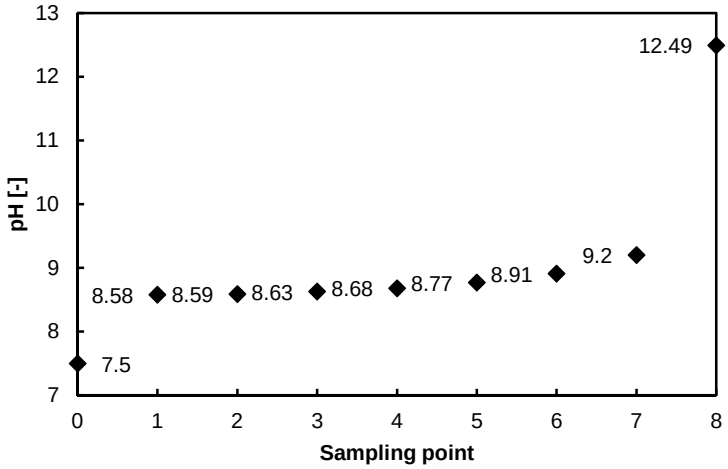

Figure 7.24: pH trend for the TEST 9, with 8 alkaline solution injection and a reactor with double length than the tests 1-8.

The pH is practically constant in almost all the reactor, increasing only in the final sampling point where all the magnesium was recovered as magnesium hydroxide. Although in this test was fixed a stoichiometric condition, the pH in the sample 8 is higher than 10.5, the value required for the total conversion of magnesium into magnesium hydroxide. This fact confirms that a small error in the alkaline solution flow rates can have an important effect on the process pH control.

In order to better show the behaviour of this set-up on the granulometric size distribution, both trends, with and without sonication are reported.

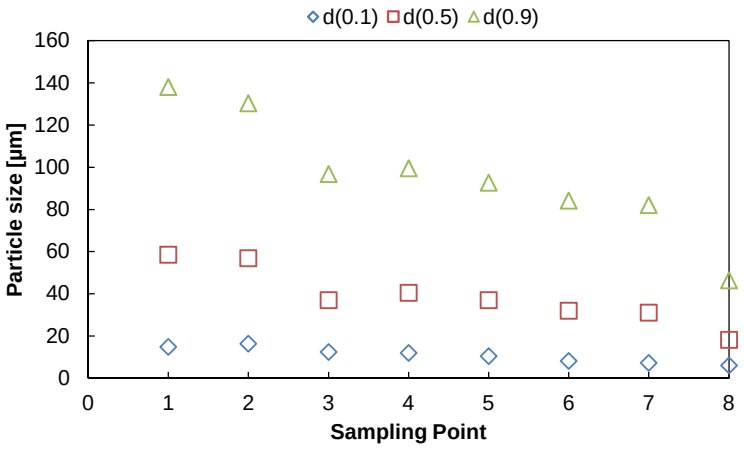

Figure 7.25: Characteristic particles size (d10, d50 and d90) for TEST 9 with eight alkaline solution injections.

The collected samples were treated with a sonicator at 20 kHz for two minutes, highlight a particular effect of it on the particle size distribution.

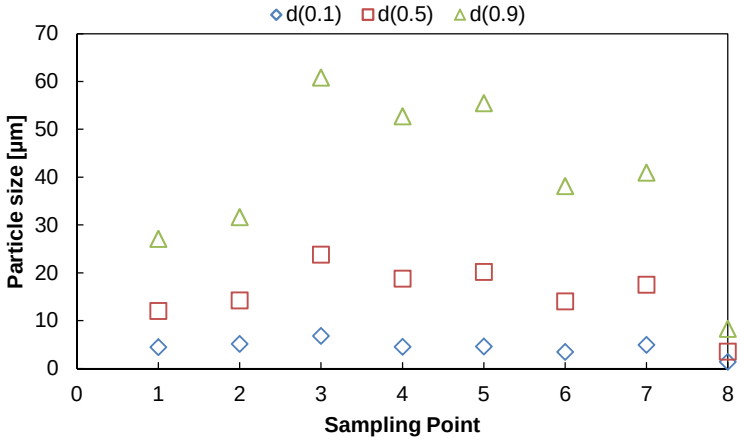

Figure 7.26: Characteristic particles size (d10, d50 and d90) for TEST 9 with eight alkaline solution injections. Samples were sonicated at 20 kHz for 2 minute.

Due to the particular trend shown in Figure 7.26, the analyses were performed two times highlighting the same trend. It seems that in the middle reactor part, the obtained

particles have higher size, likely due to a higher agglomeration effect even if the samples were sonicated at high intensity.

The same reactor was exploited in the TEST 10 investigating the effect of a longer PFR with only four alkaline solution injections. The same experimental parameters than TEST 6 were fixed also in this TEST 10, having only a double resident time and a double length between an ignition and the subsequent one.

The pH trend is following reported.

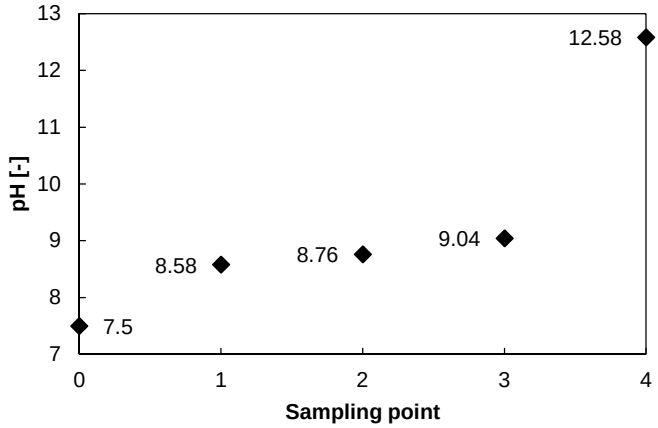

Figure 7.27: pH trend for the TEST 9, with 4 alkaline solution injection in a reactor with double length than the tests 1-8.

The trend is in line with the other tests previous analysed. The granulometric distribution was compared with the result of TEST 6, in order to compare the effect of a longer reactor on the particles size distribution. The comparison is following reported.

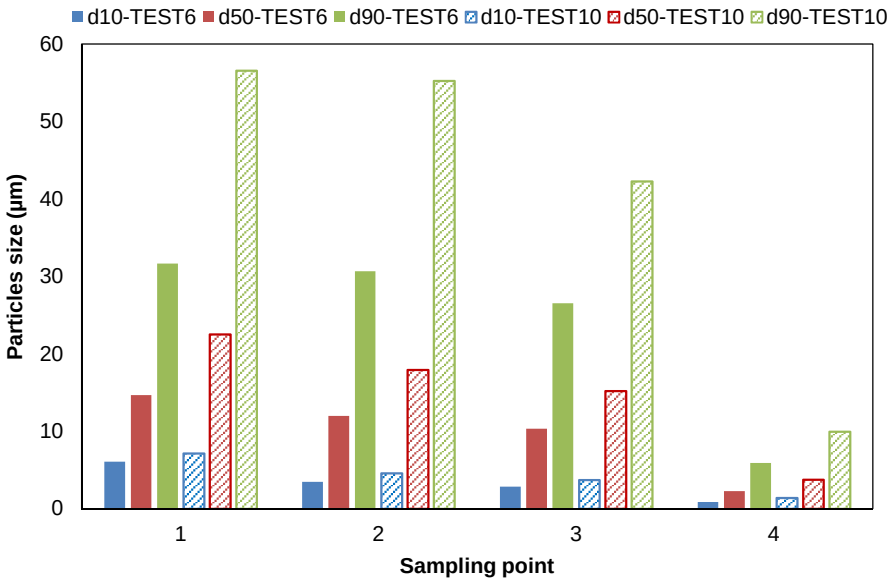

Figure 7.28: Comparison of characteristic particles size (d10, d50 and d90) for TEST 6 and TEST10 with a double reactor length. Samples were sonicated at 20 kHz for 2 minute.

It is evident from Figure 7.28 that the average particle distribution is higher for the tests made with a longer reactor.

The powder of magnesium hydroxide obtained had a purity higher than 99.5%.

7.5 Conclusions and remarks on MF-PFR

As it was demonstrated in all the tests described in the previous sections, magnesium can be recovered from saltwork waste brine by means of Multiple Feed-Plug Flow Reactor. The effect of different operative parameters were investigated with the lab test-rig, highlighting that a short reactor with intermediate brine flow velocity (8 cm/s) and sodium hydroxide at 4M, give the best condition in terms of particles size distribution for using it as flame retardant additive. It was also demonstrated that magnesium hydroxide with purity higher than 99.5% can be obtained also using a desalinated water so it is not strongly influenced by the quality of water used for the alkaline solution preparation. This fact is important if this process would be applied in an industrial scale.

In order to confirm the quality of the magnesium hydroxide produced with the MF-PFR, the flame retardant magnesium hydroxide benchmark (MAGNIFIN® H5 by Huber) was analysed and compared with the powder produced in the TEST 6.

In Table 7.5 are reported the main characteristic declared by the company.

Table 7.5: Magnesium hydroxide technical specification for MAGNIFIN® H5 [175].

$Mg(OH)_2$	[%]	≥ 99.8
Particle Size - d10*	[µm]	0.7 – 1.0
Particle Size – d50*	[µm]	1.6 – 2.0
Particle Size – d90*	[µm]	2.4 – 4.4
Specific Surface Area (BET)	[m^2/g]	4.0 – 6.0

* measured by MALVERN MASTERSIZER 2000 (laser diffraction)

An Ion Chromatograph (IC 882 Compact Plus – Metrohm) was used to analyse a MAGNIFIN® H5 sample confirming that the purity is higher than 99.5% as obtained also for the magnesium hydroxide precipitated in the TEST 6. This was also confirmed by EDAX analysis (Figure 7.29)

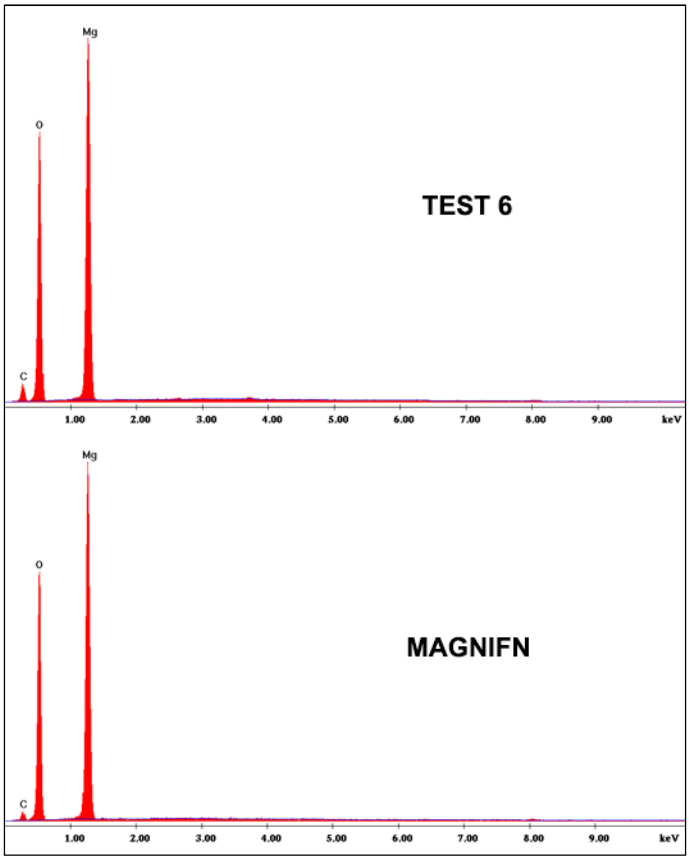

Figure 7.29: EDAX analysis for the magnesium hydroxide from TEST 6 and MAGNIFIN.

A Laser Granulometer (MALVERN MASTERSIZER 2000) was exploited to assess the particle size distribution declared by Huber Company for its product. The results were compared with the value found in the TEST 6 and shown in Figure 7.20. The comparison is reported in Figure 7.30.

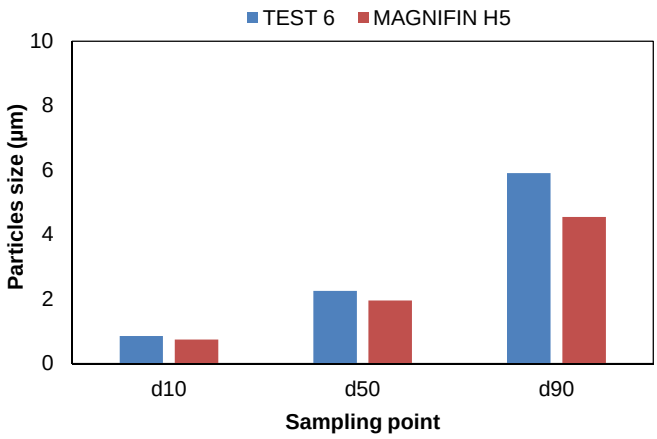

Figure 7.30: Comparison of particles size distribution for the TEST 6 with MF-PFR and the flame retardant magnesium hydroxide benchmark (MAGNIFIN® H5). Samples were sonicated at 20 kHz for 2 minute.

The particles size value d10, d50 and d90 reported in the technical datasheet were confirmed by the results reported in Figure 7.30. Furthermore it was highlighted that the distribution obtained in the TEST 6 is only slightly higher than the best value of the flame retardant specific market.

In order to confirm these results, a Specific Surface Area (BET) was measured discovering that the value for the magnesium hydroxide powder from the TEST 6 is one order of magnitude (~ 50 m^2/g) higher than the MAGNIFIN. A Scanning electron microscope (SEM) was exploited to see the real structure of the two samples, and the pictures at different magnifications are following shown.

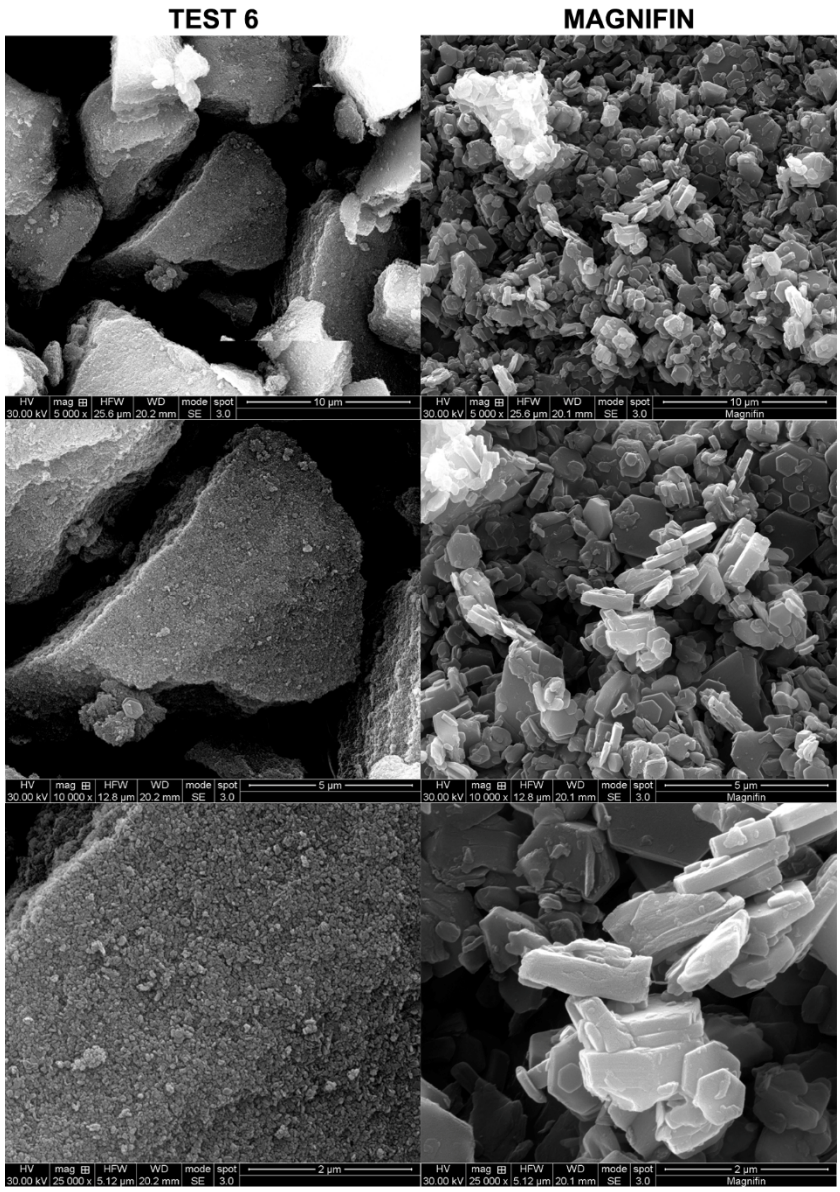

Figure 7.31: SEM pictures at different magnifications (5000X, 10000X and 25000X) of the magnesium hydroxide and MAGNIFIN H5 samples.

It is clear from Figure 7.31 that the magnesium hydroxide produced with the MF-PFR are agglomerates of small crystals (100-500 nm) whereas the MAGNIFIN is constituted by single crystal with the right dimensions in the range 1-5 µm. Likely, the nucleation is

much higher than grown in the MF-PFR and the small crystals are compacted in strong agglomerations that cannot be broken with the sonicator. This could be the reason that the trends previous shown from the laser granulometer are not coincident with the SEM results.

Nevertheless the magnesium hydroxide produced by MF-PFR is not still usable for the flame retardant material, it was demonstrated the possibility to recover magnesium from a waste saltwork brines with really high purity (always more than 99%). However, another important big market for the magnesium hydroxide, as reported in the section 6, is the nutraceutical and pharmaceutical field. In that case, the most important restriction is the solid purity and high Specific Surface Area, both characteristics already obtained with the MF-PFR.

In the next part of the thesis will be described other activities focused on the study of the reactive precipitation process; in particular, new configuration will be analysed in order to improve the grown stage at the expense of the nucleation. For this purpose, a classic CSTR is used due to its process flexibility.

8 CRYSTALLIZER WITH ION EXCHANGE MEMBRANE

Abstract

In this chapter, a patented Crystallizer with Ion Exchange Membrane (CrIEM) is proposed for the production of magnesium hydroxide from exhausted brine. The device consists of two channels with different electrolyte solutions, i.e. a brine and an alkaline solution, separated by an ionic exchange membrane. The membrane allows the selective transfer of OH^- ions from the alkaline solution to the brine which reacts with Magnesium, precipitating as Magnesium Hydroxide. In the opposite direction Cl^- anions diffuse through the membrane, significantly contributing in generating the actual driving force of the process, i.e. the different electrochemical potential of anions between two channels.

The big advantage of CrIEM technology is that the two solutions are not mixed, thus any kind of alkaline solution can be adopted, even if in conventional crystalliser this could give rise to a lower product purity due to co-precipitation phenomena.

Thus, in CrIEM technology low-cost reagents can be used to produce high-quality product thanks to the selective transferring of ions.

In this chapter, the design, construction and testing of different prototypes of CrIEM reactor are presented, analysing their performance also changing several operative parameters. The main operational issues arisen in the membrane crystallizer have been identified and some solutions have been proposed and tested.

8.1 Introduction and state of art on the Crystallizer with Ion Exchange Membrane

As widely described in the previous sections, magnesium hydroxide is valuable chemical that can be precipitated from concentrated brines by mixing them with an alkaline reactant. Even if common bases are suitable for the process, several limitations arise from direct reactive precipitation: by-products formation and dilution phenomena could prevent to reach a proper purity or a complete magnesium recovery (see chapter 7).

A novel crystallizer based on ion exchange membranes (CrIEM) was developed to overcome process limitation. An anionic exchange membrane segregates the alkaline solution from the brine, allowing Cl^- and OH^- to be exchanged between the two solutions under a self-generating electrochemical potential gradient. As the brine pH arises above 9, the supersaturation is quickly reached and $Mg(OH)_2$ precipitates.

CrIEM technology is a novel ion exchange application, patented by Cipollina et.al in 2015 [170], that allows reactive crystallization for separation of valuable species (e.g. Mg from brines) with a large flexibility in the choice of reactants. The use of IEM prevents undesired species to induce low product purity. Nevertheless, some bottlenecks have been identified: (i) channel plugging phenomena and (ii) high area requirement in a possible up-scale application arise respectively from the suspension formation and low fluxes recorded. For this reason, the core of R&D activities reported in this thesis is focused on fluid dynamics analysis, on novel prototype geometries and on new IEMS able to guarantee high fluxes, high selectivity and low cost.

In more details, the CrIEM technology allows the controlled mixing of ionic solutes from two different solutions, aiming at a reactive crystallization process, finely controlling the presence of useful reactive species and the absence of dangerous ones through the use of an ion exchange membrane. A CrIEM reactor consists of two channels separated by an ionic exchange membrane, one for the feed stream from which a product has to be crystallized, and the other for the stream containing the ionic reagent. Figure 8.1 reports a scheme of a generic reactive precipitation process utilizing the CrIEM technology with an alkaline solution as precipitating agent.

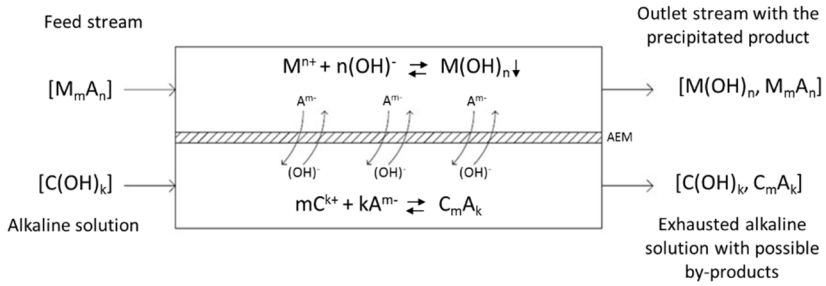

Figure 8.1: Process scheme of the CrIEM technology for the precipitation of a generic species M(OH); M= element to be precipitated, A=anion related to M, C=cation related to the alkaline reactant, OH= hydroxyl group of the alkaline reactant, n and k are stoichiometric coefficients [170].

The "feed stream solution" has the "M" ion that we want to precipitate and a counterion "A" (anion in the example). The ionic exchange membrane allows the selective transfer of anion "A" but not cation "M". At this point, there isn't a charge equilibrium that forces the hydroxide ion passing from one channel to the other channel. The hydroxide ion reacts with the cation "M" producing a molecule slightly soluble that precipitate, obtaining a suspension in which there is the required product (Outlet stream with the precipitated product). The anionic exchange membrane, being selective only for anion, it doesn't allow the pass of the cation "C" (the hydroxide's counterion), not allowing a concurrent precipitation reducing sensibility the required product. The driving force that allows the ions movement is an electrochemical potential different between the two channels. The difference between the CrIEM and the classic precipitation technology, in which the precipitation allows with direct contact between the reagents, is that in the first one it possible to use every kind of reagents without any risk to have product with low quality.

The CrIEM technology is applied in this thesis work to produce magnesium hydroxide from exhausted brine. The precipitation of $Mg(OH)_2$ from such brines has been demonstrated as technologically feasible. However, an alkaline reactant is required for the reactive precipitation process. NaOH has been successfully tested, but its high cost, can significantly affect the economic competitiveness of the process. On the other side, the use of low-cost reactants (e.g. $Ca(OH)_2$) leads to dramatic losses in the product purity, due to the co-precipitation of by-products, as shown with the MF-PFR. A CrIEM reactor can, therefore, be used to face and solve the problem according to the following process schemes:

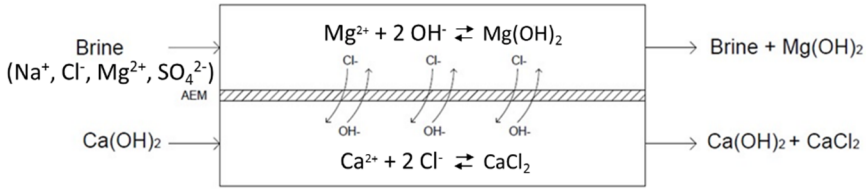

Figure 8.2: Illustrative scheme of the CrIEM process to precipitate $Mg(OH)_2$ from exhausted brine with $Ca(OH)_2$ [170].

In the CrIEM technology is involved the use of low-cost reactants (e.g. $Ca(OH)_2$) to precipitate magnesium hydroxide from exhausted brine (Figure 8.2). In this case, the membrane allows the passage of hydroxide ions from alkaline solution, but rejects calcium ions, thus avoiding any contamination of the final product. Chloride ions pass in the opposite direction to restore the electroneutrality, generating a $CaCl_2$ solution. This demonstrates how to use a low-cost reactant as calcium hydroxide, obtaining purities greater than conventional processes.

According to the characteristic of the CrIEM technology, this can be proposed as a viable alternative to conventional systems for reactive crystallization. The main innovative characteristics of CrIEM technology are highlighted below:

- Possibility of using of low-cost reagents not suitable for conventional reactive crystallization processes, due to the formation of by-products when mixed with the feed solution, thus affecting the final product purity;
- Possibility of dramatically reducing the environmental impact of the reactive crystallization process, by selecting with large flexibility the best performing and less polluting reactant;
- No moving parts, thus minimizing the risk of mechanical failure as in the CSTR;
- Modular process and device;
- Low footprint of the plant;
- High potential for technological development linked to the development of optimized membrane.

The idea of the CrIEM reactor was also inspired by the technical and scientific literature that has showed in the last years several processes that utilize ionic exchange membrane for different application, ranging from electrical energy production (reverse electrodialysis), to desalination (electrodialysis). On the other side, reactive crystallization

is a well-known process used for the separation of high-value compounds from solutions. However, no example of membrane reactive crystallizer has been developed so far for similar application.

The CrIEM‘s closest example of using IEMs for shift reactions is the Donnan dialysis process, where cationic or anionic exchange membrane are used in a stack as shown in the following Figure 8.3.

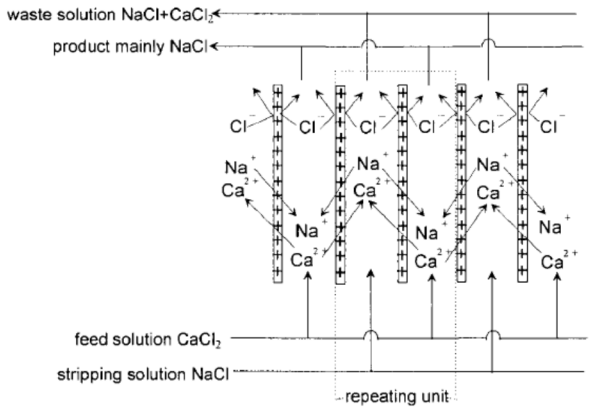

Figure 8.3: Scheme of Donnan dialysis process [129].

The driving force for ions transport is the different species concentration in the solutions separated by the membrane. A typical application of Donnan dialysis is the removal of bivalent ions such as Ca^{2+} (softening) through the exchange of monovalent ions such as Na^{+}. In the example showed in Figure 8.3, a solution containing $CaCl_2$ and a stripping solution with high concentration NaCl are fed alternately in the channels of a stack with cation exchange membranes. Due to the concentration gradient, Na^{+} ions diffuse through the membrane from the "stripping solution" to "feed solution", while Cl^{-} ions cannot pass through the cationic exchange membrane. The lost in electro-neutrality forces Ca^{2+} ions to migrate in the opposite direction, removing such bivalent cations from the "feed solution" [129].

Other applications of the Donnan dialysis concern the removal of ionic species from aqueous solutions. For example, removal of boron from desalinated water [176] or bromide from industrial waste water [177], fluorinated compounds from contaminated solutions [178], or, finally, nitrates from waste waters [179]. Many other processes have

been studied in recent years for the removal of heavy metals in dilute solutions, but when the concentration of the components in the solutions increase, the osmosis processes significantly reduce the process efficiency [180]. In all these examples, the ionic exchange membranes are used essentially for the removal of species from a stream, but for reactive precipitation. The reactive precipitation processes are widely described in the scientific literature; in particular, batch, semi-batch, CSTR reactors, MF-PFR or electrolytic cells are often presented as options for the required equipment, but no device adopting ion exchange membranes has been presented so far.

The possible recovery of magnesium from waste brine was widely demonstrated by Cipollina et. al [6,7] and in the present thesis work. However, the high cost of the reagent used (NaOH) significantly reduces the profitability of the process. On this basis, the idea of developing the technology CrIEM can directly face the issue of adopting low-cost reactants, not suitable for conventional reactive precipitation processes, in order to induce a revolutionary change in the economy of the process itself.

8.2 Design and construction of the first version of CrIEM (v01)

One of the activities carried out within this thesis work, was the realization of a benchtop prototype of a membrane reactor. The flat geometry was chosen for the equipment: this configuration is well suited for laboratory scale studies due to the simplicity of construction and assembly, and the possibility to monitor externally the process. Figure 8.4 shows a conceptual scheme of the constitutive elements of the first version of CrIEM. The section shows: a membrane film (red element) separated by two channels obtained by means of a polymeric gasket (blue element); an external Plexiglas plate ensures the equipment tightness by means of clamping bolts (white element) whereas a spacer, i.e. a woven knit network, ensures that any membrane deformations do not obstruct the channel (green element). During the equipment commissioning, the solutions flow in the two compartments through the spacer, following the channel tracing from the inlet to the outlet of the module, modifying its concentration due to the driving force for the different concentration.

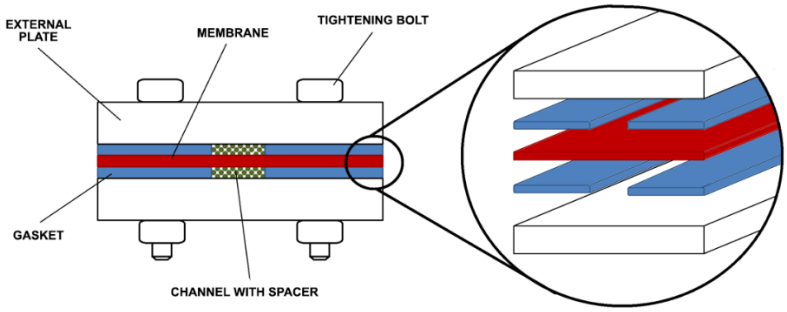

Figure 8.4: Constituting elements of the membrane module (first version). In white, the external plates; in blue, the gaskets; in green, the spacer; in red, the membrane.

The ion exchange membrane is positioned between the gasket and then by the two Plexiglas plates. These last elements had a thickness of 2 cm to avoid a warping of the plate and to distribute the stress homogeneously over the entire surface. The CAD scheme with the dimensions is reported in Figure 8.5.

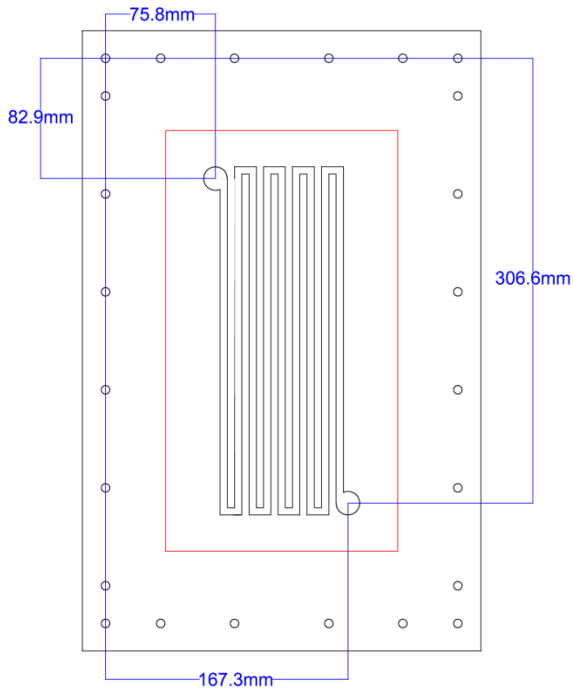

Figure 8.5: CAD scheme of the first version of CrIEM reactor with the construction dimensions.

The red rectangle represents the membrane whereas the path was realized in a polymeric gasket. The channel has a width of 5 mm and a total length of 192 mm. In each path stretch was positioned a plastic spacer with thickness of 700 µm to mechanically support the membrane.

After the first sealing tests, the rector was slightly modified adding other twelve bolts closer to the channels to avoid a leakage from one channel to the others. These details can be observed in the picture shown in Figure 8.6.

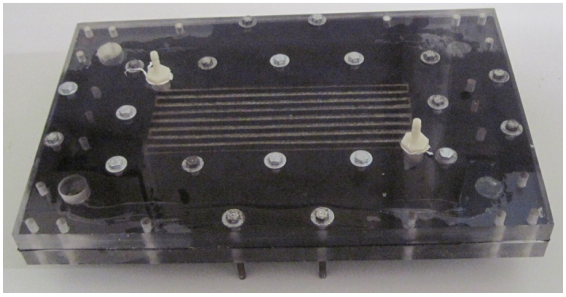

Figure 8.6: First version of the CrIEM reactor.

8.2.1 Test description and experimental procedure with the first test-rig of CrIEM (v01)

A critical parameter in the experimental campaign was the choice of membranes. Unlike solidly developed applications, such as electrodialysis, there are no membranes specifically developed for the precipitation of magnesium hydroxide from brine. Ideally, the membrane to be used should possess certain properties such as: high permselectivity, high chemical resistance, low specific resistance and low water permeability. Some of these features are in clear contrast: a membrane that achieves high ionic flows is normally hydrophilic and, therefore, has high water permeability.

The pH resistance was key parameter that guided the choice among the commercially available membranes. The only membranes chosen for the first experimental campaign were: Selemion AHO (AGC), Fumasep FAA-3-PK-130 (Fumatech) and Fujifilm RP1. The technical characteristics are presented in the following table.

Table 8.1: Chemical-physical properties of Fumasep, Selemion and Fujifilm membranes.

Properties	Fumasep FAA	Selemion AHO	Fujifilm RP1
Thickness [μm]	130	300	120
Ion exchange capacity [meq/g]	1.43	n/a	1.28
Membrane resistance [Ω cm^2]	1.9	20	1.84
pH stability range	1-14	1-12	4-12
Thermal stability range [°C]	n/a	5–60	n/a

The experimental set-up exploited in the preliminary tests is represented in the following scheme.

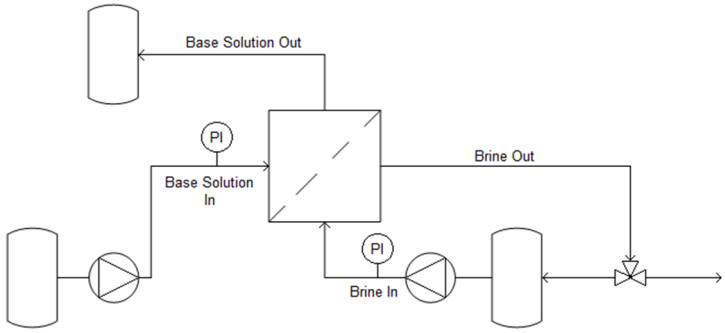

Figure 8.7: Generic experimental set-up for the tests made with CrIEM.

A fresh alkaline solution was fluxed in an open loop from a tank to another whereas the brine was continuously re-circulated in a closed loop in order to increase the pH to appropriate values for the precipitation. The solutions were moved by peristaltic pumps and pressure gauges were used to check the pressures during the test.

Before each tests, water was fluxed in both channels from two graduated tanks in order to check possible leakage between base and brine compartment. The seal in the channel path of each side was optimized using silicone grease in order to avoid possible bypasses consequently reducing the solution permanent time in the reactor.

The preliminary experimental tests have the purpose to proof the concept of the CrIEM technology. Different commercial ion exchange membranes were tested estimating the migratory flux of hydroxyl ions with different basic reagents. In the first stage of the experimental campaign, artificial brine with 4M of NaCl was used to investigate the transport phenomena through the membrane. Only after estimating the flux, the artificial

saline solution was replaced with the real brine. Table 8.2 lists the experimental condition for the tests carried out with the CrIEM (v01). The two membranes presented above were tested with three different solutions: distilled water, calcium hydroxide and sodium hydroxide.

Table 8.2: Experimental condition for the preliminary tests with CrIEM (v01)

Test		**NaCl solution**			**Alkaline solution**	
Membrane	**Base Sol.**	**Conc [mol/l]**	**pH**	**Cond [mS/cm]**	**Conc [mol/l]**	**pH**
Fumatech	Water	4	6.92	229	-	-
Fumatech	$Ca(OH)_2$	4	6.8	235	5.87E-03	12.07
Fumatech	NaOH	4	6.8	235	1.07E-02	12.03
Selemion	$Ca(OH)_2$	4	6.8	235	5.87E-03	12.07
Selemion	NaOH	4	6.8	235	1.07E-02	12.03
Fujifilm	$Ca(OH)_2$	4	6.8	235	5.87E-03	12.01
Fujifilm	NaOH	4	6.8	235	1.07E-02	12.09

Distilled water. Water represents a potential basis due to the autoprotolysis reaction, namely the self-ionization of water forming hydronium and hydroxyl ions. The autoprotolysis equilibrium of water results in a concentration of the two ionic species equal to 10^{-7} mol/l at 25 °C. However, this equilibrium can be altered by the electrochemical potential gradient of a concentrated NaCl solution in a CrIEM reactor, segregated by an anionic membrane, according to the diagram shown in Figure 8.10.

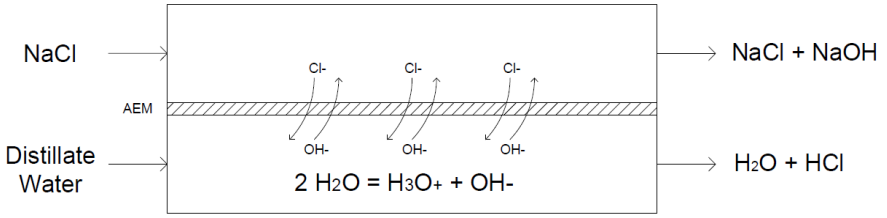

Figure 8.8: CrIEM functioning with NaCl/distilled water, by water splitting induced by the electrochemical potential gradient.

The concentration difference and the electrical potential established close to the membrane induces the chloride ions to migrate from the NaCl solution to the water. For

the principle of electroneutrality, this migration flux can be sustained by the Na^+ ions or, assuming a perfect permselectivity of the membrane, by an opposite flux of negative ions present in the receiving channel. But, since in the distilled water the concentration of dissolved salt is negligible, the only ions able to migrate to the NaCl solution are the OH^- from the water splitting. It should be noticed that the autoprotolysis reaction of the water requires energy, supplied by the system through the concentration gradient: The electrochemical studies fixes 1V as limit potential difference for the water splitting, less than the electrical potential associated with the concentration gradient of chlorides in the NaCl/distilled water system.

The feasibility of this test, would allow to use simple distilled water as a reagent for the precipitation of magnesium hydroxide, with a whole series of advantages: low cost of the reagent, no environmental or safety risk, no risk of contamination of the precipitated product.

Obviously, the two critical conditions on which the technological feasibility of the experiment is concerned are water quality and membrane permselectivity. From a practical point of view, the experimental test is characterized by extreme simplicity: the membrane reactor is fluxed into the two channels with the NaCl solutions and distilled water. The distilled water flows continuously, while a certain volume of solution is kept in recirculation inside the membrane reactor. A simple pH measurement indicates the performance of the test, resulting in an accumulation of hydroxyl ions in the saline solution. The arrangement of the equipment is shown in Figure 8.9.

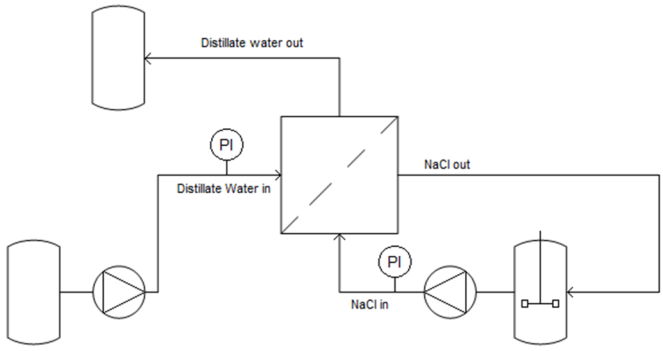

Figure 8.9: Experimental set-up with CrIEM (v01) using water as OH^- source.

The analysis of the resulting curve allows the estimation of the average ions flux across the membrane. Commonly, the flux is defined as the moles of ions that passed through the membrane per time and surface unit. The equation (8.1) allows calculating the molar flux of hydroxyl ions N from the pH variation and, from this, the total average flux J (equation (8.2)); the terms with the apex 0 are referred at the beginning of the test.

$$\bar{N} = \frac{n - n^0}{t - t^0} = \frac{V \cdot C - V^0 \cdot C^0}{t - t^0} \tag{8.1}$$

$$\bar{J} = \frac{\bar{N}}{A_{membrane}} \tag{8.2}$$

Calcium hydroxide. An alternative solution to water splitting is the introduction of hydroxyl ions using a strong base. As already discussed, the membrane reactor has the advantage of segregating cations in the relevant compartments: this system is thus suitable for the use of calcium hydroxide that does not contaminate the product as shown in the experiments with MF-PFR (Figure 8.7)

Since the expected fluxes are greater than the test with distilled water, the arrangement of the circuits was modified, circulating both solutions in an open loop. The experimental set-up is shown in Figure 8.10.

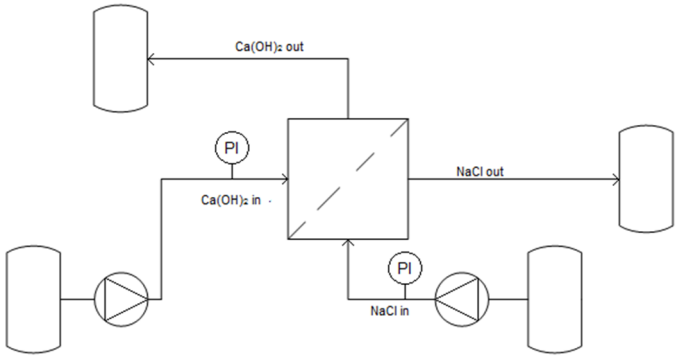

Figure 8.10: Experimental set-up with CrIEM (v01) using calcium hydroxide solution as OH^- source.

An appropriate time was waited to reach a steady state condition and then a pH measurement gives the average flux obtained with this configuration. Since in this case

the system works in steady state, the relation to the flow calculation differs from that used in the batch test. Naming with Q the volumetric flow rate (constant assumption) fed in the module, a matter balance allows to calculate the molar flux N through the membrane with the following relation:

$$\bar{N}_{tot} = Q \cdot (C - C^0) \tag{8.3}$$

Known the average flow, the flow is calculated with equation (8.3). It should be noted that, unlike the previous test, in this case the diffusion flux of the hydroxyl ions coupled with the cations of the alkaline solution could become non-negligible. It is essential to estimate the contribution of the migratory and diffusive flux with a chromatographic analysis in order to determine the calcium ion content in the NaCl solution.

Sodium hydroxide. The sodium hydroxide test does not present any conceptual difference with the previous one, neither in the operating principle nor in the practical operation.

8.2.2 Results with the CrIEM (v01) using different membranes and different alkaline solutions

The water test was carried out by recirculating 200 ml of 4M NaCl solution in the reactor for 416 min. The test showed no appreciable variation in the pH of the saline solution. However, important osmotic effects have emerged: the volume of the solution almost doubled during the test, from 200 ml to 380 ml. Osmotic phenomena are imputed at the saline gradient. This is a negative effect that dilutes the brine solution and decreasing the hydroxyl ions concentration.

It is clear from this preliminary tests that in order to use water as precipitating agent, specific membrane have to be developed to reduce the osmotic effect and the consequently dilution problem.

The experimental test conducted with lime has shown that the pH of the NaCl solution reaches the value of 10.9 with a single pass in the module. With a fixed velocity equal to 1 cm/s, the calculated flux is 1.85E-08 mol/cm^2 min and the molar flow rate is 1.67E-06 mol/min.

The pressure drops with the Fumatech membrane are not negligible: by flowing with water at the beginning of the test the pressure gauge recorded a value at the entrance of the channels of 0.15 bar, whereas with the NaCl solution the value was 0.25 bar. This can be explained by the fact that the saline solution has a density and viscosity higher than distilled water. Moreover, this increase in pressure drop involves a differential pressure between the two channels, leading to a crushing of the membrane on the lime compartment; the relative reduction of the section useful for the passage of the alkaline solution is responsible for the increase of the load losses in the calcium hydroxide channel. An important note to the test is the chromatographic analysis conducted on the dialysate sample. The presence of only traces of calcium ions in the sample analysed, confirms how the membrane reactor is able to solve one of the limits emerged with the MF-PFR reactor when calcium hydroxide is used.

In the test with caustic soda, the pH of the saline solution reached the value of 11.28 with a single passage in the module. At the same velocity (1 cm/s), the pH measurements have allowed to calculate the flux, equal to 4.45E-08 mol/cm^2 min. The hydroxyl ions molar flow rate is 4.00E-06 mol/min.

Two tests were performed at the same alkaline solution conditions using an Asashi Selemion AHO membrane. The pH recorded at the same brine flow velocity (1 cm/s), is 10.53 for lime and 10.35 for sodium hydroxide solution. The migrative flux was estimated equal to 7.91E-09 mol/cm^2 min for lime solution and 4.45E-08 mol/cm^2 min for caustic soda. Similar pressure drops than lime where recorded with this alkaline solution.

At the same condition, as reported in Table 8.2, two more tests were also performed with Fujifilm RP1 membranes. Poor results were found with this membrane obtaining a flux equal to 6.29E-9 mol/cm^2 min with NaOH solution and 4.44E-9 mol/cm^2 min with $Ca(OH)_2$ solution.

In Figure 8.11 is reported a comparison of the ion flux experimentally obtained with lime and caustic soda alkaline solutions, with the Fumatech Fumasep FAA, Asashi Selemion AHO and Fujifilm RP1 membranes, respectively.

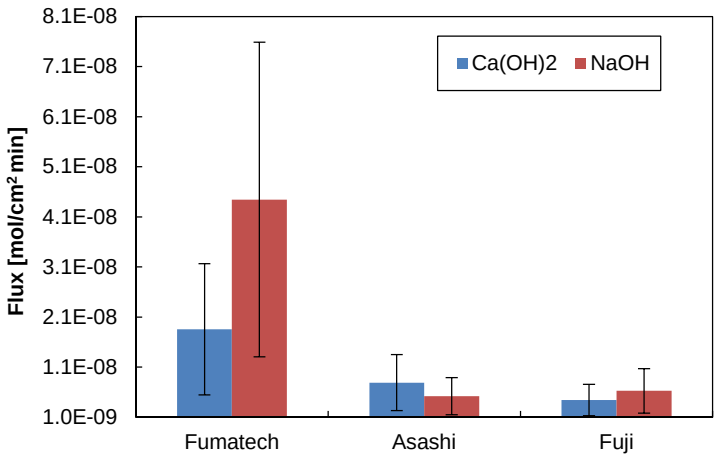

Figure 8.11: Comparison between the fluxes made with Fumatech, Selemion and Fujifilm membranes in a CrIEM reactor. Tests were conducted with a solution 4M of NaCl and with alkaline solutions at pH 12.

Fumatech membrane gives a flux almost an order of magnitude higher than Selemion and Fujifilm membranes. Likely, thanks to its reduced thickness and high hydrophilicity grade. However, these characteristics that makes its installation in the reactor really difficult due to the almost instantaneous swelling behaviour. Furthermore, the extremely reduced thickness diminishes the mechanical properties of the membrane with a tendency to corrugate, reducing the channel section and increasing the pressure drops. On the contrary, the Selemion and Fujifilm membranes are stabilized by particular support, whose rigidity favours the installation in the module. The high degree of hydrophobicity of these membranes ensures a low swelling but it should be guarantee a higher permselectivity.

The effect of the alkaline solution is opposite for the membranes: with Selemion membrane the greater flux is made by lime, vice versa is the soda solution with the Fumatech and Fujifilm membranes. The estimation of the flux is very sensitive to the measurement of pH, given the exponential relationship that binds the two quantities, for this reason the error bars are so evident.

From the comparison reported in Figure 8.11, among the tested membranes, the best performance is ensured by Fumatech. The potential of the use of lime or ammonia is interesting, especially if compared transversally with the traditional MF-PFR reactor: the membrane reactor is the only technology able to supply hydroxyl ions from calcium

hydroxide or ammonia solutions remaining indifferent respectively to the co-precipitation of calcium salts and to the possible dilution effect of ammonia.

A preliminary test was made with Fumatech membrane and real waste brine from saltwork. Due to the low flux obtained at pH 12, it was made the test using NaOH at pH 13 trying to increase the driving force and likely the flux. 30ml of brine was recirculated in the module during the test. After ten minutes, magnesium hydroxide start to precipitate but the test was stopped due to the high-pressure drop recorder (around 1 bar). Plugging phenomena were observed. However, a sample was filtrated and analysed with ion chromatography, confirming the precipitation of magnesium hydroxide (purity higher than 99%) with a conversion of 15%.

This first experimental test of reactive precipitation leads to several important conclusions. The membrane reactor is capable to precipitate magnesium hydroxide from waste brine. Furthermore, unlike traditional MF-PFR reactors, the technology is suitable for the use of reagents such as lime and ammonia. Finally, as was conceivable, the main issue is the scaling phenomena, whose management will determine the technology progress. The CrIEM and the set-up were changed in order to solve these problems.

8.3 Design and construction of the second version of CrIEM (v02)

A new version of CrIEM reactor (v02) consists of two Plexiglas plates, each carved with a rectangular snake-like shaped channel, with dimension of 20 mm x 270 mm x 165 mm. Two hose connectors are used to feed the solution into the module; because of high salinity of brine, plastic material was adopted also in this case to avoid corrosion phenomena. Between the plates a sheet of a Fujifilm anionic exchange membrane was inserted, resulting in a net mass transfer area of 106 cm^2. Even if the Fujifilm membrane has demonstrated the worst results (see 8.2.2), it has the best mechanical resistance and it is easy to position between the two plates. Moreover, the longer deep collaboration between the University of Palermo and the Company could help in the problem solving for this new application with the possibility to develop new specific ion exchange membrane dedicated to the magnesium precipitation.

In this new configuration, spacers are not used in order to reduce scaling problems.

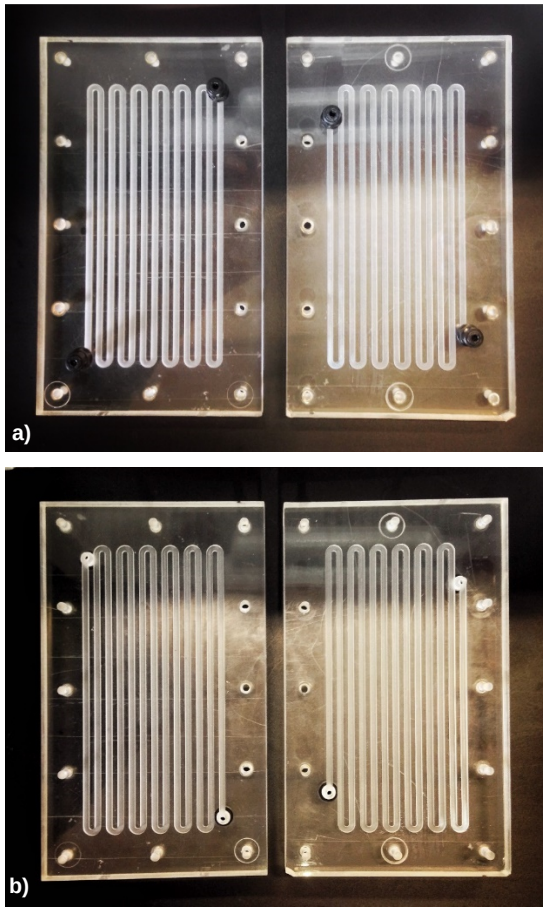

Figure 8.12: Second version of CrIEM reactor (v02). a) front view; b) internal view.

As can be observed in Figure 8.12, the inlet solution holes are created not in the same position, in order to avoid the possibility that the membrane is broken if it is mechanically stressed from both sides in the same point.

The auxiliary items for the experiment include two peristaltic pumps (Vederflex M025), 4mm diameter plastic tube for fluid handling and the relevant solution storage tanks. Figure 8.13 illustrates the apparatus of the process whereas the scheme is the same represented in Figure 8.7.

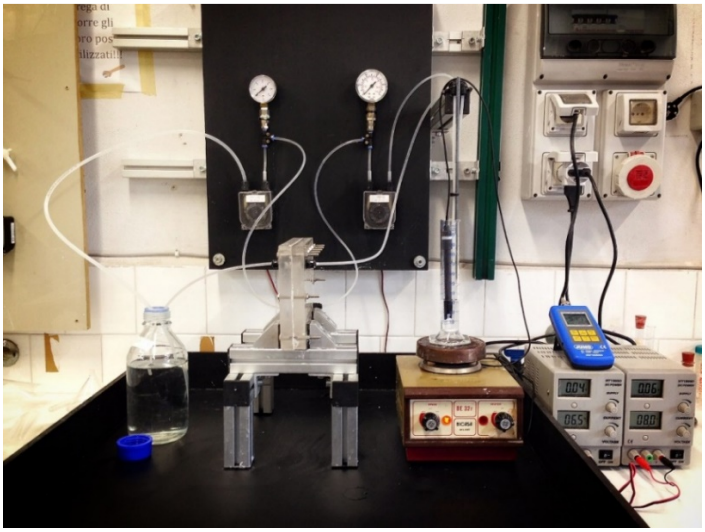

Figure 8.13: Experimental set-up with the second version of CrIEM (v02)

A typical brine composition used for the magnesium precipitation is reported in Table 8.3. A certain amount of brine is continuous recirculated in one side of the reactor whereas the alkaline solution is fed in an open loop to guarantee the maximum driving force for the duration of the test. The volumetric flowrates of the two solutions were chosen in order to obtain an average velocity inside the channels equal to 1 cm/s. All solutions were prepared using demineralized water, while the composition was analyzed with an ionic chromatograph (Metrohm, IC 882 compact plus).

Table 8.3: Typical brine composition used in the experiments with CrIEM (v02)

Ion	**Concentration [g/l]**
Na^+	25.6
K^+	7.2
Mg^{2+}	33.4
Ca^{2+}	0.3

Two preliminary tests were run using a lime solution (pH: 12.9) in order to confirm the possibility to precipitate magnesium from brine with the new CrIEM (v02) reactor while a second experimental campaign was focused on the study of the effect of two alkaline solutions (lime and ammonia) at different test duration.

8.3.1 Experimental procedure

During the experiment, the CrIEM module carries out the mass transfer between the two solutions: ideally, the only ions able to migrate across the membrane are those negative charged; nevertheless, small amount of cations could permeate between the channels because of the non-ideality of membrane permselectivity and internal leakages. Furthermore, the strong salinity gradient leads to a water flux from the diluted solution toward the concentrated one. Among these secondary effects, however, only the osmotic flux affects significantly the experiment execution.

In the first part of the test, the brine pH increasing is recorded by a digital pH-meter. From the starting value of 7.3, it rises dynamically to the proper range of magnesium hydroxide precipitation (9 ± 0.1). To avoid long transients, the dead volume of piping has minimized by chosen the smallest commercial available inner diameter tube. Normally, as observed in the preliminary tests, 30 ml of brine need 2 hours to complete the pH increasing.

Until the complete conversion of Mg^{2+} ions is reached, every OH^- injection precipitates $Mg(OH)_2$ rather than increase the pH. A small amount of the solid product is carried out by convection from the brine flow rate, even if the majority of crystals stay attached to the membrane, wherever they are formed. With time, agglomerations grow and reduce the cross section available to the fluid flow, thus a certain head losses could be recorded by the in-line manometer.

After a specific time, the experiment is shut down, the CrIEM module is disassembled and cleaned, and magnesium hydroxide suspension was directly collected from the membrane. The suspension is filtered, resulting in a solid product that is washed and dried. The conversion reached by the reaction can be estimated as ratio between the actual product get and the theoretical value obtainable starting from the brine Mg^{2+} content:

$$X_{pwd} = \frac{m_{actual}}{m_{theoretical}} \cdot 100 = \frac{m_{actual}}{C^{brine}_{Mg^{2+}} \cdot V_{brine} \cdot Mw_{Mg(OH)_2}} \cdot 100 \qquad (8.4)$$

Another, independent, conversion estimation can be get from the residual magnesium content in the brine, at the end of the experiment, as described in the paragraph 8.2.1, and here reported with slightly different formulation. Once noted the final brine volume, the suspension is filtered and diluted with demineralized water to reach the functional

analytical range of chromatograph (1-100 ppm). Once the residual magnesium concentration is known, the conversion can be calculated as variation of magnesium mass in the brine normalized to the initial Mg^{2+} mass:

$$X_{filt} = -\frac{\Delta m_{Mg^{2+}}}{m_{Mg^{2+}}^{brine}} = \frac{V_0 \cdot C_0^{Mg^{2+}} - V_{fin} \cdot C_{fin}^{Mg^{2+}}}{V_0 \cdot C_0^{Mg^{2+}}} = 1 - \frac{V_{fin} \cdot C_{fin}^{Mg^{2+}}}{V_0 \cdot C_0^{Mg^{2+}}} \quad (8.5)$$

Apart from the way conversion is calculated, it allows to quantify the ionic flux across the membrane, i.e. the moles of OH^- transferred per unit of time and membrane area:

$$\bar{J} = \frac{n_{OH^-}}{t * A_m} = \frac{2 \cdot n_{Mg(OH)_2}}{t \cdot A_m} = \frac{2 \cdot X \cdot n_0^{Mg^{2+}}}{t \cdot A_m} = \frac{2 \cdot X \cdot V_0 \cdot C_0^{Mg^{2+}}}{t \cdot A_m} \quad (8.6)$$

In eq. (8.6) t is the net precipitation time, A_m the membrane area available to the mass transfer, X is the conversion, $n_0^{Mg^{2+}}$ the initial magnesium ions, calculated as product between the brine initial volume V_0 and the relevant initial molar concentration $C_0^{Mg^{2+}}$.

The last process performance parameter is the solid purity. It contributes to define the market value of magnesium hydroxide, ranging from technical to food and pharmaceutical grade or as flame retard. The purity can be expressed as mass ratio of magnesium ions to the overall cations content. To reach the highest possible purity, after the first washing cycle the solid is smashed and washed a second time to remove every soluble salts traces or brine entrapped inside crystals agglomeration. The powder is than neutralized with stoichiometric 1M HCl and diluted with demineralized water to obtain a 100 ppm ionic solution to analyze by IC chromatograph as also done in the MF-PFR tests.

8.3.2 Preliminary experimental results with the CrIEM (v02)

According to the experimental procedure, two preliminary experiments were conducted, named respectively A and B, using lime solutions as precipitating agent. Results relevant to experiment A are summarized in Table 8.4

Table 8.4: Experiment results in the test A with CrIEM (v02).

Total experiment time [min]	480	
Precipitation time [min]	360	
Solid mass precipitated [mg]	293	
Product purity [%]	≥99	
	Solid mass based	**Residual magnesium based**
Conversion [%]	13	11
Flux [mol OH^-/cm^2 min]	2.89E-07	2.51E-07

The experiment lasted 8 hr, 6 of which of net precipitation. The pressure losses, negligible in the beginning, rose until 0.3 bar during the first 4 hr of precipitation, then they kept constant until the end of the experiment. 293 mg of powder was collected, and the analysis show its purity overcame 99%. Even if $Ca(OH)_2$ was used, there was no calcium salt contamination. This represent an important result, because highlights the suitability of the CrIEM technology where conventional direct contact reactors fails. Either based on solid precipitated or the residual magnesium in the brine, the conversion stated near 10%. Note that the two results are in good agreement, even if the calculation path is independent. This agreement holds true also for the final flux value, of 2E-07 OH^- moles per unit of time and membrane area.

A second experiment (B) was performed in the same operative conditions, in order to validate the results. Furthermore, a series of intermediate brine sampling has allowed monitoring the flux trend during the experiment; for these intermediate analyses a linear variation of the brine volume has been assumed, between the initial and the final value. Figure 8.14 shows the plot pH versus time during the transient of pH increasing from 7.3 to 9.

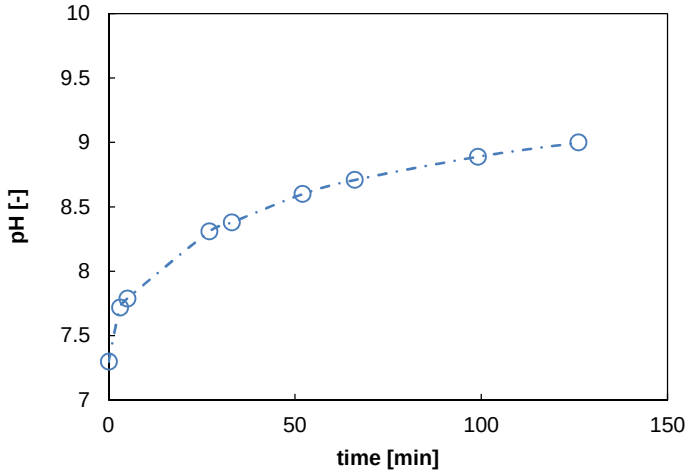

Figure 8.14: pH trend during the initial transition step in the B experiment with CrIEM (v02).

Table 8.5 summarizes the overall results of the experiment. As in the previous case, the transient took 2 hr, then precipitation accurses. The amount of solid product attached to the membrane was less the before, but the quantity of crystals dispersed in the suspension increased. The chromatographic analysis showed that the product was high purity magnesium hydroxide. The pressure losses slight increased form 0.2 bar to 0.3 bar, without affect the reactor proper operation.

Table 8.5: Experiment results in the test B with CrIEM (v02).

Total experiment time [min]	460
Precipitation time [min]	340
Solid mass precipitated [mg]	111
Product purity [%]	≥99

From the intermediate samples analysis, the conversion and the relevant flux was calculated, the data are presented in Figure 8.15. With time the flux seems to increase, but the trend could be due only to the volume linear variation. By increasing the thickness of the solid product layer on the membrane, the flux is expected to decrease or ideally keep constant. The conversion trend is linear with time, increasing until near 10%.

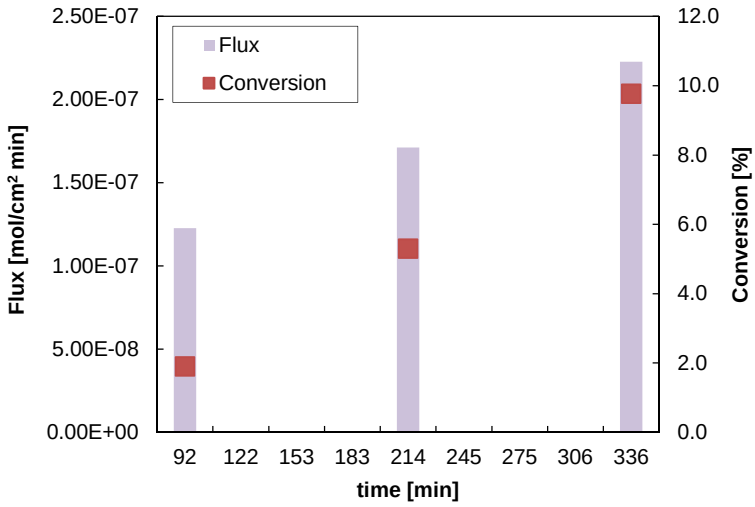

Figure 8.15: Flux and conversion results for the precipitation of magnesium from waste brine using the CrIEM reactor equipped with Fujifilm Ionic Exchange Membrane and $Ca(OH)_2$ solution as precipitating agent.

The flux value, 2E-07 mol/cm^2 min, confirms the result of the A experiment, showing the operation of the CrIEM prototype is reliable. If this value is compared with those calculated by pH variation in experiment with synthetic NaCl 4M solution (see Figure 8.11), it results much higher. In particular, for the Fujifilm membrane with the same $Ca(OH)_2$ solution and operative condition, the flux was two orders of magnitude higher with real brine. This discrepancy could be adduced either to (i) the accuracy of the experimental procedure, higher with the estimation by chromatograph analysis or (ii) the physical effect of precipitation that prevent pH to rise beyond 9 until the complete magnesium conversion is reached; in this way the driving force couldn't reduce because of the equaling of OH- concentration in the two solutions.

In conclusion, two preliminary experiments were performed with the CrIEM (v02). They confirm the flux value (2.2E-07 mol/cm^2 min) achieved by using real saltworks brine and calcium hydroxide 20mM. The precipitation lasted near 6 hr, resulting in a conversion of 10%. Two independent method estimation agreed on this result. Finally, the magnesium hydroxide powder is a high purity product, with a mass fraction of magnesium higher than

99%. Unlike direct mixing reactors, the CrIEM technology is able to process calcium hydroxide as alkaline solution, without any product contamination.

In order to understand the effect of a different alkaline solution and longer test time, five more experiments were conducted with the CrIEM (v02) and the results are shown in the next section.

8.3.3 Experimental campaign results with the CrIEM (v02)

In the preliminary tests with the second version of CrIEM, the total conversion achieved in both tests was around 10% after 8 hours. In order to assess the possibility to recover the total amount of magnesium present in a saltwork waste brine sample, some long run test were performed. Ammonia solution and lime were tested in this experimental campaign. The concentration of calcium hydroxide solution was fixed at 0.021 mol/l, close to the maximum saturation point (0.023 mol/l) whereas the ammonia, due to its weak base characteristic, was used directly as a concentration equal to 25% in weight. The operative condition adopted for the tests are reported in Table 8.6.

Table 8.6: Operative conditions summary for the tests performed with CrIEM (v02)

Test	**Time**	**Reagent**	**pH alkaline solution**	**Brine volume [ml]**	**Mg^{2+} conc. [g/l]**
1	Short run	NH_3	11.3	66	25.65
2	Long run	NH_3	11.3	386	25.65
3	Long run	$Ca(OH)_2$	12,5	106	24.56
4	Long run	$Ca(OH)_2$	12,5	106	24.56
5	Long run	$Ca(OH)_2$	12.5	106	24.56

Test 1 and test 2

Two tests were conducted using ammonia: a short run to estimate the flux of hydroxyl ions, and a long run. In the tests 2, the volume of brine to be processed was estimated on the basis of the information obtained from the first test.

The ammonia was used at a molar concentration of around 13 mol/l and in this case, a proper volume was recirculated during the tests.

The pH trend for the test 1 is shown in (Figure 8.16). After a transient time of around 1 hour, a value of 9.6 is achieved confirming the reactive precipitation started.

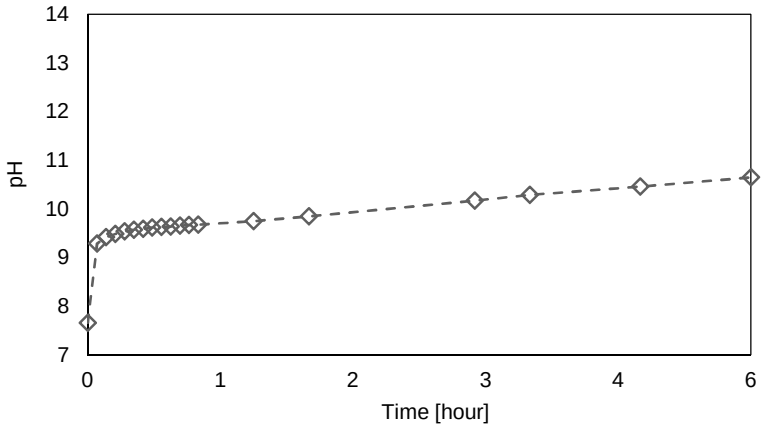

Figure 8.16: pH trend for the test1 (short run) with ammonia solution and CrIEM (v02)

In the following table is reported a results summary.

Table 8.7: Summary results of test 1 with ammonia and CrIEM (v02)

X_{pwd} [%]	49,36
X_{filt} [%]	88,01
Flux OH^- (X_{pwd}) [mol/cm^2 min]	1.79E-06
Flux OH^- (X_{filt}) [mol/cm^2 min]	3.20E-06
Solid Purity [%]	99,65

The conversion estimated on the bases of solid precipitated is almost half than the other procedure. Likely, this discrepancy is imputed to the solid lost in the tubes and due to scaling phenomena. However, the fluxes are similar in both calculation procedures.

Once the flux with the short-run was estimated, test 2 was carried out in order to obtain with a long run tests the complete conversion of magnesium into magnesium hydroxide.

On the basis of the information collected in the previous test, the time required for the complete conversion was estimated for a fixed sample volume of brine. From the calculations made it emerged that for 386 ml of brine, the duration of the test is equal to 72 hours.

However, due to scaling phenomena highlighted during the test, it was not possible to complete it; in fact, after a time of about 20 hours, the experiment was stopped due to the

clogging of the hydraulic circuit in which the pressure drops were equal to 3 bar. Pictures of the scaling on the membrane and into the reactor are shown in (Figure 8.17).

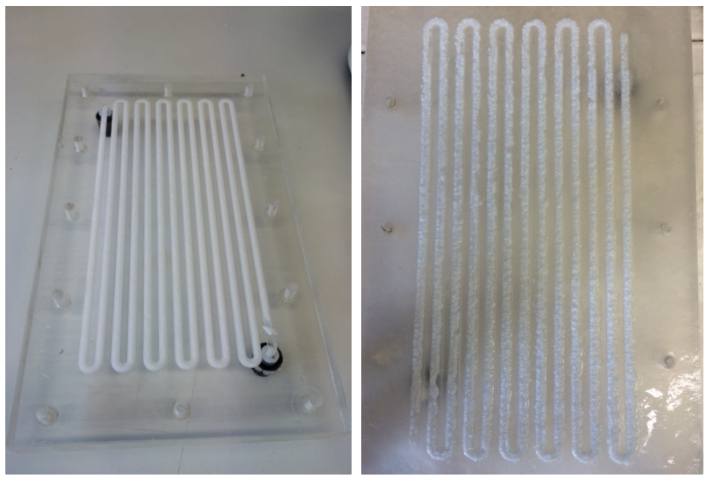

Figure 8.17: Magnesium hydroxide deposit on the membrane and into the reactor channels.

Although the test was not completed, the following data are collected for the first 20 hours.

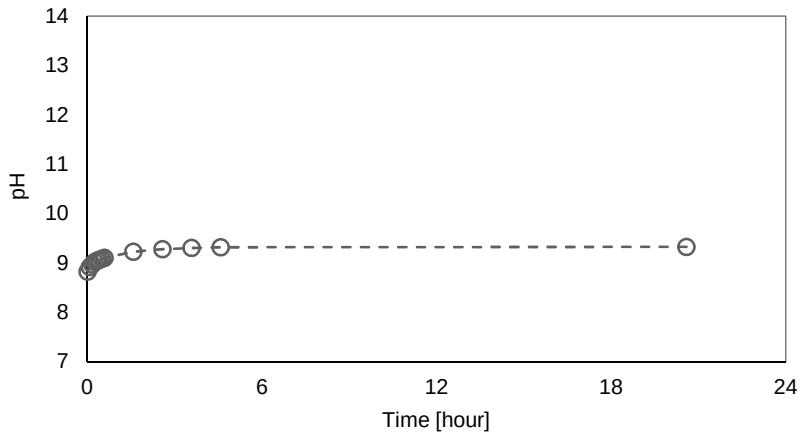

Figure 8.18: pH trend in the test 2 (long run) with ammonia in a CrIEM reactor (v02)

In the following table is reported a results summary for the test 2 (long run) with ammonia.

Table 8.8: Summary results of test 2 with ammonia and CrIEM (v02)

X_{pwd} [%]	69.10
X_{filt} [%]	42.64
Flux OH^- (X_{pwd}) [mol/cm^2 min]	1.22E-06
Flux OH^- (X_{filt}) [mol/cm^2 min]	7.58E-07
Solid Purity [%]	98.54

Due to the discrepancy of the conversion calculated with two methods and to the higher accuracy of the way with ion chromatography, only the conversion X_{filt} will be reported for the next results. Obviously, the total conversion was not obtained but the estimated fluxes are similar to the value found in the test 1.

Tests 3-5

Calcium hydroxide solution was used for the test 3, test 4 and test 5. Using the information collected in the preliminary tests, a volume of 106 ml of brine was treated with in the reactor for 72 hours.

In the following picture is represented the pH trend for the test 3

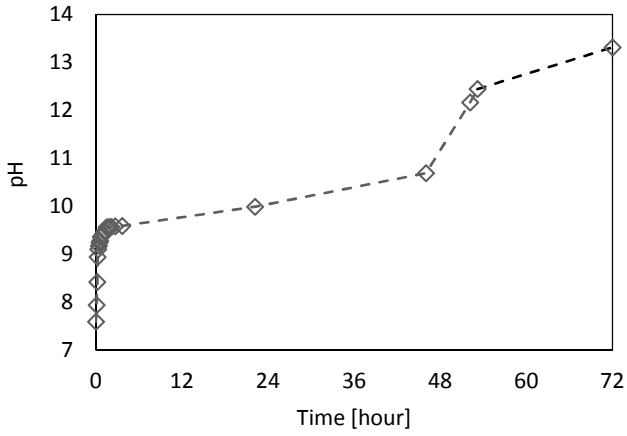

Figure 8.19: pH trend in the test 3 (long run) with lime in a CrIEM reactor (v02)

The trend has the characteristic shape of the magnesium precipitation with alkaline solution, after 48 hours the pH starts again to increase strongly because all the magnesium is precipitated. Similar test are observed in the test 4 and test 5.

In order to prevent the scaling problems found in the previous studies, in the test 4 the CrIEM reactor was introduced in a sonicator bath, trying to reduce this important issues. However, the scaling problems were only slightly reduced, even if more precipitated was directly collected in the brine tank.

In the test 5, instead, the conversion trend in time was investigated collecting small samples during the test and analysing them with the ionic chromatography. The conversion in time is reported in (). The conversion is not linear in time and this confirm that the driving force decreases during the precipitation, not for the alkaline reactant solution but because the concentrations in the brine declines.

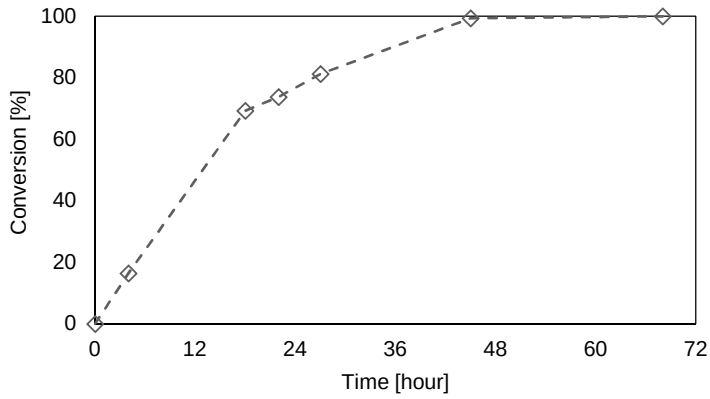

Figure 8.20: Conversion vs time for the test 5 with lime solution in the CrIEM (v02)

It can be observed a good agreement between the pH prevision and the conversion trend. After 48 hours, all the magnesium is converted into magnesium hydroxide.

The performance parameters for these three tests are represented in

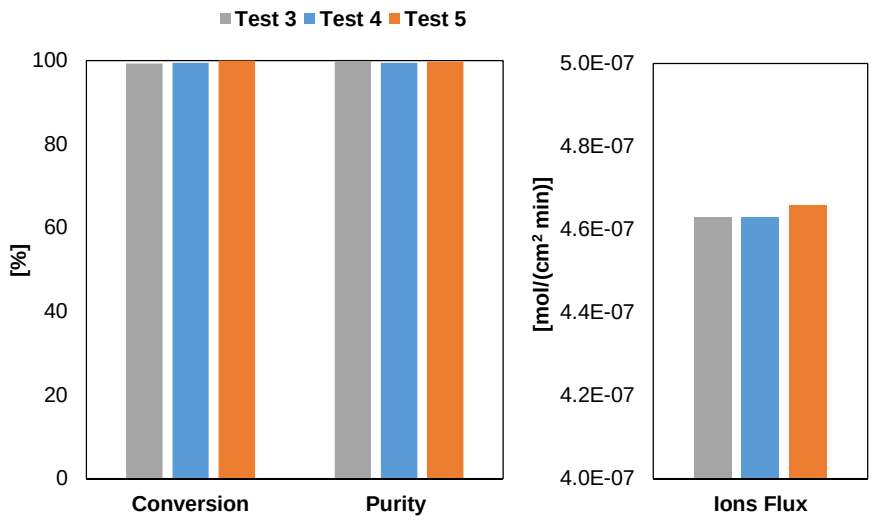

Figure 8.21: Performance parameters (conversion, purity and ions flux) for the test 3, test 4 and test 5 with the CrIEM (v02) reactor and calcium hydroxide solution as precipitating agent

In all the three tests, the value obtained for the conversion, purity and ions flux are the same.

8.4 Design and construction of the third version of CrIEM (v03)

The issues highlighted in the first experimental campaigns have address the research towards the design and implementation of a new version of CrIEM (v03). The reactor used keeps the same starting CrIEM idea but with some appropriate modifications. It consists of two Plexiglas plates (270 mm x 210 mm x 25 mm) on which two circuits were dig, as the previous version but with different shape and dimensions ().

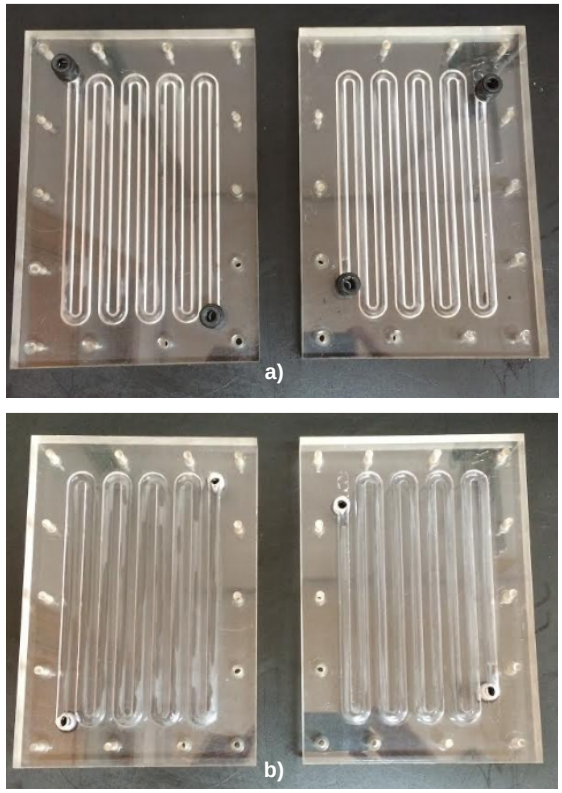

Figure 8.22: Third version of CrIEM reactor (v03). a) front view; b) internal view.

The circuit shape has not rectangular section as in the CrIEM (v02) but it is semi-circular. This is fundamental for solutions adopted to reduce the scaling problem. The pumps were substituted with a new pump “If biofluid, model WT/600/S” with a double head.

The new set-up is reported in Figure 8.23.

Figure 8.23: Experimental set-up with the third version of CrIEM (v03).

Among the possible solutions for the scaling problems, some were selected and tested with the new CrIEM (v03), trying to solve or at least minimize the issue, important if a scale-up is imagining with this new rector. The solution tested are listed below:

- *Cleaning balls*: balls of spongy material used, in general, for cleaning the heat exchanger tubes. These balls were introduced into the hydraulic circuit of the brine in order to scrape the solid deposited on the membrane surface;
- *Air*: using compressed air at a pressure of 0.6 bar, it is possible to create turbulence inside the channel and promote the removal process of the accumulations generated during the process.
- *Filtration*: the suspension is filtered during the test and the clear solution is send back to the reactor; it is also possible to observe a cleaning action by the liquid itself.

In some cases, these practices were performed all together. The tests were run using calcium hydroxide solution as source of OH^- ions. Two membranes were tested, both made by Fujifilm Company and in some cases were cleaned and re-used for more tests. A summary of the operative condition adopted in this new experimental campaign is presented in the Table 8.9.

Table 8.9: Summery of the operative conditions used in the experimental campaign performed with CrIEM (v03)

Test	Time	Reagent	pH alkaline solution	Brine volume [ml]	Mg^{2+} conc. [g/l]	Membrane (Fujifilm)
6	Long run	$Ca(OH)_2$	12.5	55	25.21	RP1
7	Long run	$Ca(OH)_2$	12.5	45	25.21	RP1
8-9	Long run	$Ca(OH)_2$	12.5	45	24.21	RP1
10-11-12	Long run	$Ca(OH)_2$	12.5	40	25.53	E1

Before starting the experimental campaign, the proposed solutions to solve the scaling problem were tested in few spot tests. It was noted that the turbulence made with the air helped the membrane self-cleaning process whereas the cleaning balls, if continuously circulated in the reactor caused the membrane to break. For this reason, in all the tests, the air was flushed continuously whereas the cleaning balls were used only few times per test or if more test were made with the same membrane, only when the membrane was cleaned to re-use it in the next test. The suspension instead was filtered each times it became not clear anymore.

8.4.1 Experimental campaign results with the CrIEM (v03)

The first four tests were made using Fujifilm RP1 membranes whereas the other three tests were performed with Fujifilm E1 membrane.

Test 6 and test 7

The tests 6 was performed in order to evaluate the ions flux using the new reactor with the same other conditions exploited in the previous experimental campaign. The pH trend is report in

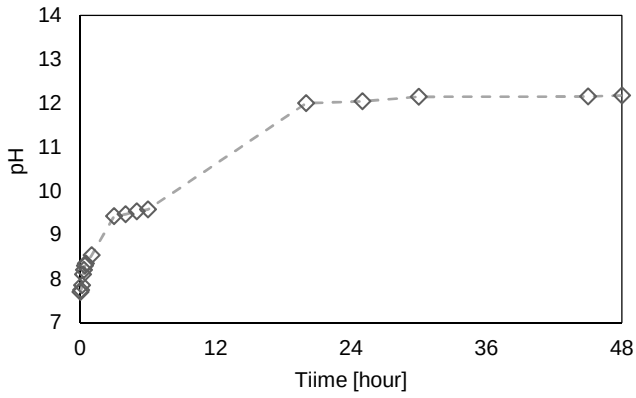

Figure 8.24: pH trend for the test 6 with the CrIEM (v03) using calcium hydroxide as OH^- source

The pH trend is similar to the other found with the previous version of CrIEM reactors.

Test 7 was made at the condition in order to confirm the performance of test 6 and better evaluate the ions flux through the membrane. Taking few samples after the first 12 hours, the total conversion was already achieved in both cases after 20 hours. Using the final ions flux estimated in the previous tests overestimated the time required for the total conversion, this also due to the fact that the flux decreases during the test.

The performance result for these two tests are following shown.

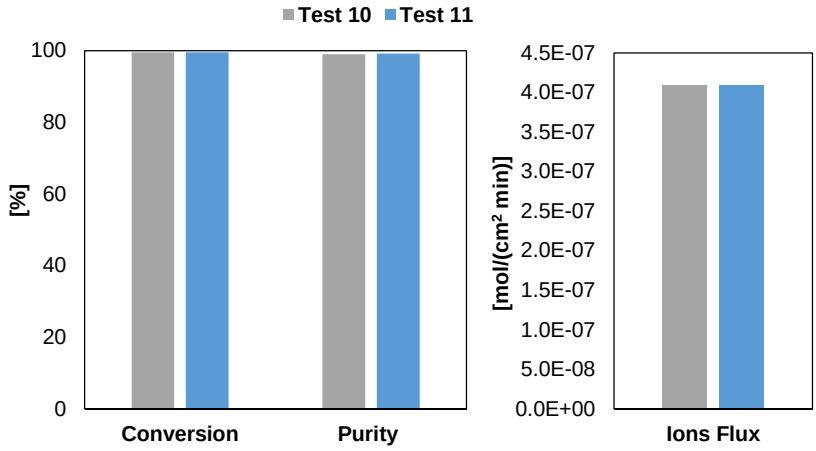

Figure 8.25: Performance parameters (conversion, purity and ions flux) for the test 6 and test 7 with the CrIEM (v03) reactor and calcium hydroxide solution as precipitating agent

The performance results are comparable in both the cases. It was demonstrated that the solution applied help the cleaning of the membrane reducing the scaling problem and the possible channels clogging phenomena.

Test 8 and test 9

These two test were performed at the same condition, testing the possibility to use the same membrane more times. After 24 hours of the test 9, the membrane was broken and the test was suspended. However, the data collected shown the same results obtained in the tests 6 and 7. Purity higher than 99% with a conversion of test 8 around 99.5 %. Also this experimental test confirmed that after 24 hours there was a total conversion.

Test 10, test 11 and test 12

These three test were made using the same membrane three times. In this case, the membrane adopted was the new Fujifilm membrane E1. This membrane has a higher mechanical resistance respect to RP1 membranes. The performance were keep practically constant in all the three tests. The results are shown below.

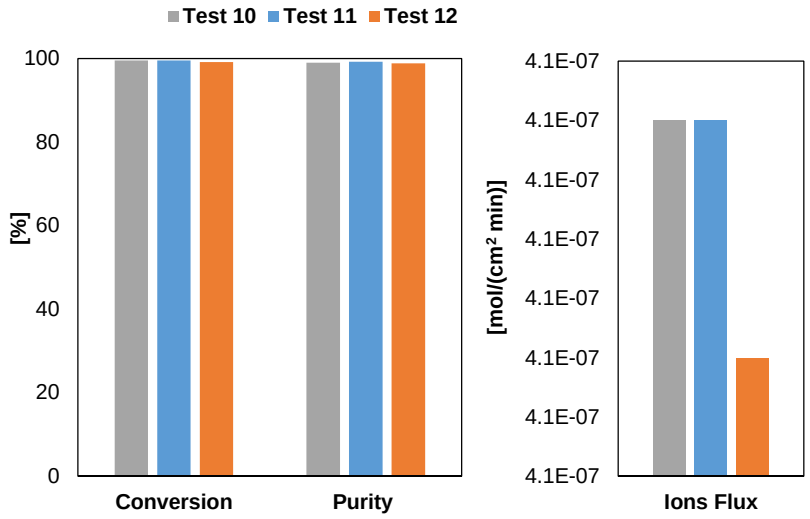

Figure 8.26: Performance parameters (conversion, purity and ions flux) for the test 10, test 11 and test 12 with the CrIEM (v03) reactor and calcium hydroxide solution as precipitating agent. Tests made three times with the same membrane.

The value reported above confirmed the possibility to re-use the same membrane more times exploiting the turbulence created with the air, the continues solution filtration and the use of the cleaning balls between one test and the other helping to clean the membrane surface without disassembling the reactor.

Further studies are needed before bringing this technology to a higher TRL with the use of new membrane and new configuration, in order to solve the main issues highlighted in these experimental campaigns.

9 STUDY ON MAGNESIUM HYDROXIDE CRYSTALS GROWTH AND FUTURE PERSPECTIVES

Abstract

The reactive crystallization process of magnesium hydroxide is influenced by many parameters. The use of ammonia or sodium hydroxide as reactant can dramatically modify crystals morphology. A strong base promotes the formation of small crystals while a weak base can improve the growth. Also the quality of feed brine used in the process strongly affects the crystal morphology.

After reporting a literature overview on processes for magnesium hydroxide crystals modification, an experimental campaign with a traditional CSTR is presented. This reactor was used to better understand the growth process involved in the reactive precipitation. Different parameters were changed and the final results were compared.

All the samples were analysed with Ion Chromatography, Laser granulometry and wth a Scanning Electron Microscope. Using internal recycle with long resident time, the crystal morphology was modified compared to the standard. Once-through configuration.

9.1 Crystals of magnesium hydroxide and methods for its modification

The ability of an alkaline solution to precipitate magnesium hydroxide from a saline solution containing Mg is known from a long time. A critical aspect of this reactive crystallization process, however, concerns the morphology of the particles and how these are influenced by the process parameters involved.

In 2003, Henrist et. al [159] have demonstrated that magnesium hydroxide precipitate mainly in two crystal morphologies as shown in the following figures.

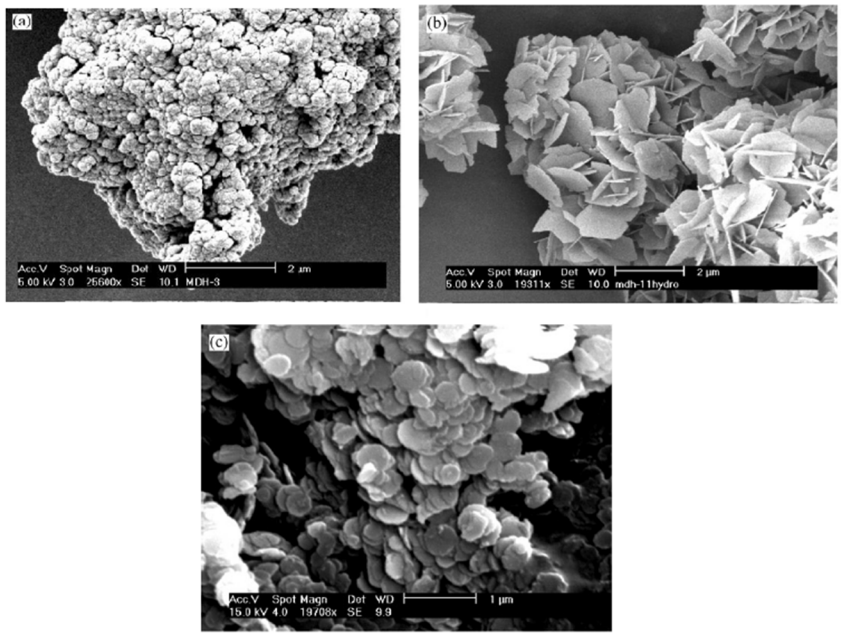

Figure 9.1: Magnesium hydroxide crystal morphology. a) globular cauliflower-like agglomerates; b) and c) platelet-shaped particles [159].

In Figure 9.1A is shown the typical globular cauliflower structure of magnesium hydroxide that was also obtained with the MF-PFR as reported in Figure 7.31, while Figure 9.1B and Figure 9.1C shown the plated-shaped particles with different states of aggregation.

According to literature works [159,181], it was demonstrated that the chemical nature of the base precipitant is of prime importance on the crystal morphology. The reagent effect is twofold and have to be described in terms of both pH of the crystallizing solution

and of the cations chemical nature. The pH value of the basic solution have to be compared with the isoelectric point of the magnesium hydroxide, i.e. with that particular pH value which does not result in any excess of charge adsorbed on the crystals surface. The isoelectric point of magnesium hydroxide has been experimentally determined and it is around 12. This implies that the use of caustic soda (pH = 13) and ammonia (pH = 10) completely changes the sign of the adsorbed charge on the crystals. The negative charge excess, in the case of soda, attracts the positive ions resulting in a greater local supersaturation and a nucleation increasing despite the growth process.

Furthermore, the incorporation of positive ions into the crystal lattice is not a selective process and strongly depends on the nature of the cations in solution. The ionic radius of the different species determines a certain steric encumbrance, resulting in different impediment in the adsorption respect to the magnesium ion. In the case of soda, the high mobility of the sodium ion, together with a higher supersaturation due to the excess of the pH with respect to the isoelectric point, determines the overabundant birth of nuclei. These uncontrolled growth, determines the peculiar globular structure of the crystalline aggregates. However, these considerations are reversed in the case where the precipitation is carried out with ammonia: lower local supersaturation and the steric impediment of the ammonium group improve the crystals growth obtaining more regular shape.

The temperature also has a strong effect, mainly on the agglomeration behaviour and particles size. The particles show a tendency towards intergrowth at 60°C, while at lower temperature, single and circular platelets are obtained, with a mean diameter depending on the synthesis and ageing temperature: the lower the temperature, the higher the diameter. Varying the magnesium source modifies the chemical nature of counter-ions in solution. Magnesium nitrate and magnesium chloride both gives rise to the desired morphology. Magnesium sulphate appears to promote agglomeration of primary nuclei, but this behaviour is not totally understood [159].

Submitting the powders in solution to a mild hydrothermal treatment induces a pronounced improvement of the particles morphology, as well as an increase of their mean size, with subsequent decrease of their specific surface area. Kumari et al. [182] demonstrated that $Mg(OH)_2$ microdisks, nanodisks and polyhedrons can be obtained with an hydrothermal treatment at 200 °C for 3, 12 and 48 h, respectively.

Today, the path to success, as most studies demonstrate, is the obtaining of nanoproducts with specific particle morphologies and with hydrophobic properties. Apart the reactive precipitation, different other methods have been proposed for the magnesium hydroxide production such as sonochemical, sol-gel, electrochemical and solvo-and hydrothermal methods to those using microwaves, a vapour phase deposition or the traditional use of raw minerals. Moreover, different methods, as the hydrothermal process already cited, have been proposed to modify the surface of magnesium hydroxide such as the use organic and inorganic compounds [181].

The morphology obtained in the tests with the MF-PFR reactor is globular cauliflower (Figure 7.31), not usable as additive in the flame retardant. Due to its high purity and high surface specific area is applicable in the pharmaceutical and nutraceutical fields. Some of the issues presented above that create globular particles are present in the reactive crystallization process from waste saltwork brine. Above all, the presence of sulphates and the use of NaOH strongly contribute to form agglomeration of small nuclei.

In order to study the parameters that can modified the morphology of the magnesium hydroxide crystals from saltwork brines, a lab Continuous Stirred Tank Reactor (CSTR) was designed and constructed. This traditional reactor is more flexible than MF-PFR and CrIEM and is more suitable to study the effect of different parameters on the growth process.

9.2 Study on magnesium hydroxide crystals growth with a CSTR reactor

A CSTR is a continuous reactor consisting of a tank fed by a constant flow rate, equipped with an agitation system. Obviously it is totally different than the other two reactors studied in this PhD thesis but it is more suitable for the study of magnesium hydroxide crystals growth. This is a rector where the condition change in time while in the MF-PFR change along the reactor space.

The lab CSTR is shown in Figure 9.2 and is constituted by a Plexiglas cylinder (1 l) and a stirrer for the mixing. The solutions are fed from the top while the outlet is collected from the bottom. Peristaltic pumps are used to feed all the fluids. Four tanks are provided to store the inlet and the outlet solutions.

Figure 9.2: CSTR lab test-rig.

The CSTR was tested with different resident times (τ) but were chosen with the same order of magnitude used in the MF-PFR tests. A summary of the operative conditions adopted in the first experimental campaign is reported in the table below.

Table 9.1: Operative conditions adopted in the first experimental campaign with CSTR

Test	$[Mg^{2+}]$ **[g/l]**	Q_{brine} **[ml/min]**	**[NaOH] [mol/l]**	$\frac{N_{base}^{real}}{N_{base}^{stoich}}$	Q_{base} **[ml/min]**	**N [rpm]**	**τ [sec]**
1	25.1	735	4	1	379	400	54
2	25.1	735	4	1	379	400	54
3	25.1	735	4	1	379	800	54
4	25.1	1450	4	1	749	400	27
5	25.1	376	4	1	191	400	108

The first test was performed at the same resident time of the best test performed with MF-PFR (8 cm/s). The second test was performed at the same condition of test 1 but it

was a long run (60 minutes) in order to confirm the first results and to evaluate the stability of the properties of the particles produced. The third test was performed at higher rotational speed while the last two tests were performed with other two different resident times.

In a second experimental campaign, the test-rig was slightly modify in order to install streams recycles with the purpose to reduce the local supersaturation in the reactor and to promote the growth phenomenon. The operative conditions adopted are reported in Table 9.2.

Table 9.2: Operative conditions adopted in the first experimental campaign with CSTR

Test	**Mg^{2+}**	**Q_{brine}**	**NaOH**	**$\frac{N_{base}^{real}}{N_{base}^{stoich}}$**	**Q_{base}**	**$Q_{recycle}$**	**N**	**τ**
	[g/l]	**[ml/min]**	**[mol/l]**		**[ml/min]**	**[ml/min]**	**[rpm]**	**[sec]**
6	24.1	743.7	4	1	367.4	-	400	54
7	24.1	743.7	4	1	367.4	3670	400	54
8	24.1	743.7	4	1	379	3670	400	54
9	24.1	66.9	4	1	33.1	3670	400	600
10	24.1	66.9	4	1	33.1	3670	400	600

Test 6 was performed in order to repeat the test made in the first experimental campaign and to use it as reference. All the other four tests were compare with this reference. In the test 7 was introduced a recycle: a high flow rate of solution (3670 ml/min) was get from the bottom of the reactor and it was recirculated on the top after mixing it with the inlet brine. In this way, the inlet magnesium concentration is reduce without a dilution of the inlet brine. Test 8 was made at the same operative condition of test 7, but in this case the recycled solution was mixed with the alkaline solution before entering again into the reactor. This configuration would reduce the local supersaturation in order to promote the crystal growth. Test 9 and test 10 instead were performed using a long resident time (10 min). Both tests were made recycling the suspension in the alkaline solution circuit, but in the test 10 the alkaline solution was pumped at the aspiration of the recycle pump in order to prevent clogging problem (as happened in the test 9).

In each test, each sample was collected after a time equal to 4 times the resident time. All the samples were analysed in order to investigate the granulometry distribution and

the purity. Scanning Electron Microscope was exploited to see the real shape of the particles and the real size of the crystals.

A pH meter was installed at the outlet and the flow rate were fine adapted in order to perform the test at around 11 pH. This was taken into account in the second experimental campaign while in the first campaign, the calculated flow rate were fixed without a pH control.

At the beginning of each tests, the reactor was filled up with brine and alkaline solution at stoichiometric condition until a litre of suspension was obtained. After this batch stage, the inlet pumps were simultaneously switched on. In this way, the steady state condition was achieved rapidly.

9.2.1 Results of the first experimental campaign with lab CSTR

A laser granulometer (Malvern Mastersizer 2000 with Hydro 2000MU) was adopted to evaluate the particles size distribution. All the samples were sonicated at 20 kHz for 2 minute to reduce the effect of the agglomeration. Different samples were collected and measured for each test, but only the data of the last samples are reported in Figure 9.3:

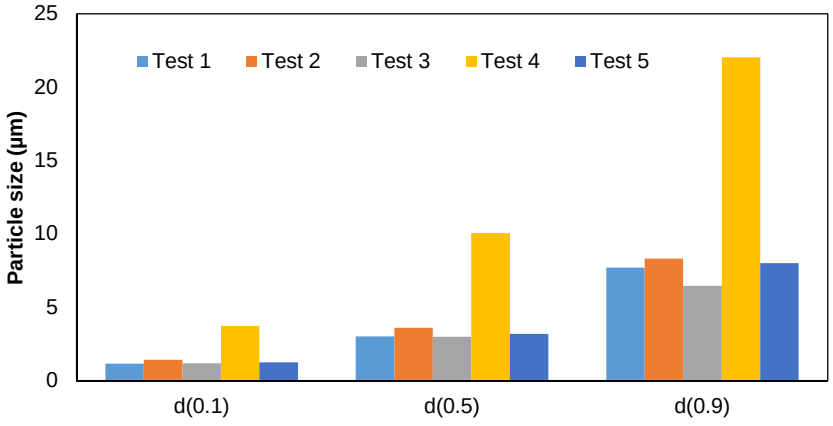

Figure 9.3. Granulometric size distribution of the tests made in the first experimental campaign.

As can be observed in Figure 9.3, test 1 and test 2 have similar results than the test made at the same resident time with MF-PFR (8 cm/sec). The same trend was obtained with a CSTR at higher rotation speed. Instead, the resident time has a strong effect on the

particle size distribution, in particular lower time gives higher size whereas higher resident time gives lower size. These tests have demonstrated that some parameters can have an influence on the particle size distribution, in particular at different condition, the agglomeration is promoted.

In this experimental tests, the pH was un-controlled and the value measured were always higher than 12.5 pH in all the samples collected. On one side this confirm that all the magnesium is precipitated, value obtained also with the chromatographic analysis, on the other side this high pH promotes the formation of small nuclei instead of grow them. However, all the $Mg(OH)_2$ samples collected were 100% pure after two washing steps.

9.2.2 Results of the second experimental campaign with lab CSTR

The first test was made at the same condition of the test 1. This was considered as reference test in order to compare it with other tests made with recycles. A laser granulometer (Malvern Mastersizer 2000 with Hydro 2000MU) was adopted to evaluate the particles size distribution but also a Scanning Electron Microscope was exploited in order to visually check the particles.

The results of granulometric analysis are reported in Figure 9.4. Also in this case were compared only the last samples collected, when the steady state was certainly reached.

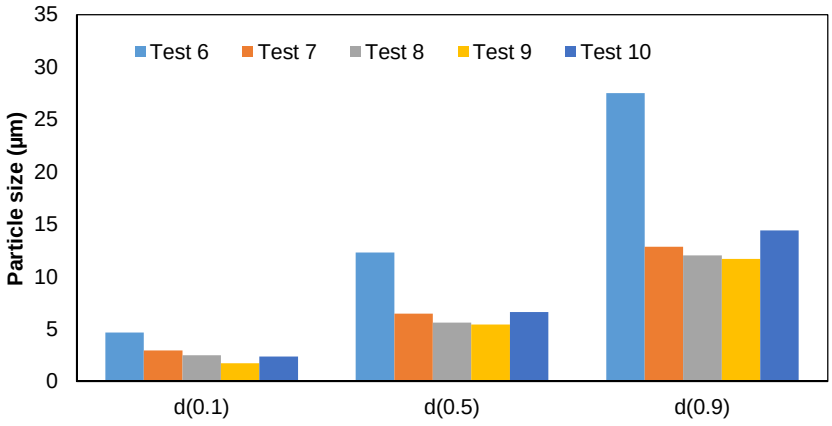

Figure 9.4: Granulometric size distribution of the tests made in the second experimental campaign

As can be observed in the previous figure, the recycle has a strong effect on the particle size distribution. Test 6, made at the same condition of test1, has particles larger than the

test made without a pH control. Moreover, it was experimentally noted that the particles dispersed in the suspension were rapidly separated by the mother liquor only by gravity. This suggested that a pH control change the agglomeration condition.

The recycle gives a marked effect on the particle size distribution, reducing the values, but seems that the different configuration does not have evident effects. The values obtained in the test 9 and test 10 with higher resident time are in line with the other results.

All the sample were analysed with ion chromatography confirming the maximum purity of magnesium hydroxide and the total conversion.

SEM analysis were made in order to analyse the effect of these different configurations on the crystals morphology.

The pictures were compared with the MAGNIFIN H5 magnesium hydroxide, the best reference in the flame retardant field at different magnifications (Figure 9.5, Figure 9.6 and Figure 9.7). As can be noted in the SEM analysis, the recycle, the pH control and high resident times (Test 9 and Test 10) modified the morphology of the crystals. If compared test 6 with tests 9, it is evident that structure changes from globular to flat. The crystal sizes are still in the range of hundred nanometres, unfortunately not suitable for the flame retardant. However, if the sample of CSTR test 9 is compared with another commercial magnesium hydroxide for flame retardants (HYDROFY), the performance became closer or much higher in terms of purity. The HYDROFY is obtained from milling some stones in smaller pieces, but in this way the crystal size distribution is random even if a size selection can be done.

According to the above discussion, the morphology and the size of the $Mg(OH)_2$ crystals obtained by reactive precipitation from waste brine can be modify if the process is run in specific condition. The presence of sulphate in the brine and the use of NaOH make the process challenging. More investigation are needed. Likely the only way to obtain crystals as those of MAGNIFIN is to have a post hydrothermal treatment. However, the magnesium hydroxide produced has high purity (always higher than 99.5 %) and a high specific surface, the main characteristics needed in the pharmaceutical and nutraceutical field.

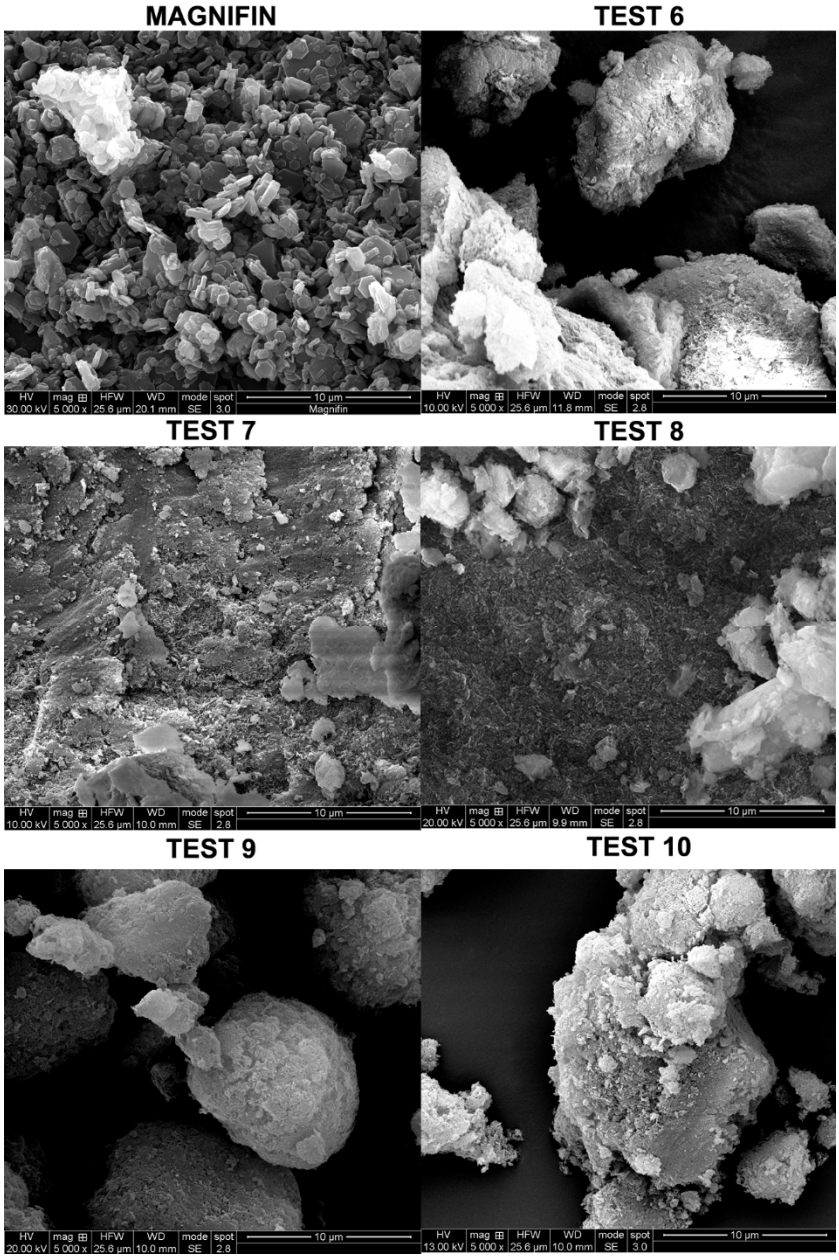

Figure 9.5: SEM pictures with magnification of 5000 X of the magnesium hydroxide collected in the CSTR tests (6-7-8-9-10) and MAGNIFIN H5.

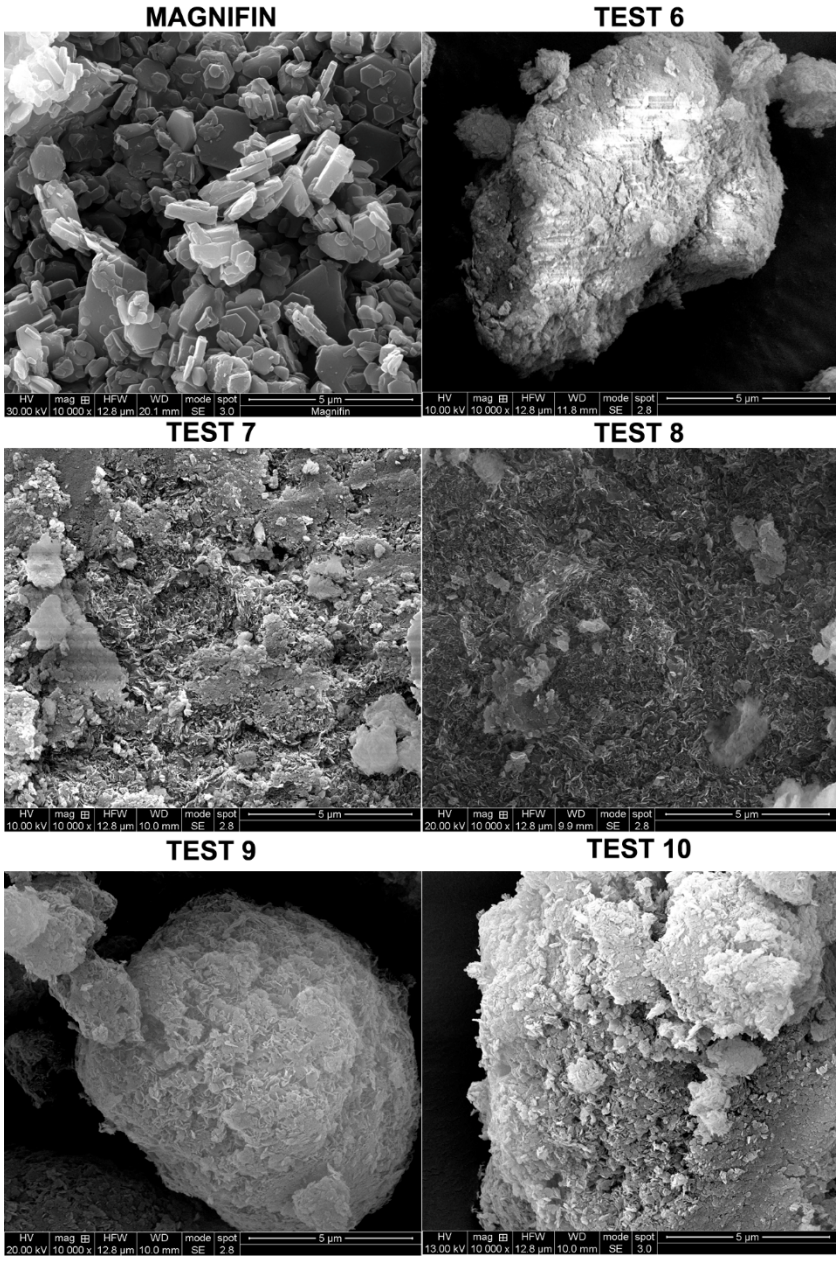

Figure 9.6: SEM pictures with magnification of 10000 X of the magnesium hydroxide collected in the CSTR tests (6-7-8-9-10) and MAGNIFIN H5.

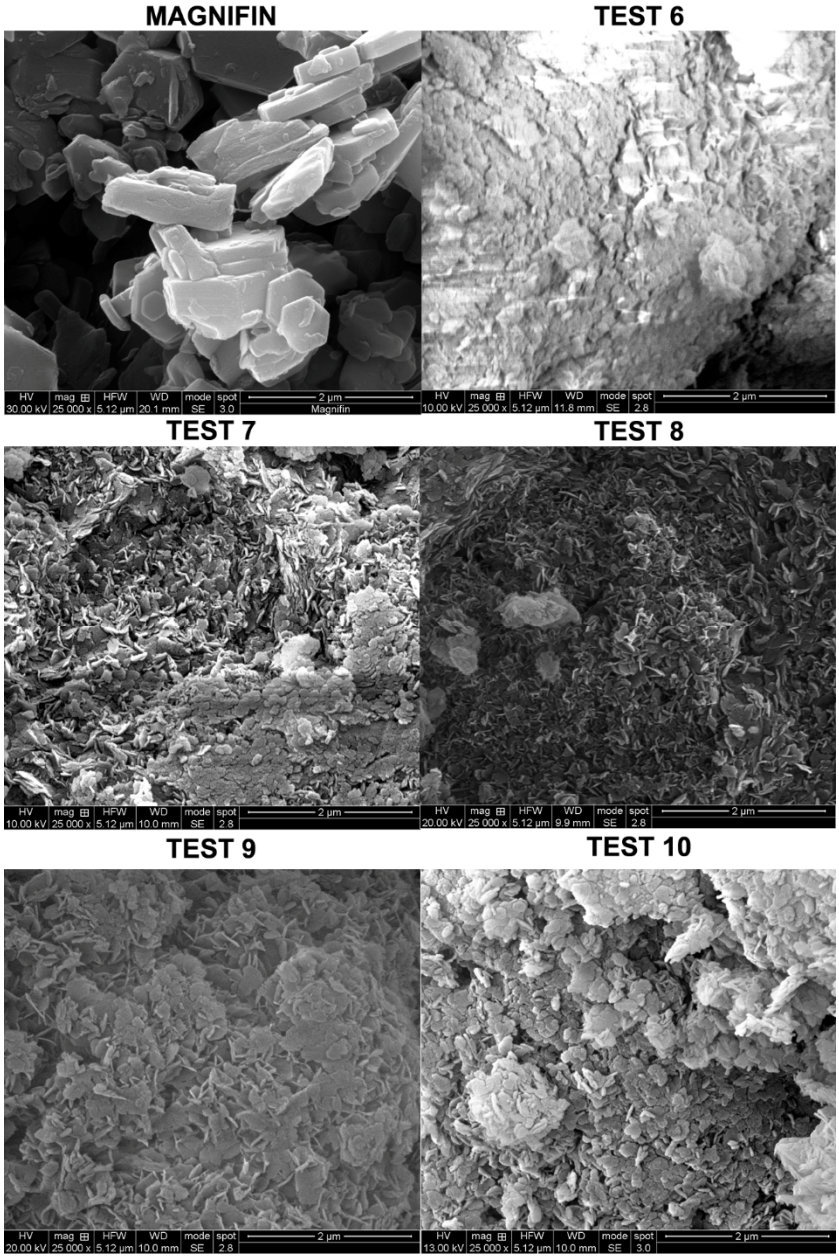

Figure 9.7: SEM pictures with magnification of 25000 X of the magnesium hydroxide collected in the CSTR tests (6-7-8-9-10) and MAGNIFIN H5.

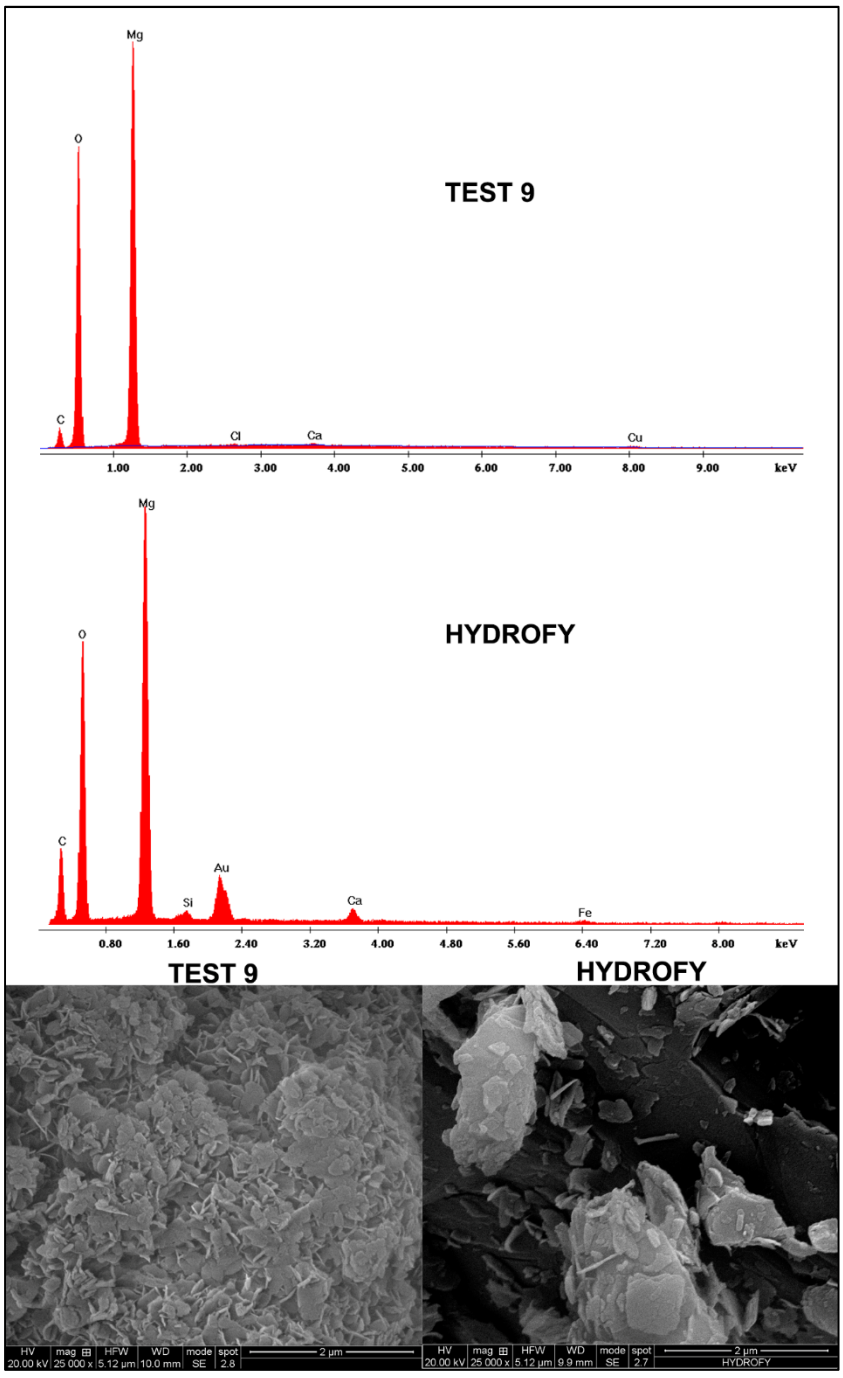

Figure 9.8: SEM pictures and EDAX analysis with magnification of 25000 X of the magnesium hydroxide collected in the CSTR test 9 and HYDROFY.

9.3 Future perspectives of magnesium hydroxide production from waste saltwork brines.

Good indications were obtained in the first experimental campaigns of the CrIEM reactor described in the chapter 8. In order to move the CrIEM to a higher TRL, a new reactor was designed and constructed with the purpose to increase the membrane exchange area and consequently the reactor capacity. The new CrIEM version (v04) is represented in Figure 9.9.

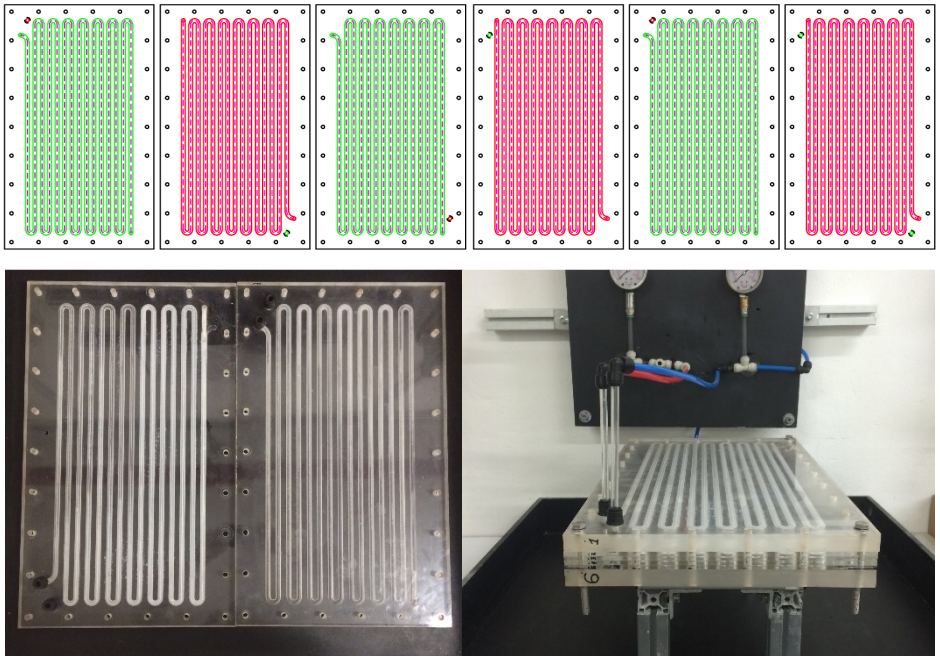

Figure 9.9: Version 4 of CrIEM reactor with 5 times larger surface exchange area.

More plates can be piled in the new CrIEM version, in this way three membranes instead of one can be inserted between the green and the red plates (Figure 9.9). Preliminary experimental tests were performed with a waste industrial brine showing good performance. This new reactor can treat a nominal flow rate of around 60 litters of solutions per day with a concentration of 3 g/lt of magnesium. The new reactor will be tested with different brines, in particular the performance with waste saltworks brine will be the object of the future experimental campaign.

The idea of the integrated cycle, widely described in the previous chapters, has become the business idea of a new Spin-off of the University of Palermo with the name ResourSEAs srl. The author of this manuscript is one of the co-founders. In particular, the idea to recovery magnesium from brine is the main business line. A first pilot plant with a nominal capacity of 7 kg/h of $Mg(OH)_2$ will be installed in 2018 in a real saltwork in Trapani. The reactor will be a new version of MF-PFR in which the alkaline solution is fed along the reactor by a coaxial tube positioned inside the main tube. In this way only one inlet is needed for the reactant. A 3D sketch is shown in Figure 9.10.

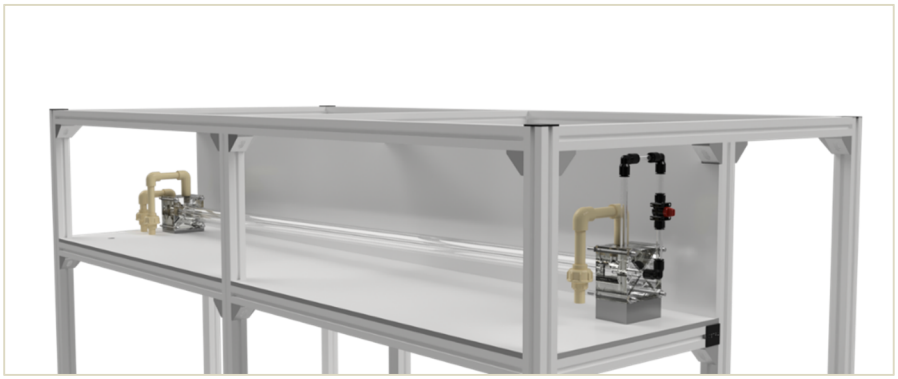

Figure 9.10: New MF-PFR reactor rendering made with Autodesk Fusion360®.

A final P&I of the plant with all the devices needed including the separation stage is already define. All the part of the plant will be assembled with the purpose to have an operative plant in 2018.

CONCLUSIONS SECTION II

Part of the thesis work, described in **Section II**, was dedicated to develop different methods and reactors for the recovery of minerals from natural waste streams. Waste brine of traditional saltworks was identified as the ideal source for magnesium recovery. The brine Mg concentration is 30 times higher than seawater and Mg can be recovered from brines by reactive crystallization. Starting from a literature review, some novel continuous reactors (MF-PFR and CrIEM) were proposed, designed, constructed and tested to produce high purity $Mg(OH)_2$ from waste brines. The carried out activities are here reported:

(i) analysis of the seawater integrated cycle concept, focusing the attention on the magnesium hydroxide production from brine using a Multiple Feed - Plug Flow Reactor (MF-PFR);

(ii) development of a new crystallizer with ion exchange membrane (CrIEM) to recovery magnesium from saltworks waste brine using low-cost alkaline solution;

(iii) investigation on processes to enhance magnesium hydroxide crystals growth with a CSTR reactor

(i) The idea of an integrated cycle that involves four processes is described. Seawater desalination, table salt production, magnesium manufacture and energy generation by salinity gradient power technologies can be linked through the use of waste brine of each process to be used as feed solution of the other.

Starting from seawater, this can be converted into fresh water by means of a desalination process. One important issue of this process is the waste brine disposal. If this brine is used to feed a saltworks, the salt table production can increase up to 30% more. The saltworks, in turn produces a bittern that in normal practice is disposed back into the sea. This bittern is rich of magnesium (up to 45 g/l) and it is almost free of calcium ions. This waste is a perfect saline solution from which magnesium can be recovered as magnesium hydroxide through reactive crystallization. After recovering magnesium, the exhausted brine, free of bivalent ions, can be exploited in an reverse electrodialysis unit to produce electrical energy.

In this manuscript, the attention was focused only on the magnesium recovery process. Different versions of Multiple Feed - Plug Flow Reactor (MF-PFR) were tested at different operative conditions trying to direct the process towards the production of crystals with granulometries in the 1-6 micron range, the specification needed in the flame retardant field. Different analytic techniques were adopted in order to measure the particles size distribution, the purity of the magnesium hydroxide produced and other performance parameters. The best results were obtained using a MF-PFR with a brine flowing velocity of 8 cm/s and four inlets for the alkaline solution (NaOH).

(ii) A new membrane reactor with ion exchange membrane has been developed as described in chapter 8. This patented Crystallizer with Ion Exchange Membrane (CrIEM) can lead to the recovery of high purity magnesium hydroxide from waste saltworks brine adopting any kind of alkaline solution. The OH^- ions pass through the membrane from the alkaline solution to the brine. Chlorides present in the brine goes in the opposite direction to rebalance the electro-neutrality, thus enhancing the OH^- ions flux driving force. The OH^- reacts with the magnesium ions in the brine forming magnesium hydroxide. The anion exchange membrane creates a barrier for the cations, which can not pass from the alkaline solution to the reacting volume, thus allowing the use of low-cost alkaline solution, such as calcium hydroxide, which normally presents co-precipitation problems of calcium compounds in the product.

Three CrIEM prototype units were designed, constructed and tested. The performance of different alkaline solutions and different operative conditions were analysed. Air as increaser of turbulence and cleaning balls were adopted to reduce fouling phenomena on the membranes. Good results were obtained using calcium hydroxide as alkaline solution: purity higher than 99.5% was observed with a total conversion. Some tests were also performed three times using the same membrane and obtaining stable performance in terms of purity and conversion.

(iii) The final part of the section II is dedicated to the study of the magnesium hydroxide crystals growth phenomena.

One of the main challenge, regarding the reactive precipitation of magnesium from brine, is the control of the particles morphology. Using a traditional CSTR reactor, two experimental campaign were performed, analysing the effect of internal recycles,

residence time and pH control. It was demonstrated by SEM analysis that, even if the crystals size are around hundred nanometres, their morphology changes if the alkaline solution is diluted by an internal recycle (thus reducing local supersaturation) with long residence times.

Future perspectives look at the installation of a pilot plant for magnesium hydroxide production (nominal capacity of 7 kg/h of $Mg(OH)_2$) in a real saltworks in Trapani. A new compact MF-PFR has been already designed and constructed. The final P&I including the process control has been elaborated. This activity will be developed in collaboration with a Spin-off company of the University of Palermo (ResourSEAs SrL) of which the author is one of the co-founders.

The research activities reported in this manuscript contributed to the obtainment of the prize “II edizione - Premio al talento e all’innovazione alla memoria di Daniele Ragaglia” by the Department of Industrial and Digital Innovation (DIID) of the University of Palermo in 2017.

NOMENCLATURE

C^*_{sat}	Maximum conventional solubility (mol/l)
$\bar{J}$	Total average flux of OH^- (mol s^{-1})
$\bar{N}$	Molar flux of OH^- (mol s^{-1})
$n_0^{Mg^{2+}}$	Initial magnesium ions (mol l^{-1})
Δp	Pressure difference (Pa)
Δp	pressure drops [Pa]
ΔV	Potential difference (V)
A	Active area of one cell pair [m^2]
a	Activity (mol l^{-1})
Ac	Crystal area (m^2)
A_m	Membrane area in the CrIEM reactor (m^2)
b	Membrane width (m)
b	Nucleation rate order with respect to supersaturation (-)
B°	Nucleation speed (# s m^{-3})
C	Molar concentration (mol l^{-1})
C_{br}	Magnesium concentration in the brine (mol/l)
C_{fix}	Fixed charge density (meq l^{-1})
d10	Diameter at the intercepts for 10% of cumulative volume (µm)
d50	Diameter at the intercepts for 50% of cumulative volume (µm)
d90	Diameter at the intercepts for 90% of cumulative volume (µm)
$d_{h,void}$	Hydraulic diameter [m]
D_p	Diameter of a single element of the random packing (m)
D_{salt}	Co-ion diffusion coefficient (m^2 s^{-1})
D_T	Inner diameter of the column (m)
E_{cell}	Electric voltage (V)
E_{stack}	Stack voltage [V]
F	Faraday constant (C mol^{-1})
f	Void fanning friction factor [-]
f_h	Spacer shadow factor perpendicular to the membrane (-)
F_i	Flow rate (m^3 s^{-1})
g	Growth rate order with respect to supersaturation (-)

G	Linear growth rate (m/s)
H	Channel thickness [m]
HETP	Height equivalent to a theoretical plate (m)
Ht	Total height of the packing material (m)
IEC	The number of fixed charges per unit weight of dry polymer (meq/g)
I_{stack}	Stack current [A]
j	Electrical current density (A/m^2)
J_i	Molar flux (mol/s)
J_{salt}	Salt flux ($mol\ m^{-2}\ s^{-1}$)
k	Electrical conductivity (S/cm)
k_a	Agglomeration rate coefficient ($g_{solution}\ \#^{-1}\ s^{-1}\ \mu m^{-3}$)
k_g	Growth rate coefficient ($\mu m\ s^{-1}$)
k_n	Nucleation rate coefficient ($\#\ s^{-1}\ g_{crystal}^{-1}$)
l	channel length [m]
L	Particle length (m)
m	Molal concentration ($mol\ kg^{-1}$)
m	Mass of membrane (dry or wet)
m_s	Mass of solid (kg)
M_T	Magma density ($kg\ m^{-3}$)
N	Cell pairs number [-]
n	Population density ($\#\ m^{-3}\ m$)
N_{base}	Mole of OH^- (mol)
N_{stoich}	Stoichiometric concentration of OH^- needed for the total conversion of Mg in the brine (mol)
N_t	Number of theoretical stages
OCV	Open Circuit Voltage (V)
P	Electric power [W]
P_d	Electric power density [$W\ m^{-2}_{cell\ pair}$]
Q	Thermal power (kW)
Q1	Thermal power in the heat exchanger (W)
Q2	Thermal power in the heat exchanger (W)
$Q_{air,dry}$	Dry air stream entering the saturation column (l/min)
Q_{br}	Brine flow rate (l/min)

Q_L	Feed flow rate (l/min)
Q_{sol}	Flow rate of the solutions feed to the air stripping (l/min)
Q_{spec}	Specific duty (kWh m^{-3})
Q^{tot}	Total (i.e. inclusive of all channels) feed flow rate [m^3/s]
Q_{wh}	Thermal power of the waste heat (W)
R	Ideal gas constant (J mol^{-1} k^{-1})
R_{AEM}	Resistance of the anion exchange membrane (Ω)
R_{blank}	Blank resistance [Ω]
R_{cells}	Cell pairs resistance [Ω]
R_{CEM}	Resistance of the anion exchange membrane (Ω)
R_{dilute}	resistance of diluted solution [Ω]
Re	Void Reynolds number [-]
R_{ext}	External resistance [Ω]
R_G	Growth rate (kg m^2 s)
R_{HIGH}	Resistance of the diluted compartments (Ω)
R_i	Membrane resistance (Ω m^2)
R_{LOW}	Resistance of the concentrated compartments (Ω)
R_{stack}	Internal stack resistance [Ω]
s	Fractional supersaturation (-)
S	Supersaturation degree (-)
SD	Swelling degree (%)
t	Net precipitation time (s)
T	Temperature (K)
T_{cold}	Temperature of the sink (°C)
T_{hot}	Heat source temperature (°C)
T_i	Transport number (-)
V	Potential (V)
v	velocity (m s^{-1})
v	Velocity [cm/s]
vf	Volume crystal factor (-)
$v_{m,void}$	mean velocity along the main flow direction (void channel) [cm/s]
V_{susp}	Suspension volume (m^3)

W	Power produced by heat engine (W)
X	Conversion (%)
z_i	Valence (-)
z_p	Distance between two liquid redistributors (m)

Greek letters

γ	Activity coefficient (-)
α	Membrane permselectivity (%)
δ	Spacer thickness (m)
Λ_0	Equivalent conductance of salt at infinite dilution (S cm^2 mol^{-1})
δ_m	Membrane thickness (m)
μ	solution dynamic viscosity [Pa s]
$A\gamma$	Model parameters to calculate the activity coefficients ($Kg^{1/2}$ $mol^{-1/2}$)
A_Λ	Model parameters to calculate equivalent conductance
$B\gamma$	Model parameters to calculate the activity coefficients (-)
$C\gamma$	Model parameters to calculate the activity coefficients (-)
C_Λ	Model parameters to calculate equivalent conductance (S cm^2 l mol^{-2})
$D\gamma$	Model parameters to calculate the activity coefficients (-)
$E\gamma$	Model parameters to calculate the activity coefficients (-)
ε	Channel porosity (-)
η	Energetic efficiency (%)
η_c	Cycle energetic efficiency (%)
η_{ex}	Exergetic efficiency (%)
β	Form crystal factor (-)
ϑ	Solid purity (%)
ρ	solution density [kg m^{-3}]
$\Delta\rho/\Delta m$	Parameter to calculate solution density (kg^2 mol^{-1} l^{-1})
Λ	Equivalent conductance (S cm^2 mol^{-1})
	(S $l^{0.5}$ cm^2 $mol^{-1.5}$)
ρ	Solution density (kg l^{-1})
B_Λ	Model parameters to calculate equivalent conductance ($l^{0.5}$ $mol^{-0.5}$)

Superscripts

CEM	Cation exchange membrane
AEM	Anion exchange membrane

Subscripts

a	Anions
AEM	Anion exchange membrane
blank	Blank potential or resistance; in the first case the potential measured immersing the electrodes in 3M solution of potassium chloride, in the second case the portion of stack resistance due to the electrode compartments.
c	Cations
CEM	Cation exchange membrane
conc	Concentrated
corr	Corrected value (of power output, stack voltage, stack current) obtained by using the stack resistance without the contribute of the blank resistance
dil	Diluted
exp	Experimental
ext	External circuit
filt	Filtrate
HIGH (high)	Concentrate solution
IN	Inlet stream
LOW (low)	Dilute solution
max	Maximum value
meas	Measured (potential)
net	Net value (of power output) measured after subtracting the power losses due to the pumping of feed solutions
OUT	Outlet stream
pwd	Powder
sat	Saturation
theor	Theoretical (potential)

Acronyms

AEM	Anion exchange membrane
AmBC	Ammonium bicarbonate
AmCb	Ammonium carbamate
BPE	Boiling point elevation
CAGR	Compound Annual Growth Rate
CC	Carbon carrier Cycle
CEM	Cation exchange membrane
CHP	Combined heat and power system
CIEMAT	Centro de Investigaciones Energéticas, Medioambientales y Tecnológicas
CrIEM	Crystallizer with Ion Exchange Membrane
CSD	Crystal size distribution
CSTR	Continuous-flow Stirred-Tank Reactor
DAQ	Data acquisition system
DMAPAA-Q	3-Acrylamidopropyl)trimethylammonium Chloride
ELECNRTL	Electrolyte non-random two-liquid model
ENRTL-RK	Electrolyte non-random two-liquid Redlich-Kwong model
FO	Forward Osmosis
FUJI	Fujifilm Manufacturing Europe B.V.
ICP-AES	Inductively coupled plasma atomic emission spectroscopy
IEM	Ion exchange membrane
IL	Ionic liquid
IPCC	Intergovernmental panel on climate change
IWH	Industrial waste heat
KC	Kalina cycle
MD	Membrane distillation
Me(OH)	Methanol
MED	Multiple effect distillation
MFC	Microbial fuel cell
MF-PFR	Multiple Feed – Flow Reactor
Mix	Salts mixture
MR	Membrane resistance

MRC	Microbial Reverse electrodialysis Cell
OHE	Osmotic Heat Engine
ORC	Organic rankine cycles
PEPG	Piezoelectric power generation with waste heat-powered expansion/compression cycle
PRO	Pressure retarded osmosis
RED HtP	RED heat-to-power project
RED	Reverse electrodialysis
RED-CL	Reverse electrodialysis closed loop
REDHE	Reverse Electrodialisys Heat Engine
REDstack	REDstack B.V
SE	Stirling engine
SGP	Salinity gradient power
SGPHE	Salinity gradient power heat engine
SRC	Steam rankine cycle
TDEG	Thermal driven electrochemical generator
TEG	Thermoelectric generation
TLC	Trilateral flash cycle
UEDIN	University of Edinburgh
UNIPA	Università degli Studi di Palermo
UPC	Universitat Politècnica de Catalunya
V-MEMD	Vacuum multi-effect membrane distillation
WHTC	Waste heat to cold
WHTH	Waste heat to heat
WHTP	Waste heat to power
WIP	Wirtschaft und Infrastruktur GmbH & Co Planungs-KG

REFERENCES

[1] Girling, Richard, Rubbish!, 2015.

[2] S. Brückner, S. Liu, L. Miró, M. Radspieler, L.F. Cabeza, E. Lävemann, Industrial waste heat recovery technologies: An economic analysis of heat transformation technologies, Appl. Energy. 151 (2015) 157–167.

[3] L. Miró, S. Brückner, L.F. Cabeza, Mapping and discussing Industrial Waste Heat (IWH) potentials for different countries, Renew. Sustain. Energy Rev. 51 (2015) 847–855.

[4] A.B. Little, S. Garimella, Comparative assessment of alternative cycles for waste heat recovery and upgrade, Energy. 36 (2011) 4492–4504.

[5] http://www.red-heat-to-power.eu/.

[6] A. Cipollina, A. Misseri, G.D. Staiti, A. Galia, G. Micale, O. Scialdone, Integrated production of fresh water, sea salt and magnesium from sea water, Desalin. Water Treat. 49 (2012) 1–14.

[7] a. Cipollina, M. Bevacqua, P. Dolcimascolo, A. Tamburini, A. Brucato, H. Glade, et al., Reactive crystallisation process for magnesium recovery from concentrated brines, Desalin. Water Treat. 55 (2015) 2377–2388.

[8] E. Macchi, Organic Rankine Cycle (ORC) Power Systems, Elsevier Science, 2016.

[9] M. Ashouri, A.M. Khoshkar Vandani, M. Mehrpooya, M.H. Ahmadi, A. Abdollahpour, Techno-economic assessment of a Kalina cycle driven by a parabolic Trough solar collector, Energy Convers. Manag. 105 (2015) 1328–1339.

[10] A.S. Rattner, S. Garimella, Energy harvesting, reuse and upgrade to reduce primary energy usage in the USA, Energy. 36 (2011) 6172–6183.

[11] B.E. Logan, M. Elimelech, Membrane based processes for sustainable power generation using water, Nature. 488 (2012) 313–319.

[12] A. Cipollina, G. Micale, Sustainable Energy from Salinity Gradients, in: 1st ed., Woodhead Publishing – Elsevier, 2016.

[13] L. Gurreri, A. Tamburini, A. Cipollina, G. Micale, M. Ciofalo, Flow and mass transfer in spacer-filled channels for reverse electrodialysis: a CFD parametrical study, J. Memb. Sci. 497 (2016) 300–317.

[14] R.S. Norman, Water Salination: A Source of Energy, Science (80-.). 186 (1974) 350–352.

[15] S. Loeb, R.S. Norman, Osmotic Power Plants, Science (80-.). 189 (1975) 654–655.

[16] R.E. PATTLE, Production of Electric Power by mixing Fresh and Salt Water in the Hydroelectric Pile, Nature. 174 (1954) 660–660.

[17] M. Tedesco, A. Cipollina, A. Tamburini, I.D.L. Bogle, G. Micale, A simulation tool for analysis and design of reverse electrodialysis using concentrated brines, Chem. Eng. Res. Des. 93 (2015) 441–456.

[18] R.A. Tufa, E. Curcio, E. Brauns, W. van Baak, E. Fontananova, G. Di Profio, Membrane Distillation and Reverse Electrodialysis for Near-Zero Liquid Discharge and low energy seawater desalination, J. Memb. Sci. 496 (2015) 325–333.

[19] M. Tedesco, C. Scalici, D. Vaccari, A. Cipollina, A. Tamburini, G. Micale, Performance of the first reverse electrodialysis pilot plant for power production from saline waters and concentrated brines, J. Memb. Sci. 500 (2016) 33–45.

[20] M. Tedesco, A. Cipollina, A. Tamburini, G. Micale, Towards 1kW power production in a reverse electrodialysis pilot plant with saline waters and concentrated brines, J. Memb. Sci. 522 (2017) 226–236.

[21] A. Achilli, A.E. Childress, Pressure retarded osmosis: From the vision of Sidney Loeb to the first prototype installation — Review, Desalination. 261 (2010) 205–211.

[22] F. Giacalone, A. Cipollina, F. Grisafi, A. Tamburini, G. Vella, G. Micale, Characterization of pressure retarded osmosis lab-scale systems, Desalin. Water Treat. 57 (2016) 22994–23006.

[23] A. Altaee, G.J. Millar, G. Zaragoza, Integration and optimization of pressure retarded osmosis with reverse osmosis for power generation and high efficiency desalination, Energy. 103 (2016) 110–118.

[24] D.A. Vermaas, J. Veerman, N.Y. Yip, M. Elimelech, M. Saakes, K. Nijmeijer, High Efficiency in Energy Generation from Salinity Gradients with Reverse Electrodialysis, ACS Sustain. Chem. Eng. 1 (2013) 1295–1302.

[25] A. Tamburini, G. La Barbera, A. Cipollina, M. Ciofalo, G. Micale, CFD simulation of channels for direct and reverse electrodialysis, Desalin. Water Treat. 48 (2012) 370–389.

[26] H.-I. Jeong, H.J. Kim, D.-K. Kim, Numerical analysis of transport phenomena in reverse electrodialysis for system design and optimization, Energy. 68 (2014) 229–237.

[27] A.H. Avci, P. Sarkar, R.A. Tufa, D. Messana, P. Argurio, E. Fontananova, et al., Effect of Mg 2+ ions on energy generation by Reverse Electrodialysis, J. Memb. Sci. 520 (2016) 499–506.

[28] IEA, CO2 emissions from fuel combustion, Oecd/Iea. (2016) 1–155.

[29] European Enviroment Agency, Final energy consumption by sector and fuel, (2016). https://www.eea.europa.eu/data-and-maps/indicators/final-energy-consumption-by-sector-9/assessment-1 (accessed August 10, 2017).

[30] H. Lu, L. Price, Q. Zhang, Capturing the invisible resource: Analysis of waste heat potential in Chinese industry, Appl. Energy. 161 (2016) 497–511.

[31] A. Tamburini, A. Cipollina, M. Papapetrou, A. Piacentino, G. Micale, Salinity gradient engines, in: Sustainable Energy from Salinity Gradients, Woodhead Publishing – Elsevier, 2016.

[32] M. Tedesco, Reverse electrodialysis advanced modelling and scale-up, Università degli Studi di Palermo, 2015.

[33] H. Chen, D.Y. Goswami, E.K. Stefanakos, A review of thermodynamic cycles and working fluids for the conversion of low-grade heat, Renew. Sustain. Energy Rev. 14 (2010) 3059–3067.

[34] W.C. Andersen, T.J. Bruno, Rapid Screening of Fluids for Chemical Stability in Organic Rankine Cycle Applications, Ind. Eng. Chem. Res. 44 (2005) 5560–5566.

[35] Y. Chen, P. Lundqvist, A. Johansson, P. Platell, A comparative study of the carbon dioxide transcritical power cycle compared with an organic rankine cycle with R123 as working fluid in waste heat recovery, Appl. Therm. Eng. 26 (2006) 2142–2147.

[36] X. Zhang, M. He, Y. Zhang, A review of research on the Kalina cycle, Renew. Sustain. Energy Rev. 16 (2012) 5309–5318.

[37] D.Y. Goswami, Solar thermal power: status of technologies and opportunities for research, Proc. Proc. 2nd ISHMT-ASME Heat Mass Trans. Conf. (1995) 57–60.

[38] D.Y. Goswami, Solar Thermal Power Technology: Present Status and Ideas for the Future, Energy Sources. 20 (1998) 137–145.

[39] R. Vasquez Padilla, A. Ramos Archibold, G. Demirkaya, S. Besarati, D.Y. Goswami, M.M. Rahman, et al., Performance Analysis of a Rankine-Goswami Combined Cycle, in: ASME 2011 5th Int. Conf. Energy Sustain. Parts A, B, C, ASME, 2011: pp. 385–393.

[40] M.A. Iqbal, M. Ahmadi, F. Melhem, S. Rana, A. Akbarzadeh, A. Date, Power Generation from Low Grade Heat Using Trilateral Flash Cycle, Energy Procedia. 110 (2017) 492–497.

[41] E.H. Wang, H.G. Zhang, B.Y. Fan, M.G. Ouyang, Y. Zhao, Q.H. Mu, Study of working fluid selection of organic Rankine cycle (ORC) for engine waste heat recovery, Energy. 36 (2011) 3406–3418.

[42] T. Monin, A. Tessier-Poirier, E. Léveillé, A. Juneau-Fecteau, T. Skotnicki, F. Formosa, et al., First experimental demonstration of a Self-Oscillating Fluidic Heat Engine (SOFHE) with piezoelectric power generation, J. Phys. Conf. Ser. 773 (2016) 12039.

[43] J. Karthäuser, T. Öström, Method for Conversion of Low Temperature Heat To Electricity and Cooling, and System Therefore, US 2013/0038055 A1, 2012. http://patentscope.wipo.int/search/en/WO2012128715.

[44] a. T. Jones, W. Finley, Recent development in salinity gradient power, Oceans. 4 (2003) 2284–2287.

[45] M. Turek, B. Bandura, Renewable energy by reverse electrodialysis, Desalination. 205 (2007) 67–74.

[46] P. Długołęcki, A. Gambier, K. Nijmeijer, M. Wessling, Practical Potential of Reverse Electrodialysis As Process for Sustainable Energy Generation, Environ. Sci. Technol. 43 (2009) 6888–6894.

[47] J. Veerman, Reverse Electrodialysis: design and optimization by modeling and experimentation, University of Groeningen, 2008.

[48] J. Veerman, M. Saakes, S.J.J. Metz, G.J.J. Harmsen, Reverse electrodialysis: Performance of a stack with 50 cells on the mixing of sea and river water, J. Memb. Sci. 327 (2009) 136–144.

[49] E. Brauns, W. De Wilde, B. Van den Bosch, P. Lens, L. Pinoy, M. Empsten, On the experimental verification of an electrodialysis simulation model for optimal stack configuration design through solver software, Desalination. 249 (2009) 1030–1038.

[50] J.W. Post, H.V.M. Hamelers, C.J.N. Buisman, Energy recovery from controlled mixing salt and fresh water with a reverse electrodialysis system, Environ. Sci. Technol. 42 (2008) 5785–5790.

[51] J. W. Post, Blue Energy: Electricity production from Salinity Gradients by Reverse Electrodialysis, Wageningen University, 2009.

[52] J.W. Post, C.H. Goeting, J. Valk, S. Goinga, J. Veerman, H.V.M. Hamelers, et al., Towards implementation of reverse electrodialysis for power generation from salinity gradients, Desalin. Water Treat. 16 (2010) 182–193.

[53] J. Veerman, M. Saakes, S.J. Metz, G.J. Harmsen, Electrical power from sea and river water by reverse electrodialysis: A first step from the laboratory to a real power plant, Environ. Sci. Technol. 44 (2010) 9207–9212.

[54] D.A. Vermaas, E. Guler, M. Saakes, K. Nijmeijer, Theoretical power density from salinity gradients using reverse electrodialysis, Energy Procedia. 20 (2012) 170–184.

[55] D.A. Vermaas, S. Bajracharya, B.B. Sales, M. Saakes, B. Hamelers, K. Nijmeijer, Clean energy generation using capacitive electrodes in reverse electrodialysis, Energy Environ. Sci. 6 (2013) 643–651.

[56] D.A.A. Vermaas, Energy generation from mixing salt water and fresh water: Smart flow strategies for reverse electrodialysis, University of Twente, 2014.

[57] M. Tedesco, A. Cipollina, A. Tamburini, W. van Baak, G. Micale, Modelling the Reverse ElectroDialysis process with seawater and concentrated brines, Desalin. Water Treat. 49 (2012) 404–424.

[58] M. Tedesco, A. Cipollina, A. Tamburini, G. Micale, J. Helsen, M. Papapetrou, REAPower: use of desalination brine for power production through reverse electrodialysis, Desalin. Water Treat. 53 (2015) 3161–3169.

[59] M. Tedesco, C. Scalici, D. Vaccari, A. Cipollina, A. Tamburini, G. Micale, Performance of the first Reverse Electrodialysis pilot plant for power production from saline waters and concentrated brines, J. Memb. Sci. 500 (2016) 33–45.

[60] M. Tedesco, A. Cipollina, A. Tamburini, G. Micale, Towards 1 kW power production in a reverse electrodialysis pilot plant with saline waters and concentrated brines, J. Memb. Sci. 522 (2017).

[61] D.A.A. Vermaas, M. Saakes, K. Nijmeijer, Power generation using profiled membranes in reverse electrodialysis, J. Memb. Sci. 385–386 (2011) 234–242.

[62] A.E. Yaroshchuk, An analytical solution for the diffusion of electrolytes through a charge-mosaic membrane, Phys. Chem. Chem. Phys. 3 (2001) 1883–1890.

[63] A. Yaroshchuk, Influence of osmosis on the diffusion from concentrated solutions through composite/asymmetric membranes: Theoretical analysis, J. Memb. Sci. 355 (2010) 98–103.

[64] M.Y. Kariduraganavar, R.K. Nagarale, A.A. Kittur, S.S. Kulkarni, Ion-exchange membranes: preparative methods for electrodialysis and fuel cell applications, Desalination. 197 (2006) 225–246.

[65] P.E. Długołęcki, Mass transport reverse electrodialysis for sustainable energy generation, University of Twente, 2009.

[66] D.R. Lide, CRC Handbook of Chemistry and Physics, 86th ed., n.d.

[67] V.M.M.Q. Lobo J. L., Handbook of electrolyte solutions, Elsevier, 1989.

[68] A.H. Galama, D.A. Vermaas, J. Veerman, M. Saakes, H.H.M. Rijnaarts, J.W. Post, et al., Membrane resistance: The effect of salinity gradients over a cation exchange membrane, J. Memb. Sci. 467 (2014) 279–291.

[69] J. Veerman, Reverse Electrodialysis design and optimization by modeling and experimentation, 2010.

[70] Y. Tanaka, Ion Exchange Membranes: Fundamentals and applications, Elsevier, Ibaraki, Japan, 2007.

[71] O. Scialdone, C. Guarisco, S. Grispo, A.D. Angelo, A. Galia, Investigation of electrode material - Redox couple systems for reverse electrodialysis processes. Part I: Iron redox couples, J. Electroanal. Chem. 681 (2012) 66–75.

[72] M. Tedesco, A. Cipollina, A. Tamburini, W. van Baak, G. Micale, Modelling the Reverse ElectroDialysis process with seawater and concentrated brines, Desalin. Water Treat. 49 (2012) 404–424.

[73] E. Shaulsky, C. Boo, S. Lin, M. Elimelech, Membrane-Based Osmotic Heat Engine with Organic Solvent for Enhanced Power Generation from Low-Grade Heat, Environ. Sci. Technol. 49 (2015) 5820–5827.

[74] C. Luo, Q. Su, W. Mi, Thermophysical properties and application of LiNO3–H2O working fluid, Int. J. Refrig. 36 (2013) 1689–1700.

[75] A. Huicochea, R.J. Romero, W. Rivera, G. Gutierrez-Urueta, J. Siqueiros, I. Pilatowsky, A novel cogeneration system: A proton exchange membrane fuel cell coupled to a heat transformer, Appl. Therm. Eng. 50 (2013) 1530–1535.

[76] A. Paurine, G.G. Maidment, I.W. Eames, J.F. Missenden, Development of a thermo-gravity pumping mechanism for circulating the working fluids in a novel LiBr-H2O vapour absorption refrigeration (VAR) system, Appl. Therm. Eng. 47 (2012) 25–33.

[77] J. Sun, L. Fu, S. Zhang, W. Hou, A mathematical model with experiments of single effect absorption heat pump using LiBr-H2O, Appl. Therm. Eng. 30 (2010) 2753–2762.

[78] S.M. Xu, L. Zhang, C.H. Xu, J. Liang, R. Du, Numerical simulation of an advanced energy storage system using H2O-LiBr as working fluid, Part 1: System design and modeling, Int. J. Refrig. 30 (2007) 354–363.

[79] W.J. Koehler, W.E. Ibele, J. Soltes, E.R. Winter, Availability simulation of a lithium bromide absorption heat pump, Heat Recover. Syst. CHP. 8 (1988) 157–171.

[80] A. Paurine, G.G. Maidment, I.W. Eames, Development of a packed bed regenerative solution heat exchanger (R-SHX) for a single stage LiBr-H2O vapour absorption refrigeration (VAR) system, Appl. Therm. Eng. 60 (2013) 182–187.

[81] G. Yaxiu, W. Yuyuan, K. Xin, Experimental research on a new solar pump-free lithium bromide absorption refrigeration system with a second generator, Sol. Energy. 82 (2008) 33–42.

[82] R. Palacios-Bereche, R. Gonzales, S.A. Nebra, Exergy calculation of lithium bromide-water solution and its application in the exergetic evaluation of absorption refrigeration systems LiBr-H2O, Int. J. Energy Res. 36 (2012) 166–181.

[83] O. Calderone, Reverse electrodialysis for power generation from waste heat, Palermo, 2014.

[84] G.M. Geise, H.J. Cassady, D.R. Paul, B.E. Logan, M.A. Hickner, Specific ion effects on membrane potential and the permselectivity of ion exchange membranes, Phys. Chem. Chem. Phys. 16 (2014) 21673–21681.

[85] Y. An, P. Zuo, X. Cheng, L. Liao, G. Yin, Preparation and Properties of Ionic-Liquid Mixed Solutions as a Safety Electrolyte for Lithium Ion Batteries, 6 (2011) 2398–2410.

[86] R.D. Noble, D.L. Gin, Perspective on ionic liquids and ionic liquid membranes, J. Memb. Sci. 369 (2011) 1–4.

[87] J.C. Padilha, J. Basso, L.G. Trindade, E.M.A. Martini, M.O. De Souza, R.F. De Souza, Ionic liquids in proton exchange membrane fuel cells : Efficient systems for energy generation, 195 (2010) 6483–6485.

[88] T. Tsuda, C.L. Hussey, Electrochemical Applications of Room-Temperature Ionic Liquids, (2007).

[89] H. Ohno, Electrochemical aspects of ionic liquids, Wiley, 2011.

[90] X. Wang, Y. Nie, X. Zhang, S. Zhang, J. Li, Recovery of ionic liquids from dilute aqueous solutions by electrodialysis, Desalination. 285 (2012) 205–212.

[91] E.T. Fox, E. Paillard, O. Borodin, W.A. Henderson, Physicochemical properties of binary ionic liquid-aprotic solvent electrolyte mixtures, J. Phys. Chem. C. 117 (2013) 78–84.

[92] K. Haerens, P. De Vreese, E. Matthijs, L. Pinoy, K. Binnemans, B. Van Der Bruggen, Production of ionic liquids by electrodialysis, Sep. Purif. Technol. 97 (2012) 90–95.

[93] P. Keil, M. Schwiertz, A. König, Metathesis of ionic liquids: Continuous ion exchange by donnan dialysis, Chem. Eng. Technol. 37 (2014) 919–926.

[94] H. Li, H. Meng, C. Li, L. Li, Competitive transport of ionic liquids and impurity ions during the electrodialysis process, Desalination. 245 (2009) 349–356.

[95] C.M. Tenney, M. Massel, J.M. Mayes, M. Sen, J.F. Brennecke, E.J. Maginn, A Computational and Experimental Study of the Heat Transfer Properties of Nine Different Ionic Liquids, J. Chem. Eng. Data. 59 (2014) 391–399.

[96] C. Petra, B.-B. Katali, Application of Ionic Liquids in Membrane Separation Processes, in: Ion. Liq. Appl. Perspect., InTech, 2011.

[97] X. Luo, X. Cao, Y. Mo, K. Xiao, X. Zhang, P. Liang, et al., Power generation by coupling reverse electrodialysis and ammonium bicarbonate: Implication for recovery of waste heat, Electrochem. Commun. 19 (2012) 25–28.

[98] M.C. Hatzell, B.E. Logan, Evaluation of flow fields on bubble removal and system performance in an ammonium bicarbonate reverse electrodialysis stack, J. Memb. Sci. 446 (2013) 449–455.

[99] R.D. Cusick, Y. Kim, B.E. Logan, Energy Capture from Thermolytic Solutions in Microbial Reverse-Electrodialysis Cells, Science (80-.). 335 (2012) 1474–1477.

[100] R.L. McGinnis, J.R. McCutcheon, M. Elimelech, A novel ammonia–carbon dioxide osmotic heat engine for power generation, J. Memb. Sci. 305 (2007) 13–19.

[101] F. Ullman, Ullmann's encyclopedia of industrial chemistry, Wiley-VCH Verlag, Weinheim, 2005.

[102] R.H. Perry, D.W. Green, J.O. Maloney, Perry's chemical engineers' handbook, McGraw-Hill New York, 2008.

[103] J. Veerman, M. Saakes, S.J. Metz, G.J. Harmsen, Reverse electrodialysis: Performance of a stack with 50 cells on the mixing of sea and river water, J. Memb. Sci. 327 (2009) 136–144.

[104] M. Tedesco, E. Brauns, A. Cipollina, G. Micale, P. Modica, G. Russo, et al., Reverse Electrodialysis with saline waters and concentrated brines: a laboratory investigation towards technology scale-up, J. Memb. Sci. 492 (2015) 9–20.

[105] A. Daniilidis, D.A.A. Vermaas, R. Herber, K. Nijmeijer, Experimentally obtainable energy from mixing river water, seawater or brines with reverse electrodialysis, Renew. Energy. 64 (2014) 123–131.

[106] R.J. Moffat, Describing the uncertainties in experimental results, Exp. Therm. Fluid Sci. 1 (1988) 3–17.

[107] A. Tamburini, P. Pitò, A. Cipollina, G. Micale, M. Ciofalo, A Thermochromic Liquid Crystals Image Analysis technique to investigate temperature polarization in spacer-filled channels for Membrane Distillation, J. Memb. Sci. 447 (2013) 260–273.

[108] L. Gurreri, A. Tamburini, A. Cipollina, G. Micale, M. Ciofalo, CFD prediction of concentration polarization phenomena in spacer-filled channels for reverse electrodialysis, J. Memb. Sci. 468 (2014) 133–148.

[109] E.A. Werner, CXVII.—The constitution of carbamides. Part XI. The mechanism of the synthesis of urea from ammonium carbamate. The preparation of certain mixed tri-substituted carbamates and dithiocarbamates, J. Chem. Soc., Trans. 117 (1920) 1046–1053.

[110] J.B. Sumner, D.B. Hand, Ammonium Carbamate as the Intermediate Product in the Action of Urease on Urea, Exp. Biol. Med. 27 (1930) 292–294.

[111] H.J. Krase, V.L. Gaddy, EQUILIBRIA IN THE AMMONIUM CARBAMATE-UREA-WATER-AMMONIA SYSTEM, J. Am. Chem. Soc. 52 (1930) 3088–3093.

[112] K.G. Clark, L. Gaddy, Equilibria in the Ammonium Carbamate - Urea-Water System, Ind. Eng. Chem. Res. 25 (1933) 1092–1096.

[113] F. Mani, M. Peruzzini, F. Barzagli, Selective production of solid ammonium bicarbonate and ammonium carbamate in the process of carbon dioxide capture by ammonia solutions : A feasible process to produce urea in mild, in: ACS Natl. Meet. B. Abstr. - Conf. Pap., 2010: p. 1.

[114] F. Barzagli, F. Mani, M. Peruzzini, From greenhouse gas to feedstock: formation of ammonium carbamate from CO2 and NH3 in organic solvents and its catalytic conversion into urea under mild conditions, Green Chem. 13 (2011) 1267.

[115] J.E. Schmidt, D.S. Dudis, D.J. Miller, The Use of Ammonium Carbamate as a High Energy Density Thermal Energy Storage Material, MRS Proc. 1325 (2011).

[116] A.H. Galama, Ion exchange membranes in seawater applications. Processes and characteristics, Wageningen University, 2015.

[117] K. Kwon, B.H. Park, D.H. Kim, D. Kim, Parametric study of reverse electrodialysis using ammonium bicarbonate solution for low-grade waste heat recovery, Energy Convers. Manag. 103 (2015) 104–110.

[118] R.L. McGinnis, M. Elimelech, Energy requirements of ammonia–carbon dioxide forward osmosis desalination, Desalination. 207 (2007) 370–382.

[119] Merck Millipore Database:, (n.d.). http://www.merckmillipore.com/DE/de (accessed August 4, 2016).

[120] J.E. Pelkie, P.J. Concannon, D.B. Manley, B.E. Poling, Product distributions in the carbon dioxide-ammonia-water system from liquid conductivity measurements, Ind. Eng. Chem. Res. 31 (1992) 2209–2215.

[121] H. Que, C.-C. Chen, Thermodynamic Modeling of the NH_3–CO_2–H_2O System with Electrolyte NRTL Model, Ind. Eng. Chem. Res. 50 (2011) 11406–11421.

[122] P.E. Holmes, M. Naaz, B.E. Poling, Ion Concentrations in the CO_2−NH_3−H_2O System from ^{13}C NMR Spectroscopy, Ind. Eng. Chem. Res. 37 (1998) 3281–3287.

[123] Q. Zhao, S. Wang, F. Qin, C. Chen, Composition Analysis of CO_2−NH_3−H_2O System Based on Raman Spectra, Ind. Eng. Chem. Res. 50 (2011) 5316–5325.

[124] R.L. McGinnis, J.R. McCutcheon, M. Elimelech, A novel ammonia-carbon dioxide osmotic heat engine for power generation, J. Memb. Sci. 305 (2007) 13–19.

[125] J. Veerman, M. Saakes, S.J. Metz, G.J. Harmsen, Reverse electrodialysis: A validated process model for design and optimization, Chem. Eng. J. 166 (2011) 256–268.

[126] M. Tedesco, P. Mazzola, A. Tamburini, G. Micale, I.D.L. Bogle, M. Papapetrou, et al., Analysis and simulation of scale-up potentials in reverse electrodialysis, Desalin. Water Treat. 55 (2015) 3391–3403.

[127] G. Jones, C.F. Bickford, The conductance of aqueous solutions as a function of the concentration. I. Potassium bromide and lanthanum chloride, J. Am. Chem. Soc. 56 (1934) 602–611.

[128] B.R. Staples, Activity and osmotic coefficients of aqueous alkali metal nitrites, J. Phys. Chem. Ref. Data. 10 (1981) 765–778.

[129] H. Strathmann, Ion-exchange membrane separation processes, Elsevier Science, 2004.

[130] S. Pawlowski, P. Sistat, J.G. Crespo, S. Velizarov, Mass transfer in reverse electrodialysis: Flow entrance effects and diffusion boundary layer thickness, J. Memb. Sci. 471 (2014) 72–83.

[131] J. Liu, A. Iranshahi, Y. Lou, G. Lipscomb, Static mixing spacers for spiral wound modules, J. Memb. Sci. 442 (2013) 140–148.

[132] M. Bevacqua, A. Carubia, A. Cipollina, A. Tamburini, M. Tedesco, G. Micale, Performance of a RED system with ammonium hydrogen carbonate solutions, Desalin. Water Treat. 57 (2016) 23007–23018.

[133] R. Neff, Solvent extractor, US3130156 A, 1964. http://www.google.com/patents/US3130156 (accessed March 8, 2016).

[134] J.R. McCutcheon, R.L. McGinnis, M. Elimelech, A novel ammonia—carbon dioxide forward (direct) osmosis desalination process, Desalination. 174 (2005) 1–11.

[135] S.-M. Shim, S.-J. Lee, W.-S. Kim, Experimental study on the performance evaluation of vacuum distillation process for NH4HCO3 removal, J. Mech. Sci. Technol. 27 (2013) 1171–1178.

[136] Y. Kim, J.H. Lee, Y.C. Kim, K.H. Lee, I.S. Park, S.-J. Park, Operation and simulation of pilot-scale forward osmosis desalination with ammonium bicarbonate, Chem. Eng. Res. Des. 94 (2015) 390–395.

[137] X. Zhou, D.B. Gingerich, M.S. Mauter, Water Treatment Capacity of Forward-Osmosis Systems Utilizing Power-Plant Waste Heat, Ind. Eng. Chem. Res. 54 (2015) 6378–6389.

[138] M. Shahid, X. Xue, C. Fan, B.W. Ninham, R.M. Pashley, Study of a Novel Method for the Thermolysis of Solutes in Aqueous Solution Using a Low Temperature Bubble Column Evaporator., J. Phys. Chem. B. 119 (2015) 8072–9.

[139] D.H. Kim, B.H. Park, K. Kwon, L. Li, D. Kim, Modeling of power generation with thermolytic reverse electrodialysis for low-grade waste heat recovery, Appl. Energy. 189 (2017) 201–210.

[140] D.W. Green, R.H. Perry, Perry's Chemical Engineers' Handbook, Eighth Edition, 2008.

[141] C. Gatz, Conversion of Low Grade Heat to Power through Closed-Loop Reverse Electrodialysis, Palermo-Italy, 2016.

[142] Koch-Glitsch, STRUCTURED Packing, (n.d.). http://www.koch-glitsch.com/Document Library/KGSP.pdf (accessed July 25, 2016).

[143] Paolo Montesanto, Sviluppo di unità di stripping per la rigenerazione termica di soluzioni di Sali termolitici, Palermo, 2016.

[144] A. Schönbucher, Thermische Verfahrenstechnik: Grundlagen und Berechnungsmethoden für Ausrüs-tungen und Prozesse, 1st ed., Springer-Verlag, Heidelberg, 2002.

[145] E. Commission, CRITICAL RAW MATERIALS PROFILES, (2015). http://ec.europa.eu/enterprise/policies/raw-materials/files/docs/crm-critical-material-profiles_en.pdf.

[146] A. Cipollina, G. Micale, A. Brucato, A. Tamburini, M. Bevacqua, G. Cerniglia, Reattore con membrana a scambio ionico, 102015000042831, 2015.

[147] M. Tedesco, A. Cipollina, A. Tamburini, G. Micale, J. Helsen, M. Papapetrou, REAPower: use of desalination brine for power production through reverse electrodialysis, Desalin. Water Treat. 53 (2015) 3161–3169.

[148] European Commission-Enterprise and Industry, (n.d.). https://ec.europa.eu/growth/tools-databases/eip-raw-materials/en/content/european-commission-dg-enterprise-and-industry-homepage.

[149] Roskill Information Services Ltd., Salt: Global Industry Markets and Outlook, London, 2014.

[150] N. Ghaffour, J. Bundschuh, H. Mahmoudi, M.F.A. Goosen, Renewable energy-driven desalination technologies: A comprehensive review on challenges and potential applications of integrated systems, Desalination. 356 (2015) 94–114.

[151] F. Virgili, GWI Q4 Desalination Market Review and Forecast Points to Some Improvement in Contracted Capacity, IDA News. (2015).

[152] S. Loutatidou, B. Chalermthai, P.R. Marpu, H.A. Arafat, Capital cost estimation of RO plants: GCC countries versus southern Europe, Desalination. 347 (2014) 103–111.

[153] V.G. Gude, Desalination and sustainability - An appraisal and current perspective, Water Res. 89 (2016) 87–106.

[154] QYR Chemical & Material Research Center, Europe Magnesium Hydroxide Industry 2016 Market Research Report, 2016.

[155] I.S. Al-Mutaz, By-product recovery from Saudi desalination plants, Desalination. 64 (1987) 97–110.

[156] I.S. Al Mutaz, K.M. Wagialia, Production of magnesium from desalination brines, Resour. Conserv. Recycl. 3 (1990) 231–239.

[157] M. Turek, W. Gnot, Precipitation of Magnesium Hydroxide from Brine, Ind. Eng. Chem. Res. 34 (1995) 244–250.

[158] S.W. Lee, J.H. Lim, Recovery of Magnesium Oxide and Magnesium Hydroxide from the Waste Bittren, Adv. Mater. Res. 26–28 (2007) 1019–1022. http://www.scientific.net/AMR.26-28.1019.

[159] C. Henrist, J.-P. Mathieu, C. Vogels, A. Rulmont, R. Cloots, Morphological study of magnesium hydroxide nanoparticles precipitated in dilute aqueous solution, J. Cryst. Growth. 249 (2003) 321–330.

[160] Z.Q. Liu, L.J. Li, Y.F. Chen, X.K. Li, Y.L. Zhang, G.L. Shen, Optimal parameters of response surface methodology for preparation of magnesium hydroxide flame retardant, 11 (2011) 1017–1023.

[161] Q.L. Wu, L. Xiang, Y. Jin, Influence of CaCl2 on the hydrothermal modification of Mg(OH)2, Powder Technol. 165 (2006) 100–104.

[162] Y. Ding, G. Zhang, H. Wu, B. Hai, L. Wang, Y. Qian, Nanoscale magnesium hydroxide and magnesium oxide powders: Control over size, shape, and structure via hydrothermal synthesis, Chem. Mater. 13 (2001) 435–440.

[163] J. Lv, L. Qiu, B. Qu, Controlled growth of three morphological structures of magnesium hydroxide nanoparticles by wet precipitation method, J. Cryst. Growth. 267 (2004) 676–684.

[164] D. An, X. Ding, Z. Wang, Y. Liu, Synthesis of ordered arrays of magnesium hydroxide nanoparticles via a simple method, Colloids Surfaces A Physicochem. Eng. Asp. 356 (2010) 28–31.

[165] X. Song, S. Sun, D. Zhang, J. Wang, J. Yu, Synthesis and characterization of magnesium hydroxide by batch reaction crystallization, Front. Chem. Sci. Eng. 5 (2011) 416–421.

[166] X. Song, K. Tong, S. Sun, Z. Sun, J. Yu, Preparation and crystallization kinetics of micron-sized Mg(OH)2 in a mixed suspension mixed product removal crystallizer, Front. Chem. Sci. Eng. 7 (2013) 130–138.

[167] A. Alamdari, M.R. Rahimpour, N. Esfandiari, E. Nourafkan, Kinetics of magnesium hydroxide precipitation from sea bittern, Chem. Eng. Process. Process Intensif. 47 (2008) 215–221.

[168] A. Cipollina, M. Bevacqua, P. Dolcimascolo, A. Tamburini, A. Brucato, H. Glade, et al., Reactive crystallisation process for magnesium recovery from concentrated brines, Desalin. Water Treat. 55 (2015) 2377–2388.

[169] National Institute of Standards and Technology, IUPAC-NIST Solubility Database, (2017). https://srdata.nist.gov/solubility/ (accessed December 7, 2017).

[170] A. Cipollina, G. Micale, A. Brucato, A. Tamburini, M. Bevacqua, G. Cerniglia, Reattore e procedimento per effettuare reazioni selettive, 102015000042831, 2015.

[171] W.L. Mc Cabe, J.C. Smith, P.H. Harriot, Unit operations of chemical engineering., 1993.

[172] J.W. Mullin, Crystallisation, 4th Edition By J. W. Mullin. 2001. Butterworth Heinemann: Oxford, UK. 600 pp. £75.00. ISBN 075-064-833-3., Org. Process Res. Dev. 6 (2002) 201–202.

[173] W.L. (Warren L. McCabe, J.C. (Julian C. Smith, P. Harriott, Unit operations of chemical engineering, McGraw-Hill, 2005.

[174] Z. Zhang, Y. Zheng, Y. Ni, Z. Liu, J. Chen, X. Liang, Temperature- And pH-dependent morphology and FT-IR analysis of magnesium carbonate hydrates, J. Phys. Chem. B. 110 (2006) 12969–12973.

[175] Huber, MAGNIFIN H5, (2017). http://www.magnifin.com/magnifin_flame.htm (accessed December 13, 2017).

[176] H.F. Ayyildiz, H. Kara, Boron removal by ion exchange membranes, Desalination. 180 (2005) 99–108.

[177] J.A. Wiśniewski, M. Kabsch-Korbutowicz, Bromate removal in the ion-exchange process, Desalination. 261 (2010) 197–201

[178] F. Durmaz, H. Kara, Y. Cengeloglu, M. Ersoz, Fluoride removal by donnan dialysis with anion exchange membranes, Desalination. 177 (2005) 51–57.

[179] O. Altintas, A. Tor, Y. Cengeloglu, M. Ersoz, Removal of nitrate from the aqueous phase by Donnan dialysis, Desalination. 239 (2009) 276–282.

[180] D. Berdous, D.E. Akretche, Recovery of metals by Donnan dialysis with ion exchange textiles, Desalination. 144 (2002) 213–218. doi:10.1016/S0011-9164(02)00314-4.

[181] A.A. Pilarska, Ł. Klapiszewski, T. Jesionowski, Recent development in the synthesis, modification and application of Mg(OH) 2 and MgO: A review, Powder Technol. 319 (2017) 373–407.

[182] L. Kumari, W.Z. Li, C.H. Vannoy, R.M. Leblanc, D.Z. Wang, Synthesis, characterization and optical properties of Mg(OH)2 micro-/nanostructure and its conversion to MgO, Ceram. Int. 35 (2009) 3355–3364.

LIST OF ISI PUBLICATIONS AND PRESENTATIONS AT INTERNATIONAL CONFERENCES

- M. Bevacqua, A. Tamburini, M. Papapetrou, A. Cipollina, G. Micale, A. Piacentino. Reverse electrodialysis with NH_4HCO_3-water system for heat-to-power conversion. Energy, 137 (2017) 1293-1307

- M. Bevacqua, A. Carubia, A. Cipollina, A. Tamburini, M. Tedesco, G. Micale, Performance of a RED system with Ammonium Hydrogen Carbonate solutions, Desalination for Clean water and Energy, 57, (2016) 23007-23018

- A. Cipollina, M. Bevacqua, P. Dolcimascolo, A. Tamburini, A. Brucato, H. Glade, L. Buether, G.Micale, Reactive crystallisation process for magnesium recovery from concentrated brines. Desalination and Water Treatment, 55, (2015) 2377-2388

SUBMITTED PAPERS

- M. Micari, M. Bevacqua, A. Tamburini, A. Cipollina, G. Micale, W. Van Baak, T. Puts, Effect of different aqueous solutions of pure salts and salt mixture in closed-loop reverse electrodialysis system, Journal of Membrane Science – (2017)

PRESENTATIONS AT INTERNATIONAL CONFERENCES

- Tamburini, M. Bevacqua, M. Papapetrou, G. Micale, A. Cipollina, ResourSEAs company: sustainable magnesium hydroxide extraction from salty solutions via a novel membrane reactor, Desalination for Clean Water and Energy: Cooperation around the World – Tel Aviv (Israel), 9-12 May 2017

- M. Bevacqua, A. Cipollina, A. Tamburini, G. Micale, A. Piacentino, Reverse electrodialysis with NH_3-CO_2 water system for heat-to-power conversion, Sustainable Development of Energy, Water and Environment System, Lisbon, 4-9 September 2016

- M. Bevacqua, G. Plano, P. Montesanto, A. Cipollina, A. Tamburini, G. Micale, Thermal regeneration of ammonium bi-carbonate solutions for closed-loop reverse electrodialysis, Desalination for the Environment, Clean, Water and Energy, Rome, 22-26 May 2016

- M. Bevacqua, A. Cipollina, A. Tamburini, A. Brucato, G. Micale, Magnesium recovery from exhausted brine, EIP Water Conference , Leeuwarden (The Netherlands), 10 February 2016

- M. Bevacqua, A. Cipollina, A. Tamburini, A. Brucato, G. Micale, Magnesium recovery from exhausted brine, Exchange of good practices on metal by-products recovery, Brussels (Belgium), 12-13 November 2015

- Tamburini, A. Cipollina, M. Bevacqua, L. Gurreri, M. Papapetrou, W. Van Baak, G. Micale, A novel Reverse Electrodialysis application to generate power from low grade heat, EuroMembrane, Aachen (Germany), 06-10 September 2015

- M. Bevacqua, G. Cerniglia, A. Cipollina, A. Tamburini, A. Brucato, G. Micale, An Ion Exchange Membrane Crystallisation reactor for Magnesium recovery from brines, EuroMembrane, Aachen (Germany), 06-10 September 2015

- M. Bevacqua, A. Brucato, G. Cerniglia, A. Cipollina, C. Gatz, H. Glade, G. Micale, A.Tamburini, A continuous plug flow reactor for magnesium recovery from concentrated brine, Desalination for the Environment, Clean Water and Energy, Palermo, 10-14 May 2015

- M. Bevacqua, A. Carubia, A. Cipollina, A. Tamburini, M. Tedesco, G. Micale, Performance of a RED system with Ammonium Hydrogen Carbonate solutions, Desalination for the Environment, Clean Water and Energy, Palermo, 10-14 May 2015

PRESENTATIONS AT NATIONAL CONFERENCES

- M. Bevacqua, A. Cipollina, A. Tamburini, A. Brucato, G. Micale, Magnesium recovery from exhausted brine, GRICU 2016 “Gli orizzonti 2020 dell’Ingegneria Chimica”, Anacapri (Italy), 12 - 14 September 2016

- F. Giacalone, A. Tamburini, M. Bevacqua, L. Gurreri, A. Cipollina, G. Micale, RED Heat-to-Power: conversione di calore di scarto in energia elettrica mediante elettrodialisi inversa a ciclo chiuso, GRICU 2016 “Gli orizzonti 2020 dell’Ingegneria Chimica”, Anacapri (Italy), 12 - 14 September 2016

- M. Papapetrou, M. Bevacqua, A. Cipollina, A. Tamburini, D. Xevgenos, G. Micale, ZERO BRINE - From industrial waste water to resources. H2020 Innovation Action Project; Ecomondo, 7 - 10 November 2017

AWARDS

- Award “II edizione - Premio al talento e all’innovazione alla memoria di Daniele Ragaglia” by the department of industrial and digital innovation (DIID) – October 2017

- First position at “Premio Nazionale all’innovazione” with the Spin-off “ResourSEAs” in the Industrial category – Maurizio Bevacqua, Andrea Cipollina, Giorgio Micale, Alessandro Tamburini, Michael Papapetrou – December 2016

- First position at StartCup Sicilia (2016) with the Startup “Seawater Resources (ResourSEAs)” – Maurizio Bevacqua, Andrea Cipollina, Giorgio Micale, Alessandro Tamburini, Michael Papapetrou – October 2016

- First position at StartCup Palermo (2016) with the Startup “Seawater Resources (ResourSEAs)” – Maurizio Bevacqua, Andrea Cipollina, Giorgio Micale, Alessandro Tamburini, Michael Papapetrou – October 2016

- Palermo Smart City competition (2016) with the project “Utilizzo di tecnologie di produzione di energia rinnovabile da fonte idrica per la zona costa sud di Palermo” - Maurizio Bevacqua, Valentina Vaccaro, Eleonora Spada, Michele Fiorelli – April 2016